

**MULTIWAVELENGTH STUDY OF SOLAR
ERUPTIVE PHENOMENA
(SPACE-WEATHER EVENTS) AND THEIR
INTERPLANETARY RESPONSE**

THESIS

submitted for the degree of
**DOCTOR OF PHILOSOPHY
(PHYSICS)**

to

Kumaun University, Nainital

By

Pankaj Kumar

**Aryabhata Research Institute of observational
sciencES (ARIES)
Manora Peak, Nainital 263 129, India**

October 2010

DECLARATION

I hereby declare that the work presented in this thesis is a result of the investigation carried out by me at the Aryabhata Research Institute of Observational Sciences (ARIES), Nainital, under the joint supervision of Dr. Wahab Uddin (Aryabhata Research Institute of Observational Sciences, Nainital), Prof. P. K. Manoharan (Radio Astronomy Centre, Tata Institute of Fundamental Research, Ooty) and Dr. Shuchi Bisht (Department of Physics, Kumaun University, Nainital). This thesis has not been submitted for the award of any degree, diploma, associateship or fellowship of any University or Institute.

Place : Nainital

Date : October, 2010

(Pankaj Kumar)

CERTIFICATE FROM THE SUPERVISOR

This is to certify that

1. The synopsis of the thesis entitled “**Multiwavelength Study of Solar Eruptive Phenomena (Space-Weather events) and Their Interplanetary Response**” for the award of the degree of Doctor of Philosophy in Physics was approved by the Kumaun University, Nainital.
2. This thesis embodies the work of Mr. Pankaj Kumar himself.
3. Mr. Pankaj Kumar worked under the joint supervision of myself, Prof. P. K. Manoharan (Radio Astronomy Centre, Tata Institute of Fundamental Research, Ooty) and Dr. Shuchi Bisht (Department of Physics, Kumaun University, Nainital) for this thesis as a Research Fellow at the Aryabhata Research Institute of Observational Sciences (ARIES), Nainital. He has put in more than 200 days of attendance at ARIES, Nainital during this period.
4. This thesis has not been submitted before for the award of any degree, diploma, associateship or fellowship of any University or Institute.

Place : Nainital

Date : October, 2010

(Dr. Wahab Uddin)
ARIES, Manora Peak
Nainital-263129

CERTIFICATE FROM THE CO-SUPERVISORS

This is to certify that

1. The synopsis of the thesis entitled “**Multiwavelength Study of Solar Eruptive Phenomena (Space-Weather events) and Their Interplanetary Response**” for the award of the degree of Doctor of Philosophy in Physics was approved by the Kumaun University, Nainital.
2. This thesis embodies the work of Mr. Pankaj Kumar himself.
3. Mr. Pankaj Kumar worked under our supervision on this thesis as a Research Fellow at the Aryabhata Research Institute of observational sciencES (ARIES), Nainital.
4. This thesis has not been submitted before for the award of any degree, diploma, associateship or fellowship of any University or Institute.



(Dr. Shuchi Bisht)

Department of Physics, Kumaun University,
Nainital 263 002

Place: Nainital

Date : October, 2010

(Prof. P. K. Manoharan)

Radio Astronomy Centre (TIFR),
Ooty 643 001

Place: Ooty

Date : October, 2010

To my parents

LIST OF PUBLICATIONS

Related to thesis :

1. Evolution of Solar Magnetic Field and Associated Multiwavelength Phenomena: Flare Events on 2003 November 20.
Pankaj Kumar, P. K. Manoharan and Wahab Uddin, **The Astrophysical Journal (APJ)**, 2010, Vol. 710, 1195.
2. On the Source of the Super-Storm of Solar-Cycle # 23 associated with the Solar Flares on 18 November 2003.
Pankaj Kumar, P. K. Manoharan and Wahab Uddin, **Advances in Geosciences (ADGEO)**, 2010, in press.
3. Multiwavelength Study of M8.9/3B Solar Flare from AR NOAA 10960.
Pankaj Kumar, A. K. Srivastava, B. Filippov and Wahab Uddin, **Solar Physics**, 2010, Vol. 266, 39.
4. Observation of kink instability during small B5.0 solar flare on 04 June, 2007.
A. K., Srivastava, T.V. Zaqarashvili, **Pankaj Kumar** and M.L. Khodachenko, **The Astrophysical Journal (APJ)**, 2010, Vol. 715, 292.
5. Evidence of Solar Flare Triggering due to Loop-Loop Interaction Caused by Footpoint Shear-Motion.
Pankaj Kumar, A. K. Srivastava, B. V. Somov, P. K., Manoharan, R. Erdélyi and Wahab Uddin, **The Astrophysical Journal (APJ)**, 2010, in press.
6. MultiWavelength View of Flare Events on 20 November 2003.
Pankaj Kumar, P. K. Manoharan and Wahab Uddin, **Astrophysics and Space Science Proceedings (ASSP)**, 2010, 471.

Others:

1. Observation of multiple sausage oscillations in cool post-flare loop.
A. K., Srivastava, T. V., Zaqarashvili, Wahab Uddin, B. N., Dwivedi and **Pankaj Kumar**, **Monthly Notices of the Royal Astronomical Society (MNRAS)**, Vol. 388, 1899.
2. Evidence of Magnetic Reconnection Outflows in a Flare seen by Hinode/EIS.
Pankaj Kumar, A. K., Srivastava and Wahab Uddin, **Astrophysics and Space Science Proceedings (ASSSP)**, 2010, 525.
3. Major Surge Activity of Super-Active Region NOAA 10484.
Wahab Uddin, **Pankaj Kumar**, A. K., Srivastava and Ramesh Chandra, **Astrophysics and Space Science Proceedings (ASSP)**, 2010, 478.
4. Ionospheric Response to the Space Weather Event of 18 November 2003-An Investigation.
Pankaj Kumar, Wahab Uddin, Alok Taori, Ramesh Chandra and Shuchi Bisht, **Indian Journal of Radio and Space Physics (IJRSP)**, 2010, in press.
5. Multiwavelength study of Surge activity and associated Flares on 25 October 2003.
Wahab Uddin, **Pankaj Kumar**, R. Chandra, A.K. Srivastava, B. Schmieder, Shuchi Bisht, **Solar Physics (SP)**, 2010, Under Review.

ACKNOWLEDGEMENTS

I avail this opportunity to express my profound gratitude to my thesis supervisors Dr. Wahab Uddin, Prof. P. K. Manoharan and Dr. Shuchi Bisht for their guidance, inspiration and keen interest in this work. Dr. Wahab Uddin has always been a source of inspiration to me for higher studies in Solar Physics. I am grateful to him for providing me every kind of academic, moral and administrative support thought out this work. I express my heartfelt gratitude to Dr. Shuchi Bisht for her sincere guidance, understanding and moral support at each and every moment. She has always been very kind and generous for me and I feel myself fortunate to have been associated with her over the last few years. I met Prof. P.K. Manoharan for the first time in the year 2008 in National Space Science Symposium (NSSS) in Ooty and got motivated by his work. It was only in the year 2008 when our collaboration started. In spite of his busy schedule, he always gave me his valuable time for discussions. I was highly impressed by the way in which he used to guide and encourage/motivate his students. His teaching and motivating discussions have greatly improved my understanding about the subject. I learnt many things with him and started my carrier in solar physics under his guidance.

I would like to express my deepest gratitude to Prof. Ram Sagar for his guidance and encouragement. Without his cooperation and support, it was very difficult to complete this thesis. I am highly grateful to Dr. A. K. Srivastava for introducing me to several aspects of solar astronomy. We used to have tea together twice daily with wonderful discussions regarding our work. He also encouraged and guided me at various stages of my Ph.D. and we performed lots of work in collaboration. It was a great experience to work with him for many scientific expeditions and other academic programmes. I am thankful to Prof. Boris Filippov and Prof. Boris Somov for helping me at various stages of my work under Indo-Russian project. I am grateful to Prof. Eric Priest, Marks J. Aschawanden, D. Zarro, B. Welsch and Marc DeRosa for the valuable discussions time to time regarding my work. I am very thankful to Dr. Alok Chand Gupta in helping me several times whenever I go to him. I owe my sincere thanks to Dr. Ramesh Chandra and Dr. Salman Ali for their guidance in the initial stage

of my Ph.D. work. My special thanks are due to Dr. M. C. Pande for valuable discussions and motivation during my thesis. I acknowledge the observing staff of solar tower telescope at ARIES (specially Mr. Harish Tiwari) for their assistance during observations. I also thank computer staff (particularly Er. Sanjeet and Mr. Deep Pant) for their crucial help time to time. The timely help rendered by the library staff (specially Dr. Rajesh Kumar) is also thankfully acknowledged.

I thank Bindu for her very pleasant company that I experienced over the last several years. She always comes up with suggestions, consolation and encouragement, whichever is needed in academic and personal matters during good as well as hard times. It is hard to find a beautiful place to work and live like our ARIES campus elsewhere surrounded by high mountains of Nainital at one side and panoramic view of plain areas at the other side. I thank my senior researchers at ARIES Amitava, Manash, Sanjeev, Chirspin, Bhuwan, Raman, Arti, Jessy, Chhavi, Neelam and Himali for their company, timely help and suggestions. It gives me immense pleasure to thank my friends Akash, Rupak, Eshwar and Himali who shared office room with me time to time over the span of five years and always filled our office room with a lively environment.

I made a number of visits to Radio Astronomy Centre, Ooty for my research work over the last few years. It gives me a great pleasure to recall the moments spent in this beautiful hill station of south India which became like my other home town. I thank my Ooty friends Prabhu, Senthil, Mahalaxmi, Agalya, Divya, Shahida, Revathi, Manab and Mujbir Rahman for providing nice company and fun filled environment. My thanks are also due to other friends and staff members of RAC particularly RVS, Magesh, RCS, Ravi, Kalayanasundaram and Jayaram for their timely help and support that made my Ooty stays enjoyable and fruitful.

Most of all I express my gratitude to my parents for their blessings, love and affection. They have always given me the strength and wisdom to be sincere in my work and always motivating me time to time. I thank my elder brother, Diddi, Jijaji for their love and wishes.

Pankaj Kumar
10 October, 2010

Notations & Abbreviations

All the notations and abbreviations have been explained on their first appearance in the text. The most frequently used notations and abbreviations are collected here for quick referencing. If a symbol has been used in a different connection than listed here, the same has been explained at the appropriate place.

λ	Wavelength
B	Magnetic field
HXR	Hard X-ray
SXR	Soft X-ray
MW	Microwave
EUV	Extreme Ultraviolet
UV	Ultraviolet
WL	White-Light
NOAA	National Oceanic and Atmospheric Administration
AR	Active Region
keV	Kilo electron volt
kHz	Kilo Hertz
GHz	Giga Hertz
SFU	Solar flux unit = 10^{-22} W m ⁻² Hz ⁻¹
PFU	Proton flux unit = 1 particle cm ⁻² s ⁻¹ sr ⁻¹
T	Temperature
EM	Emission measure
k	Boltzman constant
MK	Million Kelvin
MHD	Magnetohydrodynamics
ϕ	Magnetic flux
CME	Coronal Mass Ejection
R_{\odot}	Solar radius
Dst	Disturbance storm time
nT	nano Tesla
AU	Astronomical unit = 1.495978×10^8 km

LDE	Long duration event
SEP	Solar energetic particles
CCD	Charge Coupled Device
IMF	Interplanetary Magnetic Field
IPS	Interplanetary Scintillation
ORT	Ooty Radio Telescope
ARIES	Aryabhata Research Institute of observational SciencES
SMM	Solar Maximum Mission
LASCO	Large Angle Spectroscopic Coronagraph
SOHO	Solar and Heliospheric Observatory
EIT	Extreme Ultraviolet Imaging Telescope
MDI	Michelson Doppler Imager
RHESSI	Reuven Ramaty High Energy Solar Spectroscopic Imager
SGD	Solar Geophysical Data
TRACE	Transition Region and Coronal Explorer
GOES	Geostationary Operational Environment Satellites
NGDC	National Geophysical Data Center
SOT	Solar Optical Telescope
EIS	Extreme-Ultraviolet Imaging Spectrometer
XRT	X-Ray Telescope
STEREO	Solar TERrestrial RELations Observatory
SECCHI	Sun Earth Connection Coronal and Heliospheric Investigation
RSTN	Radio Solar Telescope Network
ACE	Advanced Composition Explorer
NoRH	Nobeyama Radioheliograph
SDO	Solar Dynamics Observatory

Contents

1	Introduction	1
1.1	Sun and Space-Weather	1
1.2	Solar Eruptive Phenomena (Space-Weather Events)	2
1.2.1	Solar Flares	2
1.2.2	Prominence/Filament Eruptions	12
1.2.3	Coronal Mass Ejections (CMEs)	15
1.2.4	Relationship between Solar Flares, Prominence Eruptions, and CMEs	26
1.3	Theories of Solar Eruptions	31
1.3.1	Theories of Solar Flares	33
1.3.2	Models of Coronal Mass Ejections	35
1.4	Motivation of thesis and open issues	42
1.5	Organization of thesis	44
2	Data Set and Analysis Procedure	45
2.1	Introduction	45
2.2	ARIES Solar Tower Telescope	46
2.2.1	The telescope	46
2.2.2	Bernhard Halle H α filter	47
2.2.3	The detector	48
2.3	Ooty Radio Telescope and IPS measurements	50
2.3.1	The telescope	50
2.3.2	Interplanetary Scintillation	51
2.4	Other instruments and data catalogues	56
2.4.1	Solar and Heliospheric Observatory	56

2.4.2	The Reuven Ramaty High-Energy Solar Spectroscopic Imager (RHESSI)	59
2.4.3	TRACE	60
2.4.4	Hinode	60
2.4.5	STEREO	62
2.4.6	Nobeyama Radioheliograph (NoRH)	63
2.4.7	Omni data	65
2.4.8	SOHO/LASCO CME catalogue	65
3 Evolution of Solar Magnetic Field and Associated Multiwavelength Phenomena: Flare events on 20 November 2003		
3.1	Introduction	67
3.2	Observations	69
3.2.1	H α Observations	72
3.2.2	Magnetogram Images	76
3.2.3	Radio Measurements	79
3.2.4	EUV and White-light Observations	83
3.2.5	Scintillation Images and Interplanetary Data	85
3.3	Discussion	89
4 On the Sources of the Super-storm of Solar-Cycle # 23 Associated with the Solar Flares on 18 November, 2003		
4.1	Introduction	91
4.2	Observations & Data	94
4.2.1	H α Observations	94
4.2.2	TRACE and GOES/SXI images	99
4.2.3	EIT and White light observations	103
4.2.4	Radio Observations	108
4.3	Interplanetary Consequences	112
4.4	Discussions	114

5	Multiwavelength Study of Solar Flares from AR NOAA 10960	117
5.1	Introduction	117
5.2	Multiwavelength Observations of NOAA 10960 and Associated Flares	120
5.2.1	<i>Hinode</i> /SOT Observations	122
5.2.2	TRACE, STEREO/SECCHI/EUVI and <i>Hinode</i> /XRT Observations	124
5.3	Sunspot Evolution in SOHO/MDI and SOT/G Band Images	131
5.4	Kink Instability During B5.0 Class Flare	137
5.5	Discussion	139
5.6	Conclusions	146
6	Evidence of Solar Flare Triggering Due to Loop-Loop Interaction Caused by Footpoint Shear-Motion	149
6.1	Introduction	149
6.2	Observations and Data	153
6.2.1	GOES SXI and TRACE Observations	153
6.2.2	Radio and RHESSI Observations	161
6.2.3	Evolution of Active Region	165
6.2.4	Magnetic Topology of the Interacting Loop-Systems	167
6.3	Some Theoretical Estimations	172
6.4	Discussions and Conclusions	175
7	Summary and Future Scope	179
	References	202

List of Figures

1.1	The Sun, the interplanetary medium and the near-Earth environment represent the region in which space weather plays out (courtesy of NASA).	2
1.2	Sketch of the first reported solar flare. The flare was observed by Carrington in white light on 1859 September 1 (Carrington, 1859). White regions marked as A, B, C, and D are the flaring regions.	4
1.3	A schematic representation of the different phases of a solar flare as observed in the electromagnetic and particle radiation (from Kane 1974).	8
1.4	Images of different solar flares at different wavelengths. (a) A large historical two ribbon 4B/X17.2 class flare of October 28, 2003 from ARIES, Nainital (courtesy of Wahab Uddin) (b) TRACE EUV Post-flare loops of the famous ‘Bastille Day Flare’ observed at 195 Å on July 14, 2000. (c) Soft X-ray cusp-shape post-flare loop observed by Hinode/XRT on December 17, 2006. (d) and (e) Hard X-ray and Microwave images of different flares observed by RHESSI and Nobeyama Radioheliograph, respectively.	9
1.5	Filaments and Prominences observed in H α by KSO (Kanzelhoehe Solar Observatory) and BBSO (Big Bear Solar Observatory).	13
1.6	Images of filament/prominence eruptions in EUV. Left: A large eruptive prominence observed by SOHO/EIT at 304 Å (He II) on 2000 January 12. Right: A filament eruption on July 19, 2000 observed by TRACE at 171 Å.	14

1.7	Top: Protoypical “3-part CME” as observed by Solar Maximum Mission (SMM), halo CMEs from LASCO. Middle: Two views of flux rope CMEs (LASCO). Bottom-left: SOHO/LASCO image (with an EIT 195 Å image superposed) on 20 December 2001 showing the 3 part structure of a CME above the southwest limb. Bottom-right: A standard model for a “three-part” CME or eruptive flare (Forbes, 2000).	17
1.8	Dynamic solar radio spectrum showing schematically the basic types of solar radio bursts. Time runs from left to right, frequency decreases from bottom to top (corresponding to increasing height in the solar atmosphere). Time is given in minutes, frequency in MHz.	21
1.9	When a CME travels into IP space, It can create a huge magnetic cloud containing bidirectional, or counterstreaming, beams of electrons that flow in opposite directions within the magnetic loop that are cooled at both ends at the Sun. The magnetic cloud also drives an upstream shock ahead of it. Magnetic clouds are only present in a subset of observed interplanetary coronal mass ejections. (Courtesy of Deborah Eddy and Thomas Zurbuchen) .	24
1.10	Magnetic reconnection takes place at the boundary of magnetosphere if interplanetary magnetic field is southward and solar wind/CME energy is pushed into the magnetosphere, which causes geomagnetic storms at Earth due to the formation of ring current above the equator.	25
1.11	Top: Large CMEs from active region 10486 during October-November 2003 observed by SOHO/LASCO. The first two are symmetric full halos because the CMEs originated from close to the disk center. The last two CMEs occurred when AR was close to the west limb, so they appear as partial halos. Bottom: A plot of Dst index for the interval October 28 to November 7 2003. the CMEs responsible for significant Dst events are shown by arrows from Gopalswamy et al. (2005b)	27

1.12 Schematic magnetic field configuration and flow pattern for a CME and flare. The upper part of the diagram shows the flux rope model of CMEs advocated by Lin & Forbes (2000) , showing the eruption of the flux rope, current sheet formed behind it, and the post flare loops below, as well as the inflow and outflows associated with the magnetic reconnection at the current sheet. the lower part of the image is an enlarged view of the post flare loops, adapted from Forbes & Acton (1996) . The upper tip of the reconnection cusp rises as reconnection proceeds.	32
1.13 Flare model after some modification by Lang (2001)	34
1.14 Schematic representation of arcade-like and flux-rope like coronal magnetic field geometry (Klimchuk, 2001).	35
1.15 Physical analogies of five different coronal mass ejections model. From top to bottom: 1) thermal blast model, 2) dynamo model, 3) mass loading model, 4) tether cutting model, 5) tether straining model (Klimchuk 2001 ; adopted from Aschwanden 2004a).	38
1.16 Magnetic field configuration in the “Break-out” model (Antiochos et al., 1999). A force free current is created by shearing the arcade field (thick lines) at the equator. A toroidal current layer is also created as the sheared region bulges outwards. Reconnection of the field lines in the horizontal current sheet allows the sheared field lines to open outward to infinity.	41
2.1 A view of 15 cm Coudé refractor with back-end instruments, installed on a 35-feet high tower which is used for solar observations at ARIES, Nainital.	47
2.2 Schematic drawing of the Coudé refractor for H α observations. . .	48
2.3 The quantum efficiency curve for CCD detector described in section 2.2.3	49
2.4 Left: A view of the Ooty radio telescope, which is 530 m long and 30 m wide (Swarup et al., 1971). The right image shows the closer view of the telescope.	51

2.5	Schematic diagram illustrating the geometry of the formation of interplanetary scintillation. The angle between the Sun, the Earth and the radio source is the solar elongation (ϵ). Heliocentric distance to the radio path = $\sin\epsilon$ AU.	53
2.6	Variation of scintillation index as a function of distance from the Sun for the quasar 1148-001 at 327 MHz	54
2.7	Top: White-light images of the flux rope CME from LASCO/SOHO C2 coronagraphs on September 07, 2005. Bottom: A three-dimensional remote-observer view of the heliospheric density obtained from the reconstruction of Ooty IPS measurements on 07 September 2005. Each presentation covers a field of view of 3 AU and with the Sun located at the center. The orbit of the Earth is shown by an ellipse. The Earth is located to the right of each image (shown as a blue dot). In these maps, different solar wind disturbances can be observed to move outward. Flux-rope type features associated with the propagating CMEs can also be seen. The observer is located $\sim 30^\circ$ above the ecliptic plane and $\sim 90^\circ$ west of the Sun–Earth line (Manoharan, 2010).	55
2.8	This figure shows the 1995-11-10 flare. The upper (northern) radio source can be seen in common at 17 GHz, 34 GHz, while the bottom (southern) source can only be seen in left-handed circular polarization image at 17 GHz. This means this source comes from the site where the magnetic field is strong (Takano et al., 1997). . .	64
3.1	SOHO/MDI magnetogram of the active region NOAA 10501 on 20 November 2003. White light image of the active region is shown inside the box.	70
3.2	GOES soft X-ray flux measurements in 0.5-4 Å and 1-8 Å wavelength bands (top) and time profiles of the H α relative intensity with respect to the background emission for both flares.	71
3.3	H α images of the first flare (1N/M1.4) showing the evolution of filaments and their interaction. The size of each image is 315'' \times 315''.	72

3.4	Nobeyama 17-GHz contours overlaid on MDI image (top, left) and on H α image (top, middle), and GOES/SXI image showing the X-ray source location (top, right). The schematic cartoons show the evolution of the first flare, i.e., approaching and interacting filaments followed by magnetic reconnection.	73
3.5	The distance between two filaments plotted as a function of time. The straight line is the least square fit to the data points. The typical inflow speed is $\sim 10 \text{ km s}^{-1}$. The H α intensity of this event attains maximum between 01:53 and 02:00 UT.	74
3.6	H α images of the second flare (2B/M9.6) show the evolution of field lines. The dark cusp shows the mass motion at the height in the low corona. The size of each image is $315'' \times 315''$	75
3.7	Plot showing the cusp height variation and ribbon separation as a function of time during the flare. After $\sim 07:45$ UT, the H α profile attains the maximum at which the cusp height stabilizes.	77
3.8	MDI magnetograms of the active region on 20 November 2003, showing the clockwise rotation of positive polarity sunspot and anticlockwise rotation of negative polarity sunspot (shown by arrows).	78
3.9	Left: MDI contours overlaid on H α image during the second flare event. Right: MSFC shear map of the active region showing the maximum shear at the flare site in between the sunspots on 19 November 2003 at 19:36 UT, is shown for comparison.	79
3.10	The relative position change with time of opposite polarity sunspots showing the motion of the both sunspots.	80
3.11	The schematic cartoon showing the second flare evolution with one highly twisted filament destabilization in association with rotating sunspots and merging with another curved filaments, forming a cusp and resulting CME eruption.	80

3.12	Time profiles of radio flux densities observed at eight frequency bands from Learmonth observatory for the first and second flares, respectively. These plots have been made in same scales for an easy comparison of strength of these flares. It is evident that second event is complex and more intense. Time profiles of radio flux density at the reconnection time (or interaction between filaments) observed at 610, 1415, and 2695 MHz is shown in between two vertical dotted lines. The time lag of ~ 2.5 sec is evidently shown between 2695 and 610 MHz. The coronal height increases from bottom to top.	82
3.13	Type III bursts associated with both flare events on 20 November, 2003 (Learmonth, Australia). These intense bursts provide evidence for the opening of field lines at the time of reconnection.	83
3.14	EIT difference images of the second flare at the maximum (7:48 UT) (left) and coronal dimming (right), which shows the evacuation of coronal mass during the launch of the CME.	84
3.15	Difference images from C2 and C3 LASCO coronagraphs for both CMEs. Top panels show the CME associated with first 1N/M1.2 class flare whereas bottom panels display the CME associated with 3B/M9.6 flare.	84
3.16	Height-time plot of cusp movement and its CME associated with second flare.	86
3.17	3-D view of of the heliosphere obtained from a large number of IPS measurements (i.e., Manoharan 2006). The CME location with respect to the ecliptic plane is shown. The top images are 3-D view and bottom images are ecliptic view.	87
3.18	The interplanetary observations of magnetic field strength B , B_θ , southward component of magnetic field (B_z), geomagnetic index (Dst), solar wind speed and proton density. The arrival of the shock is marked by the vertical line.	88
4.1	SOHO/MDI and white-light images of the active region NOAA 10501 on 18 November 2003.	93

4.2	GOES soft X-ray, EUV flux and H α relative intensity profiles for the flares on 18 November 2003.	95
4.3	Temperature and emission measure profiles derived from soft X-ray profiles in two wavelength bands for the flares on 18 November 2003.	96
4.4	H α images showing the evolution of C3.8 flare. The size of each image is 430'' \times 360''	97
4.5	H α images showing the evolution of M3.2 flare. The size of each image is 430'' \times 360''.	98
4.6	H α images showing the evolution of M3.9 flare. The size of each image is 430'' \times 360''.	99
4.7	MDI contours overlaid on H α images at different times. White contours show positive polarity sunspots whereas black contours indicate negative polarity sunspots.	100
4.8	Potential field extrapolations for active region NOAA 10501 over MDI (top left) and H α images for C3.8, M3.2 and M3.9 flares on 18 November 2003. Green or white indicates the closed field lines whereas red or black shows the open field line structure.	101
4.9	TRACE 195 Å (Fe XII line) images showing the flare evolution with filament eruption (first one). The image at 07:41:56 (second top) shows the H α filament contours overlaid on TRACE 195 Å image. This image confirms the eruption of two different channels of the same filament (first visible in EUV and second one in H α , indicated by arrows). The second bottom image (07:56:27 UT) shows the presence of filament channel in H α while the first filament channel moved away from TRACE field of view.	102
4.10	MDI contours overlaid on TRACE 171 and 195 Å images at different times respectively. White contours show positive polarity sunspots whereas black one indicate negative polarity sunspots (contour levels=2000, 1000, 500, -500, -1000, -2000). The left panel shows the huge U shaped filament structure along the polarity inversion line (shown by arrow). The right panel shows the eruption of filament channel near the eastern footpoint of the filament. . .	103

4.11	GOES soft X-ray (SXI) images showing the filament eruption (indicated by arrow) associated with second M3.2 flare. The size of each image is $500'' \times 500''$	104
4.12	Filament eruption height-time profiles in GOES SXI, TRACE 195 Å and H α during the flare events.	105
4.13	GOES Soft X-ray flux with filament height-time profiles estimated from GOES SXR and H α images.	106
4.14	Difference images of EIT images which shows the filament eruptions (top 2 rows) and EIT wave (bottom 2 rows) during the flare events.	107
4.15	Difference images of CME from C2 and C3 LASCO coronagraphs on SOHO showing three CMEs associated with solar flares.	109
4.16	Composite radio spectra from Wind/WAVES (1-14 MHz) and Learmonth (25-180 MHz) on 18 November 2003.	110
4.17	The height-time profile of filament eruption observed in SXI (left) and H α (right), type II and CMEs associated with them (LASCO C2 & C3).	110
4.18	The interplanetary observations of magnetic field (B), B_θ , B_ϕ , Dst Index, solar wind speed, proton density and temperature during 19–23 November 2003.	111
4.19	The linkage of two merged magnetic clouds in the interplanetary medium with the solar sources.	112
4.20	Ooty 3-dimensional IPS density images showing the two merging magnetic clouds (shown inside the ellipse) hitting the Earth on 20 November, 2003.	113

5.1	Top: SOHO/MDI image of active region NOAA 10960 on 04 June 2007. The positive-polarity sunspot indicated by arrow plays an important role in triggering the M8.9/3B solar flare. The enlarged view of the sunspot group of the active region as indicated by a box in SOHO/MDI image, is shown in the SOT/blue continuum (4504 Å) image (bottom-left panel). A more closer view of the positive-polarity sunspot as indicated by a box in the SOT/blue continuum image, is also shown in the bottom-right image. Penumbra filaments, twisted in the counterclockwise direction, are clearly evident in this image.	121
5.2	GOES soft X-ray flux profiles of the flares in 1–8 and 0.5–4 Å wavelength bands on 04 June 2007.	122
5.3	<i>Hinode</i> /SOT Ca II H 3968 Å images showing the successive activation of helical twists and corresponding brightening above the positive-polarity sunspot on 4 June 2007. Secondary helical twist has been activated at ≈05:08 UT and causes the maximum of the M8.9/3B class flare brightening in the chromosphere at ≈05:13 UT. The size of each image is 60"×75".	123
5.4	TRACE 171 Å EUV images (in reversed colors) showing the temporal changes in the magnetic field configuration before the initiation of M-class flare. The size of each image is 200"×200".	125
5.5	STEREO SECCHI 171 Å images (in reversed colors) showing the temporal changes in the magnetic-field configuration and related M8.9/3B flare event. The size of each image is 200"×200".	127
5.6	MDI contours overlaid on STEREO/SECCHI 171 Å EUV images before the flare initiation and during flare progressive phase. Red contours show the positive polarity, while blue ones show the negative polarity. The size of each image is 200"×200".	128

5.7 STEREO/SECCHI A and B images of the twisted helical structure. The secondary helical twist with approximately two turns (indicated by red line) has been activated on 05:08 UT just before the maximum of M8.9/3B class flare (bottom panel). The top-left panel shows, for the comparison, three turns (indicated by red line) during the activation of the first helical twist as estimated by Srivastava *et al.* (2010). The size of each image is $80'' \times 80''$ 129

5.8 Time sequence of HINODE/XRT images of the twisted flaring loop and partial FOV of AR 10960 during 04:40 UT and 04:54 UT on 04 June, 2007. The Hinode/XRT images are co-aligned with TRACE images. 131

5.9 The selected SOHO/MDI images of the flare site. The arrow indicates the evolution of positive magnetic-flux region before and after the flare activity. The size of each image is $70'' \times 60''$ 132

5.10 The selected SOT/G-band images (4305 \AA) showing the evolution of the positive-polarity sunspot (before, during and after the M8.9/3B class flare). The dotted line and boxes reveal the orientation change and disappearance of twisted penumbral filaments respectively after the flare event. The size of each image is $25'' \times 35''$. 133

5.11 Top: Projected height (elongation) *vs.* time profiles of both twisting helical magnetic structures with soft X-ray flux profiles of the flares on 4 June 2007. This plot clearly indicates that the rise of magnetic structures is closely associated with the flare onset. Middle and bottom: Umbral and penumbral changes (indicated by “U” and “P” respectively) in intensity and area to show the link with soft X-ray flux profiles. It is evident from the plot that there are remarkable changes (umbral enhancement and penumbral decay) in both umbra and penumbra after the flare maximum. 135

5.12 Partial FOV of TRACE 171 Å image on 04:48:15 UT at 04 June 2007, which shows the coronal loop segment with strong helical twist. The co-aligned SOT G-band (left panel) and Ca II (right panel) contours are overlaid on TRACE 171 Å image, which show the sunspot position and the chromospheric part of the loop respectively. 136

5.13 Potential field source surface (PFSS) extrapolation of the NOAA AR 10960 at 00:04 UT on 4 June 2007. White lines show the closed magnetic fields whereas green lines show the open fields. 140

5.14 Schematic cartoons demonstrating the magnetic configuration of the active region before and during the flare event. Red contours show the positive-polarity sunspots whereas blue ones indicate the negative-polarity sunspots. 141

5.15 Dependence of average vertical magnetic field at different heights for the active regions NOAA 10501 (dotted curves) and NOAA 10960 (thick curves). Red and blue curves correspond respectively to the positive and negative magnetic field strength. 144

6.1 SOHO/MDI magnetogram showing the NOAA AR 10875 (in the box) at 12:47:01 UT on 27 April, 2006. The enlarged view of the active region is shown in the top-right corner of the image. 152

6.2 Soft X-ray flux, flux derivative, RHESSI and radio flux profiles for the M7.9 flare event on 27 April, 2006. The soft X-ray flux derivative matches well with the hard X-ray flux profile. This implies that the accelerated electrons that produce the hard-X-ray also heat the plasma that produces the soft X-ray (Neupert effect). The dotted line in the third panel indicates the RHESSI night time. 154

6.3	<p>GOES Soft X-ray coronal negative images (6–60 Å) showing the flare evolution with the interaction of two coronal loops on 27 April, 2006. The upper left panel shows a lower loop system (blue) underlying a higher loop system (red). The lower loop first looks brighter during flare initiation. The middle left panel shows the corresponding footpoints of both interacting loops indicated by FP1 (L1) and FP2 (L1) for loop 1 and FP1 (L2) and FP2 (L2) for loop 2, respectively. The bottom left panels shows the flare maximum due to loop-loop interaction and the bottom right panel indicates the simplified 2 loops after the flare energy release. . . .</p>	155
6.4	<p>TRACE 195 Å negative images showing the flare evolution with the interaction of two coronal loops on 27 April, 2006. The upper and middle panels show approaching and interacting loops. The flare initiation takes place as the loops approach and maximizes at the time of interaction. The corresponding footpoints of the interacting loops are indicated by FP1 (L1) and FP2 (L1) for loop 1 and FP1 (L2) and FP2 (L2) for loop 2 respectively. The arrows indicate the interaction region/reconnection site. The bottom right panel shows the relaxation and orientation changes of the loops after interaction.</p>	158
6.5	<p>The thickness of interaction region shown by blue curve (estimated from TRACE 195 Å images) plotted against GOES soft X-ray flux profile (red curve). This plot reveals that as the thickness of interaction region decreases, the soft X-ray flux increases. This may be the most likely signature of ongoing reconnection at the site of loops-interaction. The typical converging speed of interacting region is $\sim 30 \text{ km s}^{-1}$.</p>	159
6.6	<p>Left: MDI contours overlaid on TRACE 195 Å images during flare maximum (Blue contours indicate the negative whereas red contours show the positive polarity sunspots). The contour levels are $\pm 500, \pm 1000, \pm 2000, \pm 3000 \text{ G}$. Right: TRACE 195 Å contours overlaid on MDI magnetogram (Black=negative, White=positive).</p>	160

6.7 Left: PFSS (Potential Field Source Surface) extrapolations overlaid on MDI image at 00:05:00 UT on 27 April, 2006. Right: $H\alpha$ image during the decay phase of the flare showing flare ribbons on the both side of neutral line (NL), indicated by yellow line. The polarity at the location of flare ribbons is indicated by ‘+’ and ‘-’ symbols. 161

6.8 Left: TRACE 1600 Å images showing the the morphology of flare ribbons during the flare. Right: SOHO/MDI magnetic field contours overlaid on TRACE 1600 Å image. Red one indicate the positive polarity whereas blue one show the negative polarity fields. The contour levels are $\pm 500, \pm 1000, \pm 2000, \pm 3000$ G. Ribbons are formed on the both sides of neutral line (NL), drawn by yellow color. 162

6.9 Top panel: Ondrejov dynamic radio spectrum on 27 April, 2006 showing the intense DCIM radio burst during flare initiation. Additionally, there was no Type III burst during this time period (checked with Wind/WAVES spectrum). That means the opening of field lines did not take place during the flare energy release (i.e. during reconnection). The observed DCIM burst is the signature of particle acceleration from the reconnection site during loop-loop interaction/coalescence. Bottom panel: RSTN 1 sec cadence radio flux profiles in 2.6, 4.9, 8.8 and 15 GHz frequencies observed at Sagamore-Hill station. 163

6.10 RHESSI images in 12-25 keV energy bands reconstructed with the PIXON algorithm (contour levels for each image are 40%, 60%, 80% and 95% of peak flux). 165

6.11 RHESSI images in 25-50 keV energy bands reconstructed with the PIXON algorithm (contour levels for each image are 40%, 60%, 80% and 95% of peak flux). 166

6.12 TRACE white-light images of the active region showing the linear/shear motion of negative polarity sunspot (indicated by blue contours). FP1 (red) and FP2 (blue) in the top first image indicate the ‘+ve’ and ‘-ve’ footpoints of the lower loop system respectively. 166

6.13 Left: TRACE 195 Å (white) and MDI magnetogram contours overlaid on TRACE white-light image. Red contours indicate the positive polarity sunspots whereas blue one show the negative polarity spots. The contour levels are $\pm 500, \pm 1000, \pm 2000, \pm 3000$ G. Right: The photospheric velocity map obtained from FLCT (Fourier Local Correlation Tracking) technique using SOHO/MDI magnetograms. The longest arrow corresponds to velocity of 0.291 km s^{-1} 168

6.14 The linear motion of negative polarity sunspot on 27 April, 2006. One footpoint of the loop-system was anchored in this sunspot. The estimated speed of the sunspot from the linear fit is $\sim 0.2 \text{ km s}^{-1}$ (662 km h^{-1}). This motion probably caused the destabilization and interaction in the loop systems. 169

6.15 Magnetic field lines that connect the $H\alpha$ kernels FP1 (L1), FP2 (L1), FP1 (L2), and FP2 (L2) are passing through a region of primary energy release located somewhere near the top of the separator X. The flare ribbons FR1 and FR2 are formed where these field lines cross the photospheric plane PH. NL is the neutral line of photospheric magnetic field. Chromospheric evaporation creates a picture of the crossing soft X-ray loops. 170

6.16 A 3D model of the coronal magnetic field with two interacting electric currents J_1 and J_2 . Four magnetic fluxes of different linkage are separated by the separatrices S_1 and S_2 that cross at the separator X above the photospheric plane PH. The two field lines B_1 and B_2 connect the kernel FP2 (L2) with FP1 (L2) and the kernel FP2 (L1) with FP1 (L1). The coronal currents are distributed somehow inside the two magnetic cells and are shown schematically as the total currents J_1 and J_2 along the field lines B_1 and B_2 170

6.17 Schematic cartoons showing the flare triggering due to interaction of two X-ray loop-system. Black line shows the higher-loop system and dark blue line indicates the smaller underlying loop system. Due to shear motion of the right footpoint of smaller loop system, it becomes unstable and reconnects with the overlying higher loop system, triggering a flare event. After the flare event, the lower loop system becomes simplified as evident in GOES SXI image at 16:31:01 UT (Figure 6.3). 175

List of Tables

1.1	Optical classification	6
1.2	X-ray classification	7
2.1	CCD Characteristics	49
2.2	EIT observations at different bandpasses and their scientific objectives	57
2.3	System parameters for LASCO C1, C2 and C3 coronagraphs	58
2.4	RHESSI characteristics	59
2.5	TRACE Temperature Response (Handy et al., 1999)	61
2.6	NoRH Specifications	64

Chapter 1

Introduction

1.1 Sun and Space-Weather

The term space weather refers to the time-variable conditions in the space environment that may effect space-borne or ground based technological systems and, in the worst case, endanger human health or life. Therefore there are social and economic aspects of this type of research: one tries to avoid consequences of space weather events by system design or efficient warning and prediction. During the last few years space weather activities have expanded world-wide. Space weather affects spacecrafts as well as ground based systems.

The main cause for space weather effects is our Sun (see Figure 1.1). It emits a continuous stream of particles which is called the solar wind. The solar wind is variable. It is modulated by the well known 11 year solar activity cycle. Another source of space weather effects are micrometeorites and other space debris. Related to the solar activity are important effects on spacecraft such as spacecraft charging (surface charging and deep discharges) and single event effects. The effects on humans in space are also to be considered (radiation, particles). Space weather effects also play a role on high altitude/high latitude air-flight; cosmic rays penetrate to the lower atmosphere and pose problems to humans and electronic components of modern aeroplanes. Other influences of space weather include radio wave propagation, satellite-ground communications, global satellite-based navigation systems, power transmission systems etc. Changes of the solar irradiance may be one of the causes for climatic changes on the Earth. Space

1.2 Solar Eruptive Phenomena (Space-Weather Events)

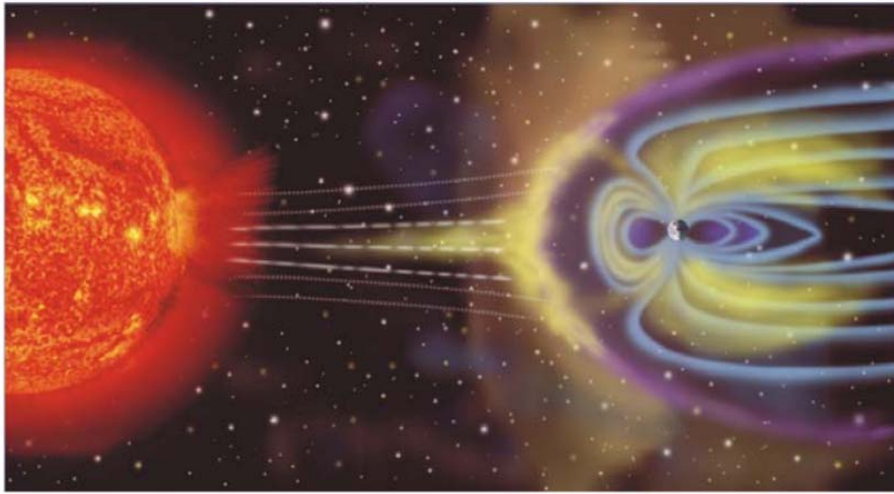


Figure 1.1: The Sun, the interplanetary medium and the near-Earth environment represent the region in which space weather plays out (courtesy of NASA).

debris, such as meteoroids, or parts of old satellites must be also be taken into account and are a permanent threat for space missions.

1.2 Solar Eruptive Phenomena (Space-Weather Events)

1.2.1 Solar Flares

A flare is defined as a sudden, rapid, and intense variation in brightness. A solar flare is an transient explosion in the solar atmosphere, involving sudden bursts of particle acceleration, plasma heating, and bulk mass motion (Priest, 1981; Sturrock, 1980; Svestka, 1976, 1981; Svestka et al., 1992; Tandberg-Hanssen & Emslie, 1988). Solar flares produce radiation across virtually the entire electromagnetic spectrum, from radio waves at the long wavelength end, through optical emission to X-rays and gamma rays at the short wavelength end. each radiation has different emission mechanism in the solar atmosphere. X-rays and UV radiation emitted by solar flares can affect Earths ionosphere and disrupt long-range radio communications. Direct radio emission at decimetric wavelengths may disturb

1.2 Solar Eruptive Phenomena (Space-Weather Events)

operation of radars and other devices operating at these frequencies.

Most flares occur in active regions around sunspots, where intense magnetic fields emerge from the Sun's surface into the corona. Flares are powered by the sudden (timescales of minutes to tens of minutes) release of magnetic energy stored in the corona. The amount of energy released is the equivalent of millions of 100-megaton hydrogen bombs exploding at the same time! As the magnetic energy is being released, particles, including electrons, protons, and heavy nuclei, are heated and accelerated in the solar atmosphere. The energy released during a flare is typically on the order of 10^{27} ergs per second. Large flares can emit up to 10^{32} ergs of energy. This energy is ten million times greater than the energy released from a volcanic explosion. On the other hand, it is less than one-tenth of the total energy emitted by the Sun every second. The frequency of flares coincides with the Sun's eleven year cycle. When the solar cycle is at a minimum, active regions are small and rare and few solar flares are detected. These increase in number as the Sun approaches the maximum part of its cycle. The Sun will reach its next maximum in the year 2011, give or take one year.

History of Solar Flare Research

The first recorded observation of a solar flare was made by R. C. Carrington in 1859 at his private observatory at Redhill, outside London. Carrington (1859) was engaged in his daily sunspot drawing in the forenoon on 1 September 1859 when he first noticed the flare (Figure 1.2). The white-light emission was initially visible at points A and B and during the course of five minutes moved about 50000 km to points C and D where it vanished as two rapidly fading dots of white light. Carrington expressed surprise that the conflagration had in no way alerted the appearance of the sunspot group which he had finished drawing before the occurrence. Fortunately, Carrington's observation was confirmed by Hodgson (1859), an amateur astronomer who was observing nearby.

The history of flare research can be divided into three main periods (for a detailed review see [Svestka et al. 1992](#)). The first period from 1859-1934 spans the careers of Carrington and Hale. This period is notable for the relative lack

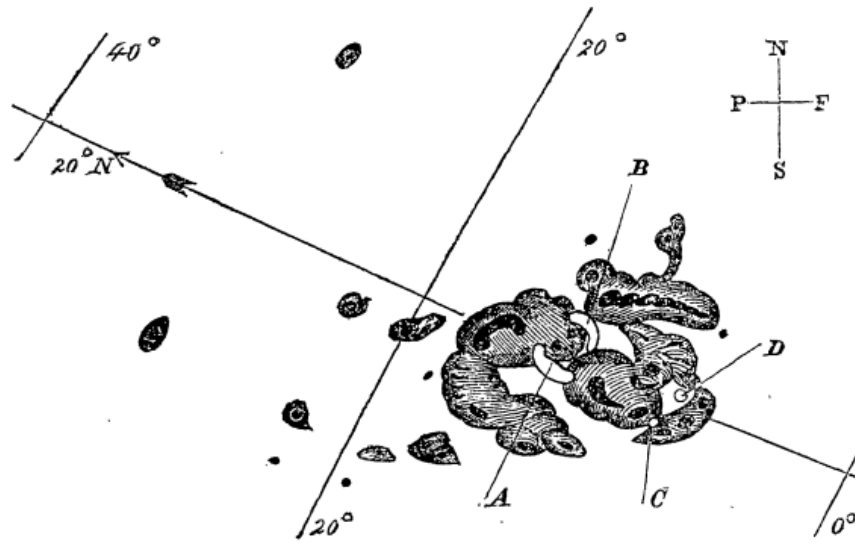


Figure 1.2: Sketch of the first reported solar flare. The flare was observed by Carrington in white light on 1859 September 1 (Carrington, 1859). White regions marked as A, B, C, and D are the flaring regions.

of progress. The published record of major flares for this 75 year interval encompasses only about 35 events, consisting of fortuitous observations of white-light flares, reports by early spectroscopists of reversals of line emission near sunspots, and, after 1892, flares observed with the Hale spectroheliograph. With this spectroheliograph, Hale obtained the first published photographs of a solar flare on 15 July 1892 (Svestka et al. 1992). The spectrohelioscope (an instrument that allowed the entire Sun to be scanned visually at selected wavelengths) developed by Hale during the 1920s was responsible for the rapid advance in the knowledge of flares that took place in the next era of flare research from 1935-1963. The institution of a world-wide flare patrol brought significant advances in knowledge of flares in the 1930s and 1940s and new windows were opened to observe flares at short (soft X-ray, which was indicated by the sudden ionospheric disturbances; Kreplin et al. 1962) and long (radio) wavelengths. In the 1950s and 1960s metric radio bursts were related to trapped energetic electrons and shocks, and two-ribbon flares were associated with energetic protons in space.

Radio and X-ray observations gave evidence for two basic types of flare processes: an impulsive phase followed by a long-duration or gradual phase. It

1.2 Solar Eruptive Phenomena (Space-Weather Events)

was found that flares were often preceded by filament activations, and growing loop prominence systems were recognized as the limb counterpart of two-ribbon disk flares. This middle era of flare research has a data survey and classification character that is well-captured by the book *Solar Flares* by [Smith & Smith \(1963\)](#).

The modern era, since 1963, is characterized by space observations and a trend toward synthesis indicated by the development of increasingly sophisticated and comprehensive models of the flare phenomena. The early 1970s brought Skylab observations of coronal mass ejections (CMEs) and arcades of coronal soft X-ray loops above two-ribbon flares. In the mid-1970s, the Kopp-Penuman reconnection model, based on configurations proposed earlier by Carmichael, Sturrock, and Hirayama, provided a framework in which the newly discovered CMEs could be related to the basic characteristic of two-ribbon flares. The 1980s brought key new results from SMM and Hinotori including images of hard X-ray flares and large-scale coronal structures associated with eruptive flares. The key new results from Yohkoh in the 1990s are: evidence for on-going magnetic reconnection in solar flares, i.e., cusp-shaped soft X-ray arcades in long-duration flares and above-the-loop-top hard X-ray sources in impulsive flares; sigmoidal soft X-ray structures in active regions identified as signatures of the likely onset of flares and CMEs; arcade formation and coronal dimming identified as the soft X-ray counter part of a CMEs ([Kosugi & Acton, 2002](#)). In the 2000s, RHESSI ([Lin et al., 2002](#)) has provided the first capability for gamma-ray imaging as well as high-resolution spectroscopy of ion-produced gamma-ray lines and X-ray imaging spectroscopy of the bremsstrahlung radiation from energetic electrons. One of the key new results of RHESSI is gamma-ray line imaging of solar flares implies spatial differences in acceleration and/or propagation between the flare-accelerated ions and electron ([Hurford et al., 2006, 2003](#)).

Classification of Solar Flares

Solar flares are classified according to their size, duration, morphology or magnetic topology and the composition of their associated energetic particles ([Cliver](#)

1.2 Solar Eruptive Phenomena (Space-Weather Events)

Table 1.1: Optical classification

Area (Millionths of a Solar hemisphere)	Area (Square degree heliographic)	Importance Faint (F), Normal(N) and Bright (B)
<100	<2.0	S (subflare)
100–250	<2.0–5.15	1
250–600	<5.15–12.4	2
600–1200	<12.4–24.7	3
>1200	>24.7	4

& Murdin, 2000). We review two types of classifications that used in this thesis.

Size Classification of Solar Flares : Soft X – ray

There are only two widely used classification systems that address flare ‘size or ‘importance. The first of these is the $H\alpha$ classification scheme (see Table 1.1) that was developed during the 1930s. A second size classification that has come into common usage since about 1970 is based on the integrated total output of soft X-rays detected from the Sun in the 1–8 Å band by Earth-orbiting satellites, such as the GOES satellites. The size of the flare is given by the peak intensity (on a logarithmic scale), in $\text{erg cm}^{-2} \text{s}^{-1}$. As shown in Table 1.2, the letters A, B, C, M and X are used to represent increasing intensities in order-of-magnitude increments. Thus a B-flare has a peak intensity of $10^{-4} \text{ erg cm}^{-2} \text{s}^{-1}$. If the peak intensity happens to be 3×10^{-4} , the flare is designated B3. Generally, flares smaller than C1 can only be detected during a solar cycle minimum when the X-ray background is low. Flares occasionally exceed class X9 in intensity; they are simply referred to as X10, X11 etc events (Cliver & Murdin, 2000).

Classification of Solar Flares in Terms of Morphology (Magnetic Topology)

In this classification, there are two main types of flare, which appear to require different physical mechanisms (Priest, 1981).

1.2 Solar Eruptive Phenomena (Space-Weather Events)

Table 1.2: X-ray classification

Class	Peak Flux (1-8 Å in W m^{-2})
A	$<10^{-7}$
B	$\leq 10^{-6}$ but $>10^{-7}$
C	$\leq 10^{-5}$ but $>10^{-6}$
M	$\leq 10^{-4}$ but $>10^{-5}$
X	$\geq 10^{-4}$

1) Simple – Loop or Compact Flare (Confined Flare)

Most flares and subflares are of this type. It is a small flare, in which essentially a single magnetic loop or flux tube brightens in X-rays and remains apparently unchanged in shape and position throughout the event (Priest, 1981). The loop may have a structure consisting of several (or a continuum of) loops and may cause a simple brightening in $\text{H}\alpha$ at the feet of the loop. Simple-loop flares vary considerably in size, and we may see brightened arches that comprise a whole fully developed active region, as well as short-lived brightenings of tiny X-ray bright points not detectable at all in the chromosphere. Generally, compact flares are short-duration impulsive flares that are not associated with CMEs.

2) Two – Ribbon or Eruptive Flare (Ejective Flare)

All major flares are of this type. It is much larger and more dramatic than a compact flare and generally occurs along a polarity inversion line (PIL) in the photospheric magnetic field and is seen in $\text{H}\alpha$ on the disc as two bright ribbons expanding outward from the polarity inversion line. Frequently, they are seen to be connected by a rising arcade of so-called post-flare loops (see Figure 1.4). Two-ribbon flares are usually long-duration gradual flares associated with CMEs.

Multi – wavelength Observations of Solar Flares

The flare observed by Carrington (1859) was an example of a relatively rare event a large white light flare - in which the optical continuum is enhanced sufficiently over the background photospheric field to be visible in contrast. Most

1.2 Solar Eruptive Phenomena (Space-Weather Events)

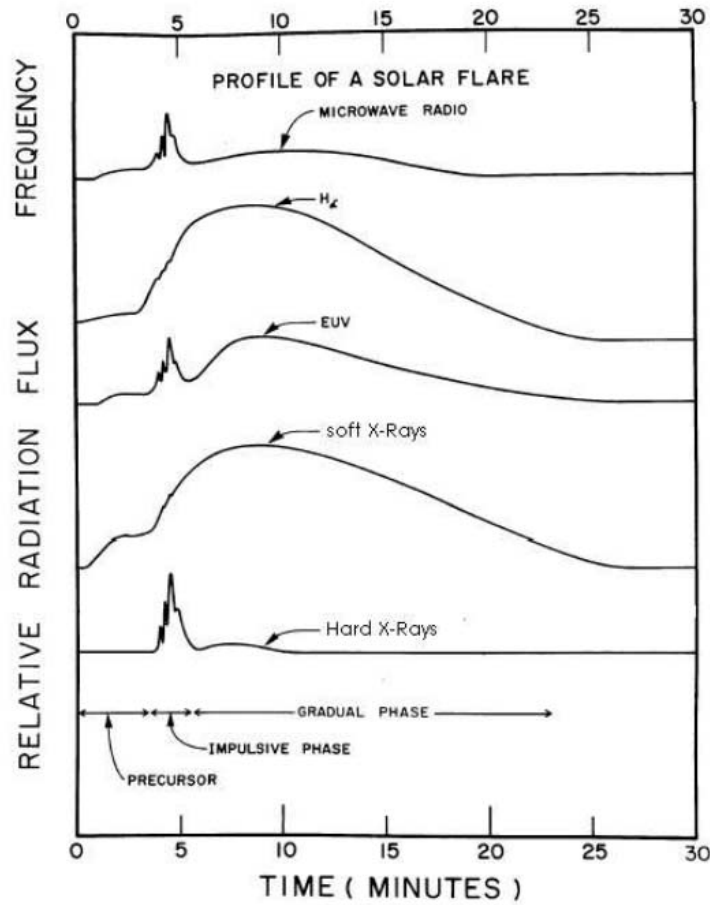


Figure 1.3: A schematic representation of the different phases of a solar flare as observed in the electromagnetic and particle radiation (from [Kane 1974](#)).

flares are not so conspicuous in visible light, they reserve their strongest enhancements for spectral lines such as H_{α} , and they also radiate copious amounts of energy in extreme ultraviolet (EUV) and soft X-ray wavelength bands ([Tandberg-Hanssen & Emslie, 1988](#)). Figure 1.3 shows the intensity of emission as a function of time for an average flare to the extent that such averaging is meaningful, since each flare is different - at a variety of wavelengths which are typically available for flare detection. These range from the radio and optical, which are available from ground-based facilities, through soft and hard X-rays, which are available only from instruments placed on satellites or high-altitude balloons. Images of

1.2 Solar Eruptive Phenomena (Space-Weather Events)

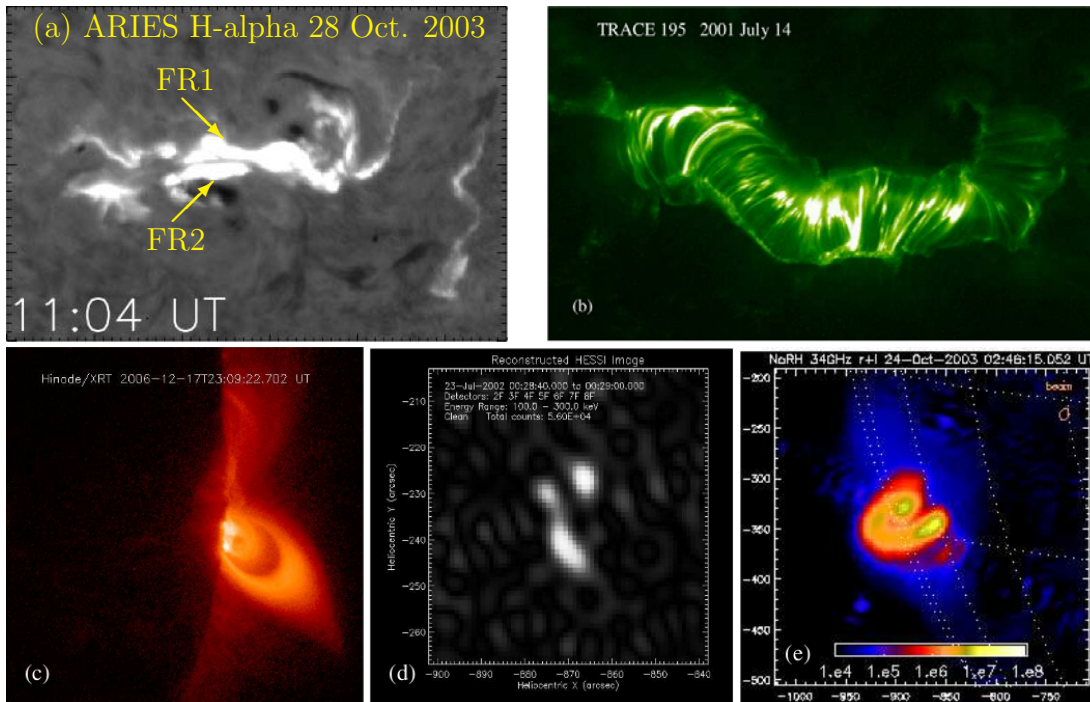


Figure 1.4: Images of different solar flares at different wavelengths. (a) A large historical two ribbon 4B/X17.2 class flare of October 28, 2003 from ARIES, Nainital (courtesy of Wahab Uddin) (b) TRACE EUV Post-flare loops of the famous ‘Bastille Day Flare’ observed at 195 Å on July 14, 2000. (c) Soft X-ray cusp-shape post-flare loop observed by Hinode/XRT on December 17, 2006. (d) and (e) Hard X-ray and Microwave images of different flares observed by RHESSI and Nobeyama Radioheliograph, respectively.

different flares in each of these wavelengths are shown in Figure 1.4. Figure 1.3 shows that the flare presents a very different appearance in terms of intensity versus time at these different wavelengths. These differences in appearance imply that flares may have several different phases, possibly representing a series of different physical occurrences, or a series of steps through which the flare instability evolves (Golub & Pasachoff, 1997). A flare can, in general, be roughly divided into three phases: preflare phase, impulsive phase and main (or gradual) phase.

(1) Preflare phase :

In the preflare phase, one often see the flare precursors at various wavelengths.

1.2 Solar Eruptive Phenomena (Space-Weather Events)

Gaizauskas (1989) defines a precursor as “a transient event preceding the impulsive phase, possibly even before the onset and not necessarily at the site of the flare itself”. Such events may include homologous and sympathetic flares, soft X-ray and Ultra- violet (UV) precursors (see Figure 1.3), microwave activity, and filament activations. Homologous flares are earlier flares in the same location with similar emission patterns. Sympathetic flares are earlier flares in different locations, but erupting in near synchronism. Soft X-ray precursors are transient enhancements in soft X-rays. lasting for several minutes, that occur in loops or unresolved kernels at, or close to, flare sites. UV precursors are mostly small-scale transient brightenings above active regions, and they exhibit a broad range of amplitudes. Radio precursors, most often observed in microwave, consists of changes in intensity and/or polarization of radio waves emitted from an active region, tens of minutes before the onset of a flare. One should note that none of the precursors given above is both necessary and sufficient for a flare. One of the earliest precursor signatures reported is the activation of filaments and prominences (Martin & Ramsey, 1972), consisting of morphological changes and darkening of filaments some minutes to tens of minutes before the first H α brightenings.

(2) Impulsive phase :

The impulsive phase of a flare is characterized by intense, rapid, and spiky emissions in γ -rays, hard X-rays, and radio. There are also associated emissions at other energies, such as EUV and optical, generated as a result of the thermal response of the atmosphere to the rapid energization associated with this phase (see Figure 1.3). Physically, the impulsive phase corresponds to the sudden release of stored magnetic energy into various forms, including accelerated particles, heating of plasma, bulk acceleration of fluid, and enhanced radiation fields (Tandberg-Hanssen & Emslie, 1988).

During the impulsive phase of a two-ribbon flare, two ribbons of H α (UV and EUV) emission form (Figure 1.4a, one on each side of the polarity inversion line and, throughout the main phase, the ribbons move apart at 2-10 km s⁻¹ . Frequently, they are seen to be connected by a rising arcade of so-called post-flare loops in the main phase. Nonthermal emission in hard X-ray (bremsstrahlung

1.2 Solar Eruptive Phenomena (Space-Weather Events)

emission) and microwave (gyrosynchrotron emission) appear when strong energy releases occur, and the sites of the radiation sources indicate where the energy is released. In hard X-rays, the dominant morphology is the double footpoint source, although single compact sources or multiple components are also frequently seen (Figure 1.4d; Sakao 1994). The microwave emission traces out the entire volume accessible to nonthermal electrons (Figure 1.4e). There are two types of microwave sources, i.e., both loop-top source and double-footpoint sources, and footpoint emission dominates at high frequencies (Bastian et al., 1998).

(3) Main phase :

After its initial abrupt release in the impulsive phase of a flare, the energy is transported to other regions of the atmosphere, often as it changes form. New areas of the atmosphere are affected, mainly due to heating, and it is this interplay of energy transport and atmospheric response that we refer to as the main or gradual phase of the flare (Tandberg-Hanssen & Emslie, 1988).

Most flares (compact flare) are short lived and they simply cool during the main phase, decaying within minutes or tens of minutes. However, the other kind of flares, i.e., two-ribbon flares, continue to release energy during their main phase, and in those flares the decay is much longer: in some events it can continue for many hours. Post-flare loops are observed during the main phase of two-ribbon flare. These loop systems are observed to rise upward slowly into the corona (Pneuman, 1981). The velocity of ascent decreases with height from about 10–20 km s⁻¹ at the beginning to a fraction of a km s⁻¹ when they are finally observed in soft X-rays at great heights. Hot loops (soft X-ray, Figure 1.4c) are first formed and often show a cusp shaped structure (Forbes & Acton, 1996; Tsuneta et al., 1992), then shrink and subsequently cooled to EUV ($\sim 10^5$ K, Figure 1.4b) and H α temperature (10^4 K, Figure 1.4a). The term post-flare as applied to these systems is, unfortunately, quite misleading, since it implies that the phenomenon occurs after the flare and is somehow a byproduct of the flare process. This designation probably originated historically, because the loops were firstly clearly seen on the limb in H α only after the system had risen quite high in the corona; that is, unless the flare occurred exactly on the limb, the loops lower down would not be clearly see against the disk. Now a days, the

comprehensive multi-wavelength observations indicate that the post-flare loops are a major aspect of the flare.

1.2.2 Prominence/Filament Eruptions

Prominences are relatively cool and dense objects that are embedded in the hotter solar corona and are commonly observed above the solar limb in $H\alpha$ emission, the first spectral line of the Balmer series of neutral hydrogen (Gilbert et al., 2001). When seen projected against the solar disk, prominences appear in $H\alpha$ as dark features called “filaments” (see Figure 1.5). Often a prominence reaches downward towards the chromosphere in a series of regularly spaced feet, which resemble great tree trunks. These feet are often located at supergranule boundaries and are joined by huge arches as shown in Figure 1.5b. Although prominences and filaments are now known to be the same structures, they were originally identified as distinct objects. We use the terms “filament” and “prominence” interchangeably in general context. The term prominence is used to describe a variety of objects, ranging from relatively stable structures with life times of many months, to transient phenomena that last for hours, or less. They have been classified in several different ways, but there appear to be two basic types (Priest & Tandberg-Hanssen, 1989) :

(1) A quiescent prominence is in its global appearance an exceedingly stable structure and may last for many months. It may begin life as a relatively small active-region (or plage) filament, which is located either along the polarity inversion line between the two main polarity regions of an active region or at the edge of an active region where it meets a surrounding region of opposite polarity. Sometimes it may enter a sunspot from one side. As the active region disperses, the prominence grows thicker and longer to become a quiescent filament. It may continue growing for many months up to 10^6 km in length, and in the process it migrates slowly towards the nearest pole.

(2) Active prominences are located in active regions and are usually associated with solar flares. They are dynamic structures with violent motions and have lifetimes of only minutes or hours. There are various types, such as surges, sprays (probably erupting plage filaments) and loop prominences: both their magnetic

1.2 Solar Eruptive Phenomena (Space-Weather Events)

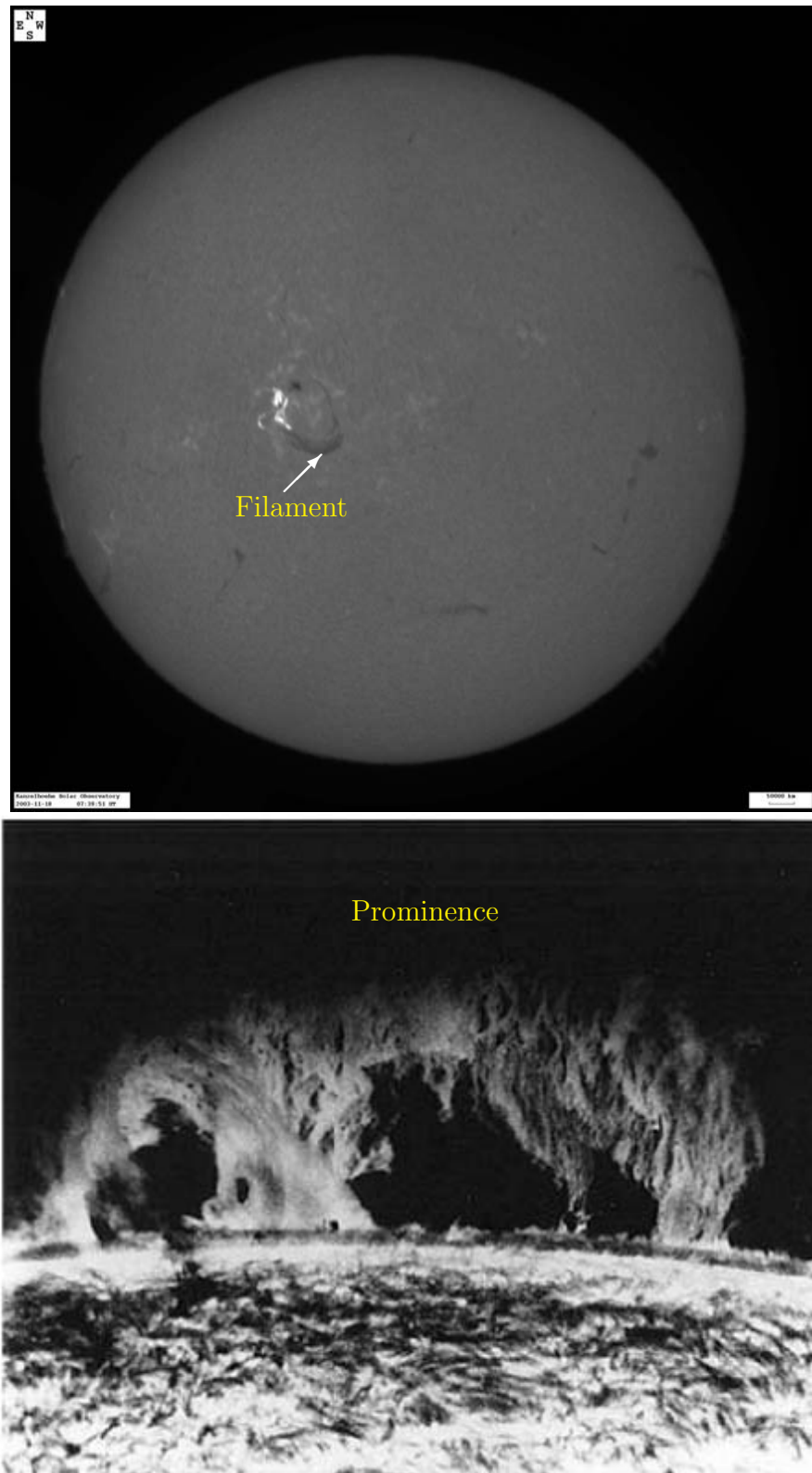


Figure 1.5: Filaments and Prominences observed in $H\alpha$ by KSO (Kanzelhoehe Solar Observatory) and BBSO (Big Bear Solar Observatory).

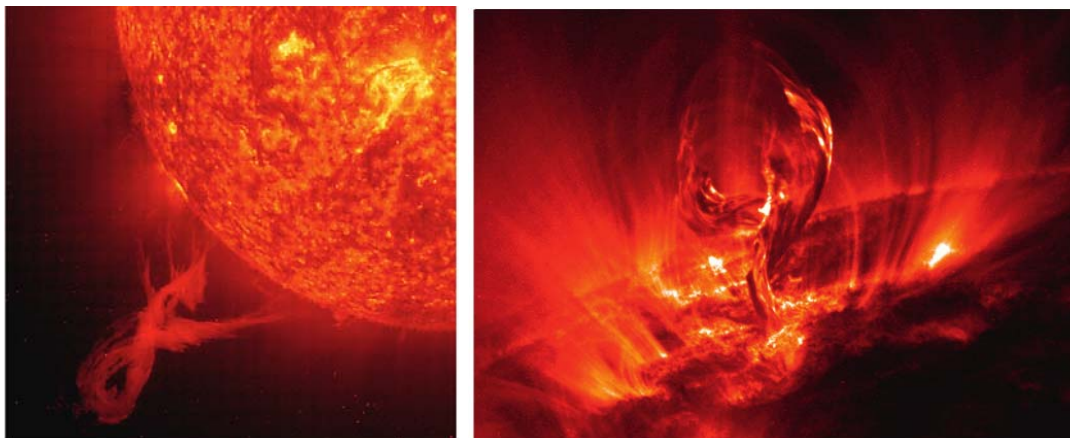


Figure 1.6: Images of filament/prominence eruptions in EUV. Left: A large eruptive prominence observed by SOHO/EIT at 304 \AA (He II) on 2000 January 12. Right: A filament eruption on July 19, 2000 observed by TRACE at 171 \AA .

field (about 100 G) and average temperature are higher than for quiescent prominences.

Prominences are formed in “channels” where the chromospheric fibrils are aligned with PIL (Foukal, 1971; Gaizauskas, 1998; Gaizauskas et al., 1997; Martin, 1990, 1998). This alignment indicates the presence of a horizontal axial magnetic field directed along the length of the channel. A handedness property known as ‘chirality’ has been discovered for filament channel and filaments (Martin et al., 1994). If we view the filament from the positive polarity side, a filament has an axial magnetic field directed to the right is called ‘dextral’, while a ‘sinistral’ filament has an axial field directed to the left. This so-called chirality of filaments is correlated with latitude on the Sun. Martin et al. (1994) showed that the mid-latitude filaments on the northern hemisphere are predominantly dextral, while those in the south are predominantly sinistral.

Filament activation encompasses a wide array of phenomena, including oscillating, eruption, rising/falling, rotating, and counter-streaming, and so on (Gilbert et al. 2007, private communication). Here, we only discuss the eruptive-like dynamic activity (which a portion of a prominence lifts significantly in a short period of time, at least $0.1 R_{\odot}$ in less than 1 hour) in filaments. Prominence eruptions were observed by D’Azambuja (1955) using daily spectroheliograms

1.2 Solar Eruptive Phenomena (Space-Weather Events)

from the the Meudon Observatory in Paris. He found that prominences tend to erupt and reform in their original place, and that many erupt more than once. Two images of filament/prominence eruptions are shown in Figure 1.6. Modern advanced studies show that prominences exhibit a wide range of eruptive activity behavior including dramatic activation with the filament mass remaining confined to the low corona (e.g. [Ji et al. 2003](#), [Alexander et al. 2006](#)), the eruption of part of the observed filament structure ([Gibson et al., 2002](#); [Gilbert et al., 2000](#); [Pevtsov, 2002](#); [Tang, 1986](#)), and the almost complete eruption of all of the prominence mass (e.g. [Tang 1986](#), [Plunkett et al. 2000](#)). To help elucidate the relation between the filament mass and corresponding supporting magnetic structure, [Gilbert et al. \(2007\)](#) developed observational definitions of “full”, “partial”, and “failed” eruptions. A “full eruption” is defined to occur when the entire magnetic structure erupts while containing the bulk (approximately 90% or more) of the pre-eruptive filament mass (i.e., the mass escapes without draining or settling back to the surface). “Failed eruptions” are defined by the dynamical evolution of the filament, which displays an initially eruptive-like acceleration persisting for a relatively short duration prior to a period in which the filament decelerates, reaching a maximum height as the mass in the filament threads drains back toward the Sun ([Alexander et al., 2006](#)). In the other words, in a “failed” eruption none of the lifted filament mass nor the supporting magnetic structure escapes the solar gravitational field, although this does not preclude localized dynamic activity, heating and flare production . “Partial” eruptions are more complicated to define observationally, since the coupling of the filament mass and its supporting magnetic structure create a couple of different sub-categories in this class. The first type of partial eruption occurs when the entire magnetic structure erupts containing either some or none of its supported pre-eruptive filament mass. The second type of partial eruption occurs when the magnetic structure itself partially escapes containing either some or none of the filament mass.

1.2.3 Coronal Mass Ejections (CMEs)

Coronal mass ejections (CMEs) are transient phenomena in the solar corona that expel a large amount of plasma and magnetic field into interplanetary space. The

1.2 Solar Eruptive Phenomena (Space-Weather Events)

concept of mass leaving the Sun was thought possible over 100 years ago from the observations of prominence material that was seen to be moving outward at speeds in excess of the escape velocity (for a historical review see [Howard 2006](#)). Mass ejections may be identifiable on eclipse photographs from 1860 ([Eddy, 1974](#)) and 1893 ([Cliver, 1989](#)). However, the first coronagraph observations of CMEs were made by the space-borne coronagraph on board the Orbit Solar Observatory-7 ([Tousey, 1973](#)) and Skylab ([Gosling et al., 1974](#); [MacQueen et al., 1974](#)) in the early 1970s. Typical coronagraphs have an occulting disk to artificially eclipse the bright photosphere, so CME is detected because of photospheric light Thomson-scattered off free electrons in the corona. After Skylab, the most extensive observations of CMEs were made by the coronagraphs in space such as those in the SOLWIND (1979-1985; [Michels et al. 1980](#)), SMM (Solar Maximum Mission; 1980 and 1984- 1989; [MacQueen 1980](#), and SOHO (Solar Heliospheric Observatory, 1995- now). CMEs are now routinely observed from the ground with the Mark III (MK3) K-Coronameter at the MLSO (Mauna Loa Solar Observatory; [Fisher et al. 1981](#)). The CME observed by the aforementioned instruments is a projection of a three- dimensional object projected onto a flat image, in the plane of the sky. This provides a few very basic questions. Is the CME loop representing the projection of a bubble, a loop or an arcade? The latest mission with a coronagraph is the STEREO (Solar TERrestrial RELations Observatory) mission which was launched in October 2007. The mission objective is to understand the 3D nature of CMEs, their initiation and propagation. To do this, STEREO has sent two identical instrumented spacecraft into a heliospheric orbit, one leading Earth (Ahead) and one trailing (Behind).

CMEs often display spatial structures, commonly referred to as the ‘three-part- structure’ (a bright frontal loop, a dark cavity, and a bright core; [Hundhausen 1999](#)). Figure 1.7 shows a time sequence of SMM coronagraph images showing a typical CME initiation and eruption observed in white light. This CME originates from a helmet streamer that has been slowly rising or swelling outward days before the eruption. A clear three-part structure of the CME is seen (bottom-left panel). The frontal loop overlies the cavity, which contains the bright core. The core has shown to be the eruptive prominence by comparing coronagraph and $H\alpha$ observations. Eclipse pictures often show the three-part

1.2 Solar Eruptive Phenomena (Space-Weather Events)

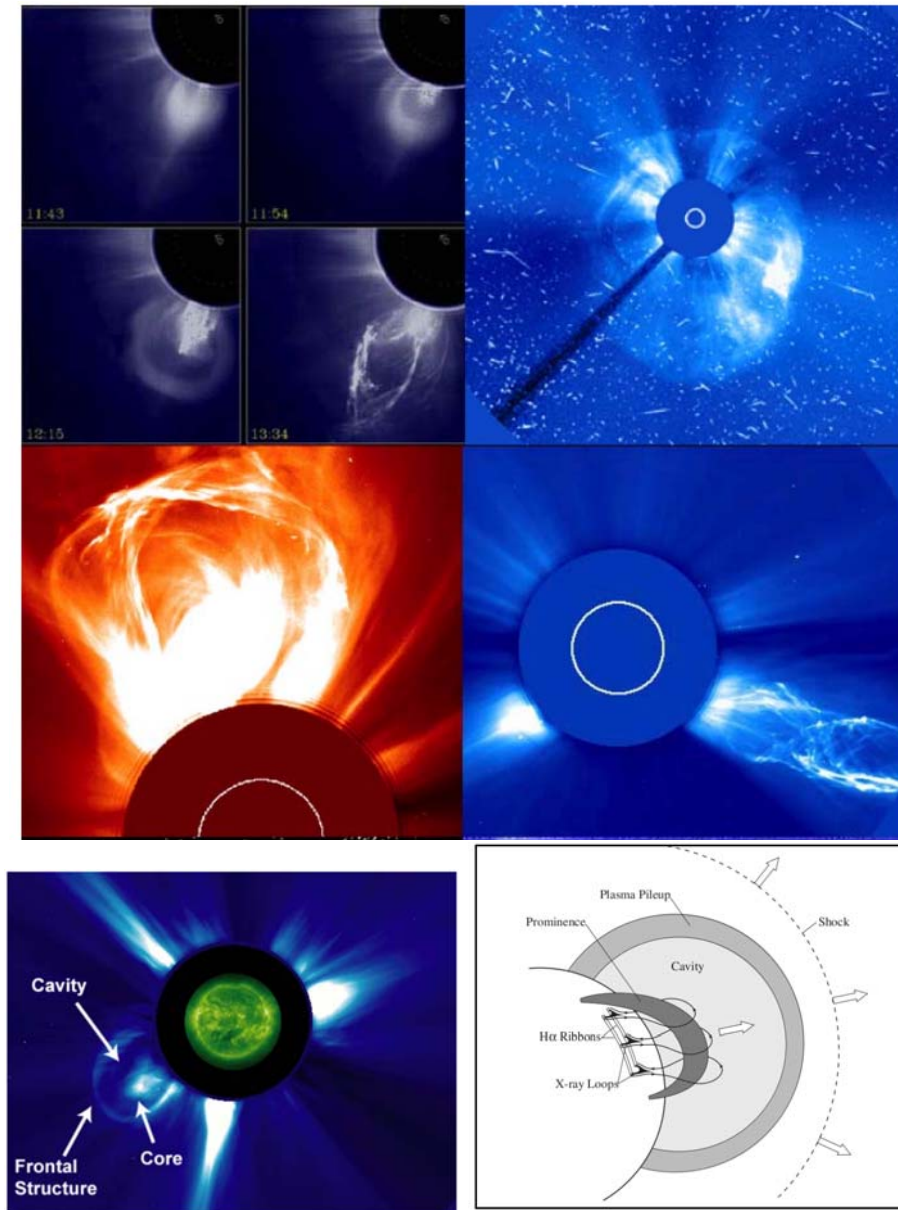


Figure 1.7: Top: Prototypical “3-part CME” as observed by Solar Maximum Mission (SMM), halo CMEs from LASC0. Middle: Two views of flux rope CMEs (LASC0). Bottom-left: SOHO/LASCO image (with an EIT 195 Å image superposed) on 20 December 2001 showing the 3 part structure of a CME above the southwest limb. Bottom-right: A standard model for a “three-part” CME or eruptive flare (Forbes, 2000).

1.2 Solar Eruptive Phenomena (Space-Weather Events)

structure in the pre-eruptive stage, where the helmet streamers takes the place of the frontal loop. Not all CMEs show the three-part structure either due to geometrical reasons (Cremades & Bothmer, 2004) or due to the nature of the source region (Gopalswamy, 2006). A standard model for a “three-part” CME or eruptive flare is given by Forbes (2000) (bottom-right). The combined representation includes compressed material at the leading edge of a low-density, magnetic bubble or cavity, and dense prominence gas. The prominence and its surrounding cavity rise through the lower corona, followed by sequential magnetic reconnection and the formation of flare ribbons at the footpoints of loop arcade.

The basic attributes of a CME are its speed, width, acceleration, and central position angle (CPA), all with reference to the sky plane (Gopalswamy, 2006). These are obtained from a time sequence of coronagraphic images, in which the CME can be recognized as a moving feature occupying a well-defined region. The angular extent of the moving feature defines the width. The central angle of this extent with reference to the solar north is CPA. The speed is normally determined from a linear fit to the height-time (h-t) plots. But CMEs often have finite acceleration, so the linear-fit speed should be understood as the average value within the coronagraphic field of view. Quadratic fit to the h-t plots gives the constant acceleration, which again is an approximation because the acceleration may also change with time.

The measured sky-plane speed ranges from a few km s^{-1} to $\sim 3000 \text{ km s}^{-1}$ (see Gopalswamy 2006; and references therein), with an average value of $\sim 483 \text{ km s}^{-1}$. The CME speed has a lognormal distribution (Yurchyshyn et al., 2005). Most of the height-time plots fall into three types: accelerating, constant speed, and decelerating, indicating different degrees of propelling and retarding forces acting on CMEs (Gopalswamy et al., 2001). The mass of a CME is estimated as the excess mass in the coronagraphic field of view assuming that the entire mass is located in the sky plane (see Vourlidas et al. 2002). The mass changes during the early phase of the CME before stabilizing to a new-constant value, which is used as the representative mass. The mass ranges from a few times 10^{13} g to more than 10^{16} g . The kinetic energy obtained from the measured speed and mass ranges from $\sim 10^{27} \text{ erg}$ to $\sim 10^{32} \text{ erg}$, with an average value of $5 \times 10^{29} \text{ erg}$.

1.2 Solar Eruptive Phenomena (Space-Weather Events)

Some very fast and wide CMEs have kinetic energies exceeding 10^{33} erg, generally originating from large active regions ([Gopalswamy et al., 2005a](#)).

The apparent angular width of CMEs ranges from a few degrees to more than 120° , with an average value of $\sim 46^\circ$. The average width was computed for CMEs with width $\leq 120^\circ$. Depending on their width, CMEs are categorized as non halo, partial halo, and full halo to CMEs with width lower than 120° , between 120° and 320° and greater than 320° , respectively ([Lara et al., 2006](#)). The true width of halo CMEs ([Howard et al., 1982](#)), which appear to surrounding the occulting disk, is unknown.

The CME plasma is multi-thermal with the prominence core at ~ 8000 K and the outer structure at a few MK. Occasionally, CMEs may consist of flare ejecta with temperature exceeding 10 MK. The magnetic field in CMEs is not directly measurable near the Sun. The magnetic field in prominences is typically up to 30 G, while it can exceed 1000 G in the active region cores. The field strength in the outer corona is typically less than ~ 1 G. The coronal cavity overlying the filament may also have field strengths higher than the overlying corona for pressure balance requirements. How frequently do CMEs occur? The occurrence of CMEs shows a strong solar cycle dependence. During solar minimum, one CME occurs every other day. The rate goes up to several per day during solar maximum. The daily CME rate averaged over Carrington Rotations (27.3 days) was found to exceed 6 per day during solar cycle 23 ([Gopalswamy, 2006](#)).

Solar Radio Bursts associated with Eruptive – phenomena

Energy released in the solar flares heats plasma and accelerates electrons and ions to high energies. These energetic electrons interact with the ambient plasma or with magnetic field and produce various types of radio bursts. These radio bursts observations have been reported in decimetric, metric and decametric bands from ground based and space based observations. [Figure 1.8](#) illustrates the different types of radio bursts associated with the solar eruptive events. The classification of different type of radio bursts are described in the following subsections:

1.2 Solar Eruptive Phenomena (Space-Weather Events)

Type I : Type I bursts (Figure 1.8) are characterized by a very short duration (< 1 s), they have bandwidths of a few tens of MHz, and they do not show obvious drifts. Type I bursts are only observed at metric wavelengths and always appear in large numbers, forming irregular structures superposed on a continuous background. These so-called noise storms can last for hours to days. Type I emission is therefore not necessarily associated with flares. It is thought to be generated by electrons accelerated to a few thermal energies by an ongoing local energy release in closed coronal structures. Type I bursts are not particularly important for space weather studies.

Type II : Type II bursts (Figure 1.8) are narrow-band (a few MHz) emission ($0.1 - 1$ MHz s^{-1}) lanes which slowly drift towards lower frequencies. Both fundamental and harmonic band can be present, and sometimes each band is split into a higher and a lower frequency lane (with a relative separation of $\Delta f/f \sim 0.1$). For a review, see Mann (1995). Most bursts are observed in the metric range, but some are also detected in the dekameter to kilometric regimes. These are called IP type II bursts (see, e.g., Cane et al. 1987). A type II burst is generated by a magnetohydrodynamic shock wave which propagates outward through the corona. In the corona and in the IP medium, a type II-generating shock is formed when a disturbance exceeds the Alfvén speed ($V_A = B / (\mu_0 m_p \mu N)^{1/2}$), where μ_0 is the permeability of vacuum, m_p the proton mass, μ the mean molecular weight (0.6 in the corona), and N the total particle number density ($N = 1.92 N_e$ for $\mu = 0.6$). Velocities of coronal type II sources are of the order of 1000 km s^{-1} . At the shock front, electrons are accelerated to suprathermal and/or high energies. They excite Langmuir wave which are then converted into escaping radio waves by the plasma emission process. Further evidence for electron acceleration is provided by the herringbone structure observed in some type II bursts, in which small type III-like bursts emanate from the “backbone” of the emission lane. These features are interpreted as accelerated electrons which escape from the shock. Type II bursts are associated both with flares and CMEs, though there is no one-to-one correspondence. This has resulted in an extended discussion on the real nature of the shocks which produce the bursts, the candidates being a flare-generated pressure pulse (see e.g. Vršnak & Lulić 2000a and Vršnak

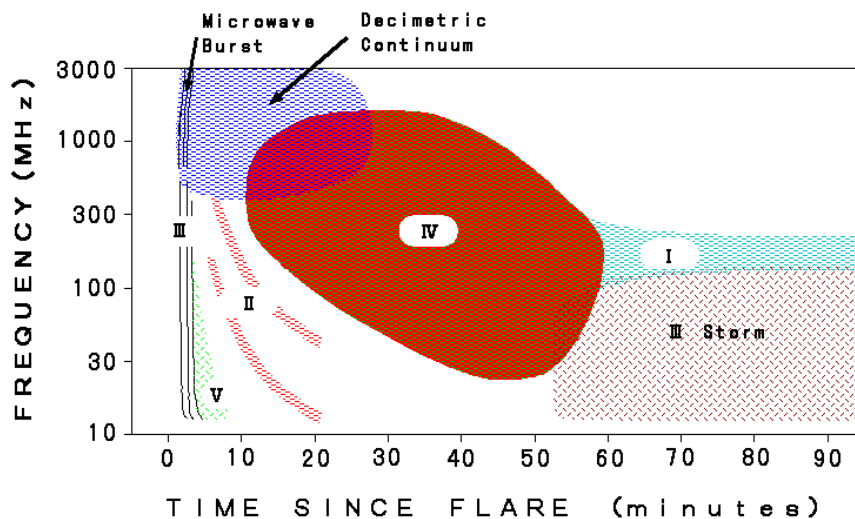


Figure 1.8: Dynamic solar radio spectrum showing schematically the basic types of solar radio bursts. Time runs from left to right, frequency decreases from bottom to top (corresponding to increasing height in the solar atmosphere). Time is given in minutes, frequency in MHz.

& Lulić 2000b) or a piston-driven shock created by a CME (Cliver et al. 1999 and references therein). The current view is that both flares and CMEs can create shocks (e.g. Claßen & Aurass 2002; Shanmugaraju et al. 2003), but it seems that the flare-generated disturbances usually cannot penetrate to IP space, since most of those bursts cease at 20 MHz (Gopalswamy et al., 1998). This is probably due to a local maximum of the Alfvén speed in the higher corona (Mann et al., 2003). Therefore, most hectometric/kilometric type II bursts seem to be generated by CME-driven shocks (Cane et al., 1987). These bursts are associated with fast CMEs, long-lived energetic solar particle events (Kahler & Reames, 2003), and IP shocks, and are therefore particularly relevant for space weather purposes.

Type III : Type III bursts (Figure 1.8) are the most common flare-associated bursts and can occur over a wide frequency range, from 1 GHz to 10 kHz, corresponding to a height range extending from the low corona to beyond 1 AU.

1.2 Solar Eruptive Phenomena (Space-Weather Events)

They are mainly defined by their rapid drift (100 MHz s^{-1}) towards lower frequencies, they have a short duration (seconds) and a relatively broad bandwidth ($\Delta f \sim 100 \text{ MHz s}^{-1}$). Many type III bursts display harmonic structure at metric to dekametric wavelengths.

Type III bursts are characteristic of the impulsive phase of solar flares, where they often occur in groups of 10 bursts, lasting a few minutes. Non-flare associated type IIIs form storm type III bursts, somewhat reminiscent of type I noise storms. The exciting agent of a type III burst is a beam of mildly relativistic electrons ($v \sim 0.3 c$) which propagates out of the corona along open magnetic field lines (the beams may also propagate in closed loops, resulting in so-called inverted-U bursts). As in the case of type II bursts, the accelerated electrons generate plasma emission. Type III bursts can propagate through IP space up to the Earth, where the radio-generating electrons can be directly observed as impulsive electron events. Type III bursts therefore give vital clues on the acceleration of electrons in flares, as well as on the propagation of these particles through IP space. A special class of type III bursts are the so-called shock-accelerated (SA) type III bursts (see [Cane et al. 1981](#); [Bougeret et al. 1998](#); [Claßen & Aurass 2002](#)). They start from a type II backbone and are somewhat reminiscent of herringbones, but contrary to them, SA type III bursts extend into the IP medium. Like the herringbones, they are thought to be generated by electron beams which are accelerated at a coronal (or IP) shock.

Type IV : Type IV bursts are flare-related broad-band continua (Figure 1.8). They are divided into two distinct categories: stationary type IV bursts show no frequency drift and are characterized as broad-band, long-lasting continuum features which show a wide variety of fine structures pulsations, zebra patterns and fiber bursts. They follow major flares and may evolve into type I storms. On the other hand, moving type IV bursts display a slow drift towards lower frequencies (corresponding to source velocities of up to several 100 km s^{-1}), while they are otherwise morphologically similar to stationary type IVs. Type IV bursts are believed to be either due to plasma emission or due to gyrosynchrotron emission. In any case, the electrons which are responsible for the emission are trapped in a closed magnetic structure. This can be a set of coronal loops (stationary type

1.2 Solar Eruptive Phenomena (Space-Weather Events)

IV), or a rising structure like an expanding loop or a plasmoid which is ejected during an eruptive event (moving type IV; see, e.g., [Stewart 1985](#)). The bulk of the electrons remains confined to the magnetic structure due to magnetic mirroring at converging magnetic field lines (i.e., at the feet of coronal loops), therefore, we observe prolonged emission. Type IV bursts are only seldomly observed in the near-Sun IP medium, but they are nevertheless interesting for solar-terrestrial studies since they can provide valuable information on the energy release mechanism of solar eruptive events. Several flare models require the formation and ejection of plasmoids, and CME cores might actually be sources of type IV bursts.

Type V : Type V bursts are continuum bursts which start during or immediately after a group of type III bursts. They are possibly created by electrons which have been removed from the type III-generating beam by pitch angle scattering. For the purposes of solar-terrestrial studies, type V bursts are not important.

CMEs consequences in near–Earth Environment : Geomagnetic storms

CMEs typically reach Earth one to five days (depending on the speed) after the eruption from the Sun. During their propagation, CMEs interact with the solar wind and the interplanetary magnetic field (IMF). As a consequence, slow CMEs are accelerated toward the speed of the solar wind and fast CMEs are decelerated toward the speed of the solar wind ([Manoharan, 2006a](#)). Magnetic clouds are the subsets of CMEs which is a transient event observed in the solar wind (Figure 1.9). It was defined in 1981 by [Burlaga et al. \(1981\)](#) as a region of enhanced magnetic field strength, smooth rotation of the magnetic field vector and low proton density and temperature. Magnetic clouds are a possible manifestation of a Coronal Mass Ejection (CME). The association between CMEs and magnetic clouds was made by [Burlaga et al. \(1982\)](#) when a magnetic cloud was observed by Helios-1 two days after being observed by SMM. However, because observations near Earth are usually done by a single spacecraft, many CMEs are not seen as being associated with magnetic clouds. Fast CMEs (faster than about 500 km s^{-1}) eventually drive a shock. This happens when the speed of the CME in the frame moving with the solar wind is faster than the local fast magnetosonic

1.2 Solar Eruptive Phenomena (Space-Weather Events)

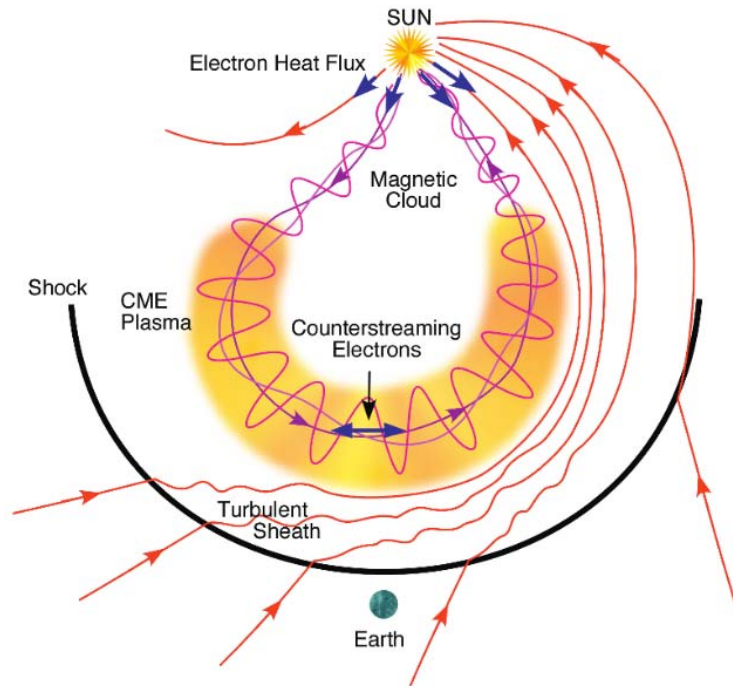


Figure 1.9: When a CME travels into IP space, It can create a huge magnetic cloud containing bidirectional, or counterstreaming, beams of electrons that flow in opposite directions within the magnetic loop that are cooled at both ends at the Sun. The magnetic cloud also drives an upstream shock ahead of it. Magnetic clouds are only present in a subset of observed interplanetary coronal mass ejections. (Courtesy of Deborah Eddy and Thomas Zurbuchen)

speed. Such shocks have been observed directly by coronagraphs in the corona and are related to type II radio bursts. They are thought to form sometimes as low as $2 R_{\odot}$ (solar radii). They are also closely linked with the acceleration of Solar Energetic Particles (SEPs).

When the CME hits in the earth's magnetosphere, geomagnetic storms are triggered. The interplanetary magnetic field (IMF), carried by solar wind has three components and when the Z component of IMF (B_Z) becomes southward to the geomagnetic field lines (Figure 1.10¹), magnetic reconnection takes place,

¹<http://www.aldebaran.cz/astrofyzika/plazma/reconnection.en.html>

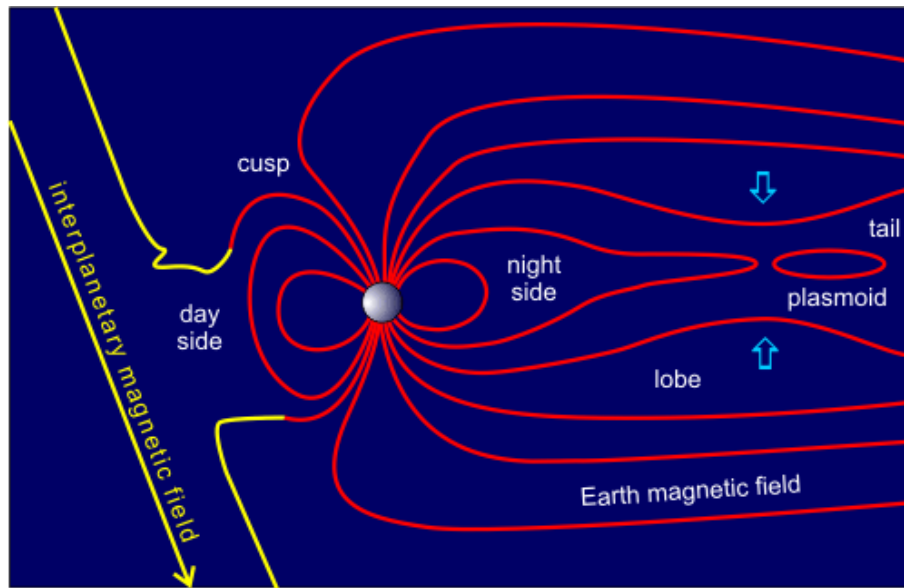


Figure 1.10: Magnetic reconnection takes place at the boundary of magnetosphere if interplanetary magnetic field is southward and solar wind/CME energy is pushed into the magnetosphere, which causes geomagnetic storms at Earth due to the formation of ring current above the equator.

which is the most suitable condition to transfer of solar wind momentum and energy to the magnetosphere. Owing to the gradient and curvature drifts acting on the charged particles in the magnetosphere, the ring current flows in the westward direction around the earth above the equator at radial distance between $2-7 R_E$, having geomagnetically trapped 10-200 keV ions (mainly H^+ , He^+ and O^+) and electrons. The magnetic field associated with the ring current is in the same direction to that of geomagnetic field, thus an increase in the ring current causes a decrease in the geomagnetic field. The variation in the geomagnetic field is called geomagnetic storms. The variation in geomagnetic field is measured by ground based magnetometers located nearby equatorial regions in terms of Dst (Disturbance Storm Time) index. The Dst index (ring current index) is an indicative of the total energy content of the particles responsible for ring current. It monitors the world wide magnetic storm level. It is constructed by averaging the horizontal component of the geomagnetic field from mid-latitude and equatorial magnetograms from all over the world. Negative Dst values indicate a magnetic

1.2 Solar Eruptive Phenomena (Space-Weather Events)

storm is in progress, the more negative Dst is the more intense the magnetic storm. The negative deflections in the Dst index are caused by the storm time ring current which flows around the Earth from east to west in the equatorial plane. The ring current results from the differential gradient and curvature drifts of electrons and protons in the near Earth region and its strength is coupled to the solar wind conditions. Only when there is an eastward electric field in the solar wind which corresponds to a southward interplanetary magnetic field (IMF) is there any significant ring current injection resulting in a negative change to the Dst index. Thus, by knowing the solar wind conditions and the form of the coupling function between solar wind and ring current, an estimate of the Dst index can be made. The geomagnetic storms with Dst between -200 nT to -100 nT are classified as ‘intense’ and other events with $Dst \leq -200$ nT as ‘super-intense’. Super-storms take place with $Dst \leq -300$ nT as observed during October-November 2003. Figure 1.11 shows the geomagnetic storms caused by the CMEs from NOAA AR 10486 during October-November 2003. These geomagnetic storms affect the earth’s ionosphere i.e. the change in ionospheric density and height.

1.2.4 Relationship between Solar Flares, Prominence Eruptions, and CMEs

Solar flare, filament eruptions, and coronal mass ejections (CMEs) are the most important solar events as far as space weather are concerned, linking solar eruptions, major interplanetary disturbance, and geomagnetic storms (Gosling et al., 1991). The majority of flare activity arises in active regions which contain sunspots, while CMEs can also originate from decaying active regions and even so-called quiet solar regions which contain a filament. Two classes of CME, namely flare-related CME events and CMEs associated with filament eruption are well reflected in the evolution of active regions, flare related CMEs mainly occur in young active regions containing sunspots and as the magnetic flux of active region is getting dispersed, the filament- eruption related CMEs will become dominant (Schmieder & van Driel-Gesztelyi, 2005). This is confirmed by statistical analyses.

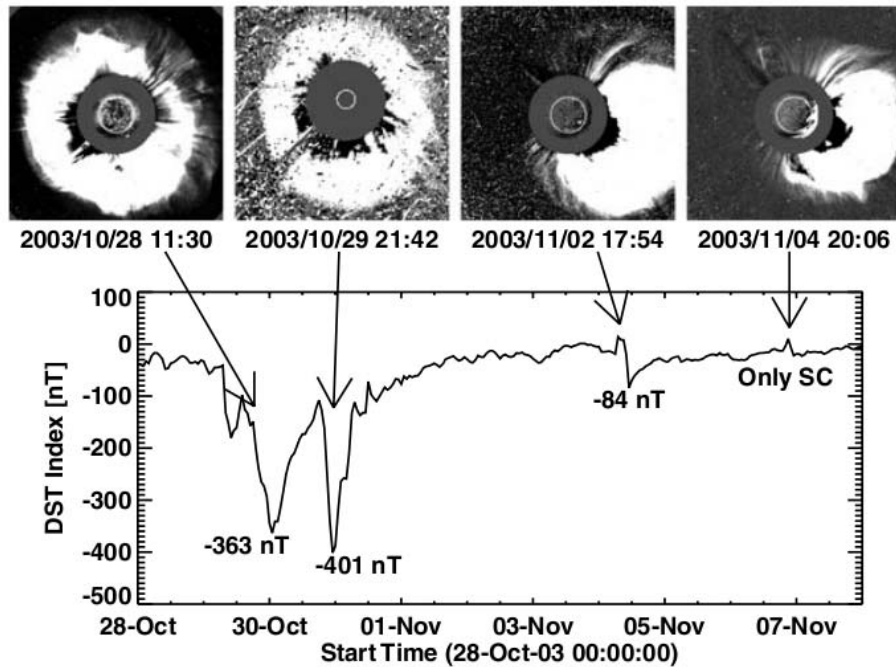


Figure 1.11: Top: Large CMEs from active region 10486 during October–November 2003 observed by SOHO/LASCO. The first two are symmetric full halos because the CMEs originated from close to the disk center. The last two CMEs occurred when AR was close to the west limb, so they appear as partial halos. Bottom: A plot of Dst index for the interval October 28 to November 7 2003. The CMEs responsible for significant Dst events are shown by arrows from [Gopalswamy et al. \(2005b\)](#).

Flare – CME relationship

The relationship between flares and CMEs remains a topic of active research. As far back as 1979, it was realized that there was an association between flare activity and CMEs by [Munro et al. \(1979\)](#), who found that approximately 40% of CMEs they studied were associated with flares, while about 70% were associated with filament eruptions. Since not all CMEs are associated with flares, many authors worked to determine the conditions under which the two types of solar phenomena are linked ([Reeves, 2006](#)). Observations using the coronagraph on Skylab indicated that CMEs associated with flares tend to be fast (averaging 775 km s^{-1}), while those associated with eruptive prominences tend to be slow (av-

1.2 Solar Eruptive Phenomena (Space-Weather Events)

eraging 330 km s^{-1}) (Gosling et al., 1976). Observations with the K-Coronameter at MLSO (MacQueen & Fisher, 1983a) and the SOHO/LASCO (Andrews, 2003; Moon et al., 2002; Sheeley et al., 1999) have also indicated that flares tend to be associated with high-speed CMEs. Combining their results with the results by Gosling et al. (1976); MacQueen & Fisher (1983b) put forward the concept of two distinct classes of CMEs: the flare-associated ones, being accelerated impulsively at low heights, and the non-flare CMEs accelerated gradually over a large height range. As many authors tried to find and discuss differences between CMEs associated with flares and those without flares, Švestka (1986) instead pointed out in the first place that in both these cases the cause of the CME is the same: an opening of magnetic field lines, previously closed in the form of arcades or helmet streamers, along the zero line of the longitudinal magnetic field; the only difference between flare-associated and non-flare-associated CMEs is the strength of the magnetic field in the region where the opening takes place (see also Švestka 2001). St. Cyr & Webb (1991) arrived at a similar conclusion when studying 73 CMEs observed by the SMM. Later on, through a large data sample from SOHO/LASCO, Vršnak et al. (2005) found that both of these two types of CMEs show quite similar characteristics, contradicting the concept of two distinct (flare/non-flare) types of CMEs. The non-flare CMEs show characteristics similar to CMEs associated with flares of soft X-ray class B and C, which is indicative of a “continuum” of events rather than supporting the existence of two distinct CME classes. On the other hand, they also found that CMEs associated with major flares are on average faster and broader than non-flare CMEs and small-flare CMEs.

There has also been research investigating which type of flare tends to be associated with a CME. Sheeley et al. (1975) studied spatially resolved Skylab observations obtained during long-duration (4.5 hr) soft X-ray events (LDEs) seen with the SOLRAD spacecraft. Their observations suggested that all LDEs are accompanied by CMEs and that most LDEs were accompanied by filament eruptions. With observations made by the Solwind coronagraph, Sheeley et al. (1983) found that the longer the duration of an X-ray event, the higher the probability of an associated CME. Webb & Hundhausen (1987) found that most of the soft X-ray events associated with the CMEs observed by SMM in 1980 were

1.2 Solar Eruptive Phenomena (Space-Weather Events)

LDEs. [Harrison \(1995\)](#) reviewed the previously published studies relating CMEs and X-ray flares and concluded: flares associated with CMEs tend to have longer durations than average flares. However, flares of any duration can be associated with CMEs, Brighter flares are more likely to be associated with CMEs. With GOES and SOHO/LASCO observations, [Andrews \(2003\)](#) found that thresholds of $6.0 \times 10^{-5} \text{ W m}^{-2}$ in peak flux, 0.07 J m^{-2} in total flux, and 4 hours in duration independently allow a 95% confidence in predicting that a CME will be observed. For flares with peak flux and duration below these thresholds, the fraction of flares with CME candidates is independent of the observed value of peak flux or duration. There are also several studies regarding the timing relationship between flares and CMEs. The CME onset time, which has to be extrapolated using the observations above the occulting disk, is found to be randomly located within windows tens of minutes wide around the flare onset time ([Harrison, 1995](#)). Prior to the SOHO observations, the ground-based MK3 K-Coronameter of the High Altitude Observatory (occulter from 1.3 to 2.2 R_{\odot} , [Fisher et al. 1981](#)) provides a viable tool to observe CMEs at low coronal heights. By examining individual events based on combined MK3 and SMM observations, it has been demonstrated that CMEs start almost simultaneously with the accompanying flares ([Dryer, 1994](#); [Maxwell et al., 1985](#)), or CMEs onset a few minutes earlier than the flare onset time ([Hundhausen, 1999](#)). Using observations made by LASCO and EIT (the Extreme Ultraviolet Imaging Telescope) onboard SOHO, [Zhang et al. \(2001\)](#) found that for all of the events studied, the initiation phase of the CME comes before the onset of the corresponding flare. In general, the CME onset appears to lead the flare onset, but there are also cases that flares appear to lead the CME onsets ([Harrison, 1991, 1995](#)).

Overall, the flare-CME relationship can be summarized as follows: (1) There is a strong statistical association between flares and CMEs, but there is NOT a one to one association between flares and CMEs; (2) There is a “continuum” of events rather than two distinct (i.e., flare/non-flare) types of CMEs. On the other hand, CMEs associated with major flares are on average faster and broader than non-flare CMEs and small-flare CMEs, (3) Longer Duration Flares (LDE) have a greater chance of association with a CME, but a CME can be associated with a flare of any duration, or can be associated with no flare at all, (4) The onset of

1.2 Solar Eruptive Phenomena (Space-Weather Events)

a CME associated with a flare appears to occur at any time within several tens of minutes of the flare onset, i.e. either can appear to lead the other, (5) The scale sizes of CMEs and flares are very different, the average CME spans some 45° whereas active regions are typically much smaller than 10° in size, (6) The flare tends to lie anywhere within the span of an associated CME, and often lie to one side.

Most of these points except point 2 are from [Harrison \(1995\)](#), who gave a thorough review of numerous pre-SOHO studies and also presented a statistical study of the flare-CME relationship. These pre-SOHO conclusions are consistent with many recent SOHO studies, for a recent review on the flare-CME relationship please refer to [Harrison \(2006\)](#). These observations led [Harrison \(1995, 1996\)](#) to conclude : “The flare and CME are both consequences of the same magnetic disease. They do not cause one another but are closely related. Their characteristics are the results of local conditions, and thus, we may witness a spectrum of flare and CME properties which are apparently unrelated, even resulting in events without the flare or CME component.” The idea that the flare and CME do not cause one another but are different responses to the same driver has become a common conclusion with a few exceptions (e.g., [Khan & Hudson 2000](#)).

Filament Eruption-CME relationship

The majority of previous statistical studies regarding the connection between filament (or prominence) eruptions and CMEs have focused on prominences because they could easily be detected, observed, and measured against the dark sky background. Moreover, CMEs, associated with the prominences, are not difficult to detect. Many prominence classifications have been proposed in the past. For example, [Gilbert et al. \(2000\)](#) developed definitions of active prominences (APs) and eruptive prominences (EPs) and studied the relationship between APs, EPs, and CMEs for 54 events. They found that 94% of the EPs had an associated CME compared to only 46% for APs. [Gopalswamy et al. \(2003\)](#) defined a prominence as a radial or a transverse event. Authors showed that the radial events have a strong correlation to the CMEs: 83% of the radial events were associated with CMEs compared to 24% for transverse events. [Jing et al. \(2004\)](#) defined

a “filament eruption” as a solar activity event with significant upward motion and with at least 50% of the material vanishing during the course of a day. Through a statistical study of 106 filament eruptions observed by BBSO, they found that: (1) excluding eight events with no corresponding LASCO data, 55% or 56% of 98 events were associated with coronal mass ejections (CMEs), (2) active region filament eruptions have a considerably higher flare association rate of 95% compared to quiescent filament eruptions with 27%, but a comparable CME association rate, namely, 43% for active region filament eruptions and 54% for quiescent filament eruptions.

In summary, the correlation between a CME and a solar flare depends on the energy that is stored in the relevant magnetic structure, which is available to drive the eruption: the more energy that is stored, the better the correlation is, otherwise, the correlation is poor (Lin, 2004; Svestka, 1986). The correlation between solar flares and CMEs depends on the strength of the magnetic field in the source region—strong fields obviously can store more flare energy. The correlation between a CME and eruptive prominence, on the other hand, depends on the plasma mass concentration in the configuration prior to the eruption. If the mass concentration in the source region is significant, CME will be associated with filament eruptions, otherwise, a CME develops without an apparent associated eruptive prominence.

1.3 Theories of Solar Eruptions

Models of the basic instability in flares may be categorized according to whether the flare is eruptive or confined. CMEs are typically associated with eruptive flares, so eruptive models are thought to apply to both phenomena. We will discuss the “standard model” of eruptive flares and its more recent extensions known as the “tether cutting model” and the “magnetic breakout model”. We will also discuss the “loop-loop interaction model”, which is often applied to non-eruptive or confined events.

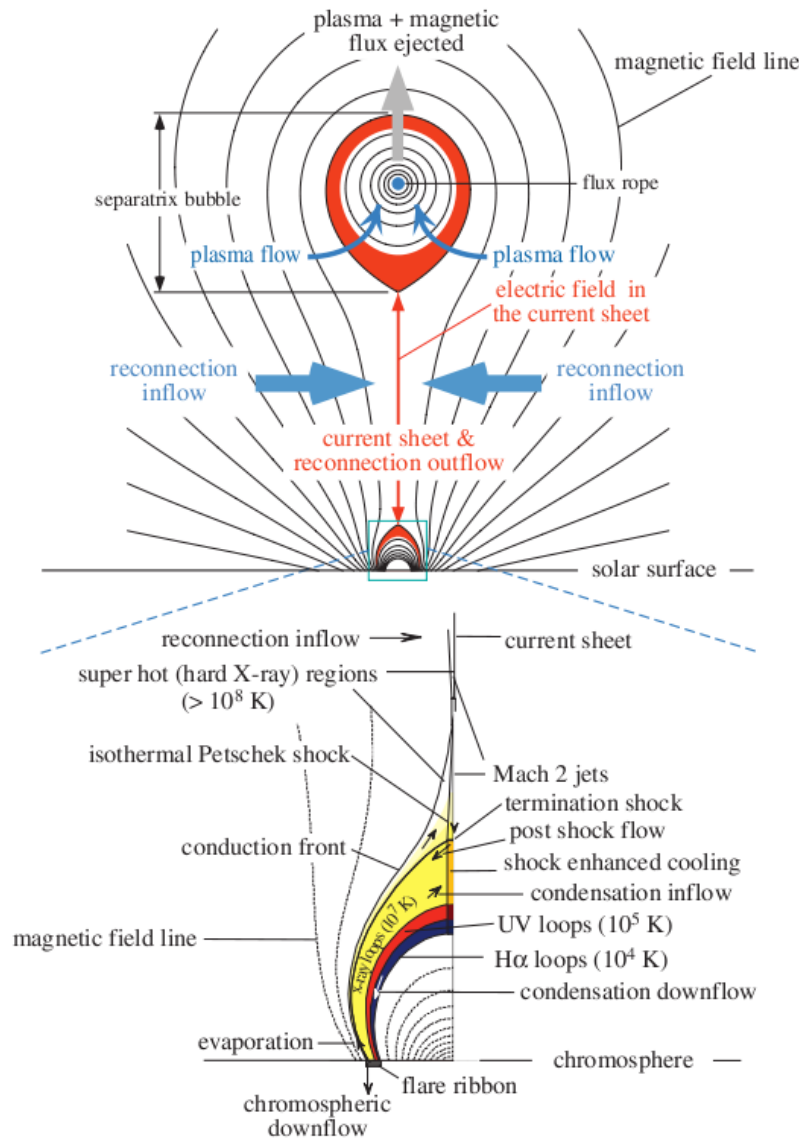


Figure 1.12: Schematic magnetic field configuration and flow pattern for a CME and flare. The upper part of the diagram shows the flux rope model of CMEs advocated by [Lin & Forbes \(2000\)](#), showing the eruption of the flux rope, current sheet formed behind it, and the post flare loops below, as well as the inflow and outflows associated with the magnetic reconnection at the current sheet. The lower part of the image is an enlarged view of the post flare loops, adapted from [Forbes & Acton \(1996\)](#). The upper tip of the reconnection cusp rises as reconnection proceeds.

1.3.1 Theories of Solar Flares

It is now widely accepted that magnetic reconnection occurs in the corona to power eruptive solar events such as flares and CMEs (for an overview see [Aschwanden 2002](#)). By the term “magnetic reconnection”, It is a process by which magnetic flux is swept into a small area where oppositely directed components annihilate each other, and the residual magnetic tension in the newly-reconnected field causes the field and plasma to be expelled from the reconnection region ([McKenzie, 2002](#)). The magnetic energy is converted into the thermal and kinetic energies of energetic particles in the flare.

The model for eruptive flares advanced primarily by Carmichael, Sturrock , Hirayama , and Kopp & Pneuman has become the ”standard model” of solar flares known as CSHKP model. It consists of two main phases: (1) the opening of a closed magnetic configuration, originally supposed to be closely related to the eruption of a filament/prominence , which creates an inverted Y-shaped magnetic configuration with a current sheet extending to greater heights above a closed magnetic configuration, and (2) long-lasting magnetic reconnection in this current sheet leading to the energy release in the main flare phase . The later includes the partial reclosing of the configuration by reconnected field lines in the downward reconnection outflow . The released energy is dumped at the magnetic footpoints in the chromosphere by energetic particle precipitation and heat conduction . This results in the formation of flare ribbons and of hot and dense flare loops through chromospheric evaporation ; these loops turn later into cooling postflare loops (Figures [1.12](#) and [1.13](#)).

Phase 2 is well-supported by a variety of observations of eruptive flares (e.g., [Svestka 1976](#), , [Tsuneta 1996](#), [Czaykowska et al. 1999](#), [Masuda et al. 2001](#), [Aschwanden & Alexander 2001](#)) and by MHD simulations (e.g., [Yokoyama & Shibata 2001](#)). However, some questions remain. Foremost are questions concerning the spatial and temporal scales on which the reconnection occurs (i.e., whether it is stationary (Petschek- like) or highly dynamic and fragmented in space), whether MHD turbulence is excited and fills substantial volumes, and whether the downward reconnection outflow jet indeed forms a standing fast-mode shock upon hitting the newly- formed flare and postflare loops.

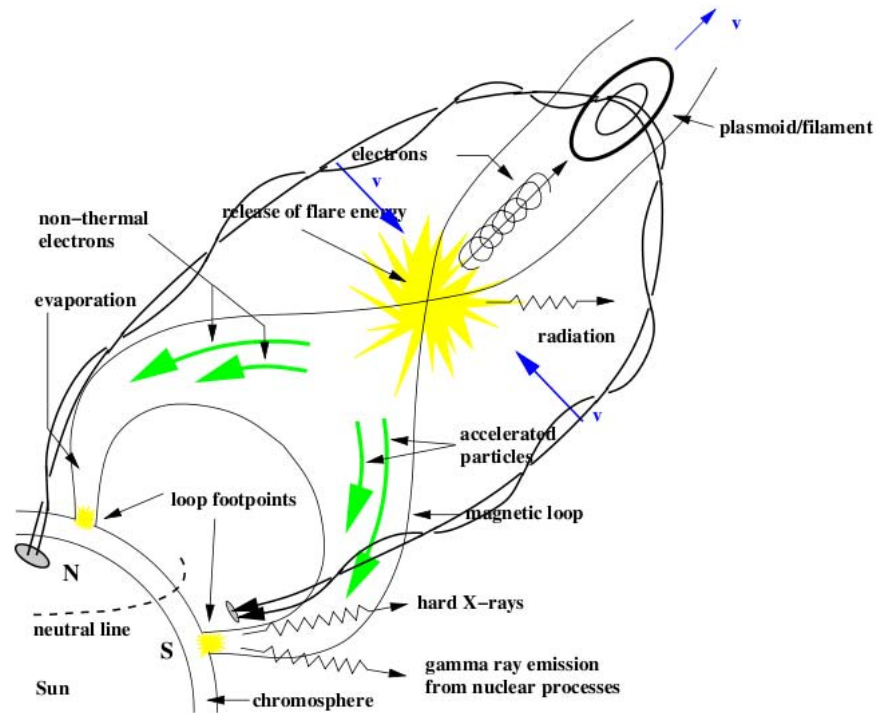


Figure 1.13: Flare model after some modification by [Lang \(2001\)](#).

The processes which open magnetic fields in flares and CMEs (phase 1) are poorly understood. The observations indicate that eruptive events originate in highly sheared magnetic flux systems oriented along a line of magnetic polarity inversion (the neutral line) in the photosphere, lying underneath a less sheared, stabilizing magnetic arcade. The erupting sheared core flux does not always contain a filament, which suggests that magnetic, not the thermodynamic effects are fundamental for its loss of balance.

Magnetic reconnection between two loops leads to two new loops—a transition between two closed configurations releasing energy. It is thus a viable model for confined (non-eruptive) flares. The process need not be restricted to a pair of single loops; groups of loops or flux bundles or the interaction between newly emerged flux and preexisting closed flux are conceivable as well. [Melrose \(1997\)](#) has investigated the process and identified the conditions required for large energy release for two favorable loop configurations: (1) interaction of two loops at a large

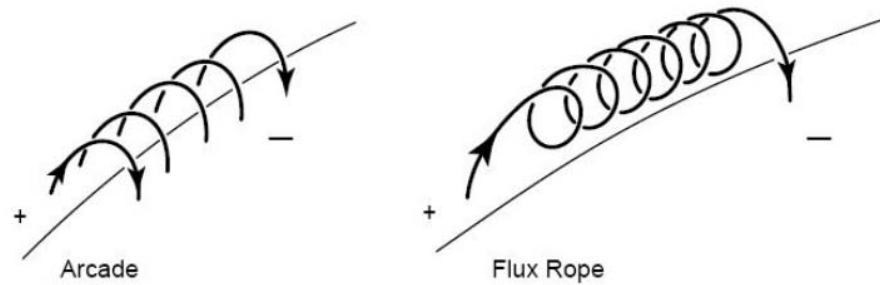


Figure 1.14: Schematic representation of arcade-like and flux-rope like coronal magnetic field geometry (Klimchuk, 2001).

angle to each other, with one of the resulting loops being very short and carrying the larger current, and (2) interaction of two coaligned loops to form a longer loop and a nested shorter loop

1.3.2 Models of Coronal Mass Ejections

The fundamental theoretical question about CME initiation has been studied for many years. A number of interesting theoretical models have been proposed to explain the nature and origin of CMEs. Here we briefly summarize the basic concept of CMEs based on a review by Klimchuk (2001). In most of CME models, the pre-eruption magnetic field has either a simple arcade-like (see Figure 1.14, left panel) or a flux-rope like (see Figure 1.14, right panel) configurations. Arcade field lines arch directly over the magnetic polarity inversion line connecting opposite magnetic polarities on the photosphere. The arcade like configuration may get sheared due to displacement of positive and negative polarities in opposite directions parallel to the polarity inversion line due to the Sun's differential rotation. Due to this shearing, the magnetic fields can gain magnetic free energy that can be released during an eruption. Left image of Figure 1.14 shows an arcade-like configuration which corresponds to a dipolar configuration. There may also exist quadrupolar configurations consisting of multiple arcades lined up side by side. The flux-rope magnetic topology is quite different from the arcade-like magnetic topology. Here magnetic field lines form a helical structure which lies above the

neutral line. Flux-rope are disconnected from the photosphere except at the ends, i.e. at their foot-points (Klimchuk, 2001). The right panel of Figure 1.14 shows a flux-rope like topology. The cartoon representing the flux-rope topology has much more twist than expected in the real structure. Sometimes a flux-rope may have one turn or less (Klimchuk, 2001) which makes the distinction between flux-rope and arcade-like topology doubtful (Titov & Démoulin, 1999). In a typical three-part CME, it is suggested that the dark cavity corresponds to a flux-rope seen edge-on (e.g., Chen et al. 1997, Dere et al. 1999). An example of a flux-rope CME is given in Figure 1.7. It is commonly believed that the embedded core represents prominence material which is trapped at the bottoms of helical field lines and dragged upward during the eruption (Klimchuk, 2001). However all CMEs are not comprised of three- parts (e.g., Burkepile & St. Cyr 1993, Dere et al. 1999). It should be noted that observations of flux-rope like topology in the corona does not imply that a flux-rope was part of the initial configuration. Gosling (1993) has suggested that a flux-rope may form due to magnetic reconnection during the eruption of a sheared arcade.

Though it is not certain, in many models it has been presumed that a CME occurs when the balance of forces that maintain the equilibrium is lost. Somehow the resultant force pointing upward becomes greater than the resultant force pointing downward (Klimchuk, 2001). There are mainly three forces in order to balance the equilibrium: The gravity force, the plasma/gas pressure, magnetic forces (magnetic pressure and magnetic tension). In many of the CME models the gravity force and gas pressure play important roles. However in many models the gravity force and the plasma pressure are ignored due to the low value of plasma beta (ratio of plasma thermal pressure to magnetic pressure), especially within active regions. On the Sun, the magnetic field spreads through the entire corona. Regions of strong magnetic fields in the corona have enhanced pressure and therefore magnetic field tends to expand into regions of weak field. On the solar surface, the arcade-like magnetic field lines arch over a flux-rope that may exist. The foot-point of these arcades are in the photosphere and the tension in the field lines act to hold the flux-rope in space. Similar kind of mechanism exist where the magnetic pressure is balanced by magnetic tension force in simple arcade-like magnetic field topology where there is no flux-rope (Klimchuk,

2001). The magnetic field strength is maximum at the center of the arcade in the equilibrium. The outward force produced by the gradient in magnetic pressure is balanced by the inward magnetic tension force.

Whenever the balance in these two forces is lost the eruption begins. If this force imbalance grows with time the eruption becomes violent. A variety of theoretical models have been proposed in order to understand the CME eruption. (For reviews see [Low 1999, 2001](#), [Forbes 2000](#), and [Klimchuk 2001](#)). [Klimchuk \(2001\)](#) classified existing CME models into five distinct classes. Based on the classification of [Klimchuk \(2001\)](#) we briefly describe the CME models.

Thermal Blast Wave : Initially flares were thought to be the main trigger of CMEs. It is assumed that the magnetic field can not sustain the greatly enhanced thermal pressure produced by a flare and thus pushes the CME outward into the heliosphere (e.g., [Dryer 1982](#); [Wu 1982](#)). An analogue to the thermal blast model is the overpressure generated by a bomb explosion (Figure 1.15, first panel). However, many CMEs have been detected without a preceding flare. Further, it was found that often the CME was launched prior to a flare ([Harrison, 1986](#)). Although sometimes the relative onset timing of flares and CMEs are very close, it is believed that the thermal blast model can not explain the onsets of CMEs (e.g., [Dryer 1996](#); [Delannée et al. 2000](#); [Zhang et al. 2001](#)).

Dynamo Model : The dynamo driven CME model is analogous to the stressing of a spring by an external force (see Figure 1.15, second panel). The rapid displacement of the foot- points of a coronal magnetic field system may generate stressing in the magnetic field which in turn leads to the inflation of the entire magnetic system ([Klimchuk, 2001](#)). In this model a sufficiently fast driver is expected to produce a CME-like eruption requiring a very fast motion of the foot points, at least two orders of magnitude more than the observed values (e.g., [Krall et al. 2000](#)).

Mass Loading Model : This model is known as the storage and release model. The storage and release model involves the slow build-up of magnetic stresses prior to the eruption. In the pre-eruption phase the mass loading process might

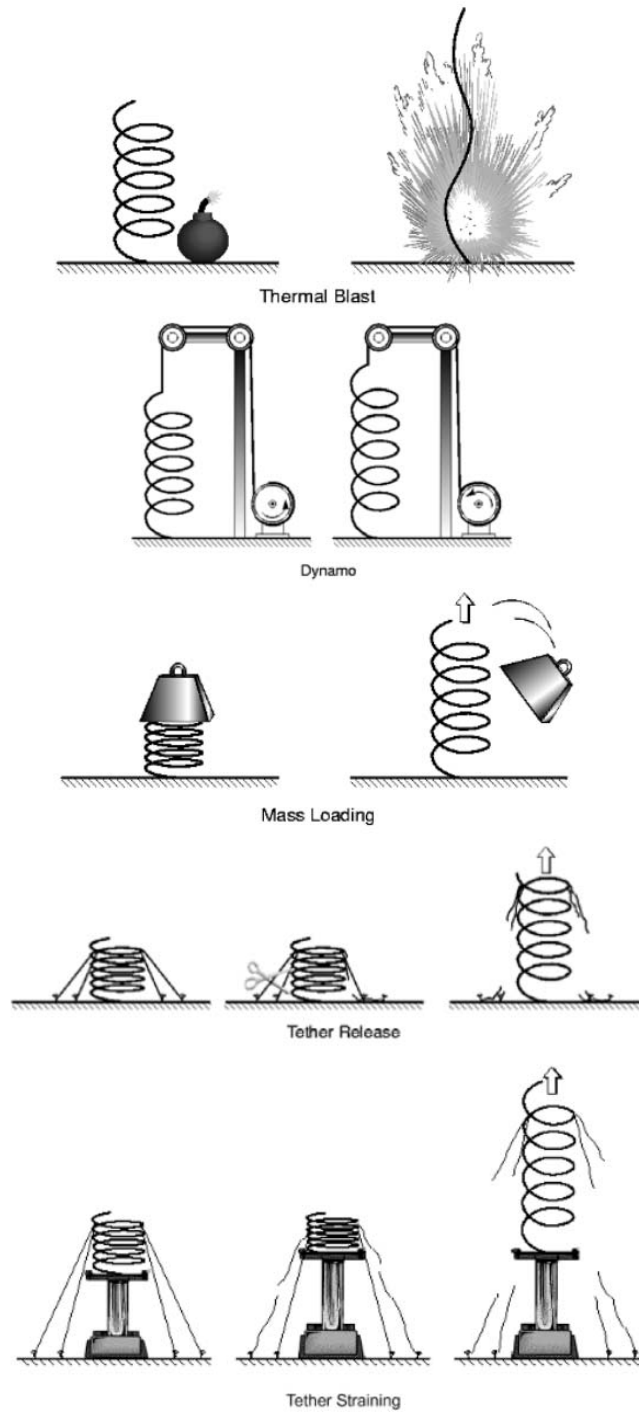


Figure 1.15: Physical analogies of five different coronal mass ejections model. From top to bottom: 1) thermal blast model, 2) dynamo model, 3) mass loading model, 4) tether cutting model, 5) tether straining model (Klimchuk 2001; adopted from Aschwanden 2004a).

be manifested through the spatial growth of a quiescent or active prominence (see Figure 1.15 third panel). There seem to exist two types of mass loading: 1) Through extremely dense compact prominences at chromospheric temperatures, 2) through dense plasma distributed over large volume which become unstable if they overlay coronal volumes of lower densities. This model proposes that the prominences play the fundamental role in CME initiation (Low, 1996, 1999), however they do not explain many CMEs not associated with prominences.

Tether Cutting Model : Moore & Roumeliotis (1992) suggested that eruptions result from a catastrophic loss of balance between the upward-directed magnetic pressure force and the downward-directed magnetic tension force within a sheared core flux system. They proposed that slow magnetic reconnection at the footpoints of the core flux system replaces short arched field lines by longer ones for which the stabilizing influence of the photospheric anchoring of the footpoints is reduced. Regarding the short arched field lines as tethers of the core flux, this reconnection can be viewed as “tether cutting” (see Figure 1.15 fourth panel). Moore & Roumeliotis (1992) suggested that the core flux then starts to slowly rise, dragging in material from the sides and forming a current sheet in which magnetic reconnection occurs. As soon as fast reconnection becomes operative, field lines of both the core flux and the overlying stabilizing flux system are efficiently cut on either side of the neutral line, and moreover, the upward reconnection outflow accelerates the further rise of the core flux system. A catastrophic loss of balance—an eruptive flare or a CME can result. Yohkoh Soft X-ray Telescope (SXT) observations motivated a recent refinement of the model: loss of balance due to reconnection between two sheared core flux systems (Moore et al., 2001). Noting that some non-eruptive flares start in much the same way as eruptive events, these authors suggest that the basic mechanism applies to all flares. The tether cutting model finds some support in the observations (e.g., Moore & Roumeliotis 1992; Moore et al. 2001). It predicts activity within the sheared core field, i.e., close to the neutral line, shortly before and at the beginning of eruptive events. This can be tested, e.g., by imaging microwave observations, which are sensitive to emissions by energetic particles near the footpoints of magnetic field lines.

Magnetic Breakout Model : The magnetic breakout model ([Antiochos et al., 1999](#)) assumes that the eruption results from the loss of balance between sheared core flux and overlying arcade-like flux and that the overlying flux is composed of two oppositely directed flux systems (which requires a quadrupolar field configuration, topologically similar to the early model by [Sweet \(1958\)](#)). Magnetic reconnection between these flux systems, possibly triggered by a swelling of the core flux, cuts the “tethers” formed by the overlying flux so that the core flux can “break out” (Figure 1.16). The breakout model is also appealing because it can be generalized to the three-dimensional magnetic field configuration of delta sunspots ([Antiochos, 1998a](#)), which are known to be the most prolific producers of big, eruptive flares (e.g., [Sammis et al. 2000](#)). On the other hand, if the reconnection above the sheared core field is regarded to be the main effect, then the flare ribbons forming at the footpoints of the field lines that emerge from the reconnection region are expected to move towards the photospheric neutral line, which is opposite to the observations. One can expect, however, that reconnection is triggered also below the rising core flux, similarly to the tether cutting model. Furthermore, it is not clear whether the supposed quadrupolar configuration is a characteristic of all eruptive events. Some observational support was given in [Aulanier et al. \(2000\)](#); [Sterling et al. \(2001\)](#), but further observations are clearly needed. Imaging at microwaves is a sensitive tool to check for the implied presence of particles, accelerated at or near the reconnection region above the core flux, at magnetic footpoints remote from the neutral line.

Many models have been developed to explain the onset and propagation of CMEs, but very few have been able to explain the exact nature of the mechanism which triggers them. For example, several models propose that CMEs are triggered by the onset of a micro-instability but they do not actually prescribe the physical process producing it ([Forbes, 2000](#)). At the present time, there is a general (but not universal) consensus that the onset mechanism involves the release of free magnetic energy associated with electric currents flowing in the corona. However, there is no consensus about the mechanism which releases the energy.

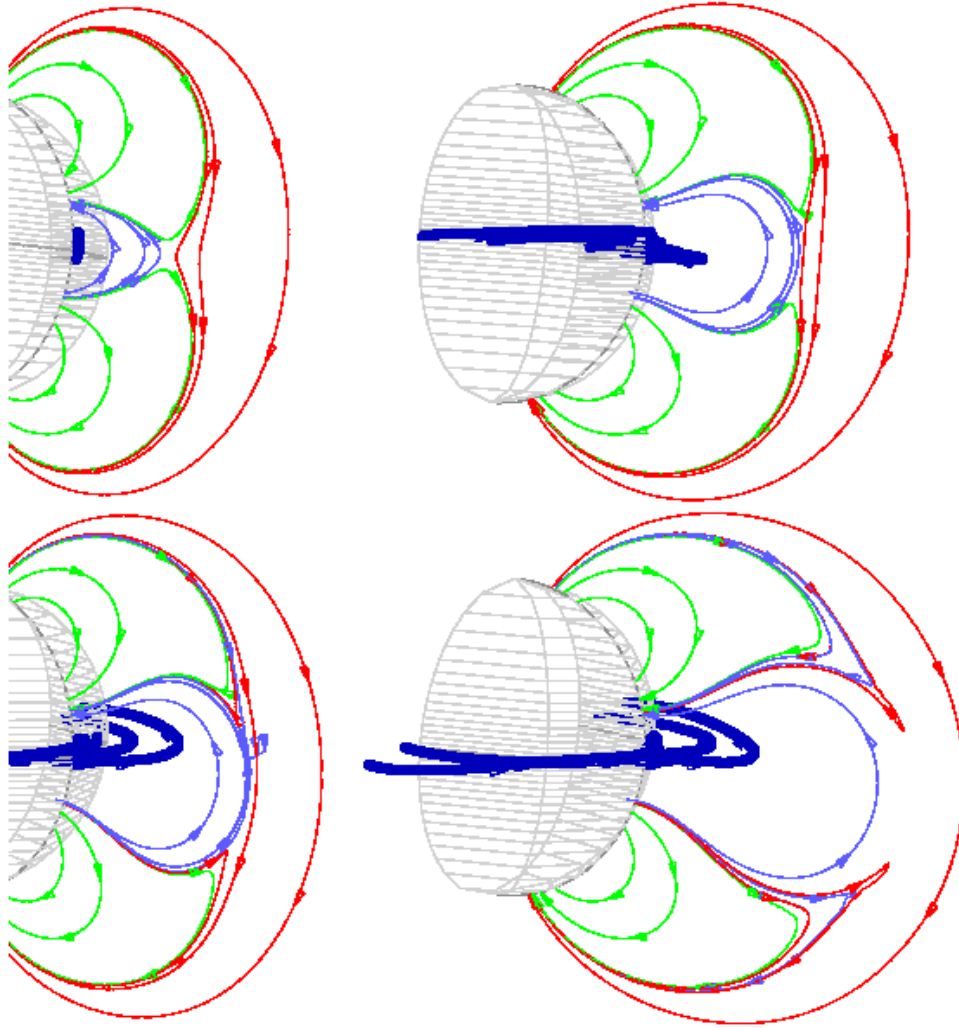


Figure 1.16: Magnetic field configuration in the “Break-out” model ([Antiochos et al., 1999](#)). A force free current is created by shearing the archade field (thick lines) at the equator. A toroidal current layer is also created as the sheared region bulges outwards. Reconnection of the field lines in the horizontal current sheet allows the sheared field lines to open outward to infinity.

1.4 Motivation of thesis and open issues

In this section, we summarize the current status of the solar flare/CME research (focus on the magnetic nature) based on the following fundamental key questions: How and where is the flare/CME energy stored? What is the trigger of the energy release? How and where is the energy released?

How and where is the flare energy stored?

It is well accepted that solar flare, prominence eruption, and coronal mass ejection are different manifestation of a single physical process that is related to the release of the magnetic free energy stored in the corona prior to the eruption. The magnetic free energy is stored by a change in photospheric boundary conditions, such as emerging flux (Heyvaerts et al., 1977; Zirin, 1983), flux cancellation (Martin et al., 1985), or sunspot motions (Gesztelyi et al., 1986). Storage of free energy requires a non-potential magnetic field, and it is therefore associated with a shear or twist in the corona away from the potential, current-free state (Priest & Forbes, 2002). Shear before flares is often observed in the chromosphere, as shown in $H\alpha$ fibrils (Tanaka & Nakagawa, 1973) and also in the photosphere, as shown in vector magnetograms near the polarity inversion line (Hagyard et al., 1984). These are suggestive of shear in the overlying corona (but sometimes there are significant differences in orientation between $H\alpha$ structures and photospheric magnetic fields (Gary et al., 1987). An indication of a stressed magnetic field in the corona is the presence of a prominence and another important one discovered by Canfield et al. (1999) with Yohkoh is the presence of sigmoidal structures. Despite all the progress, there are still questions yet to be answered, such as, are there reliable precursors of flare/CME events? Can we predict flares/CMEs? What is the coronal magnetic configuration prior to the flare? From plasma structures observed at various wavelengths, it appears that the field is in the form of a sheared arcade or half-emerging flux rope. The two possibilities are essentially indistinguishable unless the axis of the flux rope rises above the surface (Forbes, 2000). This leads to the two competing models for the pre-CME magnetic configuration. Some models (e.g., Forbes & Isenberg 1991; Gibson & Low 1998; Wu et al. 1999; Krall et al. 2000; Roussev et al. 2003) assume that a

magnetic flux rope exists prior to the solar eruption. However, the other models (e.g., [Mikic et al. 1988](#); [Mikic & McClymont 1994](#); [Antiochos et al. 1999](#); [Amari et al. 2003](#); [Manchester 2003](#)) relies on the existence of sheared magnetic arcades. The later models may create a flux rope by reconnection between the sides of the arcade during the eruption process.

What is the trigger of the energy release?

The trigger of energy release is model-dependent and must be inferred retrospectively, by comparing observations with the prediction of a model. In various CME models, eruption usually results from variations in the boundary, such as flux emergence, loss of the loaded mass, converging motion, or flux cancellation at the boundary ([Zhang & Chye Low, 2005](#)). Eruption may also result from the variations of source drivers themselves, such as twisting the field beyond a critical point. [Moore et al. \(2001\)](#) discussed three different mechanism that singly or in combination can trigger the CME: (1) runaway internal tether-cutting reconnection, (2) runaway external tether-cutting reconnection, and (3) ideal MHD instability or loss of equilibrium. For most eruptions, sorting out from observations which of these various possibilities is the trigger apparently requires (at least) high-cadence, high-resolution movies in chromospheric, transition-region, and coronal emission, such as are provided by TRACE, Hinode and STEREO along with high-cadence, high-resolution magnetograms.

How and where is the energy released?

It is generally believed that magnetic reconnection occurred somewhere in the corona is responsible for the ribbons and the set of rising post-flare loops, and such a process is well supported by numerical experiments and detailed observations from Yohkoh. The magnetic energy released via reconnection is then converted to thermal (plasma heating) and kinetic energy (particle acceleration) causing solar flare and CME. However, there are still a lot of important questions remain to be answered. Such as, what is the relative amount of energy contained in the flare vs. the CME? What is the relative amount of energy injected directly into plasma heating vs. particle acceleration? How did the reconnection lead to particle acceleration is even less understood. Particle acceleration in flares

may in principle occur in a variety of ways, such as stochastic acceleration by MHD turbulence, acceleration by direct electric fields at the reconnection site, or diffusive shock acceleration at the different kinds of magnetohydrodynamics (MHD) shock waves that are produced during the flare (Priest & Forbes, 2002). However, which of these processes is most important for producing the energetic particles that strike the solar surface remains a mystery. Magnetic energy conversion by reconnection in two dimensions is relatively well understood, but in three dimensions we are only starting to understand the complexity of the magnetic topology and the MHD dynamics which are involved (Priest & Forbes, 2002). The flare/CMEs multiwavelength observations and their initiations are aimed to address the magnetic nature of the solar eruption. We try to address the above fundamental questions, through multi-wavelengths investigations of the evolution of the highly sheared magnetic fields. Observations and their explanations with models focused on these questions are presented in Chapters 3, 4, 5, 6, based on, respectively, Kumar et al. (2010, 2010a, 2010b, and 2010c).

1.5 Organization of thesis

The thesis contains seven chapters including the introduction. The second chapter is devoted to instrumentation and data reduction techniques. The third chapter is related to the study of solar flare events on 20 November, 2003 and the associated CMEs, which were associated with filament interactions and sunspot rotation. In the fourth chapter, we have studied the solar flares/CMEs on 18 November, 2003 which produced the strongest geomagnetic storm of solar cycle 23. The fifth chapter presents the analysis of solar flares occurred on 04 June, 2007 from AR 10960. The sixth chapter contains the analysis/description of solar flare 1N/M7.9 on 27 April, 2006, which was triggered due to loop-loop interaction in AR 10875. The seventh chapter is devoted to the summary and future plans.

Chapter 2

Data Set and Analysis Procedure

2.1 Introduction

Our Sun is the only star which is close enough to observe details on its surface. We can observe sunspots, faculae, prominences, coronal holes etc., which are all summarized as solar activity phenomena. Therefore, the study of the Sun is important for astrophysics in general. Because of its close proximity, large angular size (about 31 arc min) and abundance of flux received from it, solar astronomy requires use of modest size telescopes and equipments. An optical telescope of 14 cm aperture at 5500 Å can resolve 1 arc sec size Sun's feature, corresponding to 750 km on solar disk.

The results presented in this thesis are based on data from various observing instruments and catalogues. In chapter 3 and 4, we have presented a multi-wavelength analysis of solar flares/CMEs events from active region NOAA 10501 and signature of magnetic reconnection in different wavelengths. The primary data set for both the events were obtained from Solar Tower Telescope at Aryabhata Research Institute of Observational Sciences (ARIES), Nainital, India. To understand the characteristics of propagation of the CME-associated disturbance in the interplanetary medium, we have used remote sensing interplanetary scintillation (IPS) data taken from Ooty Radio Telescope, Radio Astronomy Centre, Ooty, India. Both of these Indian facilities provide excellent data set for the study of solar flares and associated phenomena in the near-Sun region and in the interplanetary environment. In chapter 5 and 6, we have used the multiwavelength

data from different space based instruments (i.e. SOHO, TRACE, RHESSI, Hinode, STEREO etc.). In section 2.2, we describe Solar Tower Telescope at ARIES, its back-end instruments and basic procedure of image processing. The details of Ooty Radio Telescope and IPS observations are presented in section 2.3. A small description of other data sources and data catalogues is given in the final section of the chapter.

2.2 ARIES Solar Tower Telescope

2.2.1 The telescope

At ARIES, Nainital (latitude $29^{\circ} 22'$ N, longitude $79^{\circ} 27'$ E, altitude 1955 m), we use a Carl Zeiss Coudé refractor for solar activity monitoring. The refractor has an objective lens of 15 cm clear aperture and 225 cm focal length, yielding an f-ratio of 1:15. The objective along with two plane mirrors (the mirrors having highly reflecting aluminium coating are located at the intersection points between the declination axis and the polar axis) in a Coudé type configuration, results in a stationary focus (prime focus of the system) at the lower end of the polar axis. A heat rejection filter is placed ahead of the objective. This filter rejects the intense heat radiation from the incoming solar beam, keeping the telescope tube cool and protecting the $H\alpha$ filter (see subsection 2.2.2) from undesired heating and thus maintaining the quality of the image.

For making the $H\alpha$ observations of solar activity, a Barlow lens is interposed ahead of the prime focus of the refractor. The Barlow lens extends the effective focal length of the objective approximately by a factor of 2. Thus the prime image of 22 mm gets enlarged to a size of about 42 mm. The telescope can be equipped with many supplementary back-end instruments (filters and detectors), so that it becomes an excellent basic equipment for the observations of solar flares.

The telescope is installed on a 35-feet high tower to reduce the effect of seeing (i.e. the degradation of image quality by fluctuations of the refractive index in the light path) on solar observations. During the morning hours the Sun heats the ground around the observatory. Any heated surface is a source of air instability. Since the viscosity of air is small, the resulting convective motion will have a

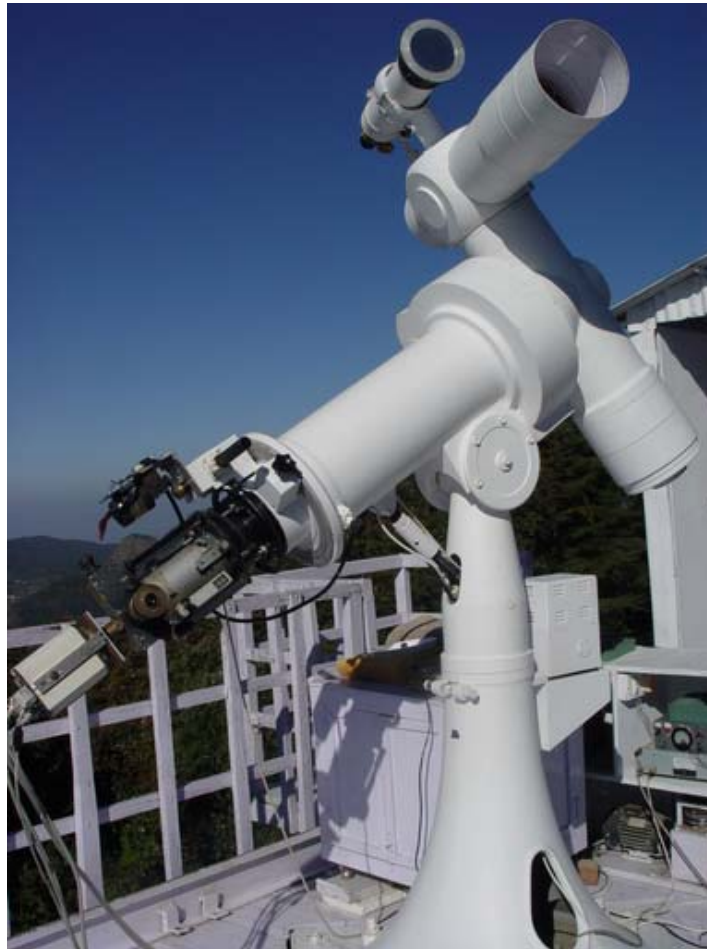


Figure 2.1: A view of 15 cm Coudé refractor with back-end instruments, installed on a 35-foot high tower which is used for solar observations at ARIES, Nainital.

large Reynolds number and therefore be turbulent. This effect of ground-level turbulence can considerably be reduced by the use of a high building ([Stix, 1989](#)).

2.2.2 Bernhard Halle $H\alpha$ filter

Bernhard Halle $H\alpha$ filter is a birefringent filter ([Stix, 1989](#)). The filter is made up to 10 main birefringent elements and an additional contrast enhancing element. All these optical elements are combined in a cylindrical housing which is kept at a constant temperature. To avoid damage to the filter optics from intense radiation, the interference prefilter is mounted at the entrance side of the cylindrical housing.

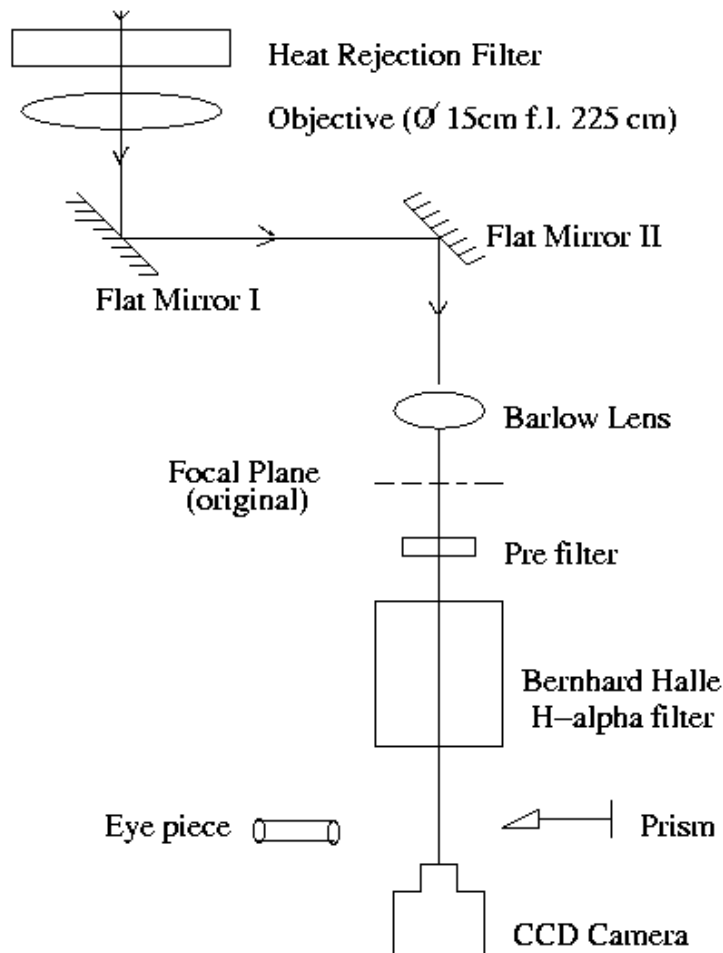


Figure 2.2: Schematic drawing of the Coudé refractor for $H\alpha$ observations.

The filter has a passband at the red Hydrogen line ($H\alpha$) when it is kept at a temperature of 46°C . This constant temperature is maintained with the help of an electronic heating circuit. The two main elements with higher resolutions and the contrast element are tunable to give the filter a scanning range of $\pm 0.7 \text{ \AA}$ with almost unreduced resolution and $\pm 1.0 \text{ \AA}$ with only weak sidebands.

2.2.3 The detector

The detector used for the observations is $384 \times 576 \text{ pixel}^2$, 16 bit frame transfer CCD camera. Each pixel has a size of $22 \mu\text{m}^2$ which corresponds to a square of $\sim 1''$ spatial resolution when mounted with the ARIES Solar Tower Telescope (cf.

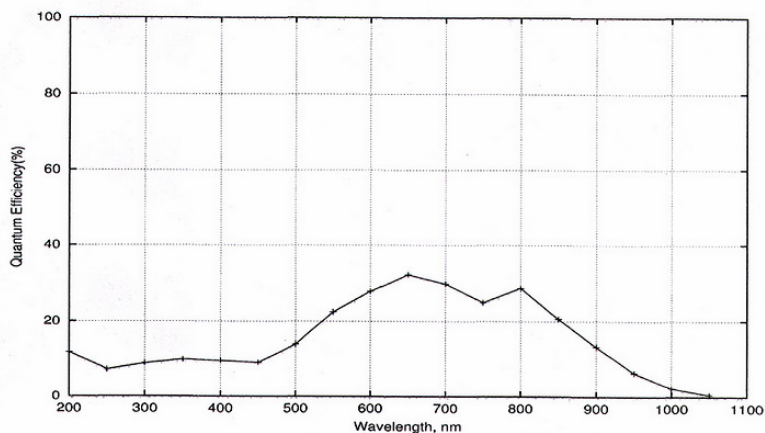


Figure 2.3: The quantum efficiency curve for CCD detector described in section 2.2.3.

Table 2.1: CCD Characteristics

Company	Wright Instruments, UK
Pixel size	$22 \mu\text{m}^2$
Operating temperature	$-20 \text{ }^\circ\text{C}$
Readout noise	18 e^-
Camera gain	$20 \text{ e}^-/\text{ADU}$
Dark current	$0.1 \text{ e}^-/\text{second}$
Resolution	16 bits
Readout rate	200 kHz.

section 2.2.1) for $\text{H}\alpha$ observations.

A typical CCD camera consists of a two-dimensional array of photon detectors in a layer of semi-conducting material silicon. Each individual detector in the array is referred to as pixel. A photon hitting the detector can release an electron, which will remain trapped inside a pixel. After exposure, varying potential differences are used to move the accumulated charges row by row to a readout buffer. In the buffer the charges are moved pixel by pixel to an analogue to digital converter, which transmits the digital value to a computer. Reading an image also clears the detector.

The thermal noise of the camera generates dark current even if the camera

is in total darkness. To reduce the dark current the astronomical CCD cameras are cooled to low temperatures. Nevertheless, the dark current can be measured by taking exposures with the shutter closed. Subtracting this from the observed image gives the real number of electrons due to incident light. Also, the sensitivity of individual pixels may be slightly different. This can be corrected for by taking an image of an evenly illuminated field (eg., by defocussing the Sun's image). This image is called flat-field. When observations are divided by the flat-field, the error caused by different pixels is removed.

Table 2.1 summarizes various characteristics of CCD used by us. One of the important characteristics is the quantum efficiency, i.e. the number of electrons per incident photons. The quantum efficiency curve for this CCD is shown in Figure 2.3 which shows that the CCD has the highest sensitivity at wavelength $\sim 6500 \text{ \AA}$.

2.3 Ooty Radio Telescope and IPS measurements

2.3.1 The telescope

The Interplanetary-scintillation (IPS) measurements presented in this thesis were made using Ooty Radio Telescope (ORT) at Radio Astronomy Centre, Ooty. This telescope operates at a frequency of 326.5 MHz with a bandwidth of 4 MHz (Swarup et al., 1971). The ORT is used for various astronomical studies. IPS observations of weakly-scintillating radio sources require a telescope of large collecting area which is capable of tracking a source for sufficient time in order to obtain stable power spectra having high signal-to-noise ratio. The ORT, which has an effective collecting area of $\sim 8000 \text{ m}^2$ and can track a radio source continuously for about 10 hours, is well suited for IPS studies. The ORT is a parabolic cylindrical antenna, 530 m long in the north-south direction and 30 m wide in east-west (see Figure 2.4). The reflecting surface of the ORT is formed by 1100 thin stainless-steel wires. The antenna is equatorial mounted, its long north-south axis lying parallel to the axis of rotation of the Earth. This is achieved by mounting the cylinder on a north-south hillside of inclination $+11^\circ 22' 50''$ to the horizontal. The latitude of Ooty is also $11^\circ 22' 50''$ N. Hence,



Figure 2.4: Left: A view of the Ooty radio telescope, which is 530 m long and 30 m wide (Swarup et al., 1971). The right image shows the closer view of the telescope.

it is possible to track a source by mechanically rotating the cylinder about its north–south axis. The telescope can cover an hour angle of -4^{h} to $+5\frac{1}{2}^{\text{h}}$. An array of 1056 dipoles is placed along the focal line of the parabolic cylindrical reflector. Group of 48 dipoles form 22 electric modules that constitute the feed system of the telescope.

2.3.2 Interplanetary Scintillation

The interplanetary scintillation (IPS) technique exploits the scattering of radiation from distant point-like radio sources (e.g., quasars or radio galaxies of angular diameter ≤ 0.4 arcsec) by the electron-density irregularities in the solar wind. That is, the plane wavefront gets phase modulated by the refractive index variations caused by the density fluctuations in the solar wind (Tatarski 1961). The resultant diffraction pattern caused by the scattered radio waves, produces temporal intensity fluctuations on the ground as shown schematically in Figure 2.5. The temporal spectrum of intensity fluctuations, $P(f)$, i.e., the power spectrum of intensity measured at the input of a radio telescope, is the Fourier transform of the auto-correlation function of intensity.

Let us consider the intensity of the source at a given time is $I(t)$ and its fluctuation about the mean is $\Delta I(t)$. The fluctuation $\Delta I(t)$ is written as

2.3 Ooty Radio Telescope and IPS measurements

$$\Delta I(t) = I(t) - \langle I(t) \rangle. \quad (2.1)$$

Angular brackets denote the ensemble average, with the average taken over a sufficiently long time, and defines the mean intensity of the source $I_0 \approx \langle I(t) \rangle \approx \langle I \rangle$. The measure of scintillation is quantified by the scintillation index

$$m = \frac{\text{rms of intensity fluctuations}}{\text{mean source intensity}} = \left\{ \frac{\langle \Delta I(t)^2 \rangle}{\langle I \rangle^2} \right\}^{\frac{1}{2}} \quad (2.2)$$

The variations of the intensity fluctuations in space and time provide the autocorrelation function of the randomly-varying intensity, which is also a measure of the scintillation,

$$\rho(\mathbf{r}, t) = \langle \Delta I(\mathbf{r}_0, t_0) \Delta I(\mathbf{r}_0 + \mathbf{r}, t_0 + t) \rangle \quad (2.3)$$

where \mathbf{r}_0 and t_0 represent any position vector and time coordinate and \mathbf{r} and t represent shifts in position and time.

The temporal spectrum of the intensity fluctuations $P_I(f)$, i.e. the power spectrum of fluctuations, measured at a single-point, is the Fourier transform of the autocorrelation function of the fluctuations. Thus, the power spectrum can be written in the form,

$$P_I(f) = \frac{1}{2\pi} \int_{-\infty}^{+\infty} \rho(0, t) e^{-i2\pi ft} dt \quad (2.4)$$

where f is the temporal frequency. The scintillation index itself can be shown to be related to the area under the temporal intensity spectrum. From eqns. 2.2 and 2.3,

$$m^2 = \frac{\rho(0, 0)}{\langle I \rangle^2} \quad (2.5)$$

and it is seen from the inverse transform of eqn. 2.4 that,

$$m^2 = \frac{1}{\langle I \rangle^2} \left[\int_{-\infty}^{+\infty} P_I(f) df \right] \quad (2.6)$$

Thus, the area under the temporal intensity spectrum gives the variance of the intensity fluctuations and the variance normalized by the square of the mean

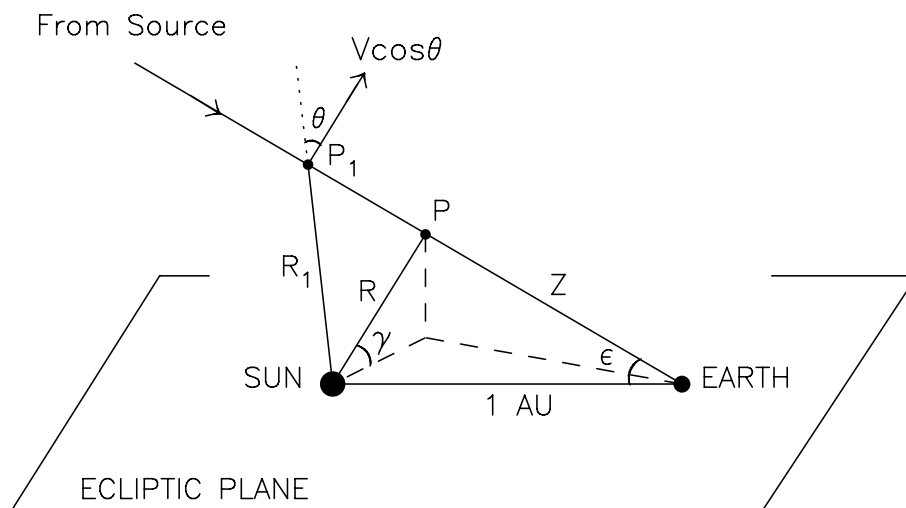


Figure 2.5: Schematic diagram illustrating the geometry of the formation of interplanetary scintillation. The angle between the Sun, the Earth and the radio source is the solar elongation (ϵ). Heliocentric distance to the radio path = $\text{sinc} \epsilon$ AU.

source intensity gives the square of the scintillation index (m^2). The temporal power spectrum can also be suitably calibrated to estimate the speed of solar wind and shape of the density spectrum (Manoharan & Ananthkrishnan, 1990).

Depending upon the observing wavelength, the IPS method can provide solar wind conditions in the three-dimensional heliosphere of radius a few solar radii to about 1 AU. An example of IPS measurements taken with Ooty Radio Telescope is presented in Figure 2.6. The Figure shows the scintillation index variation with distance from the Sun for a given radio source, 1148-001, which has a diameter of about 15 milli arcsec. The scintillation index increases with decreasing distance (R) between the Sun and the line-of-sight to the radio source, until it reaches a maximum at $R \approx 40 R_{\odot}$. In the weak-scintillation region (i.e., at $R \geq 40 R_{\odot}$), the intensity scintillation is linearly related to the electron-density fluctuations (Manoharan, 1993). The decline in scintillation at distances away from the transition point is caused by the fall of density (as well as density fluctuations turbulence) approximately as a function of inverse square of heliocentric distance. However, in the strong scintillation region ($R < 40 R_{\odot}$), the relationship between the scintillation and the density fluctuations is not straight forward and as the

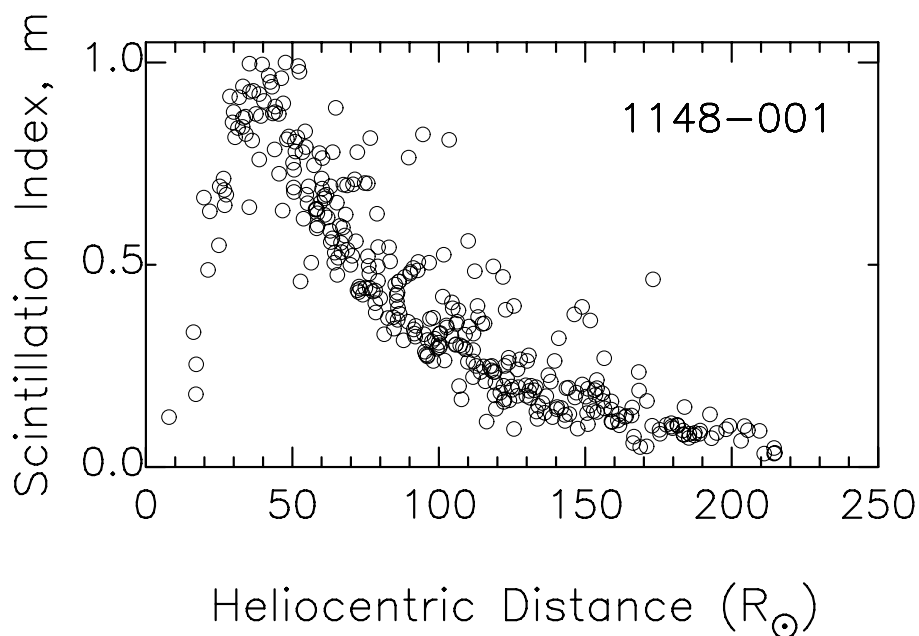


Figure 2.6: Variation of scintillation index as a function of distance from the Sun for the quasar 1148-001 at 327 MHz

radio source approaches the Sun, the scintillation index decreases steeply, which is due to the smearing caused by the angular size of the radio source (Manoharan et al., 1995). The ratio of the observed scintillation index of a radio source at a given distance from the Sun and its long-term baseline value of the scintillation index at the same distance is called the normalized scintillation index (g)

$$g = \frac{\text{observed scintillation } (m(R))}{\text{average expected scintillation } (\langle m(R) \rangle)}. \quad (2.7)$$

The normalized index, g , (and hence the rms of density fluctuations, δN) correlates strongly with the solar wind density (N) with a relationship $g = \sqrt{(N/9)}$ (Manoharan, 1993; Rickett & Coles, 1991; Tappin, 1986) and it can be used to assess the density turbulence condition of solar wind. For example, the value of g close to unity indicates the undisturbed condition of the solar wind, whereas $g > 1$ corresponds to the enhanced level of plasma density turbulence, and, $g < 1$ indicate the reduction of density in the solar wind.

Although IPS measurements are integrated along the line of sight (i.e., along the radio path), observations on a grid of large number of radio sources (i.e.,

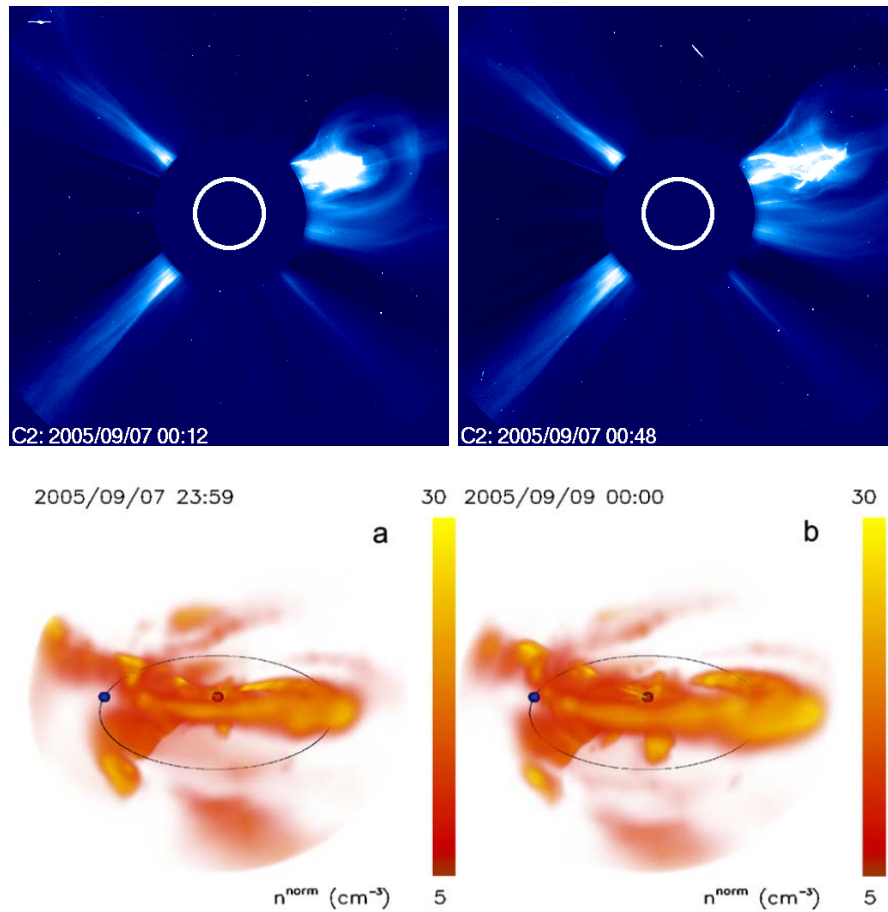


Figure 2.7: Top: White-light images of the flux rope CME from LASCO/SOHO C2 coronagraphs on September 07, 2005. Bottom: A three-dimensional remote-observer view of the heliospheric density obtained from the reconstruction of Ooty IPS measurements on 07 September 2005. Each presentation covers a field of view of 3 AU and with the Sun located at the center. The orbit of the Earth is shown by an ellipse. The Earth is located to the right of each image (shown as a blue dot). In these maps, different solar wind disturbances can be observed to move outward. Flux-rope type features associated with the propagating CMEs can also be seen. The observer is located $\sim 30^\circ$ above the ecliptic plane and $\sim 90^\circ$ west of the Sun–Earth line (Manoharan, 2010).

towards various lines of sight) can easily detect and provide the image of the large-scale structure of the quasi-stationary solar wind as well as propagating interplanetary disturbance (Manoharan et al., 2001). In the case of a propagating disturbance (e.g., a coronal mass ejection or a co-rotating interaction region), the IPS technique detects the compression region (or sheath) between the shock ahead and the pushing driver gas. Thus the increase in scintillation with respect to the background solar wind flow can identify the presence of disturbance in the interplanetary space at various distances from the Sun. At Ooty, normally scintillations towards 300 to 400 radio sources are recorded each day and the distribution of their normalized scintillation indices (eqn. 2.7) give the image of the density turbulence in the interplanetary medium. Figure 2.7 shows a typical example of flux rope CME observed by LASCO C2 (white-light) and ORT simultaneously. The twisted helical flux rope structure is evident in the scintillation images.

2.4 Other instruments and data catalogues

2.4.1 Solar and Heliospheric Observatory

The Solar and Heliospheric Observatory (SOHO¹) is a cooperative mission between the European Space Agency (ESA) and National Aeronautics and Space Administration (NASA) to study the Sun, from its deep core to the outer corona, and the solar wind (Domingo et al., 1995). The spacecraft was launched on December 2, 1995. The three principal scientific objectives of SOHO mission can be summarize as follows:

- (1) Study of the solar interior, using the techniques of helioseismology
- (2) Study of the heading mechanisms of solar corona, and
- (3) Investigation of solar wind and its acceleration processes.

For these scientific goals, SOHO is equipped with 12 different instruments. However, for the analysis of solar flares and associated phenomena, we have used data from following instruments on board SOHO.

¹<http://sohowww.nascom.nasa.gov/>

2.4 Other instruments and data catalogues

Table 2.2: EIT observations at different bandpasses and their scientific objectives

Wavelength	Ion	Peak Temperature	Observational Objective
304 Å	He II	8.0×10^4 K	chromospheric network; coronal holes
171 Å	Fe IX-X	1.3×10^6 K	corona/transition region boundary; structure inside coronal holes
195 Å	Fe XII	1.6×10^6 K	quite corona outside coronal holes
285 Å	Fe XV	2.0×10^6 K	active regions

(a) Extreme Ultraviolet Imaging Telescope (EIT): The primary scientific objective of EIT is to study the dynamics and evolution of coronal structures over a wide range of time-scales, sizes and temperatures in order to bring new insights into the mechanisms responsible for transient events, coronal heating processes and solar wind acceleration (Delaboudiniere et al. 1995). Images in coronal lines show coronal loops and their magnetic topology which changes by magnetic reconnection during a solar active phenomenon. The Extreme-Ultraviolet Imaging Telescope (EIT) is designed to provide full-disk images of the solar transition region and the inner corona to $1.5 R_{\odot}$. Its normal incident multilayer-coated optics select the spectral emission lines from Fe IX (171 Å), Fe XII (195 Å), Fe XV (284 Å) and HeII (304 Å) to provide sensitive temperature diagnostics in the range from 6×10^4 K to 3×10^6 K (cf. Table 2.2) This telescope has a $45' \times 45'$ FOV and $2.6''$ pixels which provide about $5''$ spatial resolution.

(b) Large angle spectroscopic coronagraph (LASCO): To study the characteristics of propagation of coronal mass ejections (CMEs), we have used white-light images of corona observed from the LASCO instrument. The LASCO (Brueckner et al. 1995) is a wide-field, white-light coronagraph comprising of three optical systems, C1, C2, and C3, that together image the solar corona from 1.1 to $30 R_{\odot}$. The C1 coronagraph (1.1 to $3.0 R_{\odot}$) is a newly developed mirror version of the classic internally-occulted Lyot coronagraph, while the C2 (1.5 to $6.0 R_{\odot}$) and C3 (3.7 to $30.0 R_{\odot}$) coronagraphs are externally occulted instruments.

An externally occulted coronagraph has two basic limitations. First, for a given distance from the occulting disk to the first imaging element, the instrument can only provide images of the corona for a finite distance above the Sun's limb

2.4 Other instruments and data catalogues

Table 2.3: System parameters for LASCO C1, C2 and C3 coronagraphs

Coronagraph	FOV (R_{\odot})	Occulter Type	Spectral Bandpass	Objective Element	Pixel Size
C1	1.1 – 3.0	Internal	Fabry-Perot	Mirror	5.6''
C2	1.5 – 6.0	External	Broadband	Lens	11.4''
C3	3.7 – 30	External	Broadband	Lens	56.0''

(1.5 R_{\odot}). At the inner edge of the field of view, most of the imaging element is shadowed by the occulter. Consequently, the spatial resolution in the inner corona is poor because of the very small effective apertures. Second, because of size limitations, the aperture cannot usually exceed a few centimeters.

The LASCO coronagraph overcomes these problems by using three different coronagraphs with these overlying fields-of-view. The inner corona, from 1.1 to 3 R_{\odot} , is imaged by a mirror version of the classic Lyot coronagraph without an external occulter, thus preserving the full resolution of the instrument over the whole field-of-view. The C1 coronagraph was the first internally occulted system operating in space. However C1 was in operation only during 1996–1998. The second coronagraph C2 images the Sun from 1.5 to 6 R_{\odot} . This is designed as an externally occulted instrument because of rapid decrease in coronal intensity with distances. LASCO extends the FOV to 30 R_{\odot} by adding a third coronagraph C3. The C2 coronagraph overlaps the outer FOV of C1 coronagraph and inner FOV of C3 in order to maintain the ability to obtain high spatial resolution images over the whole field from 1.1 to 30 R_{\odot} . Various parameters for three LASCO coronagraphs are summarized in Table 2.3.

(c) Michelson Doppler Imager (MDI): The MDI instrument provides high-resolution and full-disk observations of the line-of-sight magnetic field, free from atmospheric distortions (Scherrer et al., 1995). Measurements of magnetic field are of fundamental importance to understand many physical processes in solar physics.

MDI samples the Ni I 6768 Å solar absorption line with two wide field tunable Michelson interferometers that define a 94 mÅ bandpass. A longitudinal magnetogram is constructed by measuring the Doppler shift separately in right and left

Table 2.4: RHESSI characteristics

Energy Range	3 keV to 17 MeV
Energy resolution (FWHM)	≤ 1 keV at 3 keV, increasing to ~ 5 keV at 5 MeV
Angular resolution	2.3 arc sec to 100 keV, 7 arc sec to 400 keV, 36 arc sec to 15 MeV
Temporal resolution	2 s for detailed image, tens of ms for basic image
Field of view	full Sun ($\sim 1^\circ$)
Detectors	9 Germanium detectors
Imager	9 pairs of grids, with pitches from 34 microns to 2.75 mm, and 1.55 m grid separation

handed circularly polarized light. The difference between these two is a measure of the Zeeman splitting and is roughly proportional to the magnetic flux density. MDI can be operated in full disk mode (2'' pixel size) as well as in high resolution mode (0.65'' pixel size). The high-resolution FOV is roughly 650'' squared and is centered about 160'' north of the equator on the central meridian.

2.4.2 The Reuven Ramaty High-Energy Solar Spectroscopic Imager (RHESSI)

The Reuven Ramaty High–Energy Solar Spectroscopic Imager (RHESSI¹) is the sixth NASA’s small explorer mission that was launched on February 5, 2002. It is designed to investigate particle acceleration and energy release in solar flares, through imaging and spectroscopy of Hard X-ray/gamma-ray continua emitted by energetic electrons, and of gamma rays produced by energetic ions.

The RHESSI (Lin et al., 2002) utilizes a single instrument consisting of an Imaging System, a Spectrometer, and the Instrument Data Processing Unit (IDPU) containing the instrument electronics. Table 2.4 presents specifications of RHESSI instrument. The imaging system is made up of nine Rotating Modulation Collimators (RMCs), each consisting of a pair of widely separated grids mounted on a rotating spacecraft. Pointing information is provided by the Solar Aspect System (SAS) and redundant Roll Angle System (RASs). The spectrometer has

¹<http://hesperia.gsfc.nasa.gov/hessi/>

nine segmented germanium detectors (GeDs) one behind each RMC, to detect photons from 3 keV to 17 MeV. The GeDs are cooled to ≤ 75 K by a mechanical cryocooler to achieve the very high spectral resolution. The instrument's $\sim 1^\circ$ field of view is much wider than the $\sim 0.5^\circ$ solar diameter, so all flares are observed, and pointing can be automated.

2.4.3 TRACE

The Transition Region and Coronal Explorer TRACE satellite, launched on 2 April 1998 in Universal Time (UT), is a NASA (National Aeronautics and Space Administration) Small Explorer (SMEX) mission to image the solar photosphere, transition region and corona with high spatial and temporal resolution ([Handy et al., 1999](#)). TRACE enables solar physicists to study the connections between fine-scale magnetic fields at the solar surface and the associated plasma structures in the solar outer atmosphere in a quantitative way. The instrument features a 30 cm Cassegrain telescope with a field of view (FOV) of 8.5×8.5 arc minutes and a spatial resolution of $1''$ ($0.5''/\text{pixel}$). Normal incidence multilayer optics capable of observing from the photosphere to the corona enable TRACE to follow the evolution and dynamics of the solar atmosphere at selected temperatures over the range of 6000 K–10 MK. The TRACE temperature response at different wavelengths is listed in [Table 2.5](#). The TRACE observatory is a spacecraft in a sun- synchronous polar orbit. This allows for continuous uninterrupted solar observing for approximately 9 months each year. For the remaining 3 month eclipse season, the view from part of the TRACE orbit is occulted by the Earth.

2.4.4 Hinode

Hinode (Japanese meaning: Sunrise), formerly Solar-B, is a Japan Aerospace Exploration Agency Solar mission with United States and United Kingdom collaboration. It is the follow-up to the Yohkoh (Solar-A) mission and it was launched on the final flight of the M-V-7 rocket from Uchinoura Space Center, Japan on 22 September 2006. Initial orbit was perigee height 280 km, apogee height 686 km,

2.4 Other instruments and data catalogues

Table 2.5: TRACE Temperature Response ([Handy et al., 1999](#))

Wavelength (Å)	Emission	Bandwidth (Å)	Temperature (K)
171	Fe IX/X	6.4	$1.6\text{--}2.0 \times 10^5$
195	Fe XII/XXIV	6.5	$5\text{--}20 \times 10^5, 1.1\text{--}2.6 \times 10^7$
284	Fe XV	10.7	$1.25\text{--}4.0 \times 10^6$
1216	H I Ly α	84	$1.0\text{--}3.0 \times 10^4$
1550	C IV	30	$6.0\text{--}25 \times 10^4$
1600	UV Cont, C I, Fe II	275	$4.0\text{--}10 \times 10^3$
1700	Continuum	200	$4.0\text{--}10 \times 10^3$
5000	White Light	broad	$4.0\text{--}6.4 \times 10^3$

inclination 98.3 degrees. Then the satellite maneuvered to the quasi-circular sun-synchronous orbit over the day/night terminator, which allows near-continuous observation of the Sun.

Hinode is planned as a three-year mission to explore the magnetic fields of the Sun. It consists of a coordinated set of optical, extreme ultraviolet (EUV), and X-ray instruments to investigate the interaction between the Sun's magnetic field and its corona. It carries three main instruments to study the Sun:

SOT (Solar Optical Telescope)

The Solar Optical Telescope has a 50-cm aperture with an angular resolution of 0.25 arcseconds, or 175 km over the field of view of about $400'' \times 400''$ on the Sun, covering a visible-light wavelength range of 4800–6500 Å. It provides vector magnetograms, Doppler velocity, and intensity measurements of the photosphere with a temporal resolution of 5 min ([Tsuneta et al., 2008a](#)). At the SOT focal plane, the Focal Plane Package (FPP) built by the Lockheed Martin Solar and Astrophysics Laboratory in Palo Alto, California consists of three optical instruments: the Broadband Filter Imager (BFI) which produces images of the solar photosphere and chromosphere in six wide-band interference filters; the Narrowband Filter Imager (NFI) which is a tunable Lyot-type birefringent filter capable of producing magnetogram and dopplergram images of the solar surface; and the Spectropolarimeter (SP) which produces the most sensitive vector magnetograph

maps of the photosphere to date. The FPP also includes a Correlation Tracker (CT) which locks onto solar granulation to stabilize the SOT images to a fraction of an arcsecond.

XRT (X-ray Telescope)

The X-Ray Telescope is a high-resolution grazing incidence telescope, a successor to the highly successful Soft X-ray Telescope on Yohkoh, but with a better angular resolution of about 2 arcseconds over a broad temperature range of 1–30 MK with both full disk and partial fields of view and a temporal resolution as short as 2 s (Golub et al., 2007).

EIS (Extreme-Ultraviolet Imaging Spectrometer)

The Extreme-ultraviolet Imaging Spectrometer provides images of the transition region and corona with an angular resolution of 2 arcseconds and a time resolution as short as 3 s, determining the temperature and density structure of the ionized gas and measuring the flow velocity, or speed, of the solar particles with a resolution of 3 km s⁻¹ (Culhane et al., 2007).

2.4.5 STEREO

STEREO (Solar TERrestrial RELations Observatory) is the third mission in NASA's Solar Terrestrial Probes program (STP). This two-year mission, launched October 2006, provides a unique and revolutionary view of the Sun-Earth System. The two nearly identical observatories - one ahead of Earth in its orbit, the other trailing behind - will trace the flow of energy and matter from the Sun to Earth. The two spacecraft drift away from Earth at an average rate of about 22.5 degrees per year. They reveal the 3D structure of coronal mass ejections; violent eruptions of matter from the sun that can disrupt satellites and power grids, and help us understand why they happen. STEREO becomes a key addition to the fleet of space weather detection satellites by providing more accurate alerts for the arrival time of Earth-directed solar ejections with its unique side-viewing perspective. Each of the spacecraft carries cameras, particle experiments and radio detectors in four instrument packages:

SECCHI :

The Sun Earth Connection Coronal and Heliospheric Investigation (SECCHI) has four instruments: an extreme ultraviolet imager, two white-light coronagraphs, and a heliospheric imager ([Wuelser et al., 2004](#)). These instruments study the three-dimensional evolution of CMEs from their origin in the low solar corona, through the expanding solar atmosphere, and interplanetary medium, to their eventual impact at Earth.

IMPACT :

In-situ Measurements of Particles and CME Transients (IMPACT) studies energetic particles, the three-dimensional distribution of solar wind electrons and interplanetary magnetic field.

PLASTIC :

PLAsma and SupraThermal Ion Composition (PLASTIC) will study the plasma characteristics of protons, alpha particles and heavy ions.

SWAVES :

STEREO/WAVES (SWAVES) is a radio burst tracker that will study radio disturbances traveling from the Sun to the orbit of Earth.

2.4.6 Nobeyama Radioheliograph (NoRH)

Radio emission from solar flares offers a number of unique diagnostic tools to address long standing questions about energy release, plasma heating, particle acceleration, and particle transport in the magnetized plasma ([Bastian et al., 1998](#)).

Nobeyama Radioheliograph (NoRH) is a ([Nakajima et al., 1994](#); [Takano et al., 1997](#)) is a radio telescope dedicated to observe the Sun. “Helio” means the Sun “graph” means an imaging telescope. It consists of 84 parabolic antennas with 80 cm diameter, sitting on line of 490 m long in the east/west and 220 m long in the north/south. the first observation started in April, 1992 and the daily 8-hours observation has been made since June, 1992.

As the NoRH is a radio interferometer, original data are sets of correlation values of all the combination of antennas. They correspond to the spatial Fourier components of the brightness distribution of the solar disk. In most cases, it is

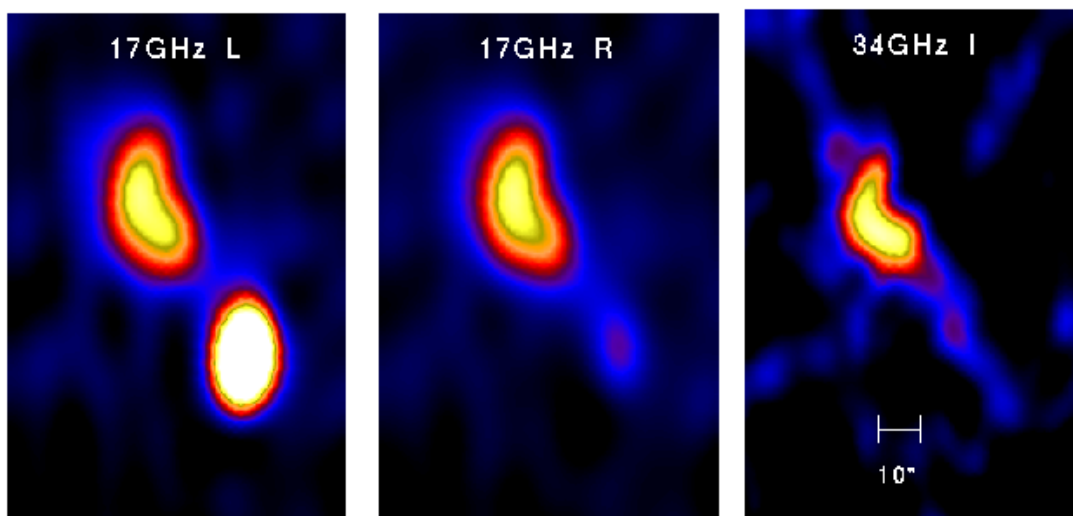


Figure 2.8: This figure shows the 1995-11-10 flare. The upper (northern) radio source can be seen in common at 17 GHz, 34 GHz, while the bottom (southern) source can only be seen in left-handed circular polarization image at 17 GHz. This means this source comes from the site where the magnetic field is strong (Takano et al., 1997).

necessary to synthesize images from the original raw data. The NoRH observe the Sun at 17 GHz (left and right circular polarization) and 34 GHz (only intensity). Figure 2.8 shows the 10 November, 1995 flare. The upper (northern) radio source can be seen in common at 17 GHz, 34 GHz while the bottom (southern) source can only be seen in left-handed circular polarization image at 17 GHz. This means this source comes from the site where the magnetic field is strong (Takano et al., 1997). The characteristics of NoRH are summarized in table 2.6. For the study of different types of radio bursts (coronal and interplanetary) associated with

Table 2.6: NoRH Specifications

Observing frequency	17 GHz (right and left circular polarization), 34 GHz (only intensity)
Field of view	Solar full disk
Spatial resolution	10'' (17 GHz), 5'' (34 GHz)
Temporal resolution	0.1 sec (event), 1 sec (steady)

eruptive phenomena, we have used different stations radio data over the globe such as Learmonth, Culgoora, Ondrejov, RSTN network and Wind/WAVES data.

2.4.7 Omni data

We have used the interplanetary (near-Earth) observational data from different space-based instruments (e.g., ACE and WIND) available at Omni web¹ maintained by NASA. It provides us interplanetary plasma (temperature, density and speed) and magnetic field parameters (B_x , B_y and B_z) observed by spacecrafts. We use the Dst (Disturbance Storm Time in nT) index data from ground based observatories (e.g., Kyoto²).

2.4.8 SOHO/LASCO CME catalogue

The SOHO/LASCO CME catalogue³ is generated and maintained by NASA and The Catholic University of America in cooperation with the Naval Research Laboratory. The catalog contains all CMEs manually identified since 1996 from the LASCO C2 and C3 telescopes.

The monthly lists provide all the basic attributes of a CME: time, central position angle, width, speed, acceleration, mass and kinetic energy. The time of first appearance of the CME in LASCO/C2 field of view (FOV) and central position angle (CPA) serve as an ID for each event. The sky-plane width of CMEs is typically measured in the C2 FOV after the width becomes stable. Each CME is characterised by three speeds: (1) the linear speed obtained by fitting a straight line (first-order polynomial) to the height-time measurements, (2) quadratic speed obtained by fitting a parabola (first order polynomial) to the height-time measurements and evaluating the speed at the time of final (last possible) height measurements, and (3) speed obtained as in (2) but evaluated when the CME is at a height of 20 solar radii. Since the time of final height measurement varies from event to event, the 20 solar radii speed is useful for

¹http://cdaweb.gsfc.nasa.gov/istp_public/

²<http://wdc.kugi.kyoto-u.ac.jp/dstdir/index.html>

³http://cdaw.gsfc.nasa.gov/CME_list/

2.4 Other instruments and data catalogues

comparing different speeds. However, the linear speed serves as an average speed within the LASCO FOV.

The acceleration of a CME can be positive, negative or close to zero meaning CMEs speed up, move with constant speed or slow down within the LASCO FOV. A minimum of three height-time measurements are needed for an estimate of the acceleration, but the accuracy increases when there are more measurements. Each CME is also characterized by a mass and a kinetic energy. There are generally large uncertainties in these numbers. Estimation of CME mass involves a number of assumptions, so the values given in the catalogue should be taken as representative. For example, most CMEs show an increase in mass when they traverse the first several solar radii, and then the mass reaches a quasi-constant value. This constant value is taken as the representative mass. Some CMEs fade away within the first few solar radii. In these cases the mass corresponds to the time of last measurements. The mass estimates of halo CMEs are also very uncertain. The kinetic energy is obtained from linear speed and the representative mass.

Chapter 3

Evolution of Solar Magnetic Field and Associated Multiwavelength Phenomena: Flare events on 20 November 2003

3.1 Introduction

¹ It is now generally accepted that the stressed magnetic energy stored in the magnetically complex active region is the source of flare energy, which is seen in a wide spectrum of energy band. The transfer of magnetic energy takes place at the reconnection site, where the localised dissipation region is formed at the current sheet and the magnetic energy is converted into thermal energy and utilized for bulk acceleration of plasma and also for changing the topology of the field lines. The total magnetic energy dissipated could roughly divide in equal parts of thermal energy and kinetic energy [Priest & Forbes \(2000\)](#).

In the case of an eruptive flare, which is known to be associated with the launch of coronal mass ejection (CME), the mechanical energy and the dissipative reconnection of the unstable MHD system can give rise to the ejection of flux rope. Observations of CMEs in the interplanetary medium confirm the ejection

¹Research work presented in this chapter has been published in [Kumar et al. \(2010\)](#), *APJ*, 710, 1195.

of ‘fluxrope’ in the form of ‘magnetic cloud’ (Burlaga et al., 1998; Marubashi, 1986). A huge quantity of coronagraph data has established that a fairly large CME can destabilize the large part of the corona and its extension is of the order of one solar radius in the near-Sun region. Thus a CME goes through considerable expansion and as it propagates to farther heights, its size evolution and the propagation speed in the inner heliosphere shows the transfer of magnetic energy to the background solar wind (Manoharan, 2006b) in the form of aerodynamical drag force.

The physical conditions to destabilize the coronal structure and to initiate a CME have been explained by several authors (Démoulin & Berger, 2003; Low, 2001). Moreover, the filament interaction followed by the reconnection and resulting eruption has also been studied (Su et al., 2007). For example, the soft X-ray images from Yohkoh satellite have provided several examples of eruption of twisted coronal loops (S or inverse-S shaped) (Manoharan et al., 1996; Pevtsov et al., 1996). Such eruptions can be triggered by the loss of equilibrium or rapid emergence of new flux in and around the active region (Kurokawa, 1987; Kurokawa et al., 1987). A cusp formation, i.e. twisted magnetic field lines rise to a considerable height, and its eruption may lead to the restructuring of the magnetic configuration. In the highly conductive corona, the dissipation of magnetic energy associated with the reconnection can be rather fast. However, the formation of a cusp and its eruption is important because it involves fast rate of reconnection as well as ejection of helicity (i.e., twisted field) into the interplanetary space. The next natural question is that how the helicity is accumulated, which leads to the formation of twisted-cusp shape. Recently several authors have reported that the sunspot rotation can lead to the building of magnetic energy, i.e., addition of helicity by emerging flux (Chandra et al., 2010; Low, 1996; Yan et al., 2008; Zhang & Chye Low, 2005; Zhang et al., 2008).

The period of October-November 2003, ‘Halloween Days’, is well known for extreme level of solar activities, corresponding to active regions NOAA 10484, 10486 & 10488. The active region NOAA 10501 (return of NOAA 10484, from the previous rotation) showed continuous emergence of magnetic flux in and around the activity site and produced 17 M-class flares (Chandra et al., 2010; Gopalswamy

et al., 2005a). Some of these Halloween-day events provided opportunities to understand the destabilization of magnetic field, formation of cusp, and associated flares and CMEs.

In this chapter, we report the rotation of sunspots, leading to the formation of cusp followed by reconnection, initiation of eruptive flares and associated CMEs in the interplanetary space. We study two homologous flare events (M1.4/1N, M9.6/2B) on 20 November in the active region 10501. During these events, the magnetic configuration at the activity site (located \sim N00 W05) was rather complex. The combined observations from ground-based $H\alpha$ and radio measurements and space-borne white-light, EUV images, and magnetograms provided opportunities to study these flares and CME events and their coronal structures. The interplanetary consequences of these events are studied based on white light, scintillation images and in-situ solar wind data at the near-Earth environment.

During both events twisted filaments observed in $H\alpha$ approached each other and initiated the flare processes. However, the second event showed the formation of cusp as the filaments interacted. The rotation of sunspots of opposite polarities, inferred from the magnetograms likely powered the twisted filaments and injection of helicity. Along the current sheet between these two opposite polarity sunspots, the shear was maximum, which could have caused the twist in the filament. At the time of interaction between filaments, the reconnection took place and flare emission in thermal and non-thermal energy ranges attained the maximum. The radio signatures revealed the opening of field lines resulting from the reconnection. The $H\alpha$ images and radio data provide the inflow speed leading to reconnection and the scale size of particle acceleration region. The first event produced a narrow and slow CME, whereas the later one was associated with a fast full halo CME.

3.2 Observations

Figure 3.1 displays the Michelson Doppler Imager (MDI) magnetogram and white-light image of AR 10501 observed on 20 November 2003. As shown by the magnetogram, the magnetic configuration of the active region was rather complex. On the above date, the active region was located close to the centre of disk, \sim N00

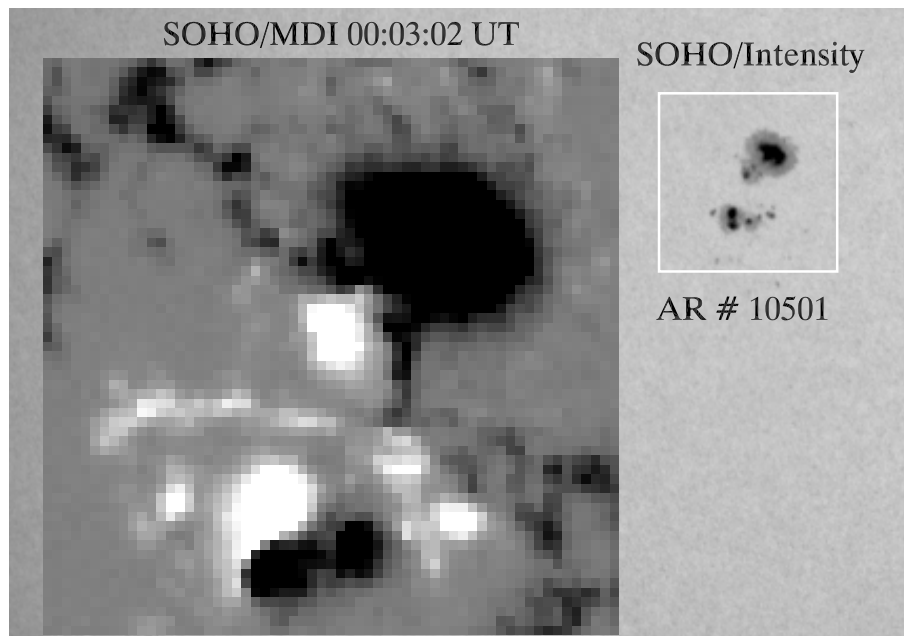


Figure 3.1: SOHO/MDI magnetogram of the active region NOAA 10501 on 20 November 2003. White light image of the active region is shown inside the box.

W05. More discussions on MDI images are given in Section 3.2.2. Figure 3.2 (top panel) shows the soft X-ray flux recorded by GOES satellite in the 0.5-4 and 1-8 Å wavelength bands during 01–09 UT. The first flare event (M1.4) started $\sim 01:45$ UT, attained a maximum $\sim 02:05$ UT and then gradually decreased. As seen in the plot, the rise as well as the fall in the X-ray flux is rather gradual and the profile is broad with an effective width of ~ 30 minute or base width of ~ 1 hour. This suggests a gradually evolving magnetic field and associated energy release. The second event starts with an impulsive weak flare (C3.8) at 07:30 UT. The X-ray profile, unlike the previous one rises quickly to the maximum at $\sim 07:45$ UT. It is however evident that the area under the curve of the first flare is equivalent to that of the second event. In this figure, the X-ray peak seen in between the above events corresponds to an activity at a different active region.

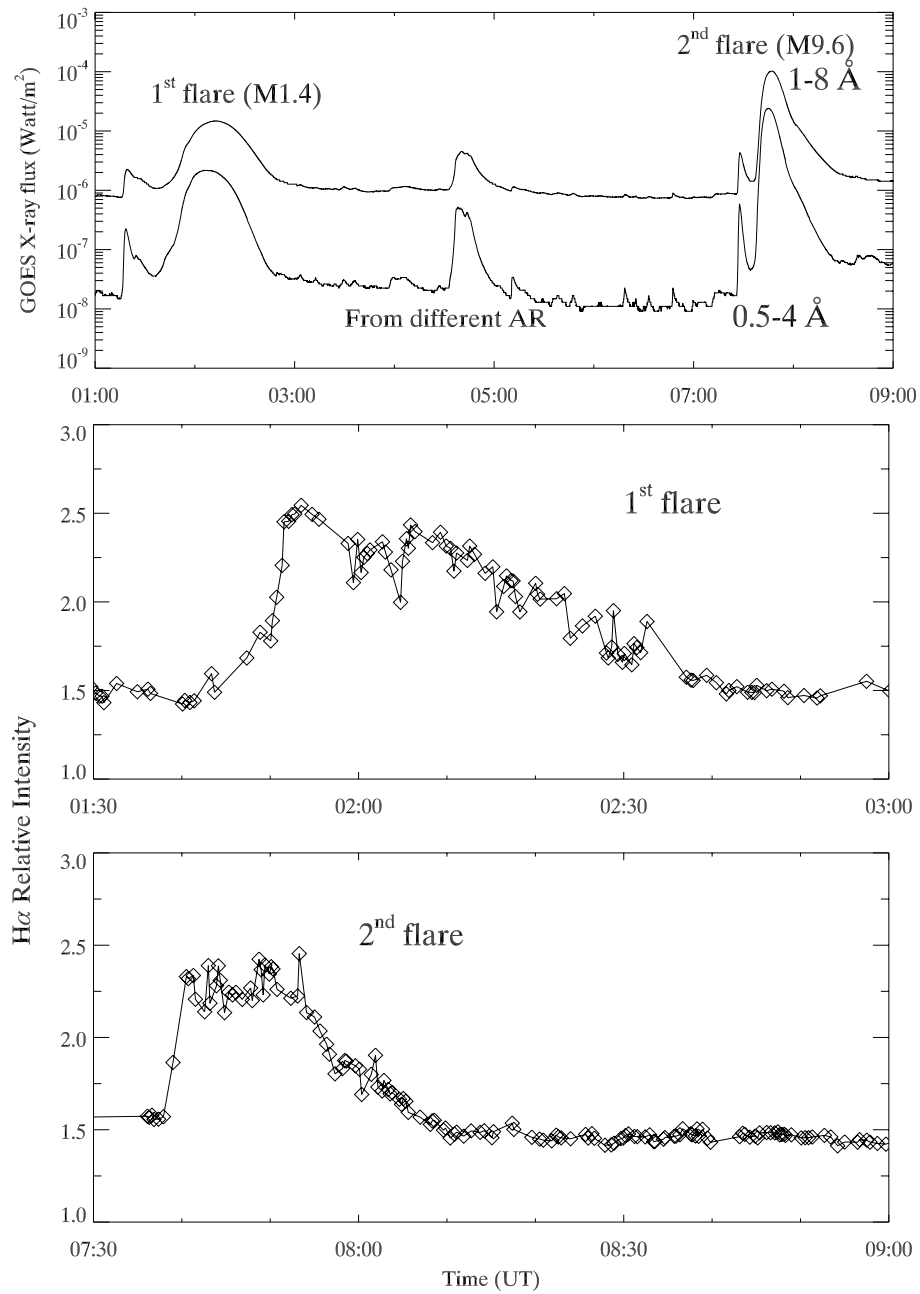


Figure 3.2: GOES soft X-ray flux measurements in 0.5-4 Å and 1-8 Å wavelength bands (top) and time profiles of the H α relative intensity with respect to the background emission for both flares.

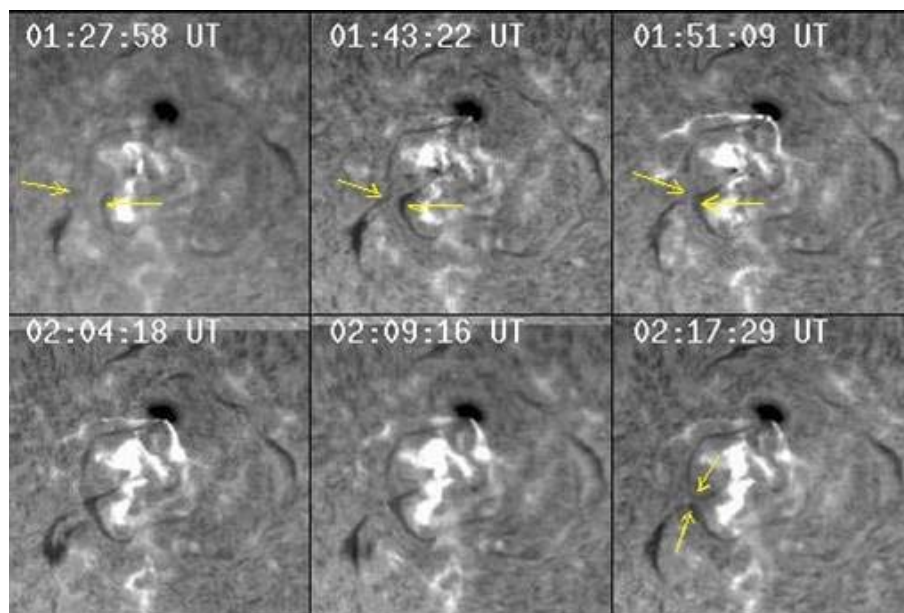


Figure 3.3: $H\alpha$ images of the first flare (1N/M1.4) showing the evolution of filaments and their interaction. The size of each image is $315'' \times 315''$.

3.2.1 $H\alpha$ Observations

The $H\alpha$ observations of these flares have been carried out at ARIES, Nainital, India, by using 15 cm f/15 coudé solar tower telescope. At ARIES, the images are enlarged by a factor of two using the Barlow lens and each image is recorded by a 16-bit 576×384 pixels CCD camera system having pixel size $22 \mu m^2$. The resolution on the image is $\sim 1''$ per pixel and the cadence is ~ 15 -20 sec per image. On 20 November, the $H\alpha$ data covered the time interval 01:25 to 08:25 UT. The relative $H\alpha$ intensity profiles of these two flare events are shown in Figure 3.2 and they look nearly similar to that of soft X-ray flux profiles.

The $H\alpha$ profile corresponding to the first event however shows a flash phase at the start of the flare, whereas the later event shows multiple peaks over the flaring period. It is evident that as seen in X-ray data, the equivalent width of the $H\alpha$ emission profile is nearly twice for the first event, compared to that of the second one. Figure 3.3 shows the evolution of the first flare (1N/M1.4) in $H\alpha$, during 01:27–02:17 UT. The active region showed several curved and twisted filaments. But the magnetic field structures evolved gradually over the period of the flare.

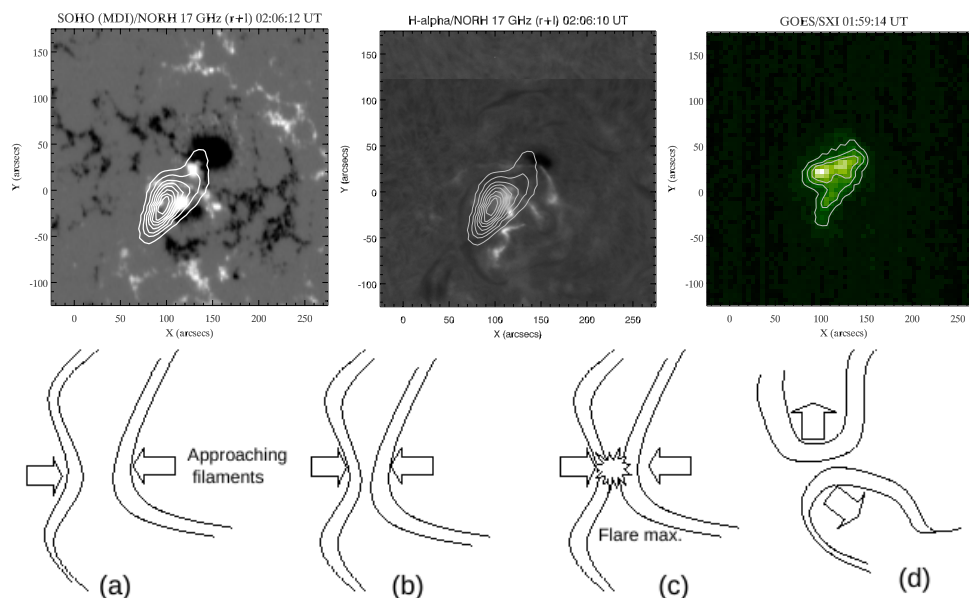


Figure 3.4: Nobeyama 17-GHz contours overlaid on MDI image (top, left) and on $H\alpha$ image (top, middle), and GOES/SXI image showing the X-ray source location (top, right). The schematic cartoons show the evolution of the first flare, i.e., approaching and interacting filaments followed by magnetic reconnection.

For example, two twisted filaments (indicated by arrows) showed structural and positional changes as the flare was developing over the period of ~ 25 minutes. The filament in the east approaches towards the filament at the west, close to the centre of the active region. But as it moves, the eastern one curves at the middle portion, where the distance between the filaments decreases. When the interaction is effective at about 01:55 UT, the reconnection takes place at the X point, we notice filaments moving to north and south directions. Figure 3.4 shows the typical cartoon for the above scenario: (a) and (b) show approaching filaments, (c) displays the interaction and resulting reconnection and (d) shows the resulting north and south moving filaments. In Figure 3.5, the observed distance between the two filament systems has been plotted as a function of time. As the distance decreases, the flare maximizes and the ‘distance-time’ profile provides a relative sky-plane speed of $\sim 10 \text{ km s}^{-1}$. Thus, the interaction of the filament systems has likely triggered the flare and it is consistent with the flare start at $\sim 01:45$

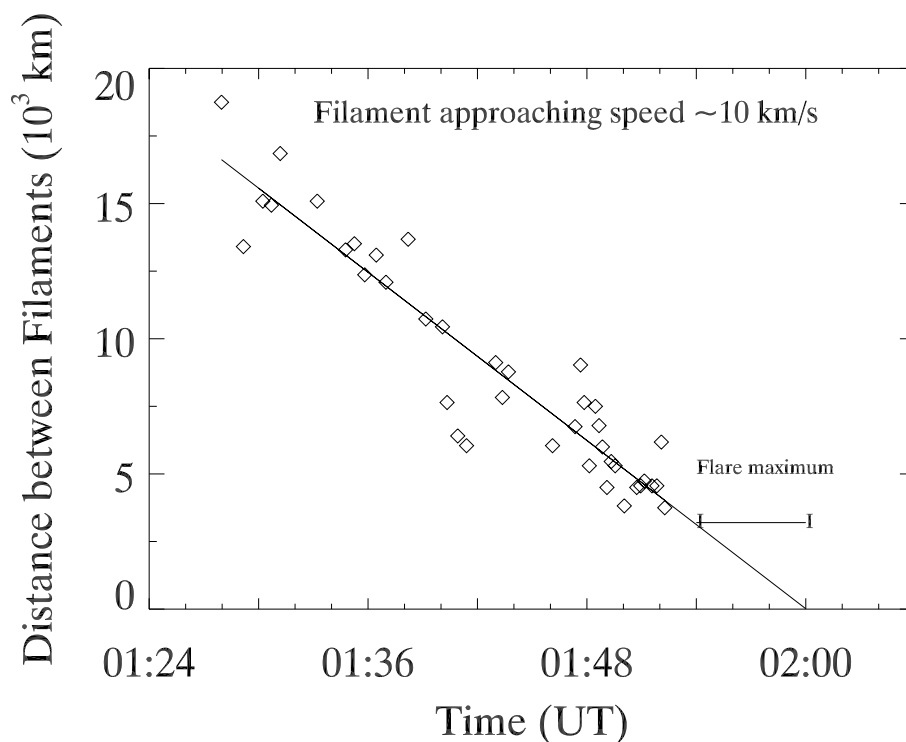


Figure 3.5: The distance between two filaments plotted as a function of time. The straight line is the least square fit to the data points. The typical inflow speed is $\sim 10 \text{ km s}^{-1}$. The $\text{H}\alpha$ intensity of this event attains maximum between 01:53 and 02:00 UT.

UT and maximum at $\sim 01:52$ UT. The interaction, merging and reconnection are shown by images taken between 01:27–01:51 UT. At the time of merging of filaments, the rearrangement of field lines has also been observed, leading to the reorientation of the filament system. It shows that the occurrence of the flare is due to the motion and the destabilization in the filament system. After the flare, the filament systems get restructured and stabilized. The following sequences: (1) approaching filaments (2) interaction (3) flare onset (4) separation of filaments in different direction (above and below the X-point) after reconnection suggest interlinked sequence of events in generating the CME. The approach speed of the filaments is in agreement with the earlier inflow speed by X-ray measurements (Yokoyama et al., 2001a).

During 02:40 – 07:30 UT, there was no significant activity at the flare site

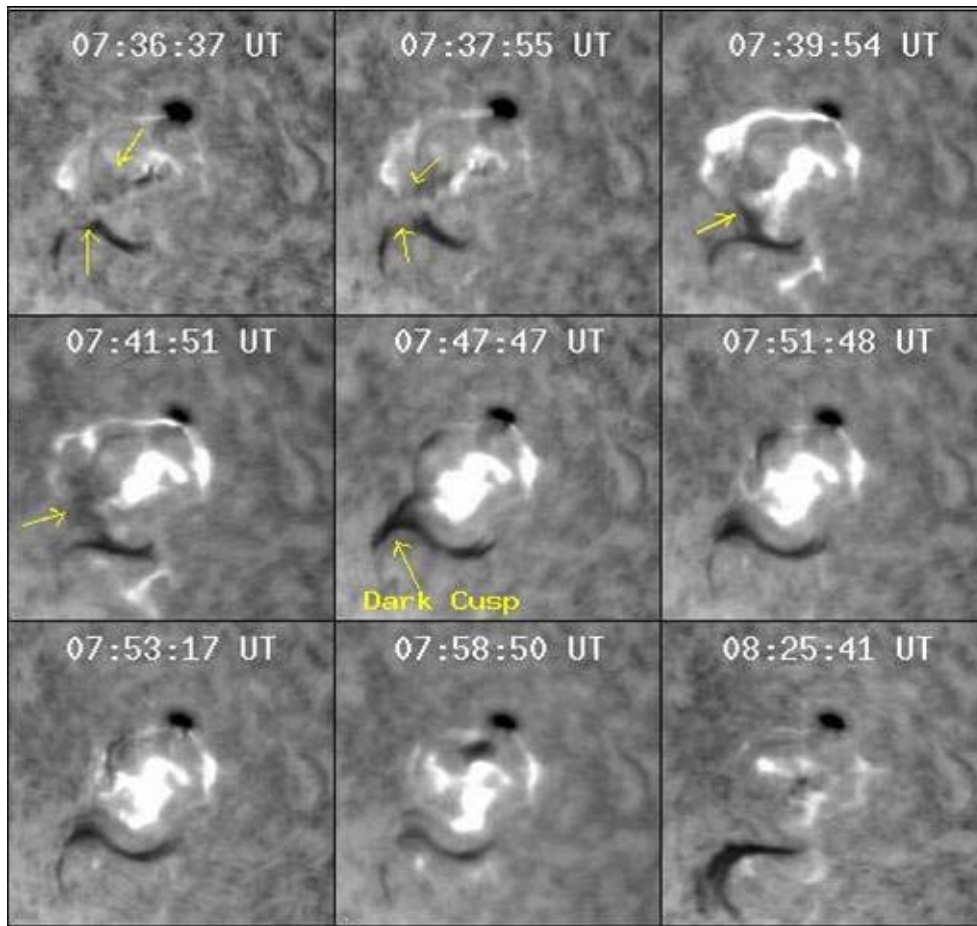


Figure 3.6: $H\alpha$ images of the second flare (2B/M9.6) show the evolution of field lines. The dark cusp shows the mass motion at the height in the low corona. The size of each image is $315'' \times 315''$.

(refer to Figure 3.1). It is likely that the energy building has been going on in this time interval. As in the above flare, during the onset of the second event, $\sim 07:30$ UT, the twisted filament systems, one foot point attached to the sunspot group, goes through heavy destabilization and filaments approach each other. But, the speed of approach has been considerably faster than the previous case. In Figure 3.6, sequence of selected $H\alpha$ images are displayed for the second flare interval, for which the intensity is significantly high during the flare maximum (also refer to Figure 3.2). At the time of flare increase, we see an arch like brightening which expands towards north-east of the flare centre. It suggests

that the reconnection process between the twisted field lines and nearby small-scale field lines. Further, as the merging of the filaments has been progressing (refer to Figure 3.6), the flare raises to the maximum of intensity (refer to Figure 3.1 and 3.2). The restructuring of filaments after the maximum has been clearly seen in $H\alpha$. The magnetic structure at 07:40 UT is associated with the pumping of the stored magnetic energy which is released during the main phase of the flare and it is in good agreement with the sudden jump in soft X-ray flux. During the flare maximum, 07:45–07:50 UT, at the top of the dark cusp shows the opening of the field lines (refer to Section 3.2.1).

The dark cusp-shaped structure formed during the flare (refer to Figure 3.6) starts to move upward. Its speed in the plane of disk is about $\sim 75\text{--}100\text{ km s}^{-1}$, during 07:45 - 07:50 UT. In the sequence of images, at 07:51 UT the cusp shape erupts and some of its material also falls back. The cusp speed suggests the possible initial speed of the CME, $\sim 100\text{ km s}^{-1}$, at the low coronal heights. More interesting point is that the cusp motion correlates with the gradual increase in the width of $H\alpha$ flaring region, at the centre of the active region. It is likely to be associated with evolution of the flare ribbons. The rate of widening of flare ribbons excellently correlates with the rising rate of the erupting height of cusp. Figure 3.7 shows the plot of ribbons separation and cusp expansion plotted against time. The high degree of correlation between their rates ($\sim 93\%$) suggests that the magnetic reconnection and the rising of filaments system have played a prime role in the formation of the CME. The interesting point is that the projected speed of the cusp is about one order of magnitude higher than that the relative speed of the filament systems, indicating the onset of CME is likely associated with the cusp outward motion.

3.2.2 Magnetogram Images

The above scenario of building and releasing of magnetic energy and the rearranging of field reconfiguration have also been revealed by images taken from MDI, onboard SOHO spacecraft. Sequence of images observed by MDI during and after the flare events clearly reveals the rotation of two sunspots of opposite polarities (north spot moving to the west and the south one moving to the east) at the flare

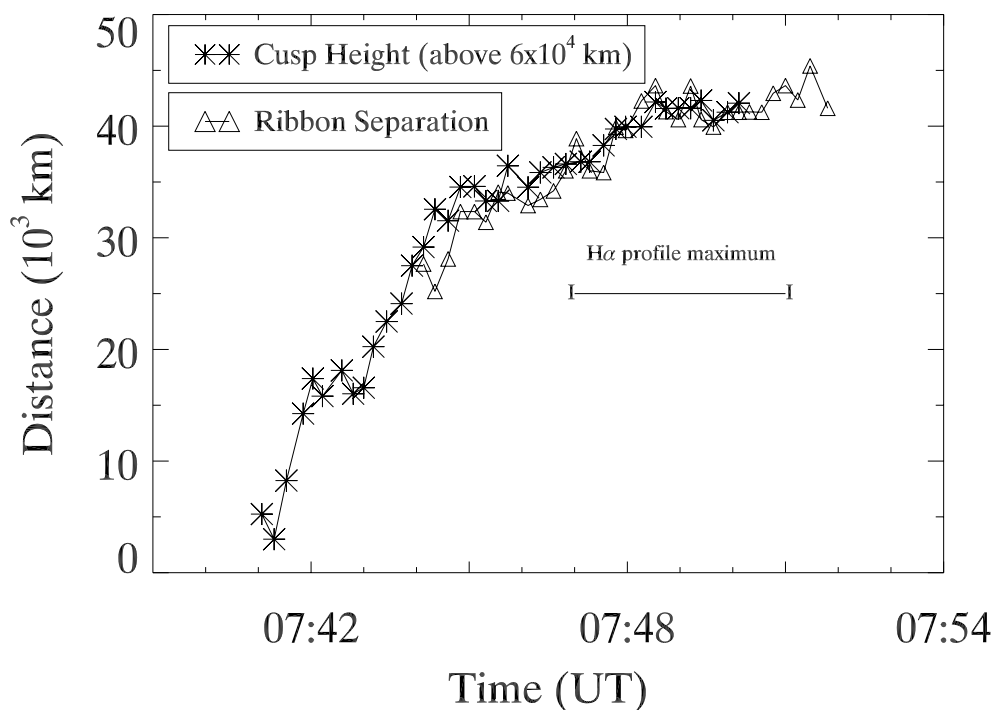


Figure 3.7: Plot showing the cusp height variation and ribbon separation as a function of time during the flare. After $\sim 07:45$ UT, the $H\alpha$ profile attains the maximum at which the cusp height stabilizes.

site. Figure 3.8 shows representative MDI magnetograms in the time interval 01:30–11:15 UT. We observe a relative shift in sunspot position $\sim 4\text{--}5 \times 10^3$ km, with an average positional shift ~ 1000 km hr^{-1} . However, the positive polarity sunspot shows rapid change in the position as well as rotation during 03:00–05:00 UT (refer to Figure 3.10).

In Figure 3.9, MDI contours over plotted on the $H\alpha$ show the typical location of the flare, which is in agreement with sunspot rotation location. Further, the X-ray location of the flare also nearly coincides on the above MDI contours. It may be noted that the recent study has suggested that the rotation of sunspots is likely to be associated with the dynamics caused by the emerging twisted field lines (Min & Chae, 2009). Thus the above magnetogram analysis reveals a considerable amount of flux emergence around the positive polarity sunspot in the time interval of 03:00–10:00 UT. However, the negative sunspot shows the rapid

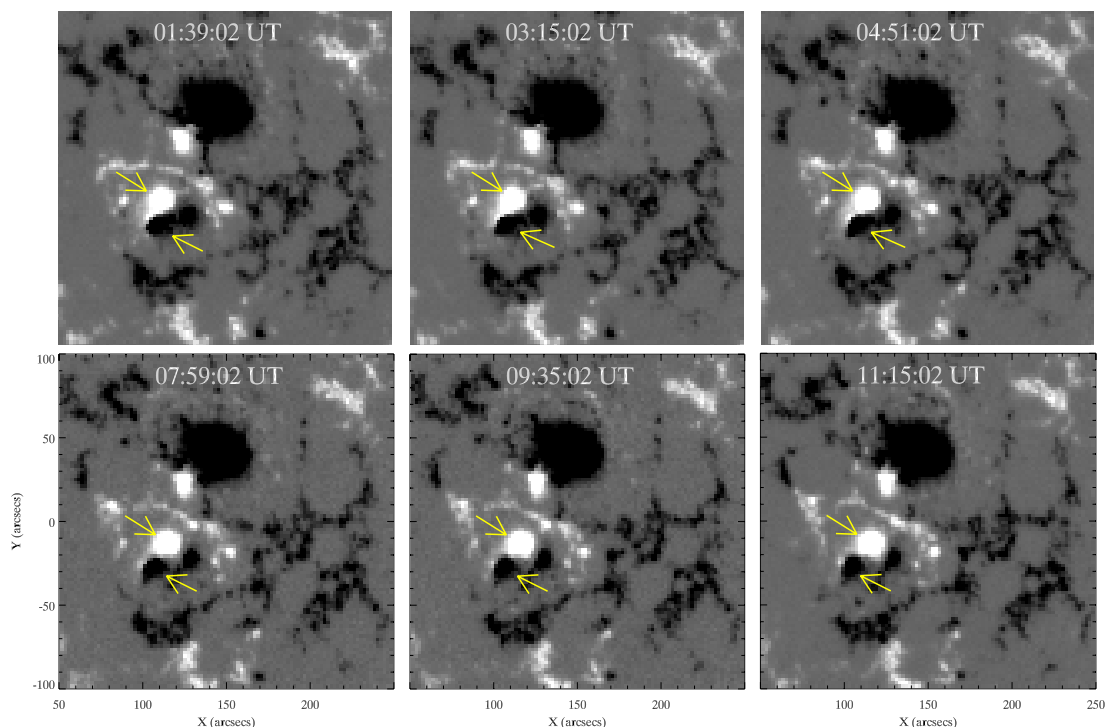


Figure 3.8: MDI magnetograms of the active region on 20 November 2003, showing the clockwise rotation of positive polarity sunspot and anticlockwise rotation of negative polarity sunspot (shown by arrows).

evolution after 08:00 UT. For comparison, we also include the shear map of the active region obtained from Marshal Space Flight Centre (MSFC) observed on 19 November 2003 at 19:36 UT (refer to Figure 3.9). A maximum shear along the current sheet between these opposite polarity sunspots has been recorded, and it probably caused the formation of twisted filaments. The shear motions and rotations of sunspots represent the energy building process, which are likely associated with the flux emergence and cancellation (Kurokawa, 1987; Kurokawa et al., 1987; Liu & Zhang, 2001). It is consistent with destabilization of filament systems and their relative motion, leading to the formation of flares and CMEs. The magnetic cloud associated with flux rope ejection has been confirmed by interplanetary measurements (see Section 3.2.5). Figure 3.11 shows the schematic cartoons to explain the second event scenario i.e. (a) curved filaments with sunspot rotation (b) filament destabilization and interaction to produce the flare (c) cusp

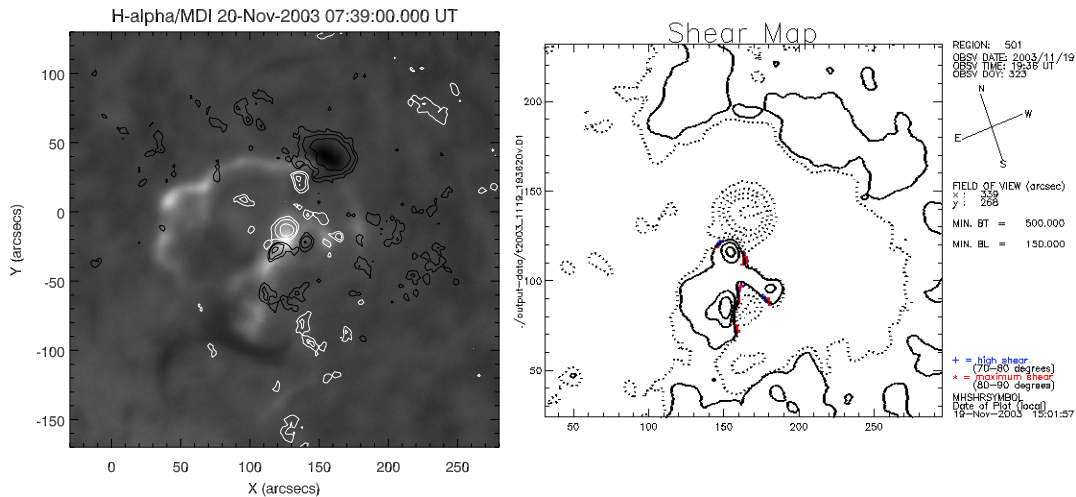


Figure 3.9: Left: MDI contours overlaid on $H\alpha$ image during the second flare event. Right: MSFC shear map of the active region showing the maximum shear at the flare site in between the sunspots on 19 November 2003 at 19:36 UT, is shown for comparison.

formation, and (d) CME eruption.

3.2.3 Radio Measurements

The above two events have also been covered well by radio observations over a range of frequency bands, 245–15400 MHz. The 1-sec radio flux density data in the above frequencies is displayed in Figure 3.12, individually for these two events. These plots have been made on same vertical scale for an easy comparison of strength of radio flux densities. It is evident in the figure that (i) the second event is complex and more intense than the first one. (ii) the metric and high frequency radio spectra during the flare event show moderate increase for the first event whereas huge enhancement can be seen for the second event. (iii) Moreover, the second event shows enhancement at high frequencies (8800 and 15000 MHz) on or after the flare maximum. It suggests that the much harder particle acceleration has resulted during the reconnection process of the flare event. Additionally, the dynamic spectra for the two-flare intervals are shown in Figure 3.13. As shown in

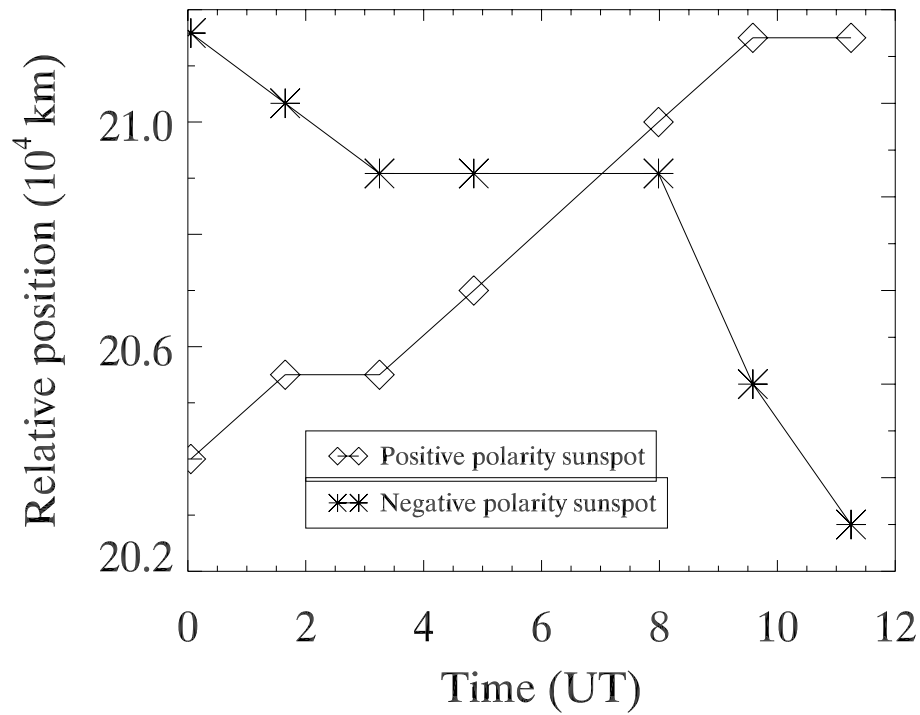


Figure 3.10: The relative position change with time of opposite polarity sunspots showing the motion of the both sunspots.

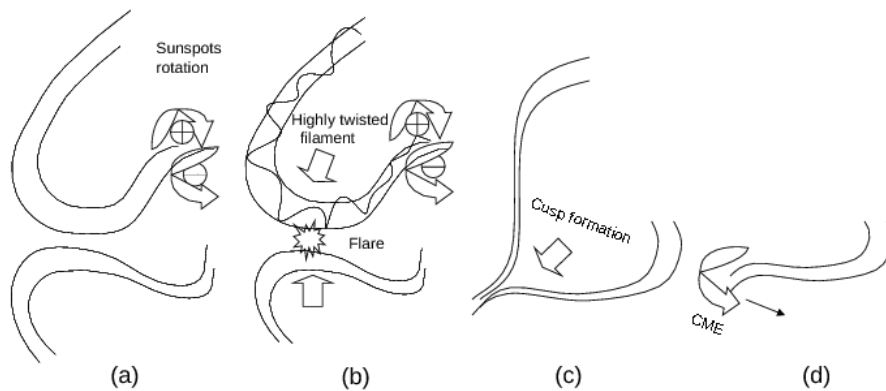


Figure 3.11: The schematic cartoon showing the second flare evolution with one highly twisted filament destabilization in association with rotating sunspots and merging with another curved filaments, forming a cusp and resulting CME eruption.

the above plots intense type III bursts have been observed at the flare maxima, respectively, at 02:50 and 07:40 UT. The bunch of intense type III bursts during the onset of flares confirms the opening of field lines and acceleration of particles along them, resulting from the merging/reconnection caused by the approaching filament systems. In the frequency range 245–610 MHz, the radio flux density profiles show large variations over a period of about 5–10 minutes. Whereas, the radio intensity profiles in the frequency band 1415–15400 MHz, show increase over a period of about 1–2 minutes then a gradual decrease with time. The flux density peak shows systematic offset to later time with the increasing frequency.

During the maximum of the second flare, in other words at the time of effective reconnection of filament systems, sharp spiky burst has been observed at 610 and 2695 MHz around 07:39 UT and it raised about 5–7 times above the flare background radio emission at 2695 MHz. This burst interval is indicated by two vertical dotted lines in Figure 3.12. However, at an intermediate frequency, 1415 MHz, the increase corresponding to the above sharp burst has been nominal and it shows slightly above the flare background. It is likely that in the population of accelerated electrons, the transition from the thermal (high frequency) to non-thermal (low frequency) state may take place at this height. Nevertheless, the important point to note in the characteristics of the sharp burst at 610 and 2695 MHz is that the profile is broad at 2695 MHz, ~ 10 sec of full width at half maximum and narrow at 610 MHz having an equivalent width of ~ 5 sec. Moreover, the 610 MHz emission peak ~ 3 sec later than the above frequency profile. The above results suggest that the reconnection between the filaments at lower heights (i.e. at 2695 MHz at lower corona) has caused, the production of copious amount of thermal particles over a larger volume (as the reconnection got initiated). But, the non-thermal emission (at 610 MHz) at the maximum phase of the flare has resulted from the channelization of accelerated particles along the field lines into the solar wind at height above the reconnection site. Then, the particle channel tends to cause intense but narrow width radio intensity profile. The appearance of the narrow spiky emission is consistent with $H\alpha$ profile (refer to Figure 3.2). The results also indicate that for the given approaching speed of the filament systems and the duration of burst, the cusp top source would

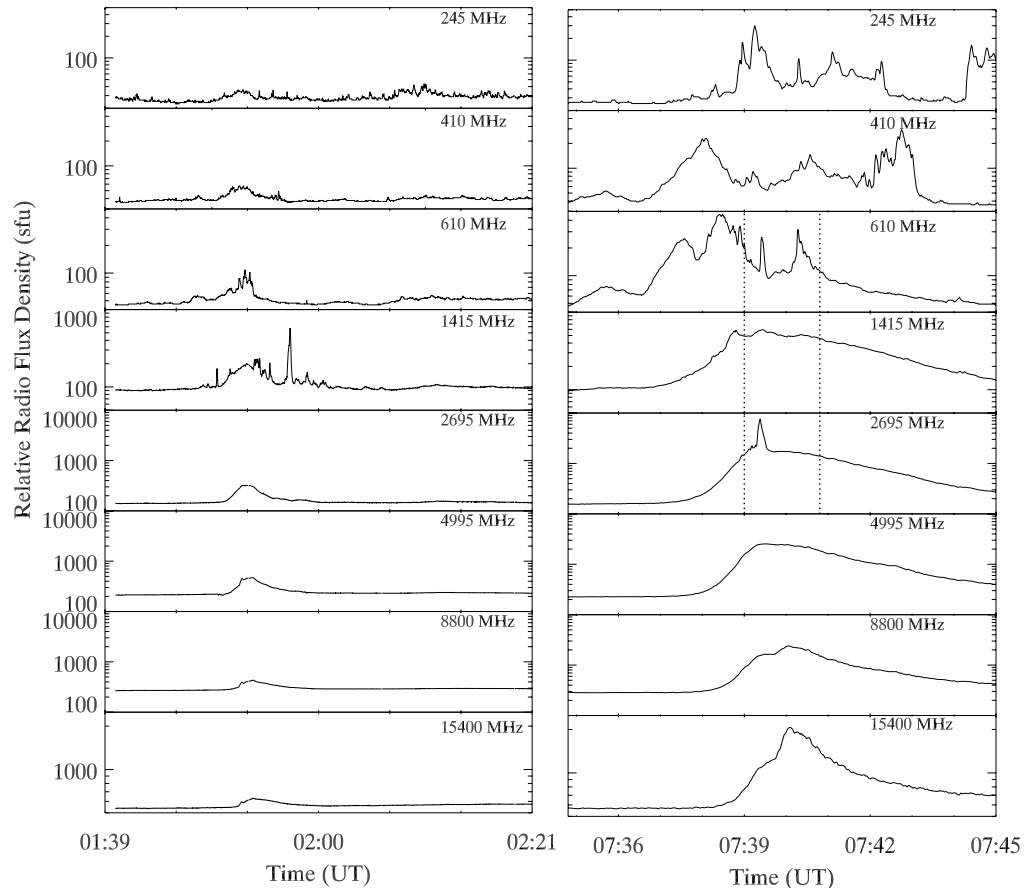


Figure 3.12: Time profiles of radio flux densities observed at eight frequency bands from Learmonth observatory for the first and second flares, respectively. These plots have been made in same scales for an easy comparison of strength of these flares. It is evident that second event is complex and more intense. Time profiles of radio flux density at the reconnection time (or interaction between filaments) observed at 610, 1415, and 2695 MHz is shown in between two vertical dotted lines. The time lag of ~ 2.5 sec is evidently shown between 2695 and 610 MHz. The coronal height increases from bottom to top.

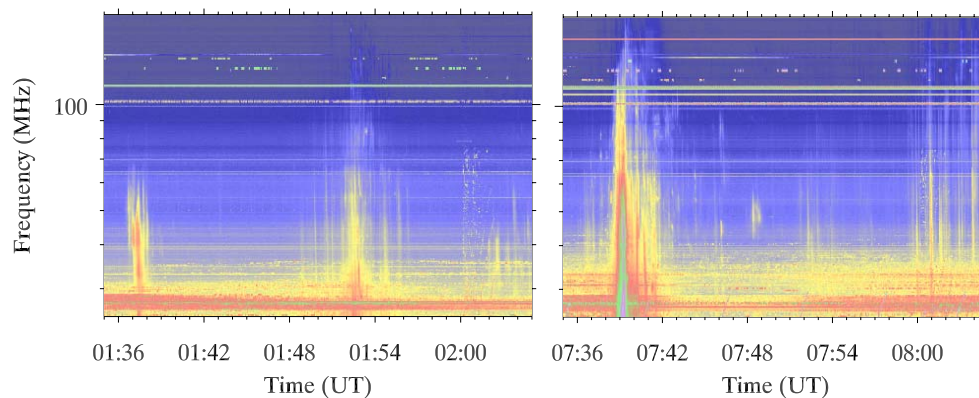


Figure 3.13: Type III bursts associated with both flare events on 20 November, 2003 (Learmonth, Australia). These intense bursts provide evidence for the opening of field lines at the time of reconnection.

size about ~ 1000 km and the cross-section of field lines leading to non-thermal radiation is much smaller than the above.

The high frequency radio measurements, made with the Nobeyama Radio Heliograph (NoRH) are consistent with the $H\alpha$ observations and radio results described above. The NoRH could cover only the first flare event. The rising of cusp after the reconnection can be seen in both 17 and 34 GHz images as a bright source, which showed systematic movement with time. The source is brightest at $\sim 01:54$ UT near the flare maximum. At 17 GHz, the foot-point sources in association with the flare ribbons could also be observed. The foot-point sources show considerable polarization, which gives a clue on the field orientation at the end of the loop. The NoRH contours are shown on $H\alpha$ and MDI magnetogram to show the relative position of the flare in different observations (refer to Figure 3.4).

3.2.4 EUV and White-light Observations

In association with the above flare events, two individual CMEs have been observed in the interplanetary medium. We also carefully examined the CME initiation using Extreme Ultra-Violet Telescope (EIT) images observed at 195 \AA and it revealed that the onset of the second event was associated with dimming above

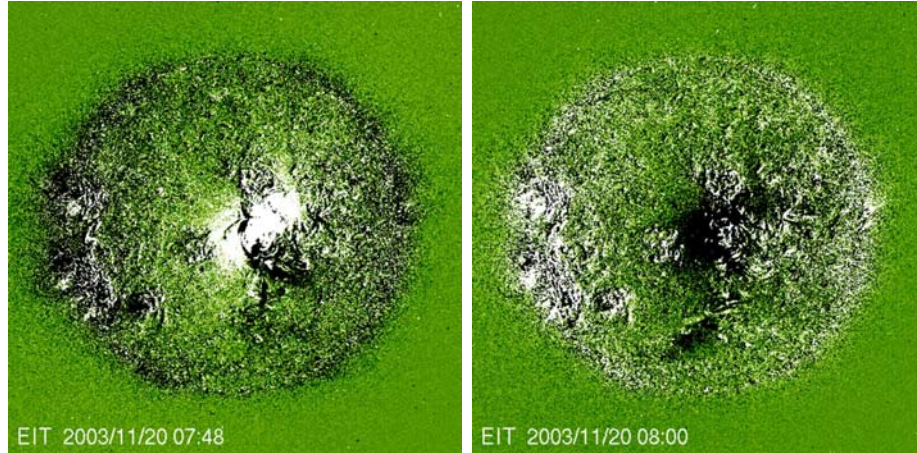


Figure 3.14: EIT difference images of the second flare at the maximum (7:48 UT) (left) and coronal dimming (right), which shows the evacuation of coronal mass during the launch of the CME.

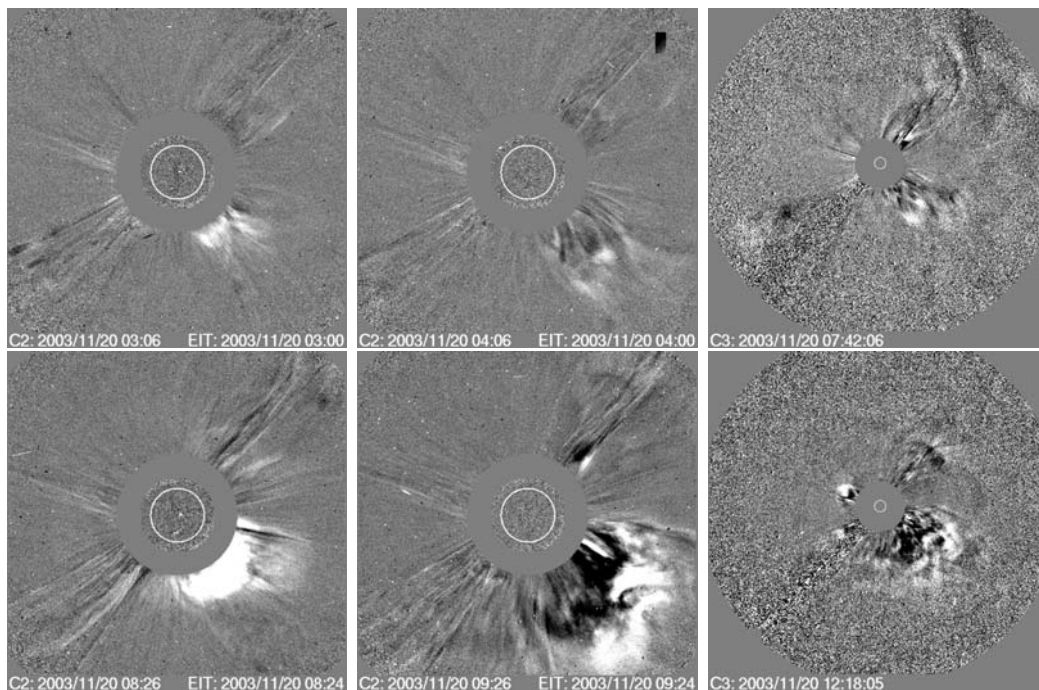


Figure 3.15: Difference images from C2 and C3 LASCO coronagraphs for both CMEs. Top panels show the CME associated with first 1N/M1.2 class flare whereas bottom panels display the CME associated with 3B/M9.6 flare.

the flare site showing material depletion (Zarro et al., 1999). The consecutive EIT images showed movement of filaments as seen in $H\alpha$ images (see Figure 3.14).

The white light images made by the Large Angle and Spectrometric Coronagraph (LASCO) C2 and C3 telescopes onboard SOHO mission, provided sequence of images of CMEs corresponding to these flare events propagating in the southwest direction. In the C2 field of view, which covers $\sim 2-6 R_{\odot}$, the first CME appeared at 02:48 UT and its subsequent appearances in the C2 and C3 fields of view provided linear speed of 364 km s^{-1} in the sky plane within about $15 R_{\odot}$, from the centre of the Sun. This CME covered $\sim 60^{\circ}$ width along the position angle $\sim 220^{\circ}$. However, the second CME was faster than the above one and it became a full halo event in the LASCO field of view. Some representative images of these CMEs recorded by the LASCO are shown in Figure 3.15. The second CME event appeared at the C2 field of view at 08:06 UT and its linear propagation speed was 669 km s^{-1} . It should be noted that the second event is more intense than the first one (refer to Figure 3.12, Section 3.2.3). When we compare the CME initiation from the cusp rise and its follow up in the near-Sun region within LASCO field of view, it is clearly seen that the CME has gone through a heavy acceleration, supported by the expansion of the magnetic flux rope system erupted at the time of CME onset. We also see the cusp mass eruption in $H\alpha$ in association with CME onset. However, the acceleration in $H\alpha$ has been enormous compare to low level of acceleration in LASCO field of view and the rate of expansion evidently reveals the transfer of magnetic energy at the initial stage of the CME. Figure 3.16 shows the ‘height-time’ plot which combines $H\alpha$, C2 and C3 measurements and the rate of expansion evidently reveals the transfer of magnetic energy at the initial stage of the CME.

3.2.5 Scintillation Images and Interplanetary Data

The above halo CME has also been traced further out in the inner heliosphere using interplanetary scintillation (IPS) observation made at the Ooty Radio Telescope, operating at 327 MHz (Manoharan, 2006b; Manoharan et al., 2001). Figure 3.17 shows the three-dimensional tomographic reconstruction of the 3-AU heliosphere obtained from the Ooty IPS measurements on November 23, 2003. The

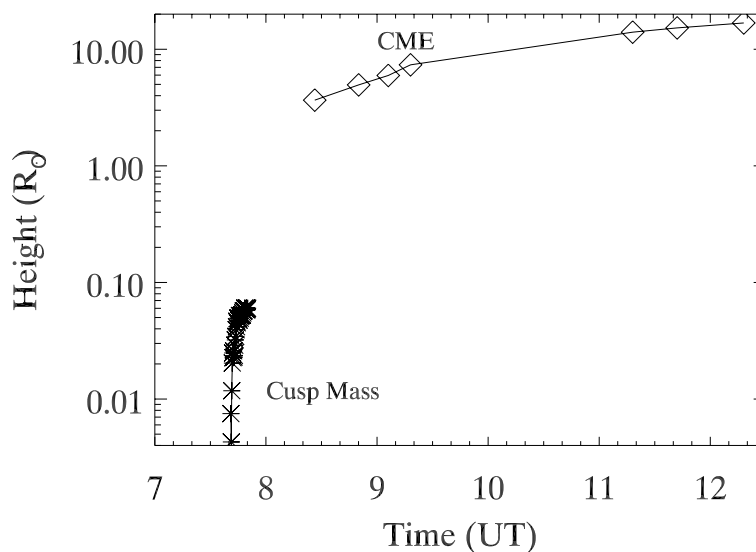


Figure 3.16: Height-time plot of cusp movement and its CME associated with second flare.

ecliptic plane images show the density and speed structures associated with the CME. However, the three-dimensional view plots for two different orientations of Earth show inclination of the CME front with respect to the ecliptic plane. That is, the flux rope is oriented $>50^\circ$ to the ecliptic plane. It is in agreement with the orientation of CME observed at 1 AU as well as the moderate magnetic storms produced by the CME at Earth's orbit. The speed measurements by the IPS technique at ~ 0.5 AU is in agreement with the speed of the interplanetary CME at 1 AU. Figure 3.18 shows the solar wind parameter associated with the shocks and CME at the near-Earth spacecraft (<http://nssdc.gsfc.nasa.gov/omniweb>). During the magnetic storms the B_θ rotates upto $\sim 70^\circ$. In this plot, the arrival of shock in front of the CME is indicated by a vertical line. The speed of the CME at the near-Sun region (LASCO measurements), in the inner heliosphere (as recorded by IPS data) and at 1 AU (by in-situ measurements) show rather very little deceleration from $\sim 670 \text{ km s}^{-1}$ to $\sim 600 \text{ km s}^{-1}$ in the entire Sun-Earth distance. It suggests that the interaction of the CME with background (or ambient) solar wind is not effective or the CME could overcome the interaction. The energy within the CME could sustain the expansion. In other word, as shown by Manoharan (2006b), the ejection of flux rope above the cusp contained sufficient

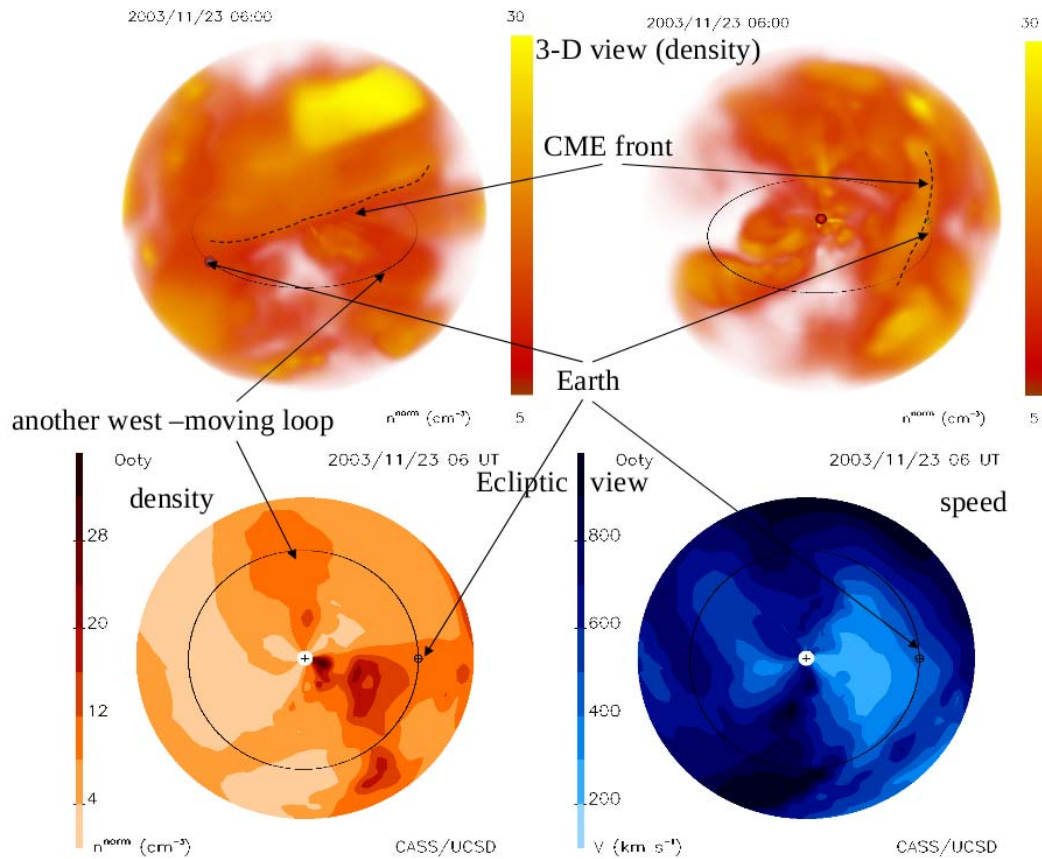


Figure 3.17: 3-D view of the heliosphere obtained from a large number of IPS measurements (i.e., Manoharan 2006). The CME location with respect to the ecliptic plane is shown. The top images are 3-D view and bottom images are ecliptic view.

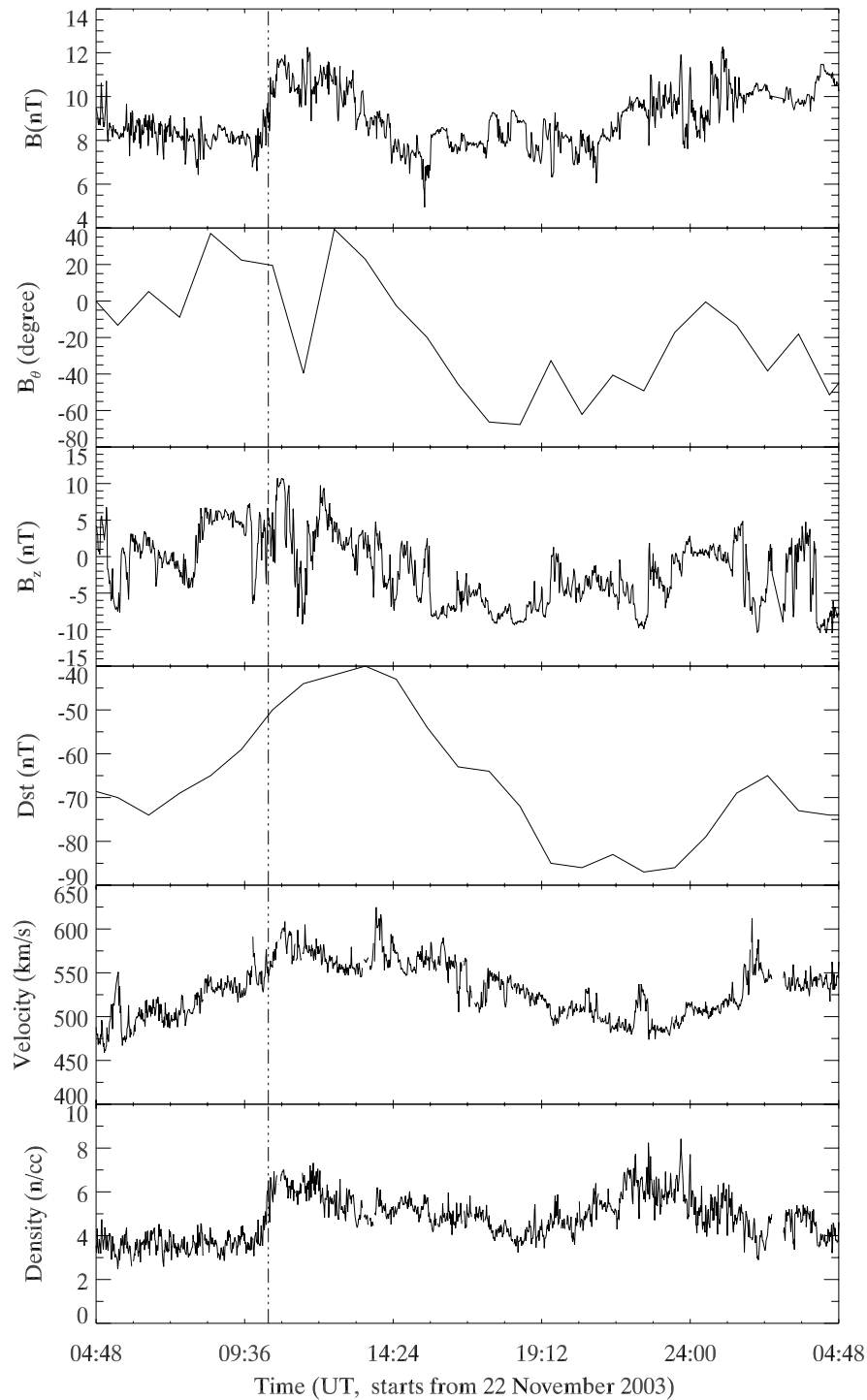


Figure 3.18: The interplanetary observations of magnetic field strength B , B_θ , southward component of magnetic field (B_z), geomagnetic index (Dst), solar wind speed and proton density. The arrival of the shock is marked by the vertical line.

amount of magnetic energy, which was utilized in the interplanetary medium to overcome the aerodynamical drag imposed by the background solar wind. However, the strength of southward B_z component of the field associated with CME, the orientation of the flux rope, and its impact speed could produce a moderate storm, $Dst \approx -85$ nT at the Earth.

3.3 Discussion

This multiwavelength study of two homologous flare events provides evidence that the opposite rotation and displacement of opposite polarity regions play a crucial role in building up the magnetic energy required for the flare process. Sunspot rotation is the primary driver of helicity production and injection into the corona (Tian & Alexander, 2006; van Driel-Gesztelyi et al., 2002). In a recent study, Chandra et al. (2010) estimated the spatial distribution of magnetic helicity injection at the active region under consideration and showed the existence of localized positive helicity injection in the southern part of the active region. Therefore, the newly emerging flux, which plays a major role in characterizing the motion as well as the small scale reconnection. The rotation characteristics indicate a rapidly emerging flux system (Liu & Zhang, 2001). Further, as shown by $H\alpha$ data, the destabilization of the filaments strongly correlated with the rapidly emerging magnetic flux and it leads to the destabilization of filaments as well as eruption of merged filaments. It is evidently shown by the $H\alpha$ images that the magnetic energy has been pumped above the cusp at the low chromosphere. The correlation between the separation of flare ribbons and expansion of cusp structure evidently shows the large-scale reconnection, ejection of flux rope, and acceleration of particle during the cusp eruption. The radio signatures confirm the opening of field lines after reconnection and related particle acceleration. The flux rope has been observed as the magnetic cloud in the interplanetary medium.

The inflow velocity is an essential factor to initiate or cause the reconnection of field lines. For example, theoretically it has been shown that inflow velocity ~ 10 km s⁻¹ would lead to Petschek-type reconnection (Petschek, 1964). In the present study, we obtain the approaching speed of the filaments ~ 10 km s⁻¹, which would nicely satisfy the initial condition for the reconnection to take place between field

lines. The present study indicates that cusp geometry is of large scale ($\sim 4 \times 10^4$ km) and the reconnection point may lie well above the photosphere. That is the twisted and injected helicity leads to sigmoid type structure. The projected reconnection height as seen from the cusp, $\sim 4 \times 10^4$ km, is consistent with the earlier observations (Sui et al., 2004). This study has also indicated the typical size of reconnection scale, ~ 1000 km. However, the accelerated particles are channeled along the field lines in a fairly narrow cross-section. The expansion of the flux rope (i.e. magnetic cloud) has aided the CME propagation and to overcome the drag force exerted by the background solar wind. For example, the drag force is proportional to the square of the velocity difference between the solar wind and CME expansion rate. The initial and arrival speeds of the CME, respectively, at near-Sun region and at 1 AU, provide evidence that the internal energy (magnetic energy) has supported to overcome the drag force (Manoharan, 2006b). The cusp shape suggests the formation of twisted loop as well as magnetic null at the high corona (Manoharan & Kundu, 2003). The typical ejected mass amounts to $\sim 10^{15}$ gm, which accounts only a small fraction of mass of filament systems. The follow-up of the CME in the Sun-Earth distance using the IPS technique shows that the flux rope is oriented $>50^\circ$ with respect to the ecliptic plane. Thus, although the CME originated close to the disk centre, it could only produce a moderate storm of Dst ~ -85 nT at the Earth's magnetosphere. However, IPS and in-situ data record a strong shock associated with the CME propagation.

In summary, this study shows evidences that the sunspot motion characteristics correspond to rapid emergence of magnetic flux. The destabilization of filaments strongly correlates with sunspot motion or rotation. The eruption of the twisted-filament system suggests that the small-scale reconnection or tether cutting and the building of magnetic energy lead to the cusp formation. The inflow speed is consistent with the fast reconnection. However, the geometry and size of the cusp indicates a considerably large magnetic energy associated with the system, and it is likely provided by the helicity injection caused by the rotation of sunspots. The observed magnetic cloud confirms the associated flux rope. This study has provided a unique example to understand the space-weather consequences of solar activities in the Sun-Earth distance.

Chapter 4

On the Sources of the Super-storm of Solar-Cycle # 23 Associated with the Solar Flares on 18 November, 2003

4.1 Introduction

¹ Solar flares are the transient explosions in the solar atmosphere during which magnetic energy stored in twisted and sheared fields is suddenly released in the form of electromagnetic radiation and particle acceleration. The gigantic clouds of ionised gas and magnetic field ejected out from the corona in association with flares are known as coronal mass ejections (CMEs). For example, a CME in the interplanetary medium is also referred to as magnetic cloud (MC), which is the ejection of the flux rope into the solar wind. It is defined by relatively intense magnetic field, large and smooth rotation of field direction over an approximate size of 0.25 AU at 1 AU, and low proton temperature ([Burlaga et al., 1981](#)). The intensity and the duration of the southward component of the interplanetary magnetic field is the most critical factor to determine the geoeffectivity of MCs. The magnetic reconnection takes place at the boundary of the magnetosphere is

¹Major part of this chapter is in press in Kumar et al. (2010c), *Advances in Geosciences*.

determined by the southward component of the CME associated field and it makes the solar wind energy to be pumped into the magnetosphere and geomagnetic storms take place due to the formation of ring current circulating around the Earth above the equator. Several authors have reported that B_Z component of IMF and CME speed are the main driver to produce intense geomagnetic storms (Tsurutani et al., 1988). However, the magnetic topology of a MC depends on its helicity, inclination of the axis with respect to the ecliptic plane and polarity, i.e. whether the field rotates from south at the leading edge to the north at the trailing edge (SN-polarity) or vice versa (NS-polarity). The geoeffectiveness of MCs with different topologies is greatly different. But still it is challenging to predict the occurrence of intense storms in terms of solar and interplanetary parameters. Thus, CMEs are the integral part of space weather.

During October-November 2003, a series of solar eruptions occurred from three solar active regions (i.e., NOAA AR 10484, 486, 488). AR 10484 returned as AR 10501 (located at \sim N00 E18) and produced the largest geomagnetic storm of the solar cycle #23 on 20 November 2003. These events have been studied by several authors (Chandra et al., 2010; Gopalswamy et al., 2005a; Möstl et al., 2008; Srivastava et al., 2009). Gopalswamy et al. (2005a) suggested that the largest geomagnetic storm was caused by a fast and wide CME originating close to the disk center. It resulted in a highly inclined MC with its axial field pointing almost always southward, which reconnected with Earth's magnetosphere. Möstl et al. (2008) compared the properties of the source region with those inferred from satellite observations near the Earth (SOHO and TRACE data), with ground-based data. They modelled the near-Earth observations with the Grad-Shafranov reconstruction technique using a novel approach in which they optimized the results with two-spacecraft measurements of the solar wind plasma and magnetic field made by ACE and WIND and found that the magnetic cloud orientation at 1 AU is consistent with an encounter with the heliospheric current sheet. Recently, Srivastava et al. (2009) estimated the temporal variation in magnetic flux, energy and magnetic field gradient for the source active region using MDI magnetograms, which provided evidence that the flare associated with the CME occurred at a location marked by high magnetic field gradient and led to the release of free energy stored in the active region.

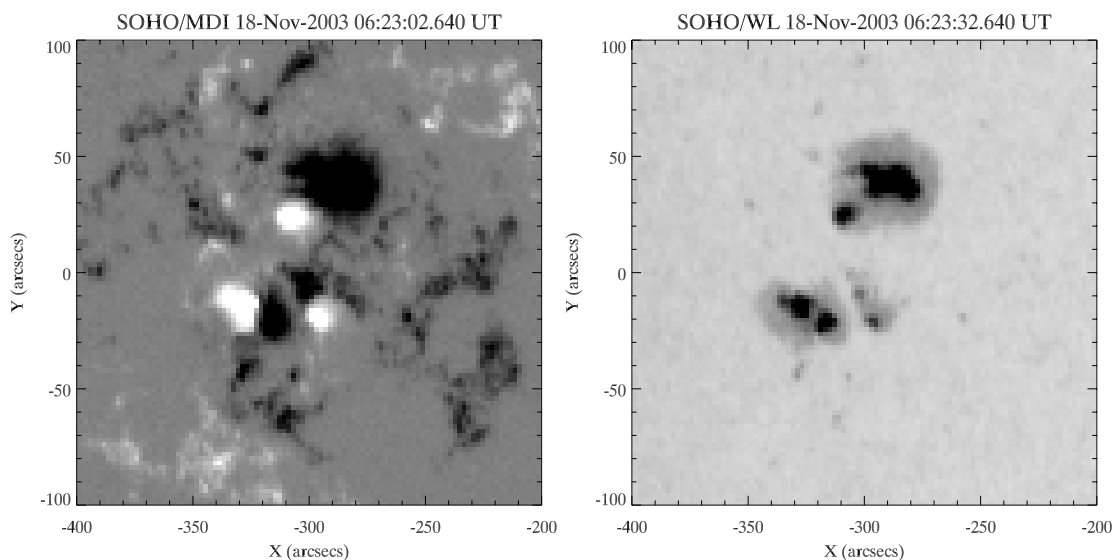


Figure 4.1: SOHO/MDI and white-light images of the active region NOAA 10501 on 18 November 2003.

In this chapter, we study the solar sources of intense geomagnetic storm of solar cycle 23 occurred on 2003 November 20 using multiwavelength ground and space based observations. The coronal mass ejections responsible for the geomagnetic storm originated from the super-active region NOAA 10501. We investigate the $H\alpha$ observations of the flare events made with 15 cm Solar Tower Telescope at ARIES, Nainital, India. The propagation characteristics of the CMEs have been obtained from the three-dimensional images of the solar wind (density and velocity) obtained from the interplanetary scintillation technique, supplemented with the other ground and space-based missions. TRACE, SXI and $H\alpha$ observations revealed the two successive ejections originated from the same filament channel, which were associated with two high speed CMEs. The interaction of these CMEs along the Sun-Earth line has led to the severity of the storm. According to our investigation, the interplanetary medium consists of two merging magnetic clouds (MCs) that preserve their identity during their propagation. These magnetic clouds make the interplanetary magnetic field (IMF) southward for a long time, which reconnects with the geomagnetic field, resulting the super-storm ($Dst_{peak} = -472$ nT) on the Earth.

4.2 Observations & Data

Figure 4.1 shows the Michelson Doppler Imager (MDI) magnetogram and white-light image of the active region NOAA 10501 on 2003 November 18. As shown by the magnetogram, the active region was rather complex with $\beta\gamma\delta$ magnetic configuration. The active region was located near to the disk center, \sim N00E18. The flare events took place at the southern part of the active region indicated by box. Figure 2 displays the GOES soft X-ray flux, Extreme ultra-violet (EUV) flux from SOHO/SEM (Judge et al., 1998) and $H\alpha$ relative intensity profiles of the flare events on the above date. The soft X-ray intensity profiles in the 0.5-4 Å and 1-8 Å bands, show three consecutive flares, C3.8, M3.2, and M3.9, respectively having peaks at 05:30, 07:52, and 08:31 UT. According to Solar Geo-physical Data (SGD), two intense flares have been reported as a single event of 2N intensity in $H\alpha$, starting at 07:16 UT and a maximum at 07:54 UT. However, as seen in soft X-ray, the $H\alpha$ measurements clearly showed the progress of these two individual flares. It may be noted that soft X-ray and $H\alpha$ flux profiles show two stage of energy release during the M3.2 flare event. Another interesting thing to note is the M3.2 flare is more intense in $H\alpha$ in comparison to soft X-ray and EUV, whereas the M3.9 flare is more intense in soft X-ray and EUV in comparison to $H\alpha$. Figure 4.3 displays the temperature (T) and emission measure (EM) profiles derived from the soft X-ray flux measurements in two different energy bands. These profiles shows high T (with two stage energy release) for M3.2 flare with low EM whereas low T for M3.9 flare with high EM. It suggests that there was less material at hot temperature ($T\sim 16$ MK) at the beginning of the bigger M3.9 flare (at $\sim 07:45$ UT), while there was more material at the second EM peak (at $\sim 08:30$ UT) but at cooler temperature ($T=12$ MK).

4.2.1 $H\alpha$ Observations

The above flares were observed in $H\alpha$ at ARIES, Nainital, India, using the 15-cm f/15 coudé solar tower telescope, equipped with Bernard Halle $H\alpha$ filter and the Barlow-lens system to enlarge the image by a factor of two. The images were recorded by a 16-bit 575×384 pixels CCD camera system having pixel size 22

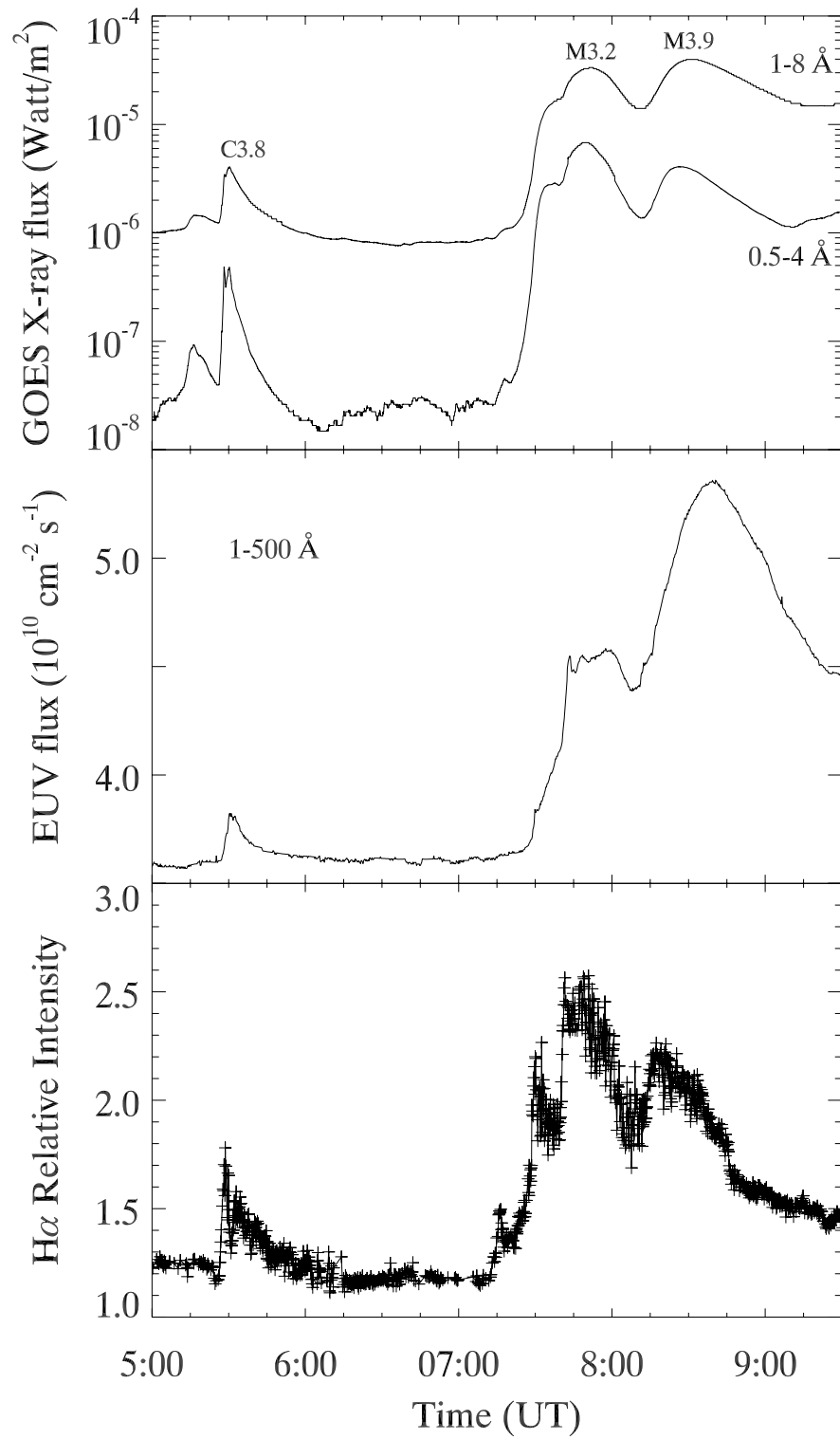


Figure 4.2: GOES soft X-ray, EUV flux and H α relative intensity profiles for the flares on 18 November 2003.

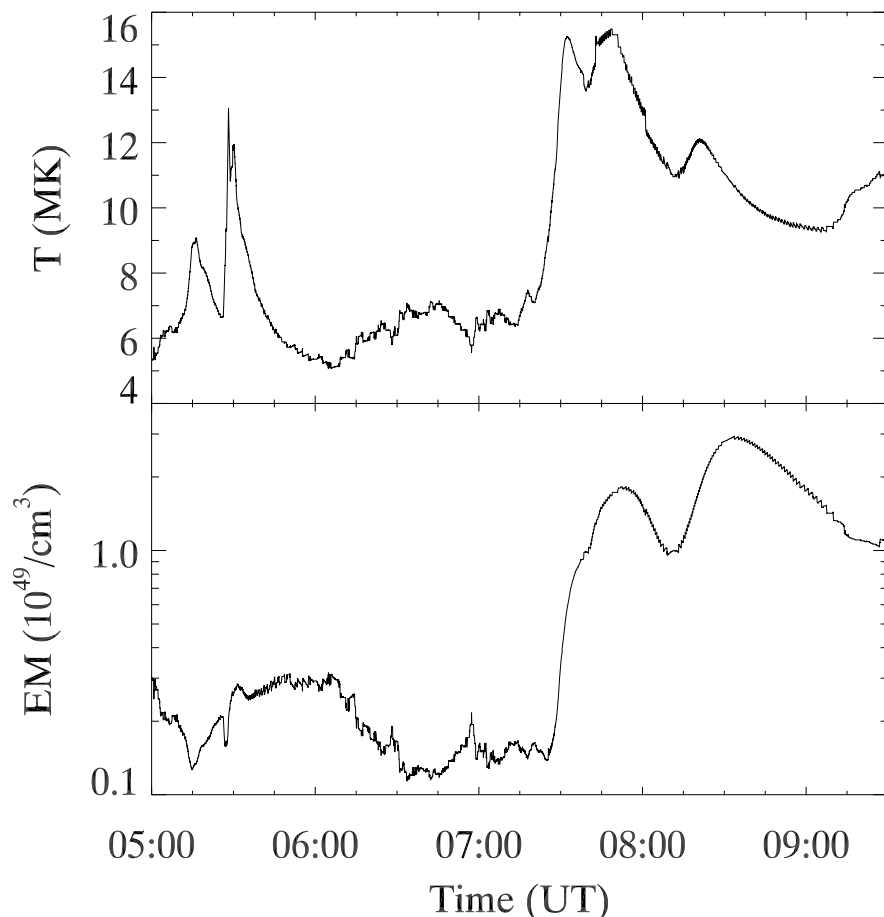


Figure 4.3: Temperature and emission measure profiles derived from soft X-ray profiles in two wavelength bands for the flares on 18 November 2003.

μm^2 , which provides a resolution of $1''$ per pixel and a typical cadence of 15–20 sec per image.

Some of the selected $\text{H}\alpha$ images are shown in Figures 4.4, 4.5 and 4.6, which reveals the evolution of C3.8, M3.2 and M3.9 flares respectively. The images taken before the flare onset at 03:19 UT show a huge U or horse-shoe shaped filament along with plage brightening near the sunspots and reveal the complex structure of the active region. Further, two channels of the filament can be seen at its south-eastern part. The C3.8 flare starts with the heating and brightening at the south-eastern footpoint of the filament and during the flare event, the filament seems to be detached from this footpoint at 05:30 UT. The curved filament at the

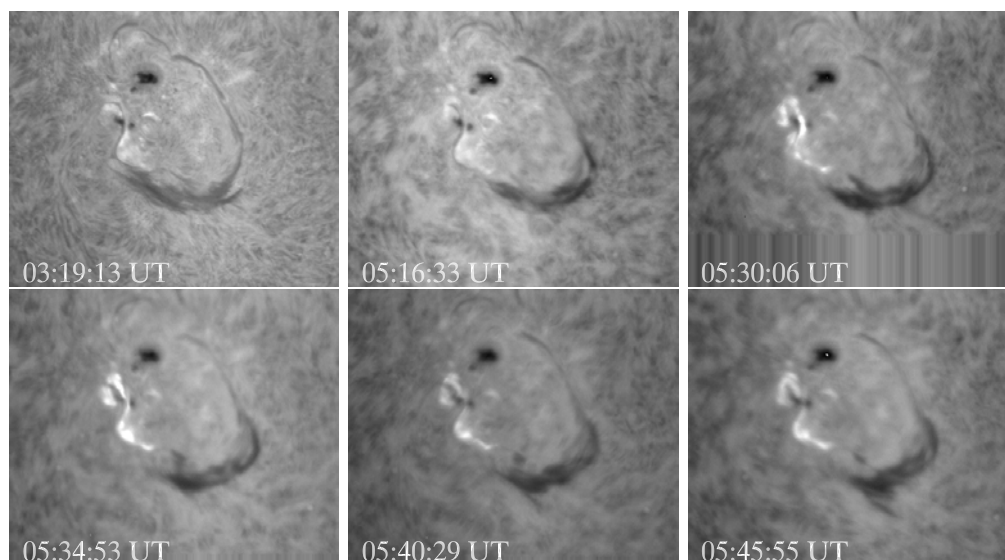


Figure 4.4: $H\alpha$ images showing the evolution of C3.8 flare. The size of each image is $430'' \times 360''$

eastern foot point got activated at the time of this flare and a part of it erupted before the peak of the second flare M3.2. The remaining filament material moved away from the active region, between 07:48 and 08:10 UT, with a speed of $\sim 100 \text{ km s}^{-1}$. The curved filament almost disappeared before the onset of the third flare, M3.9. The flare onset at the location of high shear was shown by two flare ribbons with heavy wrangles. As in the case of typical two-ribbon flare, these ribbons moved away from each other. The ribbon separation speed in $H\alpha$ was $\sim 44 \text{ km s}^{-1}$. During the flare, the $H\alpha$ ribbons showed twisted structure, indicating a high-level of shear. When the flare was in the decay phase, the flare ribbons returned to a simple parallel structure which revealed the relaxation of shear from non-potential to potential magnetic field.

The eastern leg of the filament showed high shear before the onset of the second flare M3.2 and suggested a high twist at the location of the filament. As the flare progressed, the filament destabilised and detached from the flare site. The $H\alpha$ profile clearly shows that the relative intensity of the peak of M3.2 event is more than that of the M3.9 flare. It suggests that the reconnection and heating associated with the M3.2 is taking place in the lower atmosphere where most of the energy is released as well as particles are accelerated during the filament

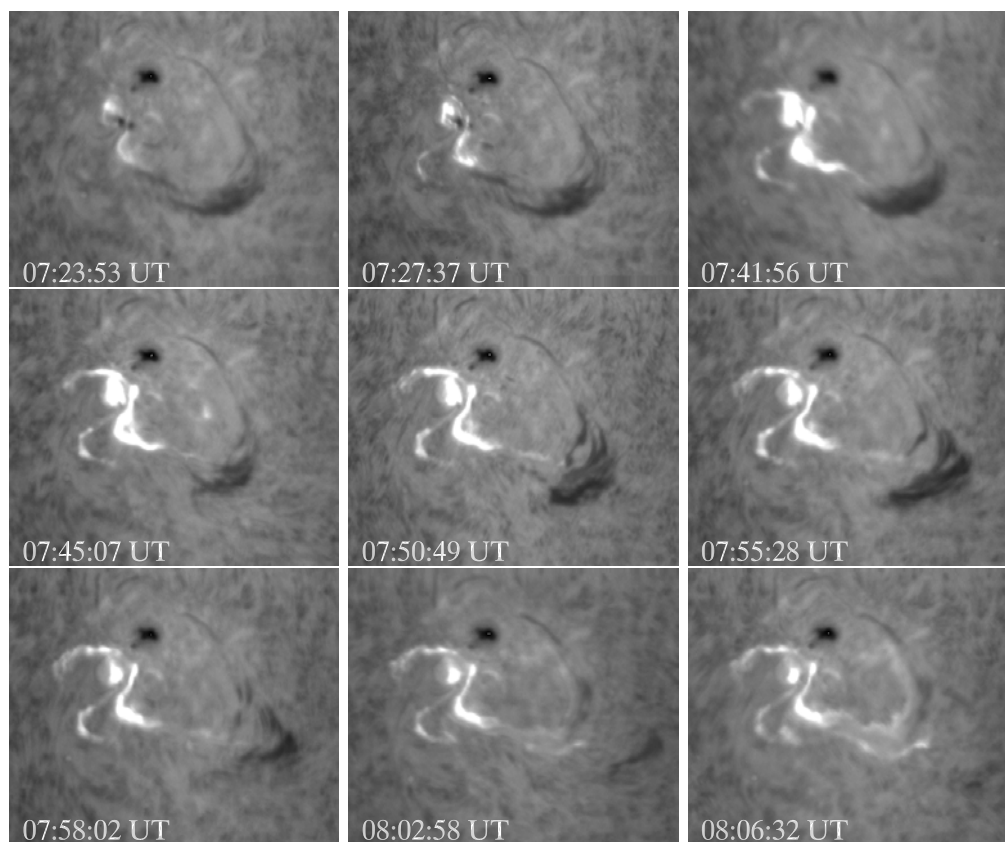


Figure 4.5: $H\alpha$ images showing the evolution of M3.2 flare. The size of each image is $430'' \times 360''$.

eruption (refer to Figure 4.2). The reconnection site is most likely at the eastern leg of the filament where two oppositely directed field lines reconnect leading to ejection of mass, followed by the tether-cutting process. As the filament moved away from the active region, the $H\alpha$ brightening enhanced rapidly. This filament system possibly destabilized or reconnected with the overlying magnetic field in the corona, as it moved upward leading to the initiation of intense X-ray flare, M3.9. It has association with the little higher height than the previous one, as shown by $H\alpha$. Figure 4.7 displays the MDI contours overlaid on $H\alpha$ images prior to the flare event (left panel) and during M3.2 flare with filament eruption (right panel) to see the typical morphology of the magnetic field. Black contour show the negative polarity whereas white one indicate the positive polarity sunspots. Left panel shows the two filament channel at its southern part and right panel

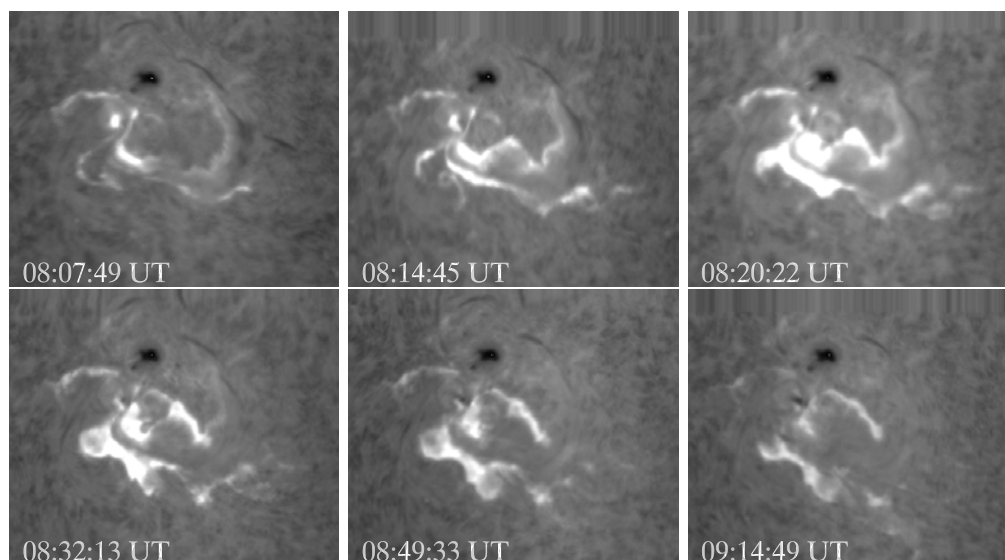


Figure 4.6: $H\alpha$ images showing the evolution of M3.9 flare. The size of each image is $430'' \times 360''$.

shows the highly sheared ribbons at the southern part of the active region, which indicates the more complex field structure at the flare site. Figure 4.8 shows the potential field extrapolations on MDI, and $H\alpha$ images for all three flare events. These extrapolations suggest the sheared field lines at the activity site.

4.2.2 TRACE and GOES/SXI images

The evolution of filament eruption with successive flare events has also been studied with the help of TRACE 195 Å images, which correspond to ~ 1.5 MK plasma (Fe XII line). Figure 4.9 displays the sequence of selected TRACE images which show the flare and the filament eruption during 07:41–07:47 UT. We have overlaid the $H\alpha$ filament contours over the selected TRACE images of the same time (07:41, 07:45 and 07:56 UT). At 07:41 UT, the filament channel (indicated by I) started to erupt at its eastern footpoint and moves away from the AR (shown by arrow). It was observed upto 07:48 UT during the M3.2 flare event. The estimated speed of the filament was $\sim 330 \text{ km s}^{-1}$. The flare intensity enhances as the filament moves up and maximum takes place at 07:52 UT and decays at 08:06 UT.

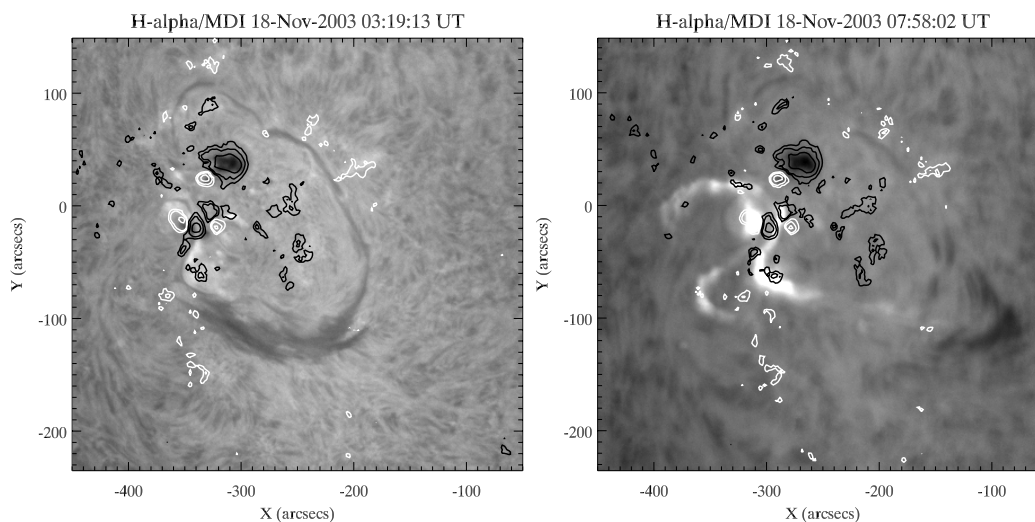


Figure 4.7: MDI contours overlaid on $H\alpha$ images at different times. White contours show positive polarity sunspots whereas black contours indicate negative polarity sunspots.

The GOES SXI (Soft X-Ray Imager) has also been observed both the flares and filament eruptions (Figure 4.11). The spatial resolution of the images is $5''$ per pixel and a cadence of ~ 1 minute per image. The filament was seen at 07:42 UT and moved away from the active region, which was visible upto 07:48 UT. The SXI images provide a linear speed of $\sim 370 \text{ km s}^{-1}$, which is in good agreement with the TRACE measurements. The $H\alpha$ filament contour overlaid on TRACE image at 07:41 clearly reveals the presence of two filament channels/parts (indicated by I and II). The image at 07:56 suggests the presence of the central part of $H\alpha$ filament (II) whereas I filament channel i.e. the eastern part of the filament, has been moved away from TRACE/SXI field of view. We compare these TRACE images with $H\alpha$ images and after a careful investigation, we found that the eastern part of the erupted filament was not visible in $H\alpha$ wavelength. This may be due to its very high temperature, which was observed only in lower wavelengths (TRACE and SXI). Figure 4.10 shows the MDI contours over TRACE 171 and 195 Å images to view the field configuration. Left panel shows the huge U shaped filament along the polarity inversion line while the right panel shows the eruption of the filament eastern part. We plotted the height-time profiles of the filament

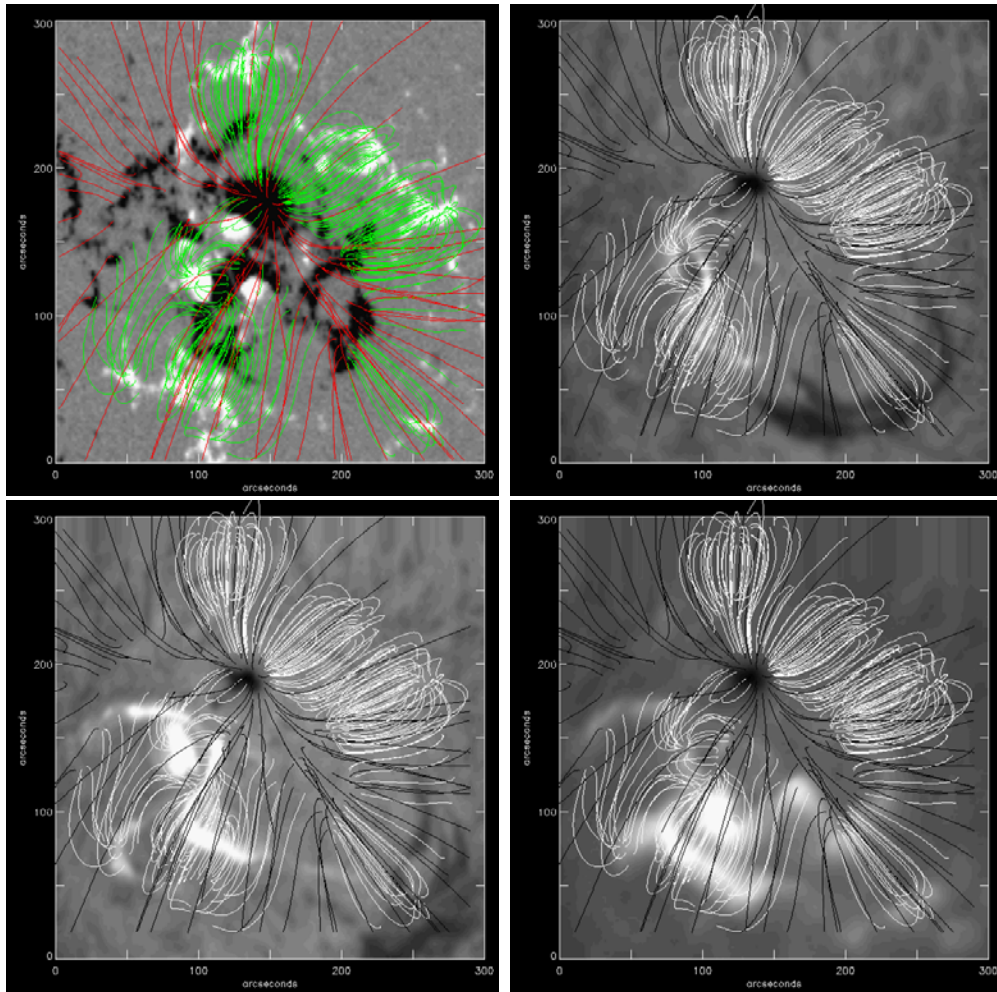


Figure 4.8: Potential field extrapolations for active region NOAA 10501 over MDI (top left) and $H\alpha$ images for C3.8, M3.2 and M3.9 flares on 18 November 2003. Green or white indicates the closed field lines whereas red or black shows the open field line structure.

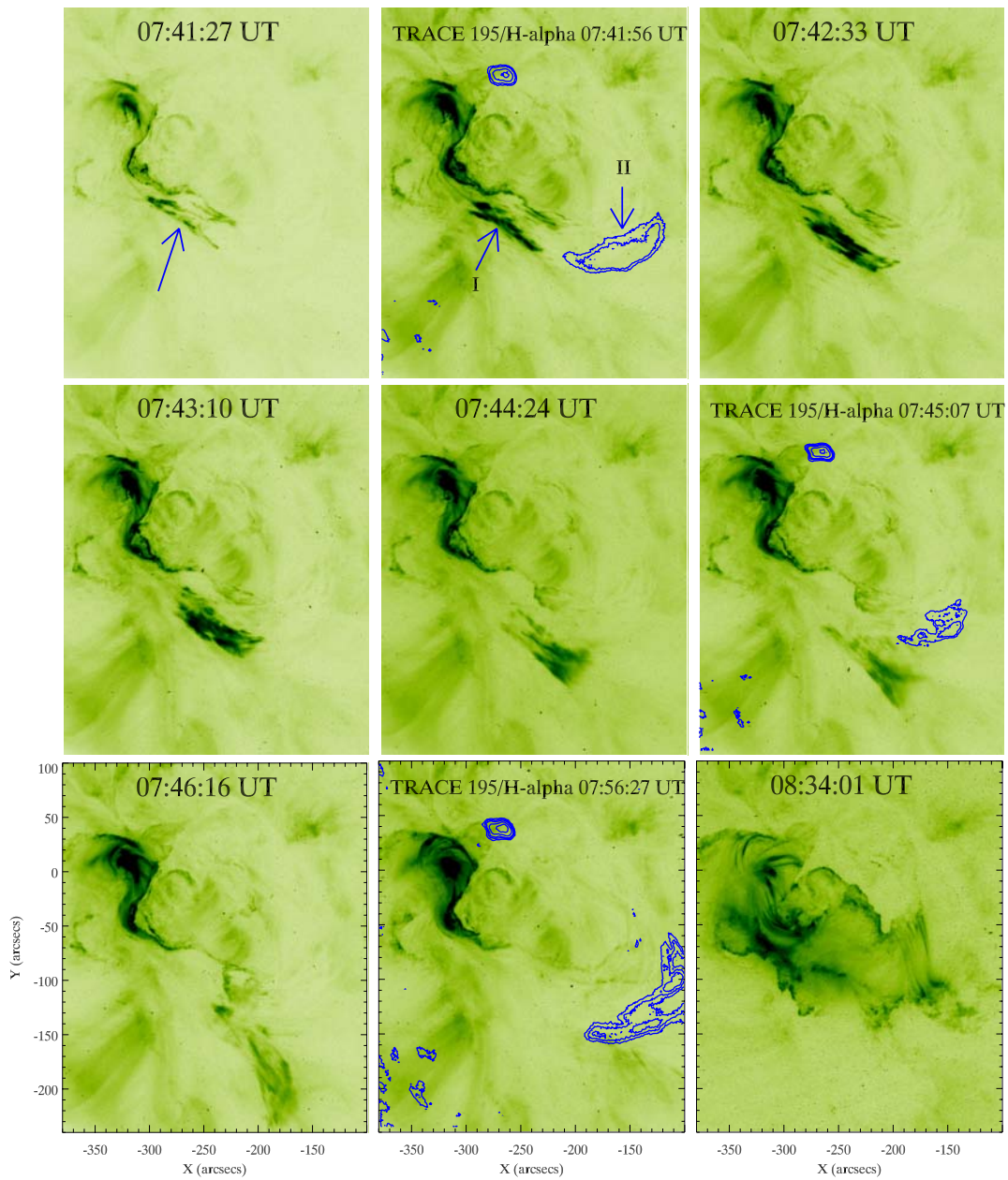


Figure 4.9: TRACE 195 Å (Fe XII line) images showing the flare evolution with filament eruption (first one). The image at 07:41:56 (second top) shows the H α filament contours overlaid on TRACE 195 Å image. This image confirms the eruption of two different channels of the same filament (first visible in EUV and second one in H α , indicated by arrows). The second bottom image (07:56:27 UT) shows the presence of filament channel in H α while the first filament channel moved away from TRACE field of view.

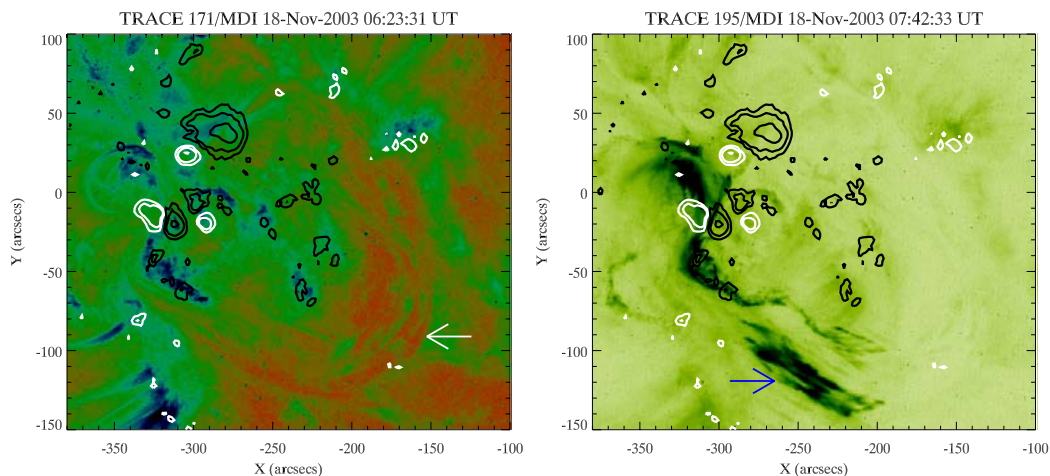


Figure 4.10: MDI contours overlaid on TRACE 171 and 195 Å images at different times respectively. White contours show positive polarity sunspots whereas black one indicate negative polarity sunspots (contour levels=2000, 1000, 500, -500, -1000, -2000). The left panel shows the huge U shaped filament structure along the polarity inversion line (shown by arrow). The right panel shows the eruption of filament channel near the eastern footpoint of the filament.

ejections observed in TRACE/SXI and $H\alpha$ (refer to Figure 4.12). It is clearly evident that these are two different ejections of the same filament moving with different speeds.

In Figure 4.13, two peaks are seen in soft X-ray during the M3.2 event, which reveals the energy release at two stages. It is likely that the energy release at the first stage of M3.2 flare, triggered the first ejection (eastern part) and when this mass moved away from the active region, flare intensity maximized around 07:40–07:50 UT and the second peak is due to the progressive reconnection with the overlying field lines. It is consistent with the ejection of filament. As this CME moved out of the inner corona, another ejection got pushed from the chromosphere, in association with the M3.9 flare.

4.2.3 EIT and White light observations

The LASCO (Large Angle and Spectrometric Coronagraph) observed two CMEs corresponding to the flares, M3.2 and M3.9. Figure 4.15 shows the sequences of

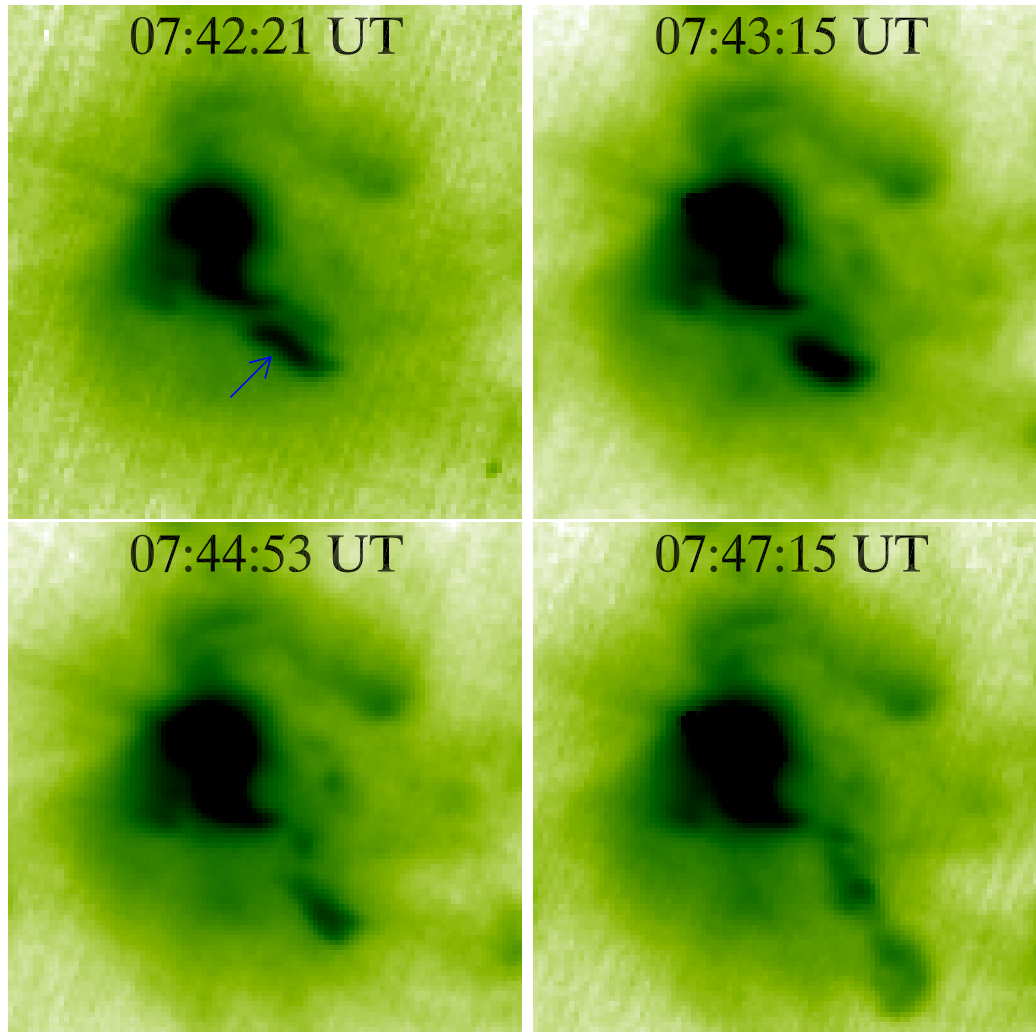


Figure 4.11: GOES soft X-ray (SXI) images showing the filament eruption (indicated by arrow) associated with second M3.2 flare. The size of each image is $500'' \times 500''$.

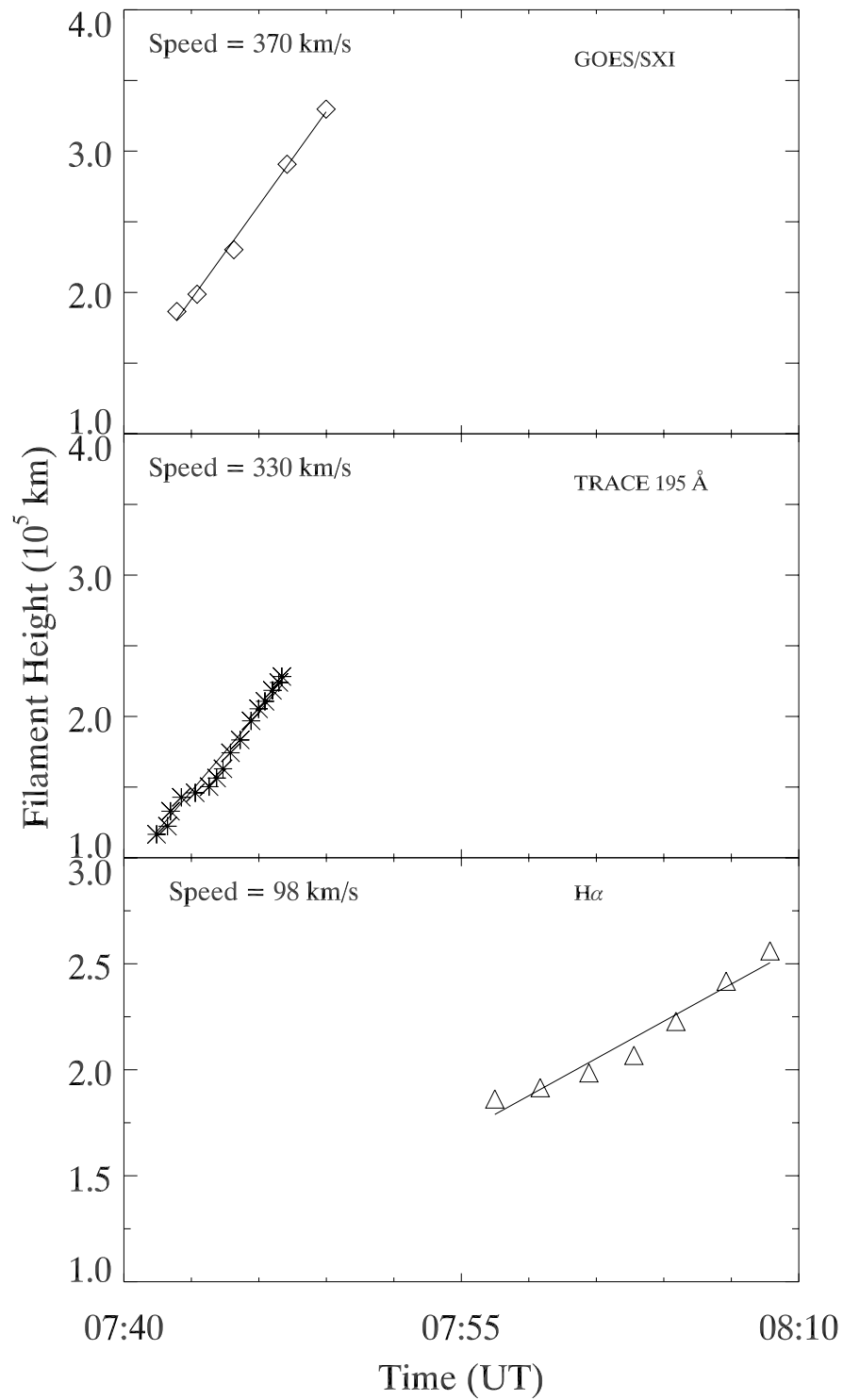


Figure 4.12: Filament eruption height-time profiles in GOES SXI, TRACE 195 Å and H α during the flare events.

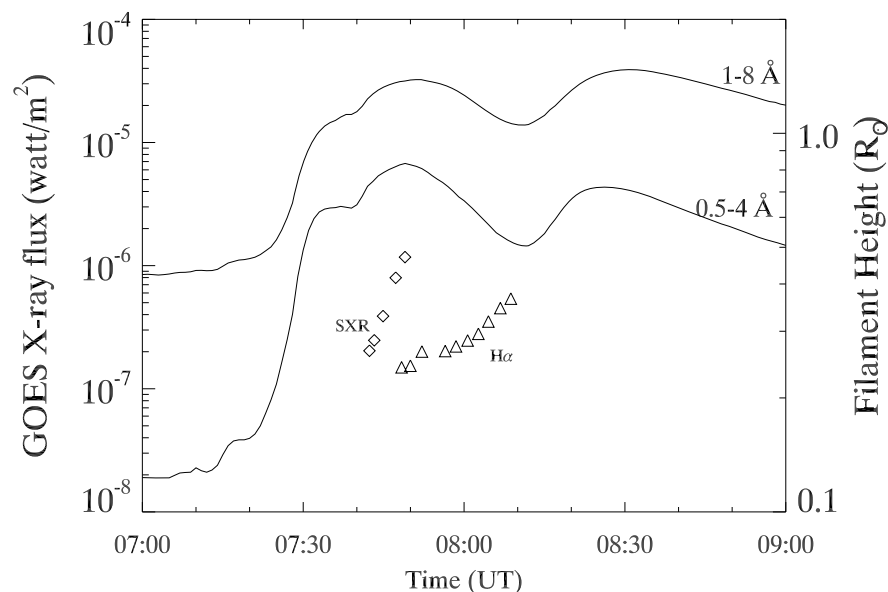


Figure 4.13: GOES Soft X-ray flux with filament height-time profiles estimated from GOES SXR and $H\alpha$ images.

LASCO C2 and C3 images. However, C3.8 flare also produced a poor narrow CME, which was observed at 05:26 UT, having speed $\sim 267 \text{ km s}^{-1}$. The first partial halo CME onset was observed in south-east (SE) direction at 08:06 UT in the C2 field of view, in association with M3.2 flare. The linear speed and acceleration of the CME were respectively 1223 km s^{-1} and 37.8 m s^{-2} . The second full halo CME was observed in south-west direction at 08:50 UT, corresponding to the M3.9 flare event. It showed two-part structure, i.e., outer and inner parts. However, the outer part may be associated with the shock at the front of the CME. The speed and acceleration were 1660 km s^{-1} and -3.3 m s^{-2} , respectively. It may be noted that there was one another CME produced at the eastern limb at 09:50 UT. Since it was very fast (linear speed $\sim 1824 \text{ km s}^{-1}$), it would not have encountered the Earth. Figure 4.17 displays the height-time profile for CME1 and CME2. These CMEs interacted at $\sim 09:20$ UT at a height of $\sim 10 R_{\odot}$. The interaction was clear in the LASCO C3 field of view. In order to see the association of these CMEs with the filament eruptions, we plotted filaments measurements (one observed in the soft X-ray and another from $H\alpha$ images). The CMEs height-time profiles show association with the extrapolation

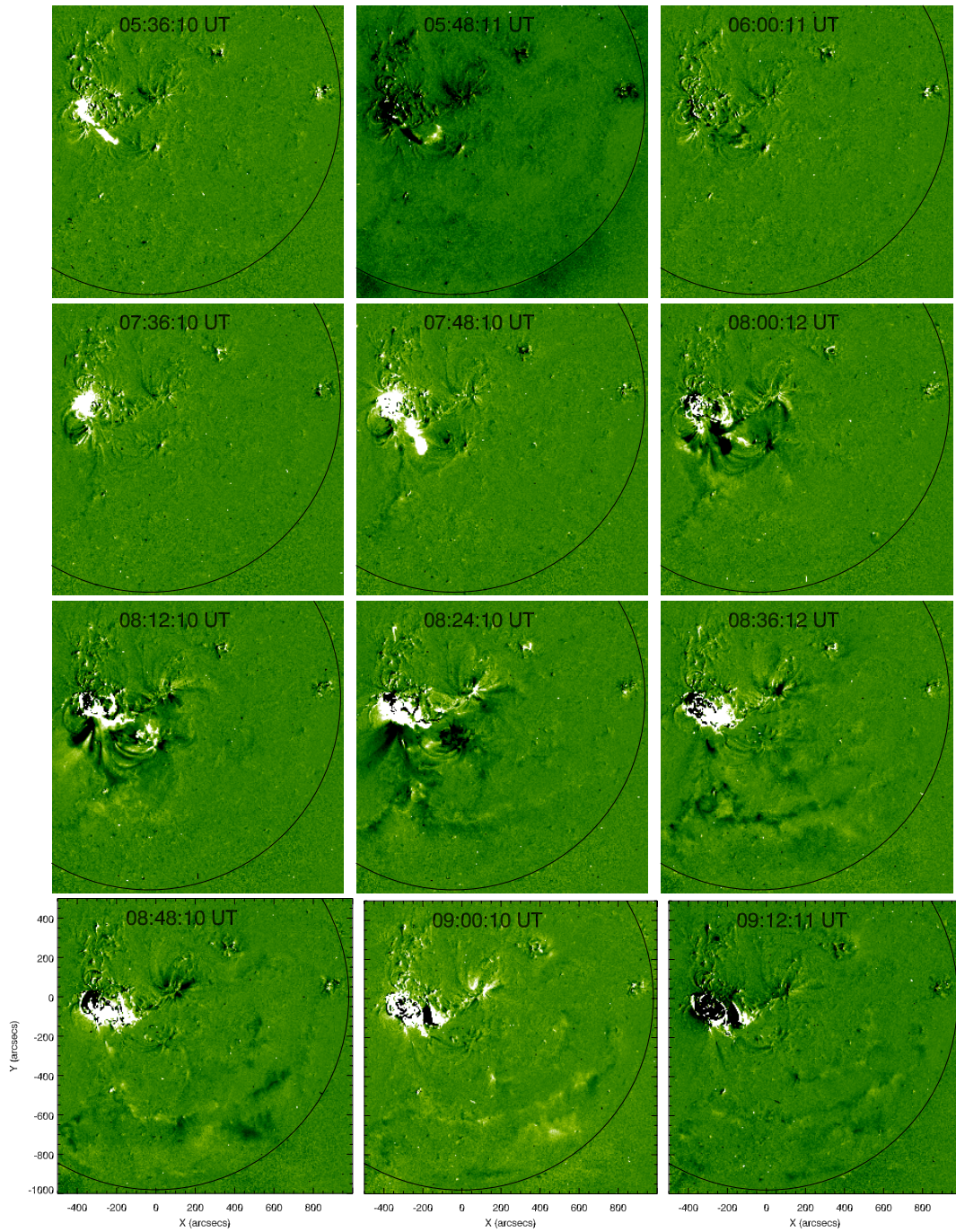


Figure 4.14: Difference images of EIT images which shows the filament eruptions (top 2 rows) and EIT wave (bottom 2 rows) during the flare events.

of filament eruption in space and time. However, Wind/WAVES dynamic spectra shows the enhanced radio signatures of CME-CME interaction at $\sim 09:00$ UT in the interplanetary medium. The radio signatures are likely to be associated with the sheath in between the shock and CME as well as CMEs (Gopalswamy et al., 2001).

4.2.4 Radio Observations

We use the radio spectral data from Learmonth (25-180 MHz) observatory to study the coronal signatures of the events. Figure 4.16 displays the composite spectra from Learmonth (25-180) and Wind/WAVES (1-14 MHz) on 18 November 2003. It shows two Type III radio burst during 07:14–07:16 and 07:25–07:44 UT respectively, Type II burst during 07:47–07:59 UT, and IV radio burst during 08:10 UT to 08:30 UT. For type II radio burst, the dynamic spectrum shows the fundamental much stronger than the second harmonic, which is unusual. It may be noted that both fundamental and second harmonic show two strips in their structure. The estimated speed of the shock from Learmonth data was ~ 440 km s^{-1} . In between the two type III bursts at 07:30–07:40 UT, one small U type burst was observed in Izmiran spectra which shows the particle acceleration along the filament when it was detached from the reconnection site at the eastern leg. The observed type III burst at 07:30 UT is basically due to acceleration of electron beam with opening of field lines during the reconnection at the eastern leg of the filament. After that eastern part of filament detached and it moves away from the AR. The speed of this part filament channel was nearly 300–400 km s^{-1} . The first coronal type II burst observed 07:47–07:59 UT, indicates the formation of shock in the corona at the front of the filament. We estimate the height of type II burst using Newkirk density model (Pohjolainen et al., 2007) and plotted with time (refer to Figure 4.17). It shows a close association with first ejection (eastern part) of the filament. Type IV burst at 08:10 UT indicate the trapped electrons within the large scale filament structure after its eruption. Moreover, another second coronal type II was also observed during 08:15–08:31 UT.

For interplanetary signature of the dynamic event, we use the dynamic spectrum from space based wind/WAVES in the frequency range 0.1-14 MHz, which

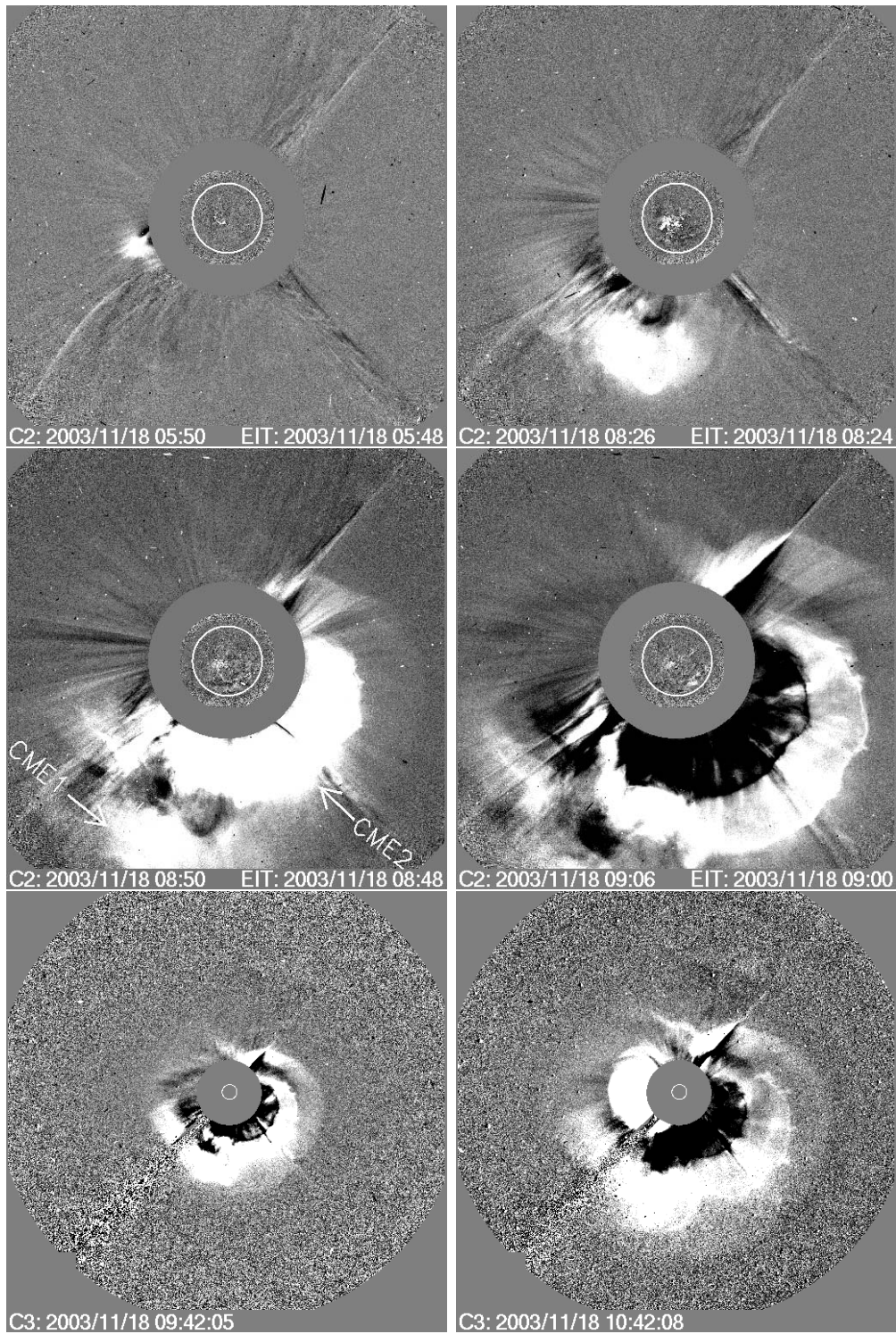


Figure 4.15: Difference images of CME from C2 and C3 LASCO coronagraphs on SOHO showing three CMEs associated with solar flares.

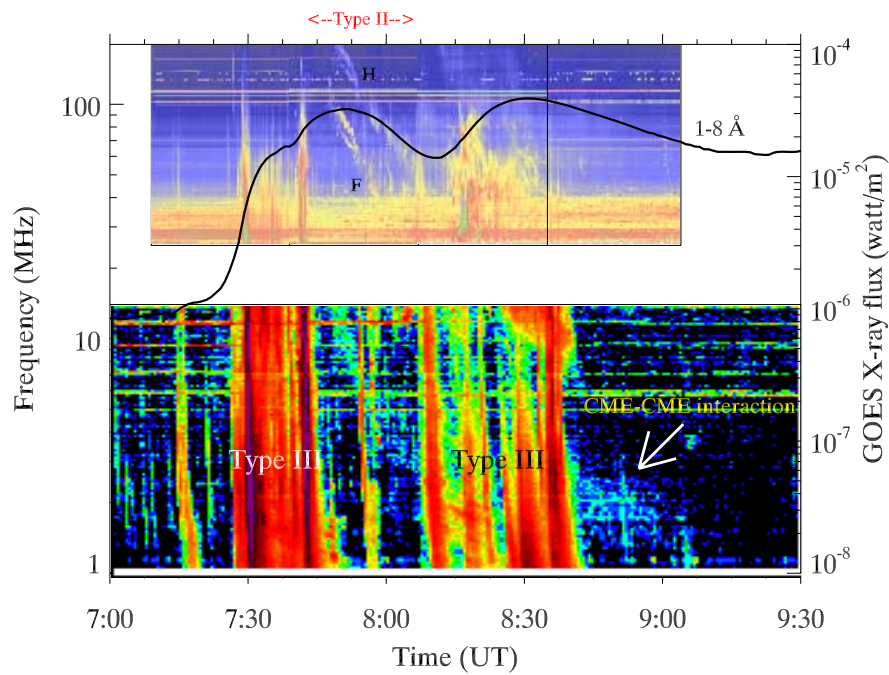


Figure 4.16: Composite radio spectra from Wind/WAVES (1-14 MHz) and Learmonth (25-180 MHz) on 18 November 2003.

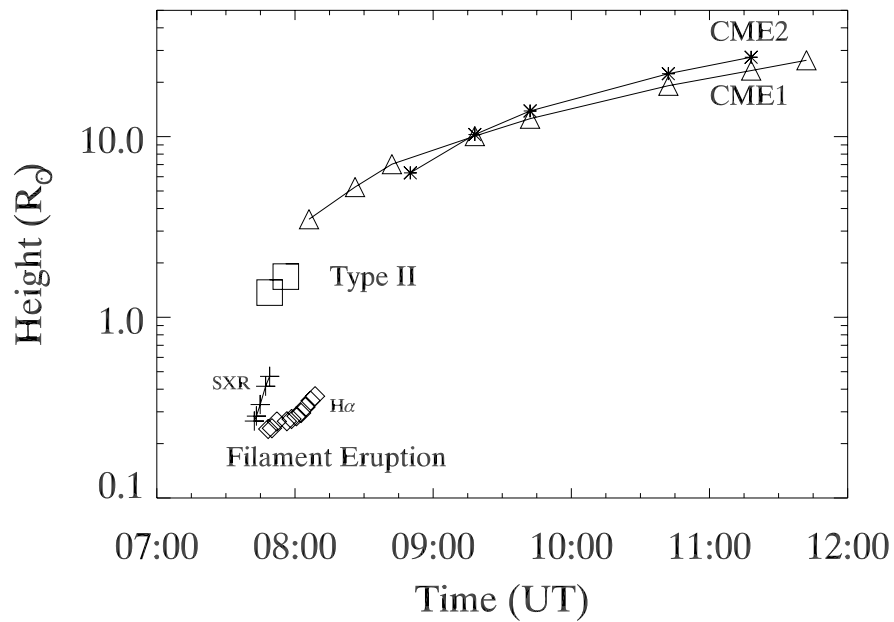


Figure 4.17: The height-time profile of filament eruption observed in SXI (left) and $H\alpha$ (right), type II and CMEs associated with them (LASCO C2 & C3).

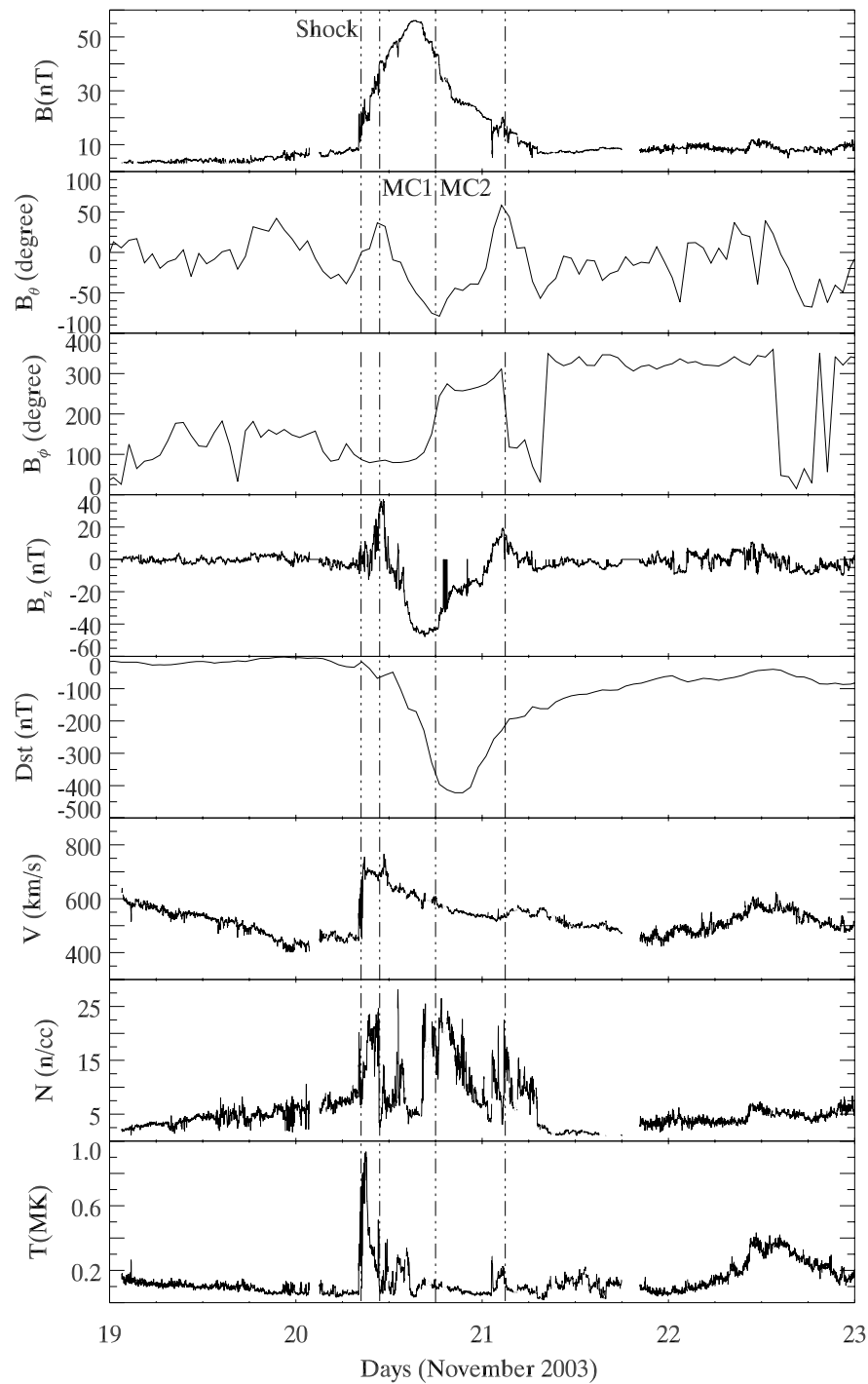


Figure 4.18: The interplanetary observations of magnetic field (B), B_θ , B_ϕ , Dst Index, solar wind speed, proton density and temperature during 19–23 November 2003.

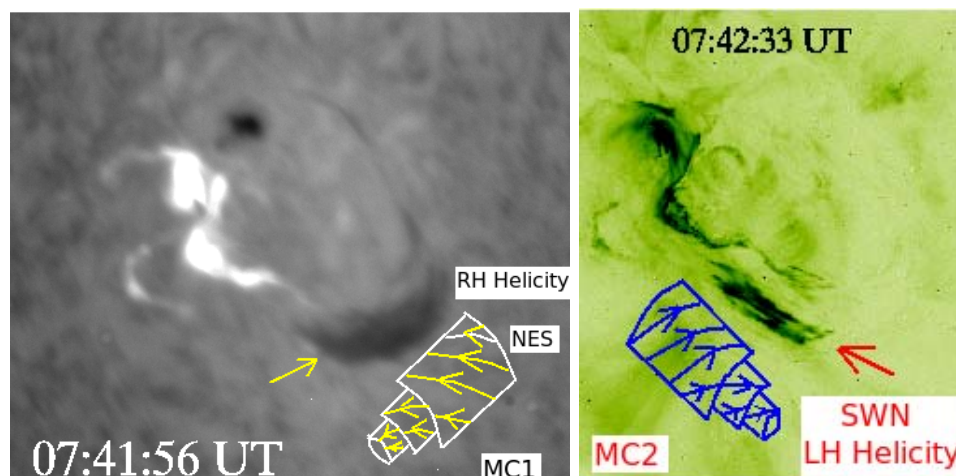


Figure 4.19: The linkage of two merged magnetic clouds in the interplanetary medium with the solar sources.

probes the plasma between $\sim 2\text{-}10 R_{\odot}$. Figure 16 shows the bunches of type III bursts during both flares. The radio flux enhancement at around 09:00 UT may be due to the interaction of two CMEs at $10 R_{\odot}$.

4.3 Interplanetary Consequences

The interplanetary signatures of the above events have been obtained from in-situ spacecraft measurements at 1 AU. Figure 4.18 shows the interplanetary parameters of the CME and associated shock. The arrival of the shock can be seen by the sudden increase in solar wind speed, density, and magnetic field and it is marked by a vertical line at 07:27 UT on November 20, 2003. The azimuthal component of the magnetic field (B_{θ}) shows two smooth rotations, which reveal the presence of two merging magnetic clouds at 1 AU (indicated by MC1 and MC2). First magnetic cloud rotates smoothly from south to north with $\phi=90^{\circ}$. Therefore, the cloud is NES type with right-handed (positive) helicity. Second cloud rotates smoothly from south to north with $\phi=270^{\circ}$. So, this cloud is SWN type with left-handed (negative) helicity (Bothmer & Schwenn, 1997). To link these magnetic clouds with their solar sources, we draw both the clouds over H α and TRACE 195 Å images respectively. The second ejection from the central

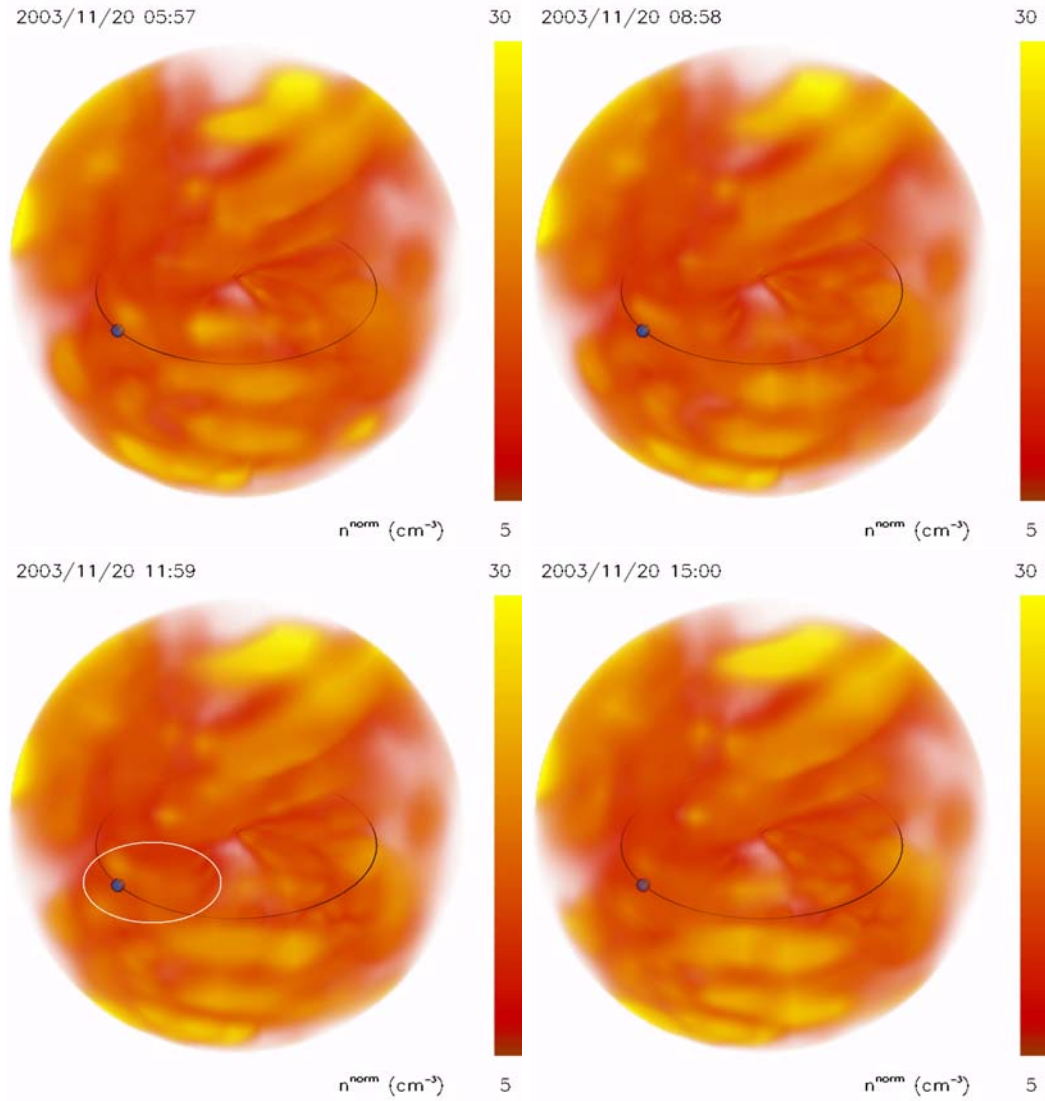


Figure 4.20: Ooty 3-dimensional IPS density images showing the two merging magnetic clouds (shown inside the ellipse) hitting the Earth on 20 November, 2003.

part of the filament confirms the linkage with first magnetic cloud as it contained the big flux rope structure moving with high speed. First ejection i.e. The eastern part of the filament linked with the second magnetic cloud (refer to Figure 4.19). The scenario shown by the in-situ measurements are in agreement with the 3-D images obtained from the interplanetary scintillation (IPS) measurements made with the Ooty Radio Telescope (ORT), operating at 327 MHz (Manoharan, 2006b; Manoharan et al., 2001). Figure 4.20 displays the 3-D IPS images of 3-AU diameter heliosphere. These images evidently show the interaction of two CMEs in the interplanetary space. The polar angle obtained from in situ data indicates that the cloud is inclined to the ecliptic plane ($\sim 74^\circ$) and always southward pointing as the cloud passed the spacecraft. In addition, the azimuthal angle shows a smooth rotation from east to west, with a step at the merging point. The position of the flux rope with respect to the ecliptic is also shown by the IPS images. The shock seems to be associated with the merged magnetic clouds. As the closed crossed, the solar wind speed changed from 700 to 500 km s⁻¹, which shows the slow expansion of the cloud. The estimated shock speed is ~ 800 km s⁻¹. The merged magnetic cloud has caused an intense geomagnetic storm. The ring current index (Dst Index) went down upto -472 nT. The maximum field intensity is about 60 nT, of which mostly point to the south ($B_z \approx -53$ nT), which has caused the intense storm. It remains southward for about 13.5 hrs. The reasons for the intense storms are (i) merged clouds, (ii) their combined speed, (iii) intense shock, and (iv) prolonged as well as (v) intense southward pointing field.

4.4 Discussions

We presented results of H α , TRACE, and SXI measurements of two consecutive flares M3.2 and M3.9 on 2003 November 18. The comparatively higher intensity in H α emission of M3.2 flare than the M3.9 event suggests the lower atmospheric reconnection processes, followed by the ejection of flux rope above the two-ribbon corridor at the flare site. In the LASCO field of view, the CME propagated at ~ 1220 km s⁻¹. The eastern part of the filament seen in soft X-ray (SXI) and EUV (TRACE) showed, respectively, speeds of 330 and 370 km s⁻¹, which confirm a

heavy acceleration at the time of CME onset. The above ejection took place at the eastern leg of the filament, where the twist was high as shown by $H\alpha$ data. In $H\alpha$, after the above partial eruption, the filament showed motion away from the AR site, with a speed of $\sim 100 \text{ km s}^{-1}$ during 07:48–08:10 UT. It might have caused destabilization in the overlying pre-existing complex coronal field structures and produced the next M3.9 flare of maximum intensity at 08:30 UT. The full halo in association with this event propagated faster than the previous one at 1660 km s^{-1} . However, its propagation towards south-east direction and associated the flare ribbons orientation nearly in the east-west direction indicate that the (i) the first CME originated at the leg of the filament and (ii) the second CME had association with the flux rope lying above the ribbons of the flare. In these events both tether cutting and emergence of flux beneath the filament system have played important roles.

The interaction of these two flux ropes and their merging have led to rather big cloud. These showed the nice linkage with the solar eruptions taking place during the flare events. The comparison of magnetic clouds properties at 1 AU suggest that the central part of the filament produced the first magnetic cloud (NES) of positive helicity whereas the eastern part of the filament produced the second magnetic cloud (SWN) of negative helicity. Wang et al. (2006) also compared the tilt angle of the curved filament with the tilt angle of the first magnetic cloud and found that the orientation of the magnetic cloud was almost parallel to the central part of the filament. Our study is also in good agreement with their study. However, the chirality of the filaments can be determined either from the direction of barbs (i.e. fine structure along the filament spine) on both sides of a filament spine, because they trace the flow field and thus the magnetic shear, or from the crossing of bright over dark (or vice versa) filament threads (Chae 2000). In our case, two different segments of the filament indicate opposite chirality. Further, on the basis of barbs orientation, Chandra et al. (2010) also confirmed that the eastern segment of the filament corresponds to a sinistral (left handedness) and western segment of the filament corresponds to dextral (right handedness). Our investigation confirms the association of both magnetic clouds of opposite helicity associated with these opposite chirality filament segments. Moreover, Chandra et al. (2010) estimated the helicity of the active region which was negative and

put a question mark on the positive helicity of the magnetic cloud. Therefore, their finding contradicts what is expected from magnetic helicity conservation. They estimated the localized helicity of the active region and found the positive helicity ejection at the southern part of the active region i.e. the source region of flares. Our results are also in consistent with the previous studies. However, the first cloud had a more favorable magnetic topology to initiate the magnetic reconnection with Earth's magnetic field. Whereas the second cloud could help to sustain the reconnection for a longer time. Therefore, the prolonged reconnection of the resultant magnetic cloud with Earth's magnetosphere has caused a very intense storm ($Dst_{peak} = -472$ nT) of the solar cycle 23.

This study illustrates the need of combining solar, in-situ interplanetary propagation of the ejecta for understanding the physical processes. Previous studies of the same event, but mostly limited, have concluded the presence of only one ejecta. But, here we confirm the two merged magnetic clouds associated with two ejecta from the sun. Finally, this event provides a unique opportunity to study flare-CME relationship, the interaction as well as merging of solar wind magnetic structures which are important in understanding the space weather.

Chapter 5

Multiwavelength Study of Solar Flares from AR NOAA 10960

5.1 Introduction

¹ Solar flares are the sudden explosions in the solar atmosphere during which large amounts of the magnetic energy, stored in the twisted and sheared magnetic fields, is released by the process of magnetic reconnection in the form of thermal energy and particle acceleration. The flares associated with the CME eruptions are known as “eruptive flares”, while the flares without association of CMEs are known as “confined flares”. The emerging magnetic flux, rapid motion/rotation of sunspots and interaction of filaments can destabilize the magnetic field, and trigger the solar eruptive phenomena, *e.g.*, flares, CMEs *etc.* (Kumar et al., 2010; Min & Chae, 2009). The S-shaped *or* inverted S-shaped sigmoids indicate the twisted field lines in the solar atmosphere. The solar eruptions usually take place due to the increase of the twist in the magnetic field configurations of an active regions (Canfield et al., 1999). Recently, the MHD models of magnetic flux tubes show that the twist $[\phi]$ of $2.5\text{--}3.5\pi$ is sufficient for solar eruptions, and the stable equilibrium of the magneto-fluid breaks when the total twist in the associated flux tubes crosses this critical value (Fan & Gibson, 2003; Kliem et al., 2004; Török et al., 2004).

¹Research presented in this chapter has been published in Kumar et al. (2010a), *Solar Physics*, 266, 39 and Srivastava et al. (2010), *APJ*, 715, 292.

Nandy (2008) has shown the formation, evolution, and ejection of the magnetic flux ropes, which originate in the twisted magnetic structures through the combined action of surface flux transport processes (such as diffusion, meridional circulation and differential rotation). Ishii et al. (1998) have investigated a flaring active region NOAA 5395 during March 1989 and found some peculiar vortex-like motion of small, satellite sunspots, which successively emerged from the leading edge of the sunspot group. They propose a schematic model of successive emergence of twisted and winding magnetic-flux loops coiling around a trunk of magnetic-flux tube, and concluded the flare triggering due to this emerging flux bundles. The twisted flux-tube model (Amari et al., 2000) and flux-injection driven model (Krall et al., 2001), both suggest that a twist-enhanced flux rope can play a crucial role in large-scale eruptive events. The primary mechanism for driving such eruptions may be due to the catastrophic loss of MHD equilibrium (Lin & Forbes, 2000). They have suggested that a flux rope is allowed to escape with a fairly small reconnection rate in the vertical current sheet created below. The highly twisted flux tubes store magnetic energy, which is necessary for the heating and particle acceleration during the solar eruptions. Wang et al. (2002) have found a rapid disappearance of a sunspot associated with the M2.4 flare from NOAA AR 9830 on 20 February 2002 with hard X-ray sources located near this disappeared sunspot. Ishii et al. (2000) have also pointed out that the occurrence of high flare activity is restricted to the location and the time at which the strongly twisted magnetic flux ropes emerged to the photosphere in the long lived and large active regions, *e.g.*, NOAA AR 4201.

The observational evidences of twisted helical structure are less abundant in the solar atmosphere. However, they may be an efficient mechanism for the triggering of solar eruptive phenomena *e.g.* flares and coronal mass ejections (CMEs). Gary & Moore (2004) and Liu et al. (2003) have observed the helical magnetic flux tubes with multiple turns, which were associated with double flares and CMEs. This observational evidence of the activation of helical flux tubes, and thus associated destabilization of large-scale magnetic fields of active region, may be important clues for the energy build-up processes of solar flares. However, we do not have sufficient understanding and observational signature of the twisted flux ropes and their evolution from the sub-photospheric level into the

corona. There are a few observational signatures related to the generation of the twist in the solar filaments, which causes the disruption of their stable magnetic field configuration and generates solar eruptive events (*e.g.*, [Liu & Alexander 2009](#); [Williams et al. 2005](#) and references cited there). [Rust & LaBonte \(2005\)](#) have also found evidence of sigmoids in the solar corona which were governed and energized by the magnetic twist, without any large-scale destabilization of magnetic fields and associated eruptions from the Sun. [Gerrard et al. \(2002\)](#) have found that the foot-point twisting motion may also generate the twisting in the active-region loops which trigger flare event after their reconnection with the surrounding opposite-polarity field lines.

In this chapter, we present a multiwavelength analysis of solar flares (B5.0, M8.9/3B) that occurred on 04 June 2007 from AR NOAA 10960. The flares were observed by several spaceborne instruments, namely SOHO/MDI, HINODE/SOT, TRACE and STEREO/SECCHI. Both the flares were initiated near a small, positive-polarity, satellite sunspot at the centre of the active region, surrounded by opposite-polarity field regions. MDI images of the active region show considerable amount of changes in the small positive-polarity sunspot of δ configuration during the flare event. SOT/G-band (4305 Å) images of the sunspot also suggest the rapid evolution of this positive-polarity sunspot with highly twisted penumbral filaments before the flare event, which were oriented in a counterclockwise direction. It shows the change in orientation, and also remarkable disappearance of twisted penumbral filaments ($\approx 35-40\%$) and enhancement in umbral area ($\approx 45-50\%$) during the decay phase of the M-class flare event. TRACE and SECCHI observations reveal the successive activation of two helical-twisted structures associated with this sunspot, and the corresponding brightening in the chromosphere as observed by the time-sequence images of SOT/Ca II H line (3968 Å). The secondary, helical-twisted structure is found to be associated with the M8.9 flare event. The brightening starts six–seven minutes prior to the flare maximum with the appearance of secondary, helical-twisted structure. The flare intensity maximizes as the secondary, helical-twisted structure moves away from the active region. This twisted flux tube, associated with the flare triggering, is found to be failed in eruption. The location of the flare

activity is found to coincide with the activation site of the helical twisted structures. The activation of successive helical twists (especially the second one) in the magnetic flux tubes/ropes plays a crucial role in the energy build-up process and triggering of the M-class solar flare without a coronal mass ejection (CME).

AR 10960 shows the successive activation of helical twisted magnetic structures on 4 June 2007, which do not cause any eruption. Recently, evidence of the kink instability has been found in the right-handed twisted loop, which causes the B5.0 class flare in this AR during 04:40–04:51 UT (Srivastava et al., 2010). We study the M8.9/3B flare event of the same active region NOAA 10960 during 05:06–05:16 UT on 4 June 2007 using multiwavelength observations. We find rare observational evidence of the activation of helical-twisted magnetic structure in the active region, which may produce the M-class flare. In Section 5.2, we present multiwavelength observations of AR 10960 and the associated flares. In later sections, we present the discussion and conclusions.

5.2 Multiwavelength Observations of NOAA 10960 and Associated Flares

The flare event was observed by various space based instruments namely SOHO/MDI, *Hinode*/SOT, TRACE and STEREO/SECCHI. The top panel of Figure 5.1 displays the SOHO/MDI image of the active region NOAA 10960 on 4 June 2007 before this flare activity. The active region is located nearby the eastern limb at S09E50 showing a $\beta\gamma\delta$ configuration. This active region produced ten M-class flares during its passage across the solar disk. However, this active region was very poor in CME production, and only two M-class flares were associated with CMEs (Yashiro et al., 2008). In the present study, the M8.9/3B flare was triggered without any CME eruption observed on 4 June 2007. The positive-polarity sunspot is indicated by an arrow, which plays an important role in triggering the M8.9/3B solar flare. The enlarged view of the sunspot group, as indicated by a box on SOHO/MDI image, is shown in the SOT/blue continuum image (4504 Å) (bottom-left panel). The closer view of the positive-polarity sunspot, as indicated by a box in SOT/blue continuum image, is also shown in the bottom-right panel.

5.2 Multiwavelength Observations of NOAA 10960 and Associated Flares

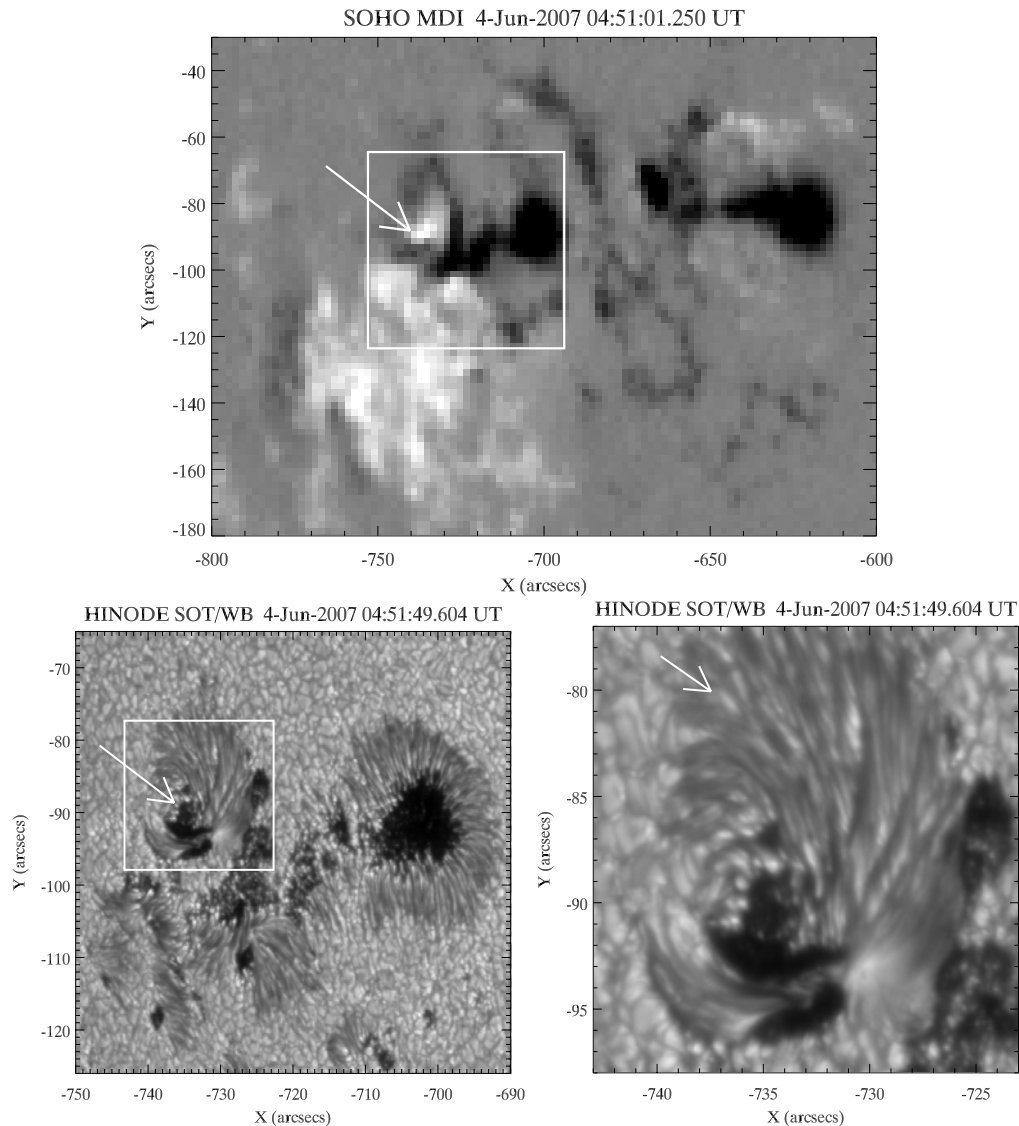


Figure 5.1: Top: SOHO/MDI image of active region NOAA 10960 on 04 June 2007. The positive-polarity sunspot indicated by arrow plays an important role in triggering the M8.9/3B solar flare. The enlarged view of the sunspot group of the active region as indicated by a box in SOHO/MDI image, is shown in the SOT/blue continuum (4504 \AA) image (bottom-left panel). A more closer view of the positive-polarity sunspot as indicated by a box in the SOT/blue continuum image, is also shown in the bottom-right image. Penumbral filaments, twisted in the counterclockwise direction, are clearly evident in this image.

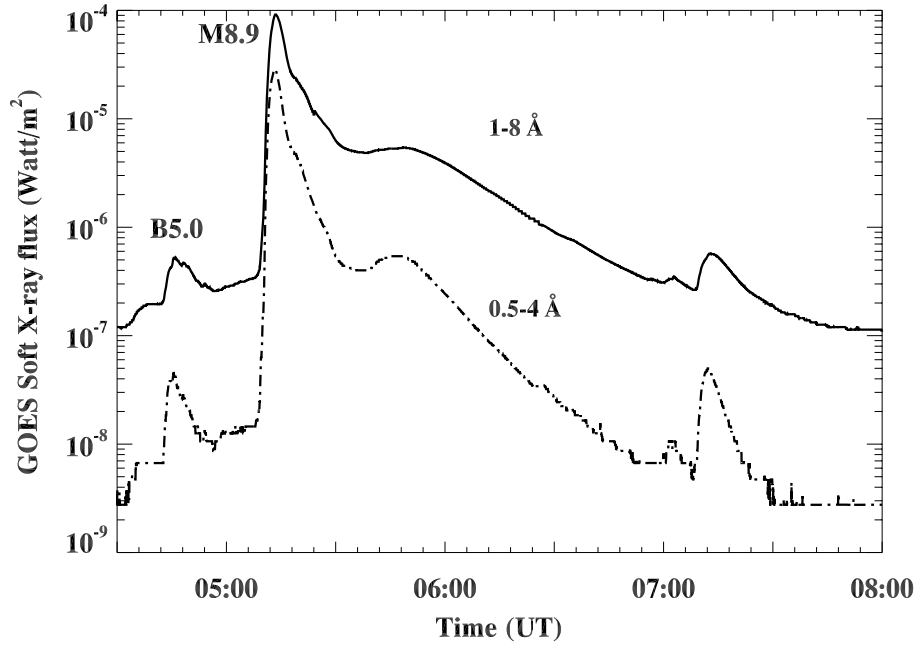


Figure 5.2: GOES soft X-ray flux profiles of the flares in 1–8 and 0.5–4 Å wavelength bands on 04 June 2007.

The penumbral filaments, twisted in the counterclockwise direction, are clearly evident in this image.

According to the GOES soft X-ray flux profiles in the 0.5–4 Å and 1–8 Å wavelength bands, the M8.9 flare starts at 05:06 UT, reaches maximum at 05:13 UT, and ends at 05:16 UT (Figure 5.2). This flare shows an impulsive rise for a short duration during the above-mentioned time period and then a gradual decay for a long time until nearly 06:45 UT. However, a small B5.0 class flare was also observed well before this flare event during 04:40–04:51 UT, which seems to be a precursor for M8.9 flare. According to the Solar Geophysical Data (SGD), the M-class flare is classified as 3B class in $H\alpha$, where, the flare starts at 05:05 UT, peaks at 05:14 UT and ends at 06:42 UT.

5.2.1 *Hinode*/SOT Observations

The high-resolution filtergrams of a flaring region in NOAA 10960 were obtained by the 50 cm *Solar Optical Telescope* (SOT) onboard the *Hinode* spacecraft.

5.2 Multiwavelength Observations of NOAA 10960 and Associated Flares

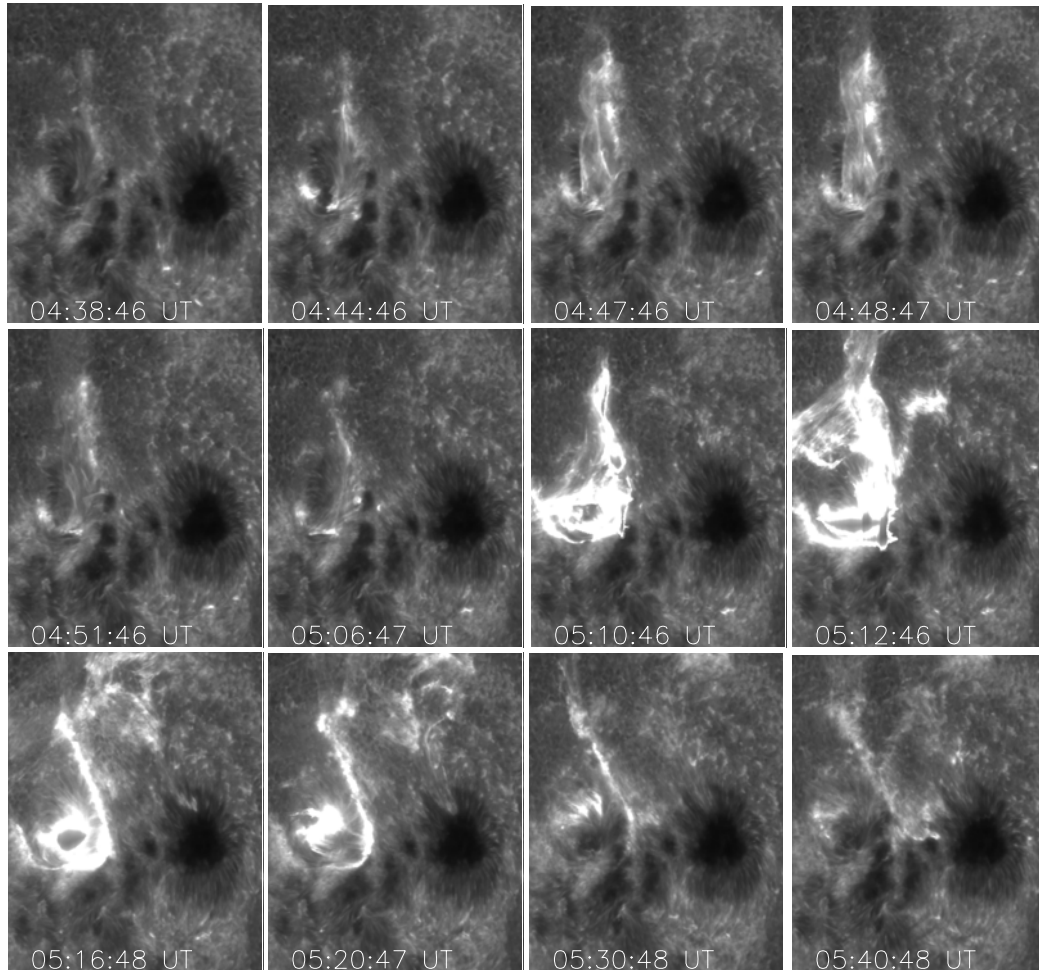


Figure 5.3: *Hinode*/SOT Ca II H 3968 Å images showing the successive activation of helical twists and corresponding brightening above the positive-polarity sunspot on 4 June 2007. Secondary helical twist has been activated at $\approx 05:08$ UT and causes the maximum of the M8.9/3B class flare brightening in the chromosphere at $\approx 05:13$ UT. The size of each image is $60'' \times 75''$.

We use the SOT/Ca II H 3968 Å chromospheric images at a cadence of \approx one minute, with a spatial resolution of 0.1'' per pixel (Tsuneta et al., 2008b). We also use SOT/blue-continuum (4504 Å) temporal image data to examine the changes and evolution of the positive-polarity sunspot which is the key place at the centre of the active region where the flare activity occurred. The *Hinode* data are calibrated and analysed using standard IDL routines in the SolarSoft (ssw) package. Figure 5.3 displays the selected chromospheric temporal images of the active region NOAA 10960 in Ca II H line. These images show the significant changes in the chromosphere before the flare. The image at 04:42 UT shows the two bright points at the two opposite edges of an umbral-bridge structure. After that, a twisted, bright structure appears near the umbral-bridge from the southern part of the sunspot. It is at \approx 29,000 km (in projection) from the sunspot location. This structure was visible for nearly six–seven minutes during 04:45–04:51 UT and then after it fades out against the chromosphere (Srivastava et al., 2010).

After this first episode, two other bright points were observed at the same site before the initiation of the M8.9 flare (refer to the image at 05:06 UT). After this, the flare starts and it covers the full sunspot at the maximum phase. The “S”-shaped single ribbon, formed at 05:16 UT, was observed until 05:26 UT. The flare continues until 05:30 UT. Therefore, at the same location, near the positive-polarity sunspot, the twisted structure showed two successive activations in association with the energy build-up and release processes in the AR 10960. It seems that the activation of secondary twist at \approx 05:08 UT plays a significant role in the triggering of M8.9/3B solar flare.

5.2.2 TRACE, STEREO/SECCHI/EUVI and *Hinode*/XRT Observations

We use TRACE 171 Å (Fe IX) EUV images to study the dynamics of the flaring active region and its response in the corona before the M-class flare event. This wavelength corresponds to 1.3 MK plasma. The image size is 1024×1024 pixels with the resolution of 0.5'' per pixel, and the cadence is \approx one minute. We have used the standard IDL routines available in the SolarSoft library for cleaning

5.2 Multiwavelength Observations of NOAA 10960 and Associated Flares

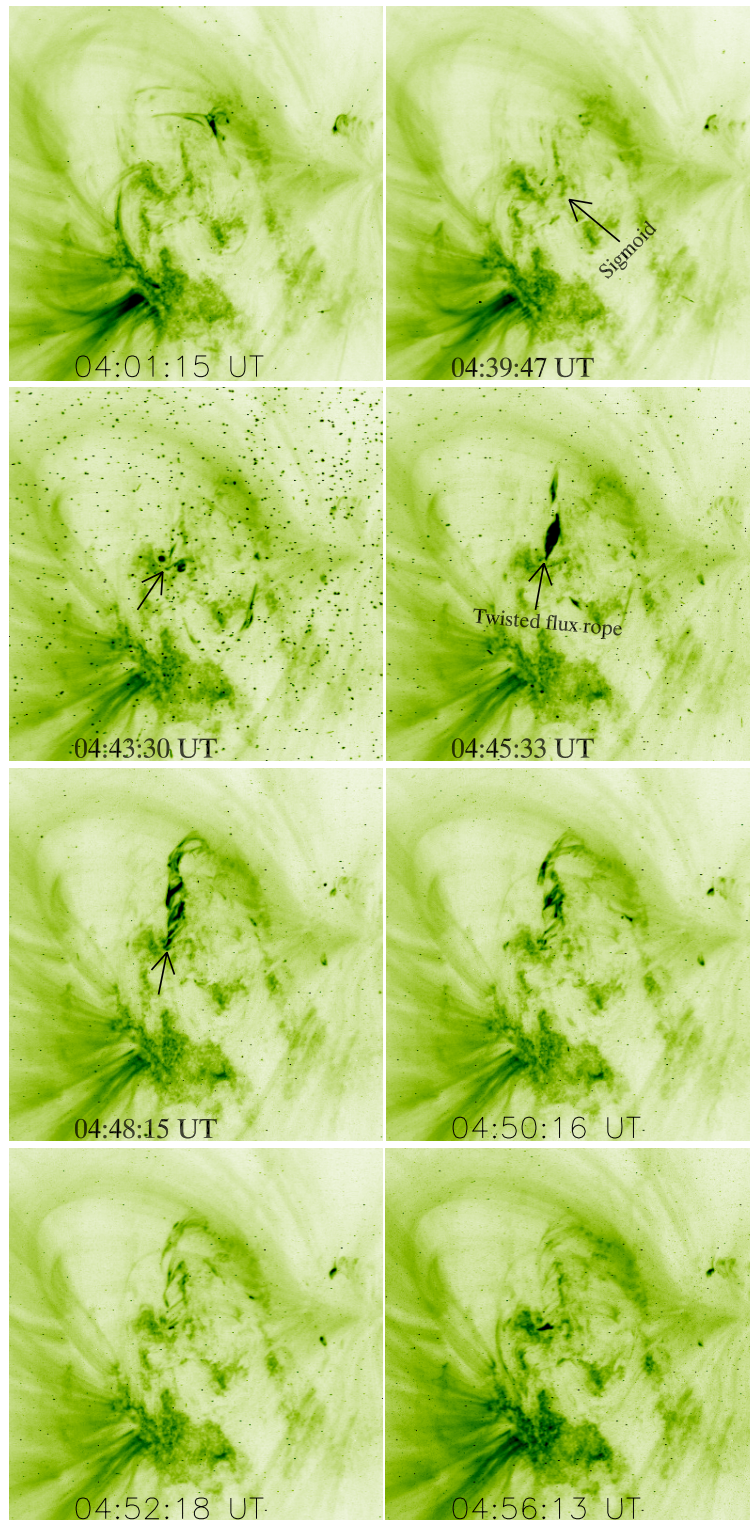


Figure 5.4: TRACE 171 Å EUV images (in reversed colors) showing the temporal changes in the magnetic field configuration before the initiation of M-class flare. The size of each image is 200'' \times 200''.

and co-aligning the images. Figure 5.4 displays the selected TRACE coronal images before the flare during 04:00–04:56 UT. The careful investigation of the TRACE movie shows the plasma flow from the flare site along the two close and smaller loops located within the big loop (see the image at 04:01:15 UT). The image at 04:39 UT shows the S-shaped sigmoid structure (indicated by an arrow) at the active-region centre. At 04:43 UT, we observe two bright points near the sigmoid structure, which is also evident in SOT/Ca II temporal image data. Therefore, the first helical twist has appeared in the loop system associated with this particular positive-polarity sunspot and also causes the brightening in the plasma there (see also the first panel of Figure 5.3). This sunspot is connected with the negative-polarity sunspot by very faint loop system in which the twist and brightening are activated, and their configuration is also highly changeable with time (Srivastava et al., 2010). The projected lower-bound speed of the activation of this twist is $\approx 200 \text{ km s}^{-1}$. It spreads to the maximum distance of $\approx 43,500 \text{ km}$ from the sunspot (see the image at 04:48 UT). It was visible for nearly seven–eight minutes. After that, the structure fades out in to the coronal background. TRACE observations of the activation of this primary helical twist correlate nicely with the SOT observations. However, the length of the structure is a little less in the SOT images in comparison to the TRACE observations. This is due to the smaller field of view of SOT (see the image at 04:48 UT in both sets), which only captured the partial field of view of the helical twisted loop system in the chromosphere. This structure, which is fully observed by TRACE, does not fit in the field of view of the SOT. However, TRACE missed the impulsive phase of this M-class flare. For the impulsive phase of the flare, we use the STEREO-A SECCHI/EUVI observations (Wuelser et al., 2004). We use Fe IX 171 Å coronal images for the present study. The size of each image is 2048×2048 pixels with $1.6''$ per pixel sampling. We use the standard SECCHLPREP subroutines for cleaning the images and other standard subroutines available in STEREO package SolarSoft library. We have used SOHO/MDI images for co-aligning the SECCHI images.

Figure 5.5 displays the selected SECCHI/EUVI coronal images during 05:03–05:56 UT. The image at 05:08 UT shows the secondary activation of helical

5.2 Multiwavelength Observations of NOAA 10960 and Associated Flares

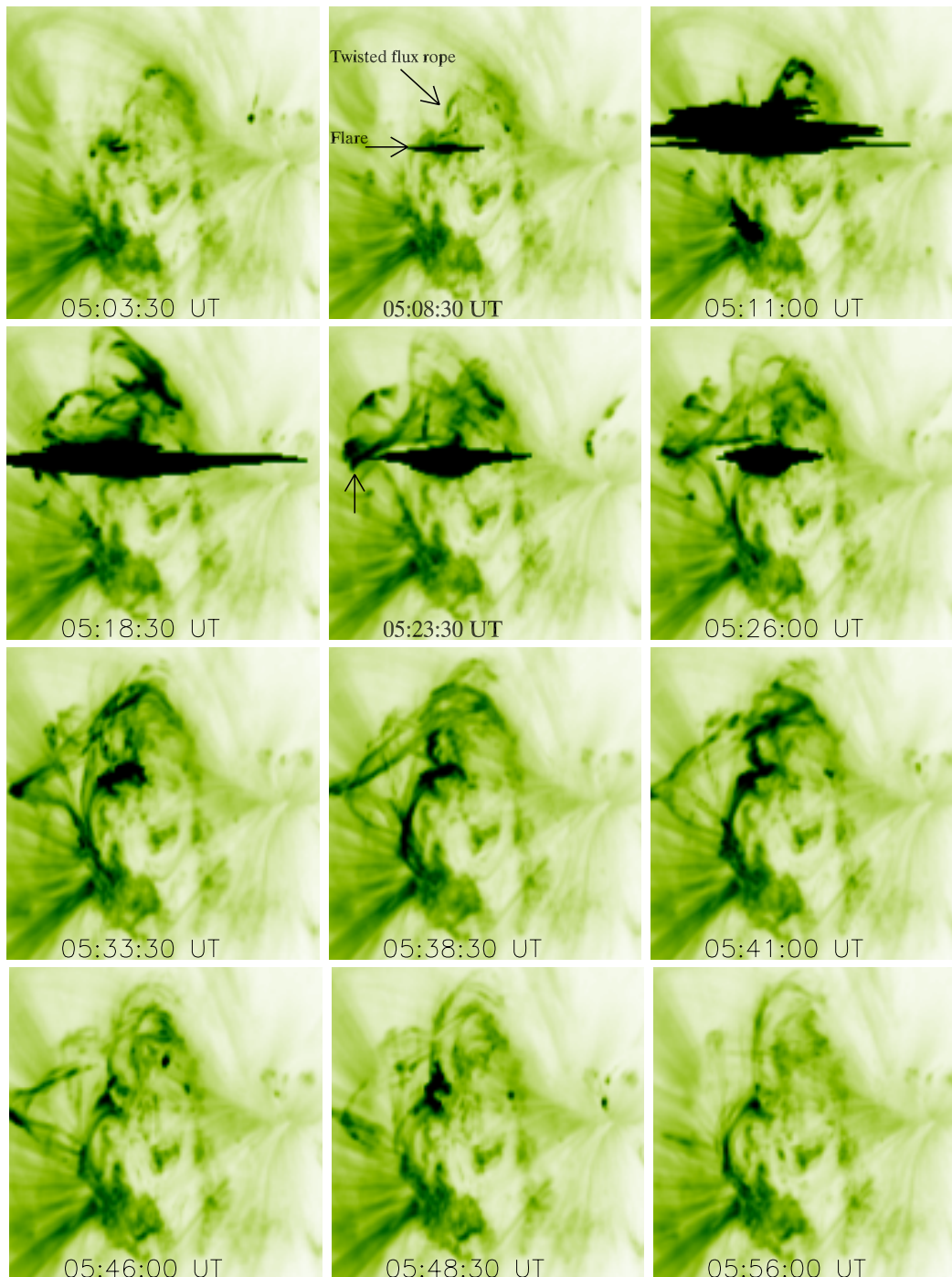


Figure 5.5: STEREO SECCHI 171 Å images (in reversed colors) showing the temporal changes in the magnetic-field configuration and related M8.9/3B flare event. The size of each image is $200'' \times 200''$.

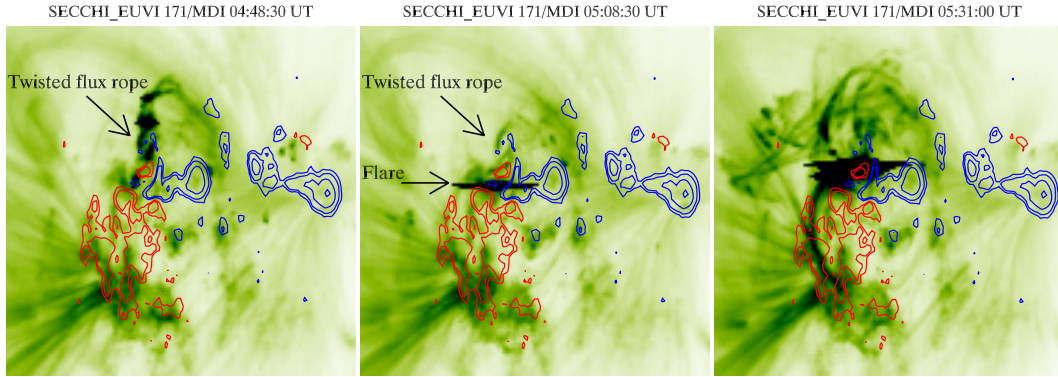


Figure 5.6: MDI contours overlaid on STEREO/SECCHI 171 Å EUV images before the flare initiation and during flare progressive phase. Red contours show the positive polarity, while blue ones show the negative polarity. The size of each image is $200'' \times 200''$.

twisted structure above the same positive-polarity sunspot which connects neighbouring, small, negative-polarity sunspot (see the middle panel of Figure 5.6). It should be noted that the successive activation of the helical twists, at the same place that cause the plasma brightening also, may be a signature of the build-up of magnetic energy in AR 10960. However, the activation of the secondary helical-twist at 05:08 UT seems to play crucial role in the energy build-up process for the M8.9/3B class flare. This activation is located near the centre of the active region where the flare initiation takes place, as it spreads away from the sunspot. The flare reaches maximum at $\approx 05:14$ UT and then decays slowly. During the decay phase of the flare, the image at 05:23:30 UT shows a twisted flux rope (one turn is visible) very close to the flare energy-release site (indicated by an arrow). This structure moves away very slowly and finally disappears at 05:48 UT. However during the maximum and decay phase of the flare, several twisted structures are visible which indicate the presence of free magnetic energy in the observed coronal volume. We overlaid the MDI positive (red) and negative (blue) polarity contours over the selected SECCHI images to view the field morphology, during the flare event (see Figure 5.6). The careful investigation of these images reveals the association of secondary helical twisted structure at 05:08 UT before the M-class flare maximum, associated with the small positive-polarity satellite

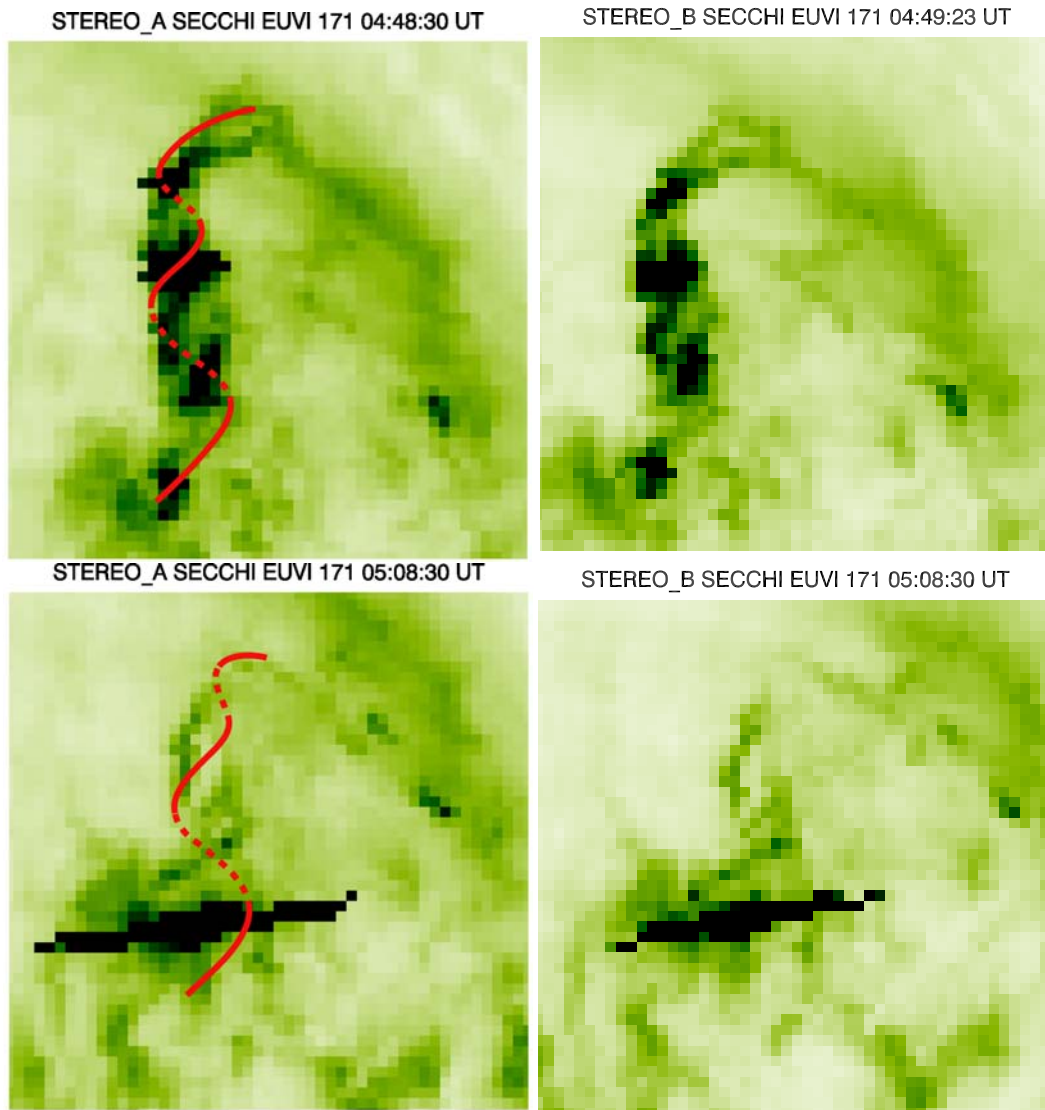


Figure 5.7: STEREO/SECCHI A and B images of the twisted helical structure. The secondary helical twist with approximately two turns (indicated by red line) has been activated on 05:08 UT just before the maximum of M8.9/3B class flare (bottom panel). The top-left panel shows, for the comparison, three turns (indicated by red line) during the activation of the first helical twist as estimated by Srivastava *et al.* (2010). The size of each image is $80'' \times 80''$.

sunspot. Activation of this twist is also clearly visible in SOT images. This structure seems to be moving to the north of the sunspot. The twist angle can be estimated by measuring the number of turns in the twisted helical structure. One turn corresponds to the twist angle of 2.0π . It is evident from STEREO/SECCHI images (see Figure 5.7) that the secondary helical twisted structure at 05:08 UT show minimum of ≈ 2.0 turns, suggesting the total twist angle probably crosses the critical limit of 2.5π (*i.e.* the total twist angle is 4π). The flare brightening takes place in between a small positive and surrounding negative-polarity regions.

The rather small scale of the twisted coronal structures does not allow us to see differences in SECCHI/EUVI images of STEREO-A and STEREO-B spacecrafts with separation of only near 10° in June 2003 as it is able to do for more large scale erupting structures (Gissot et al. 2008; Liewer et al. 2009). Figure 5.7 shows enlarged images of the twisted structure obtained by both STEREO A and B spacecraft. The upper parts of the helix are aligned with visible coronal loops, while the bottom parts are assumed to keep the same pitch angle. According to this assumption, some two turns of the helix can be recognized especially within the secondary twisted structure (bottom panel of Figure 5.7). In fact it looks like a multiple-thread screw and it is difficult to follow one particular thread through the whole flux rope length. Approximate conservation of the pitch angle can help to estimate the amount of the total twist. The primary helical twist occurred during 04:42–04:51 UT, given in the upper panel for comparison with the secondary helical-twisted structure. The primary helical twist presented here for comparison is found to be the triggering mechanism of the B5.0 class flare during 04:40–04:51 UT (Srivastava et al., 2010).

We have also analyzed XRT/Hinode Ti-Poly temporal image data of the same active region. We use the standard methods to calibrate the data and correct the orbital variations to see the co-spatial X-ray brightening of the flare in this loop (Shimizu et al., 2007). The XRT images co-aligned with the TRACE, are presented during 04:40–04:54 UT in Figure 5.8. Sudden brightening and enhancement of soft X-ray flux in the loop has also been observed around 04:49 UT by XRT/Hinode. The loop is twisted during the full span of the B5.0 flare duration, however, the twist maximizes with the flare around $\sim 04:48$ – $04:49$ UT. The right-handed (positive) twist is also clearly visible at 04:50 UT in the XRT temporal

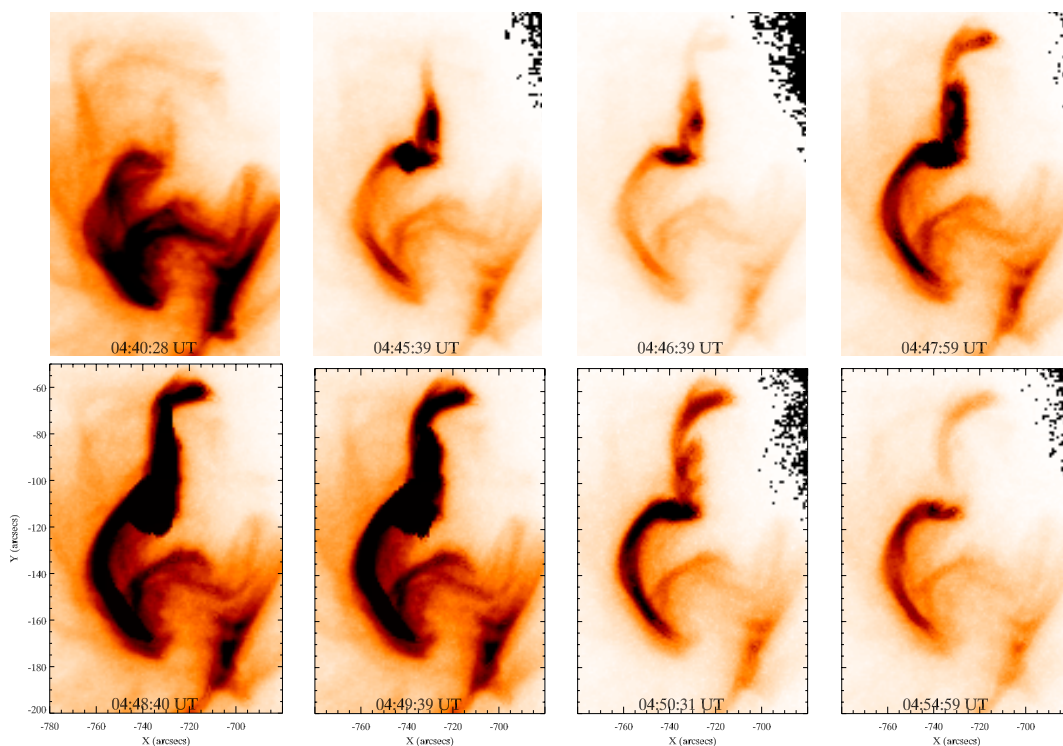


Figure 5.8: Time sequence of HINODE/XRT images of the twisted flaring loop and partial FOV of AR 10960 during 04:40 UT and 04:54 UT on 04 June, 2007. The Hinode/XRT images are co-aligned with TRACE images.

image, which confirms the nature of twist as visible in the EUV 171 Å image from TRACE. Thus, the double structure of loop top in 171 Å coincides to the enhancement of soft X-ray flux.

5.3 Sunspot Evolution in SOHO/MDI and SOT/G Band Images

We use SOHO/MDI observations to see the magnetic-field evolution during the flare. The size of each image is 1024×1024 ($2''$ per pixel resolution) with a cadence of 96 minute (Scherrer et al., 1995). We use the standard SolarSoft library to correct the differential rotation and analyze the magnetograms. Figure 5.9 displays the sequence of MDI images on 03 and 04 June 2007. The MDI movie

5.3 Sunspot Evolution in SOHO/MDI and SOT/G Band Images

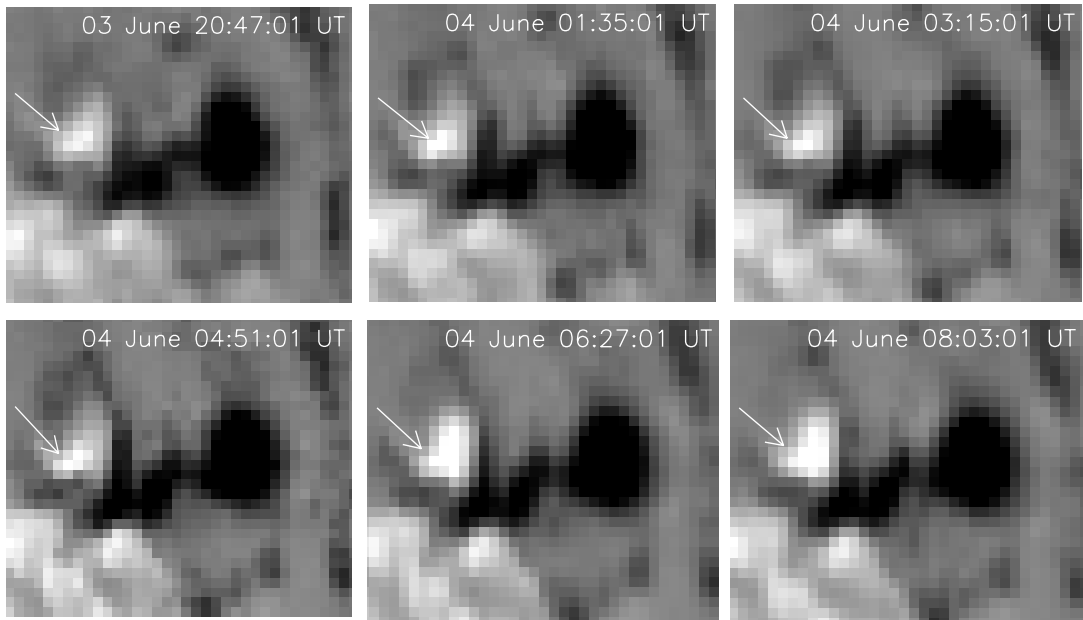


Figure 5.9: The selected SOHO/MDI images of the flare site. The arrow indicates the evolution of positive magnetic-flux region before and after the flare activity. The size of each image is $70'' \times 60''$.

and time-sequence images reveal the interesting features, which show the considerable changes (area enhancement) in the positive-polarity sunspot during the decay phase of M-class flare event.

Figure 5.10 displays the selected SOT/G-band images which show the partial field of view of the active region containing the same positive-polarity sunspot as marked by arrow. This sunspot also shown by the red contour in Figure 5.6, which is associated with successive activation of the helical twists. The evolution of the small positive-polarity sunspot initially shows the highly twisted penumbral filaments in the counterclockwise direction (*i.e.* sunspot rotation is clockwise) well before the flare activity (indicated by arrow) as the active region lies in the southern hemisphere. This secondary twist at the footpoint of the loop system associated with this sunspot may be responsible for the energy build-up process of M-class flare occurred in this active region. The brightening (two bright points) takes place at the opposite edges of the umbral part of this sunspot. Then, a secondary twisted helical structure rises up from the same site

5.3 Sunspot Evolution in SOHO/MDI and SOT/G Band Images

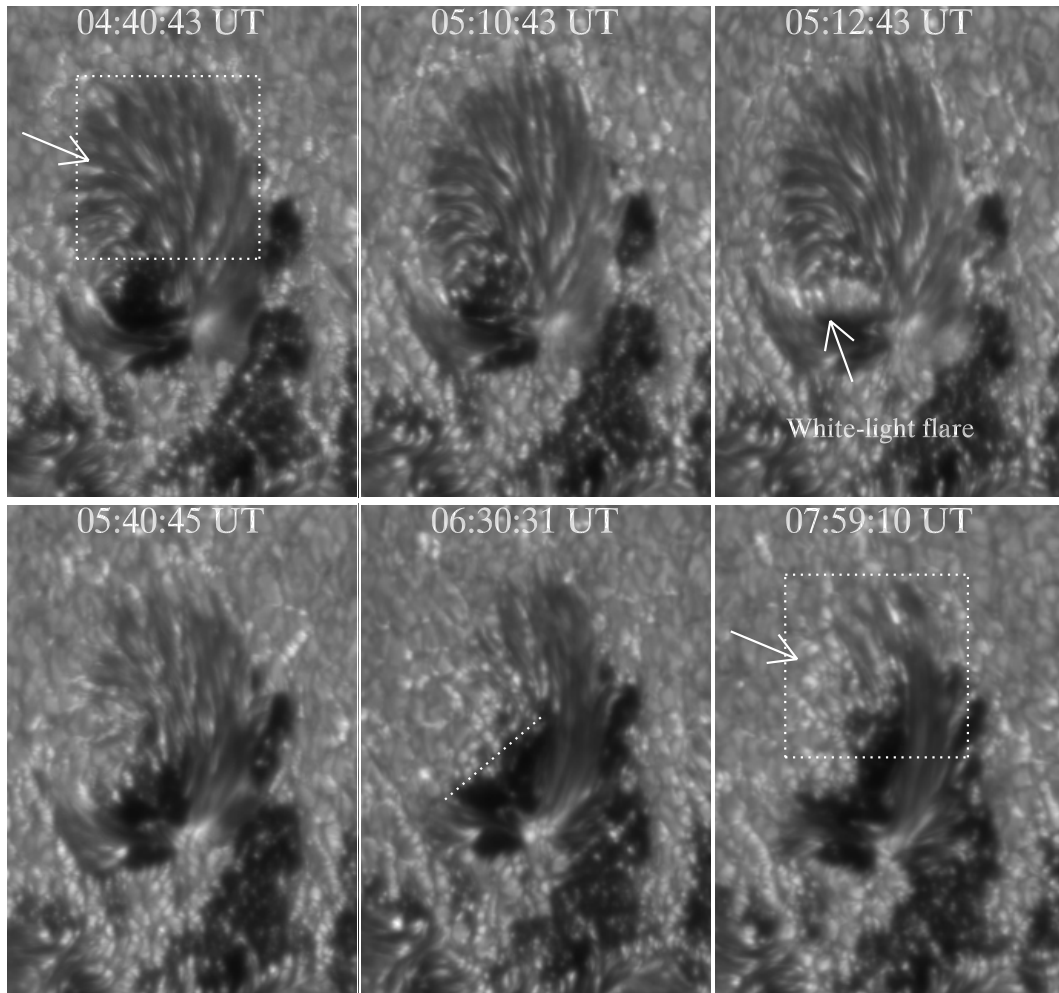


Figure 5.10: The selected SOT/G-band images (4305 \AA) showing the evolution of the positive-polarity sunspot (before, during and after the M8.9/3B class flare). The dotted line and boxes reveal the orientation change and disappearance of twisted penumbral filaments respectively after the flare event. The size of each image is $25'' \times 35''$.

5.3 Sunspot Evolution in SOHO/MDI and SOT/G Band Images

(refer to Section 2.1). The image observed at 05:12 UT shows the white-light flare at the sunspot (indicated by arrow) during its impulsive phase. During the decay phase of the M-class flare, we notice several changes in the sunspot: *i*) disappearance of twisted penumbral filaments at the northern part of the sunspot (indicated by boxes). *ii*) orientation change in the sunspot (shown by dotted line). Before the initiation of the flare activity, sunspot shows spherical shape with counter-clockwise penumbral filaments, whereas after the flare activity it shows the elongated shape with penumbral changes (i.e decay of penumbral filaments). We have estimated the projected height (elongation) *vs.* time profile of the twisted magnetic structures observed in TRACE and SECCHI measurements, following the apex of the structure from the centre of the active region and plotted against soft X-ray flux measurements (Figure 5.11, top). It is evident from the plot that the flare is closely associated with the activation and rising motion of the twisted magnetic structures/flux ropes. The co-temporal enhancement of the GOES soft X-ray flux profile with the increase of the projected height of the primary helical structure validate the findings of [Srivastava et al. \(2010\)](#) that this twist was probably responsible for B5.0 class flare. While again the co-temporal enhancement of the soft X-ray flux profile with the increase of the height of the secondary, helical twisted structure shows its association with the M8.9/3B flare event that occurred in AR 10960. We have used the SOT/blue continuum (4504 Å) images for quantitative estimation of penumbral and umbral changes during the flare event. We selected a box of 16"×22" covering the sunspot of delta configuration. We extracted the total counts less than 700 for umbral change and between 700–1400 for penumbral changes. For viewing the change in area of both umbra and penumra, we draw the umbral and penumbral boundaries using standard routines in IDL libraries and then extracted the total number of umbral and penumbral pixels of the sunspot. Figure 5.11 displays the temporal changes in umbral and penumbral intensity and area with respect to the soft X-ray flux profile. It is evident from the figure that there is a remarkable changes in umbral and penumbral structures. However, the rapid change in umbral portion at ≈05:12 UT is due to the flare that covers the sunspot umbral part. After the flare maximum, we observe considerable penumbral disappearance

5.3 Sunspot Evolution in SOHO/MDI and SOT/G Band Images

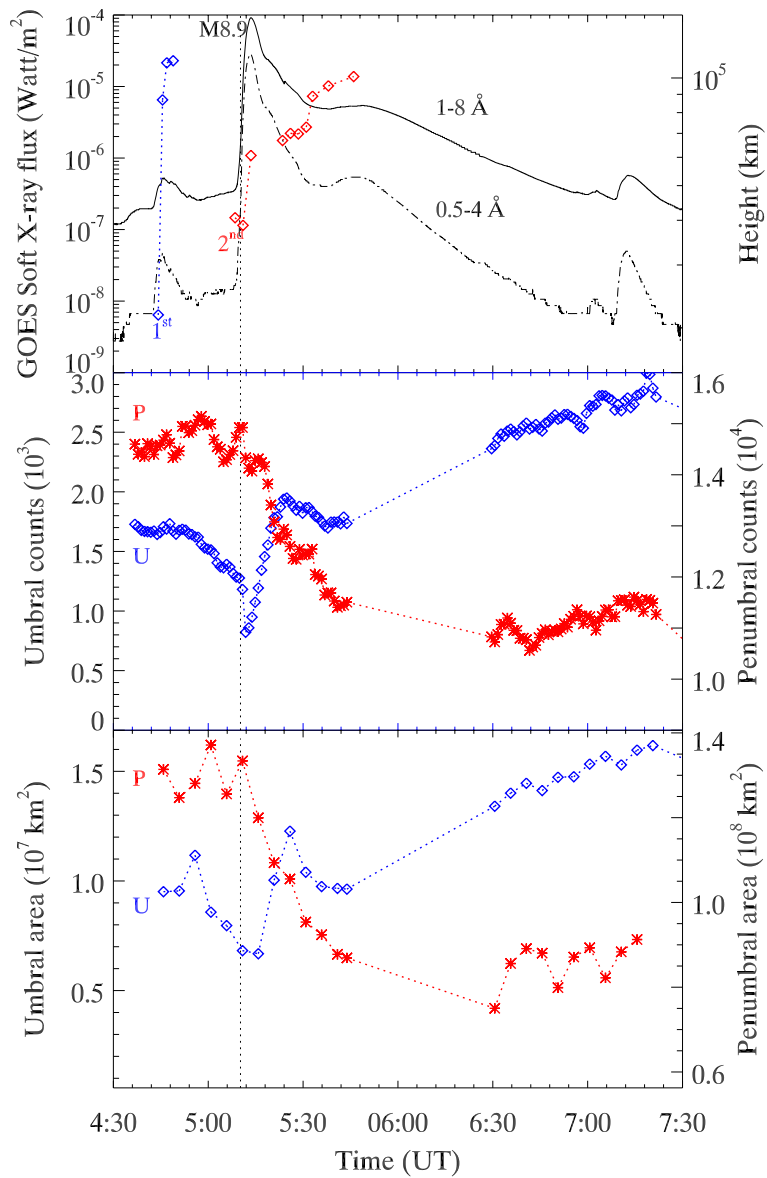


Figure 5.11: Top: Projected height (elongation) *vs.* time profiles of both twisting helical magnetic structures with soft X-ray flux profiles of the flares on 4 June 2007. This plot clearly indicates that the rise of magnetic structures is closely associated with the flare onset. Middle and bottom: Umbral and penumbral changes (indicated by “U” and “P” respectively) in intensity and area to show the link with soft X-ray flux profiles. It is evident from the plot that there are remarkable changes (umbral enhancement and penumbral decay) in both umbra and penumbra after the flare maximum.

5.3 Sunspot Evolution in SOHO/MDI and SOT/G Band Images

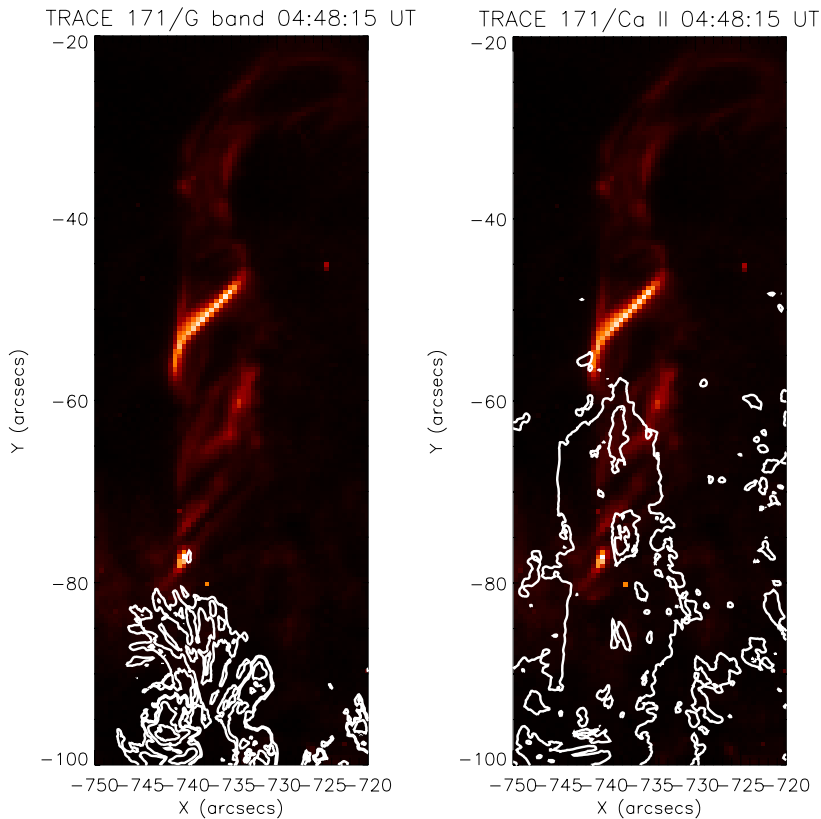


Figure 5.12: Partial FOV of TRACE 171 Å image on 04:48:15 UT at 04 June 2007, which shows the coronal loop segment with strong helical twist. The co-aligned SOT G-band (left panel) and Ca II (right panel) contours are overlaid on TRACE 171 Å image, which show the sunspot position and the chromospheric part of the loop respectively.

($\approx 35-40\%$) and enhancement ($\approx 45-50\%$) in the umbral area. This enhancement of the positive-polarity spot is evident in the SOHO/MDI magnetograms during the decay phase of the M-class flare (see Figure 5.9). This suggests that the magnetic field becomes more vertical from the initial horizontal configuration, which is in agreement with the previous studies (Liu et al., 2005; Wang et al., 2004). These changes suggest the loss of magnetic energy with sunspot evolution and that energy seems to be released in the form of flare thermal energy.

5.4 Kink Instability During B5.0 Class Flare

Figure 5.12 displays the partial field of view of TRACE 171 Å image on 04:48:15 UT at 04 June 2007, which shows the coronal loop segment with activated helical twist. The TRACE temporal image data of 1 minute cadence is calibrated and also co-aligned using Solar-Soft routines. The co-aligned SOT G-band (left panel) and Ca II (right panel) contours are overlaid on TRACE 171 Å image. The G-band contour shows the position of sunspot which probably is the source of helical twist, while the Ca II contour shows the chromospheric part of the loop segment. The coronal loop shown in this Figure exhibits a right-handed twist. Most clear image of twisted loop in TRACE 171 Å series is seen at 04:49:36 UT, therefore we use this frame for estimation of loop parameters.

The projected distance between loop footpoints is ~ 40 Mm. However, the real distance can be increased up to 50 Mm taking into account the projection effects. Using the ideal semi-torus form we may estimate the loop real length as

$$L = \pi R \approx 80 \text{ Mm}, \quad (5.1)$$

where R is the big radius of torus. The loop small radius at the middle of left side can be estimated as $a \approx 4$ Mm.

An important parameter of straight twisted tubes is

$$p = \frac{aB_z}{B_\phi}, \quad (5.2)$$

where B_z and B_ϕ are the longitudinal and azimuthal components of magnetic field, and $2\pi p$ is called as *pitch*. Then the pitch can be expressed by loop length and the number of turns over the tube length (N_{twist}) as

$$2\pi p = \frac{L}{N_{twist}}. \quad (5.3)$$

The total twist angle is then

$$\Phi = 2\pi N_{twist} = \frac{LB_\phi}{aB_z}. \quad (5.4)$$

At least, 3 different turns are seen along the left half length of the loop at 04:49:36 UT (see Figure 5.7). The right footpoint is not seen clearly, therefore

5.4 Kink Instability During B5.0 Class Flare

we can not estimate the number of turns there. However, the twist should be quasi-symmetric along the whole loop, therefore we suggest 3 more turns there. This gives the total twist angle as

$$\Phi \approx 12\pi. \quad (5.5)$$

This is a rather strong twist and therefore the loop could be unstable to kink instability, which eventually may lead to observed B-class flare. There may be a possibility of twist imbalance (Fan et al., 2009; Tian & Alexander, 2009) at the two ends of the observed loop. This is also evident from the Hinode/SOT WB full FOV image (Figure 5.10) that the positive polarity sunspot (anchoring point of loop's left footpoint) and negative polarity sunspot (anchoring point of loop's right footpoint) both exhibit imbalanced morphology, and probably imbalanced polarity strength also compared to each other (Figure 5.9). The loop's right footpoint and related arm are not visible in the TRACE images (or Hinode/XRT images) as they are very fainter. Both the footpoints of the loop are captured in the FOV of Hinode/SOT, however, the full loop is not captured by it. Therefore, the uncertainty arises in estimating the redistribution of the twist over the right footpoint of the loop as it is not visible in the TRACE, XRT, SOT/Ca II H images. Although the twist may be asymmetrically distributed in our observed loop, this asymmetric helicity (if any) does not mean that the twist will be inhomogeneous over the course of time (Fan et al., 2009). The inhomogeneous twist along the loop may be smoothed over Alfvén time. For our observed loop of length ~ 80 Mm and assuming the average coronal Alfvén speed ~ 1000 km/s, the Alfvén time ($t=L/V_A$) is estimated as ~ 80 s. This indicates that if any asymmetry arises in the twist distribution at both the halves of the observed loop, it will be smoothed within ~ 80 s. Therefore, our loop seems to possess the homogeneous twist during 04:40–04:51 UT, when B5.0 flare has been triggered.

Kink instability is caused due to the growth of $m = 1$ mode, which displaces the tube axis. General properties of classical kink instability are well studied. Kruskal-Shafranov instability criterion yields $\Phi > 2\pi$. Line tying of loop footpoints at the photospheric level generally increases the critical twist angle and the instability threshold becomes $\Phi > 2.5\pi$ (Hood & Priest, 1979). However, for the large aspect ratio (i.e. the ratio between loop length and radius), the critical

twist angle increases further (Baty, 2001). The approximate aspect ratio of our loop is $L/a \approx 20$, which is quite large. Normal mode analysis in the thin tube approximation (i.e. for large aspect ratio) gives the instability criterion as $a > 2p$ (Bennett et al., 1999; Dungey & Loughhead, 1954), which yields also large twist angle. In our loop parameters, this gives the critical twist angle of $\Phi \approx 12\pi$, which is very close to the observed one.

Numerical simulations of Török et al. (2004) have been performed for a curved loop taking into account the line-tying conditions. They used the twisted loop model of Titov & Démoulin (1999) and show that the loop is subject to ideal kink instability. They estimated the critical twist angle for different parameters of coronal loops. Török et al. (2004) solved the case of $R/a = 5$ and showed that the critical twist angle is $\Phi_c \approx 3.5$ for $R=110,000$ Mm, although these parameters are much larger comparing to our loop. On the other hand, the critical twist angle probably increases for smaller a (Baty, 2001). Unfortunately, Török et al. (2004) did not estimate a critical twist angle for loop parameters, which are close to our loop. However, general behaviour of the twisted loop could be similar to what they have shown in their paper. Namely, the double structure of loop top (Figure 3 of their paper) seems quite similar to what we have observed here (Figure 5.7).

5.5 Discussion

We study solar flare events (B5.0, M8.9/3B) on 4 June 2007 from NOAA AR 10960 using multiwavelength observations. It is shown that the small positive-polarity sunspot plays an important role in triggering this flare event, which lies at the centre of the active region and it is associated with the twisted flux tube/rope where successive helical twists have been activated before the flare event. MDI observations also reveal the considerable amount of enhancement in the area of the positive-polarity sunspot at the flare site during the decay phase of the M-class flare which is in agreement with the SOT/G-band observations. Another interesting point is that the positive-polarity sunspot seems to be highly sheared (it i.e. twisted penumbral filaments) before the flare activity. During the decay phase and after the flare event, the sunspot indicates major changes in its structure. It shows twisted penumbral filament disappearance in the northern

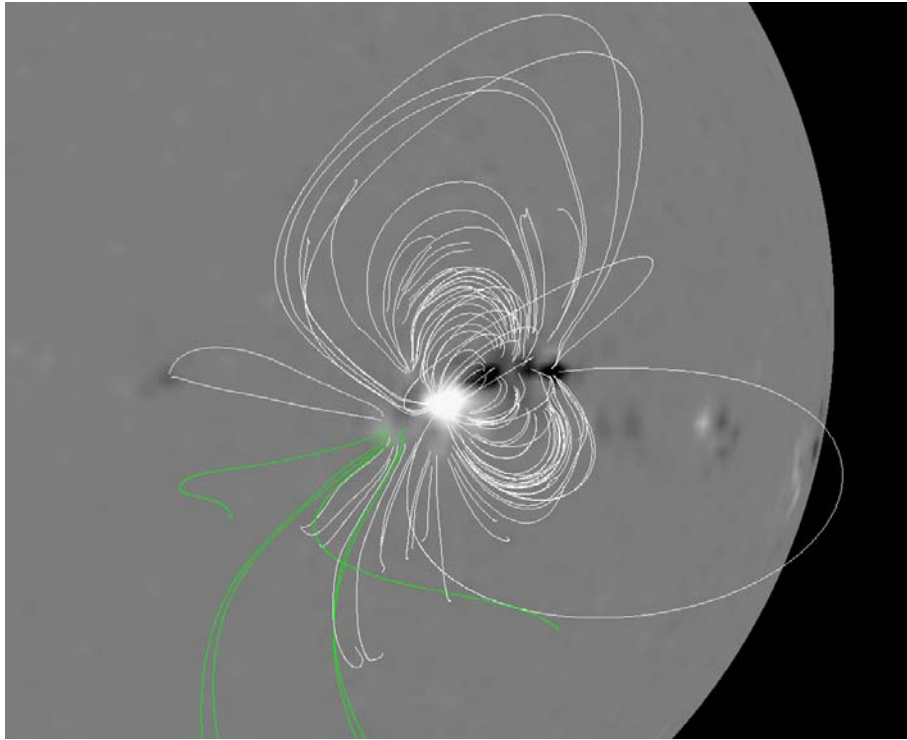


Figure 5.13: Potential field source surface (PFSS) extrapolation of the NOAA AR 10960 at 00:04 UT on 4 June 2007. White lines show the closed magnetic fields whereas green lines show the open fields.

part of the sunspot. Before the flare event, the penumbral structure was highly sheared showing anticlockwise orientation. After the flare event, it becomes more simplified with the loss of some area. This suggests the loss of twisted magnetic energy associated with the sunspot, which may be released in the form of flare thermal energy. For investigating the overlying magnetic field environment of this active region, we have used the potential-field source surface (PFSS) extrapolation (Altschuler & Newkirk, 1969; Schatten et al., 1969) before the flare event at 00:04 UT (see Figure 5.13). We rotate the SOHO/MDI image for our convenience to see the morphology of the magnetic field. However, the active region lies near the eastern limb during that time. The coronal magnetic field topology is on average in agreement with TRACE and SECCHI observations.

Figure 5.14 shows a schematic scenario of the event, which we have deduced from the multiwavelength analysis. EUV images reveal several flux tubes that

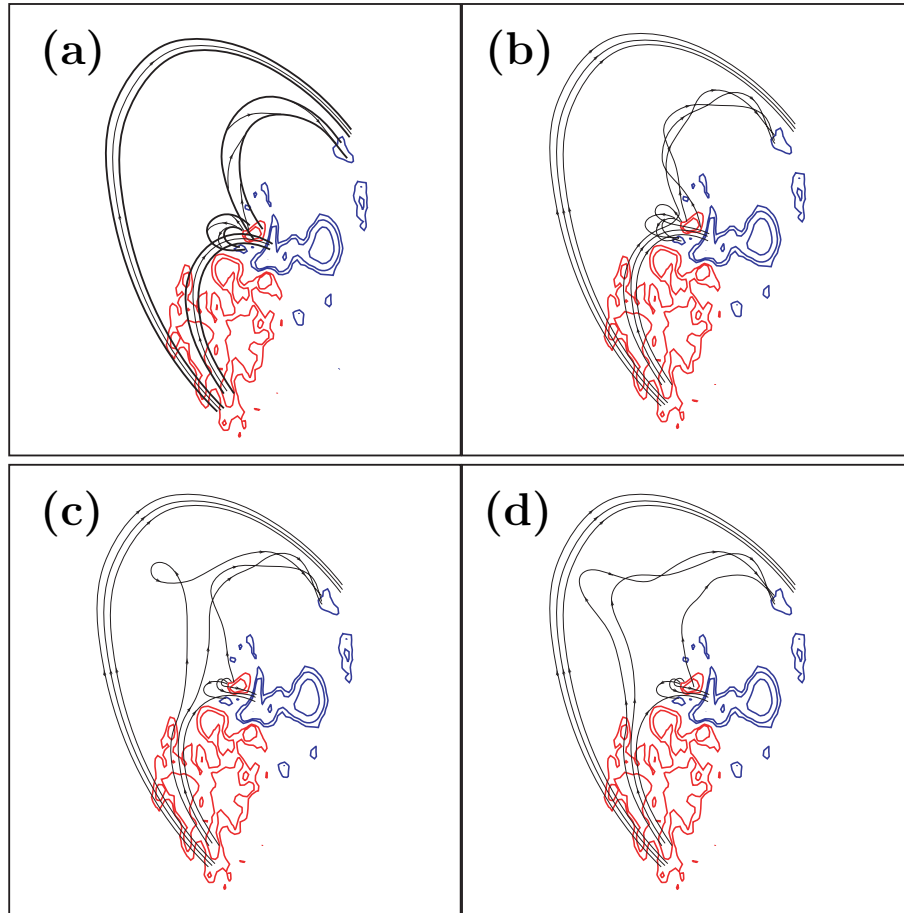


Figure 5.14: Schematic cartoons demonstrating the magnetic configuration of the active region before and during the flare event. Red contours show the positive-polarity sunspots whereas blue ones indicate the negative-polarity sunspots.

seem to play a major role in the progress of the flaring activity. There are large loops that straddle the whole active region. They connect the southern border of the large area of positive-polarity and small fragments of negative-polarity to the North of the major sunspots. Two smaller flux tubes originate from the vicinities of the footpoints of the large loop but end at the centre of the active region. The northern flux tube connects with the positive-polarity sunspot, while the southern flux tube connects with the negative-polarity magnetic flux concentrations nearby the sunspot. There is also a short flux tube connecting the dominant, positive polarity of the sunspot with the small portion of its umbra with opposite-polarity. Highly twisted structure of the sunspot penumbra indicates the presence of the twist within the short flux tube and the northern flux tube. Although, the most clear twisting of the northern flux tube becomes visible after its activation. The character of the brightening propagation allows to make conclusion that the twist within the northern flux tube does not appear during the flare activity, but existed long time before the flare event. Therefore, the positive-polarity sunspot is the footpoint of the flux rope. Some part of this magnetic flux tube/rope is connected with distant photospheric negative elements and some part is connected with the negative portion of the same umbra. After the activation, caused possibly by the emergence of a new magnetic flux which manifests itself in our region of interest as a growth of the area of positive-polarity (Figure 5.9), several field lines of the flux rope may reconnect with the field lines of the southern flux tube. As a result, a new, long flux tube is created as well as short loops also that connect the former central footpoints of reconnecting field lines (Figure 5.14b). This short loop corresponds to the post-flare loop system visible in SOT/Ca II H line images. Reconnected, long field lines move up and the twist propagates from the flux rope along the whole length of the flux tube. The field lines form a loop firstly or a noose (Figure 5.14c), and then make up a wide tangled structure (Figure 5.14d). It is most likely that the presence of the twist causes the field lines to move up, however they stop at some higher altitude. Therefore, the whole scenario may also resemble a failed flux-rope eruption (Filippov & Koutchmy, 2002; Ji et al., 2003). After the flare, the magnetic-field configuration becomes simplified. There is no longer a clear manifestation of the twisted magnetic field. Field lines of the positive-polarity sunspot become more connected to the nearby negative

polarities to the right of the sunspot. This possibly results in disappearance of penumbral filaments in the northeast part of the sunspot.

SOT and TRACE observations indicate the successive activation of helical, twisted flux bundles just above the same positive-polarity sunspot (at the edges of the twisted umbral structure) well before the flare event. As the secondary activation of the helical twist rises at 05:08 UT, the M-class flare intensity maximizes. This can be interpreted as the rising of twisted flux rope and its progressive reconnection with the surrounding opposite-polarity field region. The plasma is heated up, evaporated, and pumped into the two smaller loops (underlying a major loop system), which connect to the reconnection site with opposite magnetic polarities (refer to SECCHI images during the decay phase of the flare).

[Srivastava et al. \(2010\)](#) have observed the first activation of a highly (right-handedely) twisted flux tube in AR 10960 during the period 04:43–04:52 UT. They have estimated the length and the radius of the loop as $L \approx 80$ Mm and $a \approx 4.0$ Mm respectively, and also estimated total maximum twist angle as $\Phi \approx 12\pi$, by assuming quasi-symmetric distribution of the twist over the magnetic loop, which is much larger than the Kruskal–Shafranov instability criterion. They have found that right-handed twist may be asymmetrically distributed over the observed loop, which is smoothed with the Alfvénic time ≈ 80 seconds and possess a quasi-symmetric maximum twist. The detection of clear double structure of the loop top during 04:47–04:51 UT in TRACE 171 Å images, are found to be consistent with simulated kink instability in curved coronal loops ([Török et al., 2004](#)). They have suggested that the kink instability of this twisted magnetic loop triggered the B5.0 class solar flare, which also occurred between 04:40–04:51 UT in this active region. The co-spatial brightening in soft X-ray as observed by *Hinode*/XRT and the co-temporal occurrence of the right-handed twisting in the flux tube confirm the occurrence of the B5.0 flare during 04:40–04:51 UT probably due to the generation of the kink instability. We have also found the secondary twist of the same handedness (right-handed) in the magnetic flux tube at the same place as in the STEREO images at 05:08 UT (refer to Figure 5.7). Therefore, the activation of a second helical twist may also be associated with the kink instability in the active region which may trigger the M-class flare on 05:08 UT. In Figure 5.7, we present the twisted flux tube observed by TRACE, STEREO

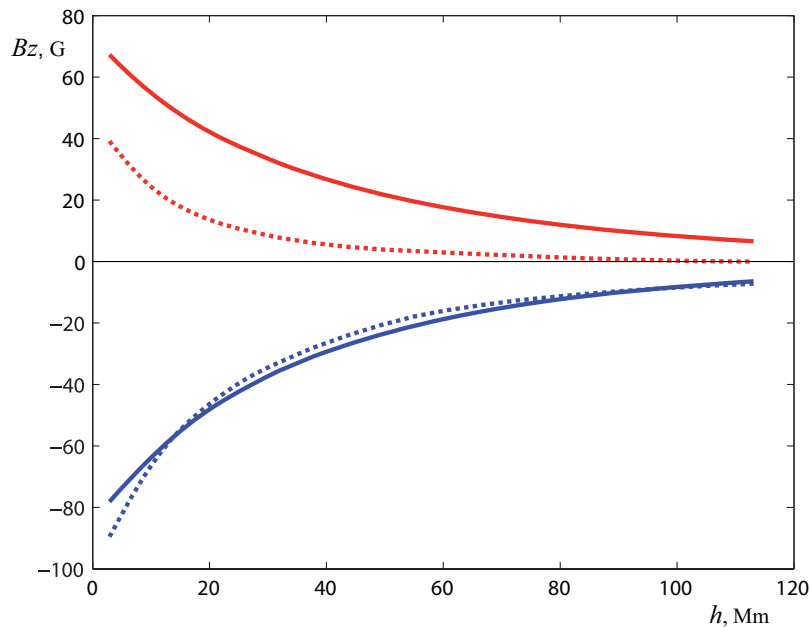


Figure 5.15: Dependence of average vertical magnetic field at different heights for the active regions NOAA 10501 (dotted curves) and NOAA 10960 (thick curves). Red and blue curves correspond respectively to the positive and negative magnetic field strength.

A and B. We find the activation of the secondary twist on the observed loop with same right handedness and \approx two turns in the flux tube (*i.e.* $\approx 4\pi$ twist) at first halve of the loop (see bottom panel of Figure 5.7). This is also crossing the threshold of minimum twist for the stability in the flux tube.

Ishii et al. (1998) also have reported that the flare productive magnetic shear is produced by the emergence of twisted magnetic flux bundle. Magnetic energy is stored in the twisted flux bundle, which is originally formed in the convection zone and released as flares in the course of the emergence of the twisted flux bundle above the photosphere. Our study provides the most likely signature of the successive activation of the helical twist in the flux tubes/ropes moving away from the active region. The location of the flare activity coincides with the area of the positive magnetic flux increase. Therefore, it may be concluded that the magnetic energy stored in the helical-twisted flux bundles is released as a flare

by reconnecting with the surrounding opposite-polarity field lines, when it moves away from AR. This active region produces M-class flare without any coronal mass ejections (CMEs) on 4 June 2007. According to analytical and numerical models of magnetic flux rope eruption, the behavior of the flux rope strongly depends on the rate of ambient magnetic field decrease with height (Forbes & Priest, 1995; Török & Kliem, 2005; Török et al., 2004; van Tend & Kuperus, 1978). If the magnetic field is strong enough at high altitude and has a significant horizontal component, the ascending motion of a flux rope can be stopped at a greater height and does not lead to formation of a CME. We compared the coronal potential magnetic field of the active region NOAA 10960 with the magnetic field of active region NOAA 10501 studied by Kumar et al. (2010), which produced a fast full-halo CME. Figure 5.15 shows the averaged vertical magnetic field [B_z] as a function of height [h] for both active regions. The area of about 220×240 Mm from MDI magnetograms was used as a boundary condition for numerical solving the Neumann external boundary-value problem (Filippov & Den, 2001; Schmidt, 1964). Magnetograms on 19 November 2003 and 7 June 2007 were chosen for the dates when the active regions were close to the center of the solar disk. The area 220×240 Mm covers all marked photospheric magnetic fields of the active regions. Positive and negative magnetic flux was calculated at different heights and then divided by the area occupied by this flux to obtain magnetic flux density or averaged magnetic-field strength. The dependence of average vertical magnetic field at different heights for the active regions NOAA 10501 (dotted curves) and NOAA 10960 (thick curves) is compared in this Figure 5.15 in which red and blue curves respectively correspond to the positive and negative magnetic field strength.

It is evident that magnetic field in the CME-productive AR falls more rapidly with height than in the other one and the magnetic flux is unbalanced. Positive flux is negligible above 30 Mm that is evidence of weak horizontal field needed to retard the flux rope ascending motion. In contrast, positive and negative fluxes in NOAA 10960 are nearly equal and decrease slowly and synchronously with height. This means the presence of large-scale, closed magnetic field that is able of supporting the flux-rope equilibrium at high altitude. As it was stressed by

Török & Kliem (2005) the decrease of the overlying field with height is a main factor in deciding whether kink instability leads to a confined event or to a CME.

Therefore, the large-scale destabilization of AR 10960 magnetic fields does not occur during this flare. Our multiwavelength and high-resolution observational results from recent spaceborne instruments reveal the dynamics of this active region and the associated M-class flare, which may be unique evidence for further theoretical modeling and observational studies of those active regions that produce solar flares but are the poor originators of CMEs. These observational evidences may also be further useful in the forecasting of the occurrence of large-scale solar eruptive phenomena from similar kinds of active regions. However, further statistical, multiwavelength studies should be carried out using forthcoming high-resolution space and ground-based observations to investigate the dynamics and mechanism respectively for multiple active regions and associated flares, which do not produce any large-scale CMEs. These studies may be useful to find the detailed physical scenario and dynamics of such unique active regions.

5.6 Conclusions

We find multiwavelength evidence of the successive activation of helical twists that may help in the energy build-up process at the flare site. The built energy is released later in the form of M-class flare after secondary activation of this critical twist in the flux tube/rope and its reconnection with neighbouring opposite fields. The main conclusions of this study may be summarized as:

i). We report the dynamics of a single positive-polarity sunspot having twisted penumbral filament structure and successive activation of twisted helical magnetic structures.

ii). The activation of two helical structures/ropes played an important role in destabilizing the field lines and in triggering the flare. The twist in the secondary magnetic structures crosses the threshold limit ($2.5-3.5\pi$), which probably produces the kink instability in this structure. The energy-release site of the M-class flare *i.e.* at the center of the AR, coincides with the activated twisted magnetic structures. Ishii et al. (1998) pointed out that the successive emergence of helical

flux bundles plays crucial role in triggering flares and showed it by a schematic cartoon, but here we provide the observational evidence of the same.

iii). The M-class flare shows agreement with the quadrupolar (closed-closed) reconnection model (breakout) between two closed field lines ([Antiochos, 1998b](#)). The asymmetric evolution is driven by footpoint shearing of one side arcade, where reconnection between the sheared arcade and the neighboring (unsheared) flux system triggers the flare. As the twisted magnetic structure moves away from the reconnection site, the flare intensity increases and reaches to maximum. This reveals the progressive reconnection of the twisted magnetic structure with the surrounding opposite-polarity fields.

iv). Penumbral disappearance during the decay phase and after of the flare event suggests that the magnetic-field structure to becomes more vertical. This indicates that the magnetic field changes from a highly inclined to an almost vertical configuration during the decay phase of the flare (just after the flare maximum), *i.e.* part of penumbral magnetic field is converted into umbral fields. Our results are in agreement with previous studies ([Liu et al., 2005](#); [Wang et al., 2004](#)).

v). The decrease of the overlying field with height is a main factor in deciding whether the kink instability leads to a confined event or to a CME ([Török & Kliem, 2005](#)). In AR 10960, the slow variation of vertical component of the magnetic field with height is found to be the most likely the cause for the failed eruption during M-class flare.

Chapter 6

Evidence of Solar Flare Triggering Due to Loop-Loop Interaction Caused by Footpoint Shear-Motion

6.1 Introduction

¹A solar flare is a sudden explosion in the solar atmosphere during which the magnetic energy (stored in the twisted and sheared magnetic fields as well as in the current layers between interacting fields) is released in the form of kinetic energy of rapidly moving plasma, accelerated particles and the thermal energy to heat-up the ambient plasma. This primary release of energy takes place in the corona and is accompanied by fast directed ejections (jets) of plasma, powerful flows of heat and accelerated particles. They interact with the chromosphere and photosphere thus creating an extremely rich picture of secondary physical processes observed as a solar flare.

It is generally believed and well supported by observations that magnetic reconnection is the key effect which plays the crucial role in annihilating the complex magnetic field structures and corresponding energy release. The solar

¹Research presented in this chapter is in press by [Kumar et al. \(2010b\)](#), APJ.

flares are mainly distinguished in two categories, e.g., the confined and eruptive flares, which are usually triggered respectively in the closed and open morphology of overlying magnetic fields. The instabilities generated in the complex magnetic fields may be one of the most probable causes to drive/trigger the solar flares after the reconnection of unstable flux tubes with the neighbourhood field configuration. The emergence of unstable and helical twisted structures can trigger the flares followed by an eruption (Liu et al. 2008, 2007; and references cited there). However, the activation of twisted helical magnetic structures may also play a crucial role in the flare energy build-up and their initiation with failed eruption depending upon the surrounding magnetic field environment (Kumar et al. 2010a, Srivastava et al. 2010 and references cited there).

Solar coronal loops may be considered as the current ($\lesssim 10^{12}$ amp.) carrying conductors. Two current carrying conductors possess net attractive force if both have resultant currents in the same direction or resultant magnetic fields in the opposite direction depending upon their orientation with each other. Collisions between current carrying loops are considered as a cause of some solar flares (Sakai & de Jager, 1996). Based on the loop orientations and size of the interaction region, the current carrying loop interactions are classified into three categories: (a) 1-D coalescence (I-type), (b) 2-D coalescence (Y-type), and (c) 3-D coalescence (X-type). The theoretical model of Gold & Hoyle (1960) firstly explains the flare triggering caused by interacting current carrying loops. However, it is not necessary that the field lines should be anti-parallel for the interaction of two current carrying conductors. There may be other mechanisms, e.g., footpoint shear motion and rotation, which can also destabilize the loop-system to trigger the flare and eruption. Stronger shear has more probability for the initiation of the solar flares and related eruptions (e.g., Tan et al. 2009 and references cited there). Yokoh is also observed some of the flaring events which show three types of loop interaction (I, Y and X-type). In the above mentioned interactions, the 3-D X-type reconnection due to coalescence is the most realistic scenario in the active regions. The necessary condition for 3-D X-type interaction is that the length of the interaction region (L) should be comparable to the loop diameter (R) (Sakai & de Jager, 1989).

[Hanaoka \(1996\)](#) has found evidence of the emergence of a small loop near one of the footpoints of a pre-existing large coronal loop using observations of various instruments including Yohkoh. The interaction of this loop with the larger loop causes flares, microflares and jets. [Liu et al. \(1998\)](#) have also observed the flare triggering by the I-type interaction of loop-systems. [Falewicz & Rudawy \(1999\)](#) have shown the flare energy release caused by two successive X-type interaction of an expanding loop with two high-lying and nearly parallel loop-systems. Furthermore, [Pohjolainen \(2003\)](#) has also studied the series of flares from AR 8996 on 18-20 May, 2000 and provided the evidence of flare triggering due to loop-loop interaction with the observation of moving magnetic features around the sunspot region. Several authors have reported the loop-loop interaction as a cause of solar flares. However, further multiwavelength studies are needed to understand the flare triggering mechanism due to loop-loop interaction, and its responses in the various layers of the solar atmosphere. In spite of the loop-loop interaction, the flare triggering followed by solar eruptions (e.g., coronal mass ejection) can also be caused by the interaction of filaments system due to sunspot rotation (e.g., [Kumar et al. 2010](#) and references cited there). We know that the interacting current loops are not located in the vacuum or isolating medium, but they are lying in the highly-conducting plasma penetrated by frozen-in magnetic fields in the solar corona. From the beginning of the evolution of a current carrying loop-system, every change in the current carrying loop-system generates currents in the surrounding plasma and magnetic field. Therefore, we have to take into account an interaction not only between the loops but also with these new currents, in particular with screening current layers between the loops. Moreover, the frozen-in magnetic fields of an active region or an activity complex are typically strong in the corona and have their specific topology determined by the photospheric sources. [Henoux & Somov \(1987\)](#) were the first to show that these effects are essential and must be considered in terms of magnetic reconnection of field-aligned electric currents (see Section 6.2.4). On the other hand, if there were no current loops related with a twist of magnetic flux tubes at all, even in this case, three-dimensional reconnection between interacting magnetic fluxes gives such distribution of reconnected magnetic fluxes in the corona that two soft X-ray loops look like interacting with each other ([Gorbachev & Somov, 1989](#),

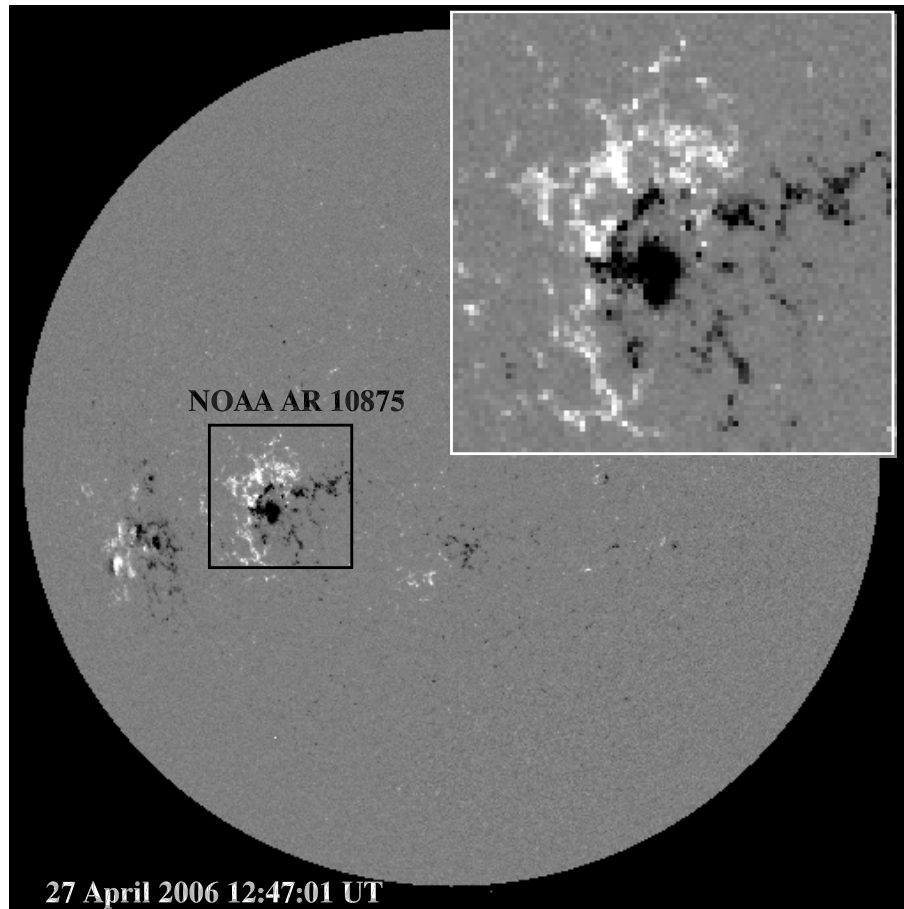


Figure 6.1: SOHO/MDI magnetogram showing the NOAA AR 10875 (in the box) at 12:47:01 UT on 27 April, 2006. The enlarged view of the active region is shown in the top-right corner of the image.

1990). That is the reason that the observations demonstrated such structures are usually considered as a direct evidence of the hypothesis of two interacting currents.

In this chapter, we present a multiwavelength study of M7.9/1N solar flare on 27 April, 2006 in AR NOAA 10875, which shows rare observational evidence of the coalescence and the interaction of two current carrying loops. We report a most likely multiwavelength signature of X-type interaction and coalescence instability in the active region which triggers the solar flare. In Section 6.2, we present multiwavelength observations of the event. We discuss our results and

conclusions in the last section.

6.2 Observations and Data

The active region NOAA 10875 was located at S10 E20 on 27 April, 2006, showing $\beta\gamma/\beta\gamma\delta$ magnetic configuration (Figure 6.1), and has produced M7.9/1N class solar flare. According to the GOES soft X-ray flux profile, the flare started at 15:45 UT, was at its maximum at 15:52 UT and ended at 15:58 UT. Figure 6.2 displays the flux profiles in the soft X-ray, soft X-ray derivative, hard X-ray and radio wavelengths. The flux derivative of soft X-ray matches well with the rise-up of hard X-ray flux profile. This implies that the accelerated electrons that produce the hard X-ray also heat the plasma that produces the soft X-ray, obeying the Neupert effect (Neupert, 1968). More exactly, this means that the impulsive heating of the solar atmosphere by accelerated electrons can dominate its heating by thermal fluxes from the high-temperature source of flare energy (see Chapter 2 in Somov, 1992). So there is a causal connection between the thermal and nonthermal flare emissions. Further, the radio flux profile shows the sharp rise-up with double peak structure mostly in 4.9 and 8.8 GHz at 15:47 UT, which shows the gyrosynchrotron emission generated by the accelerated electrons at the reconnection (i.e. loop-interaction) site.

6.2.1 GOES SXI and TRACE Observations

We have used GOES-SXI observations of the event (Hill et al., 2005; Pizzo et al., 2005). It is a broadband imager in the 6–60 Å bandpass that produces full-disk solar images with ~ 1 minute cadence. The images consist of 512 pixel \times 512 pixel with 5'' resolution. The FWHM of the telescope point-spread function is $\sim 10''$. A set of selectable thin-film entrance filters allows plasma temperature discrimination, i.e., open, three polyimide (thin, medium, and thick), and three beryllium (thin, medium, and thick). The open and polyimide filters are sensitive to the plasma below 2 MK. It is especially suitable for continuous tracking of coronal loops.

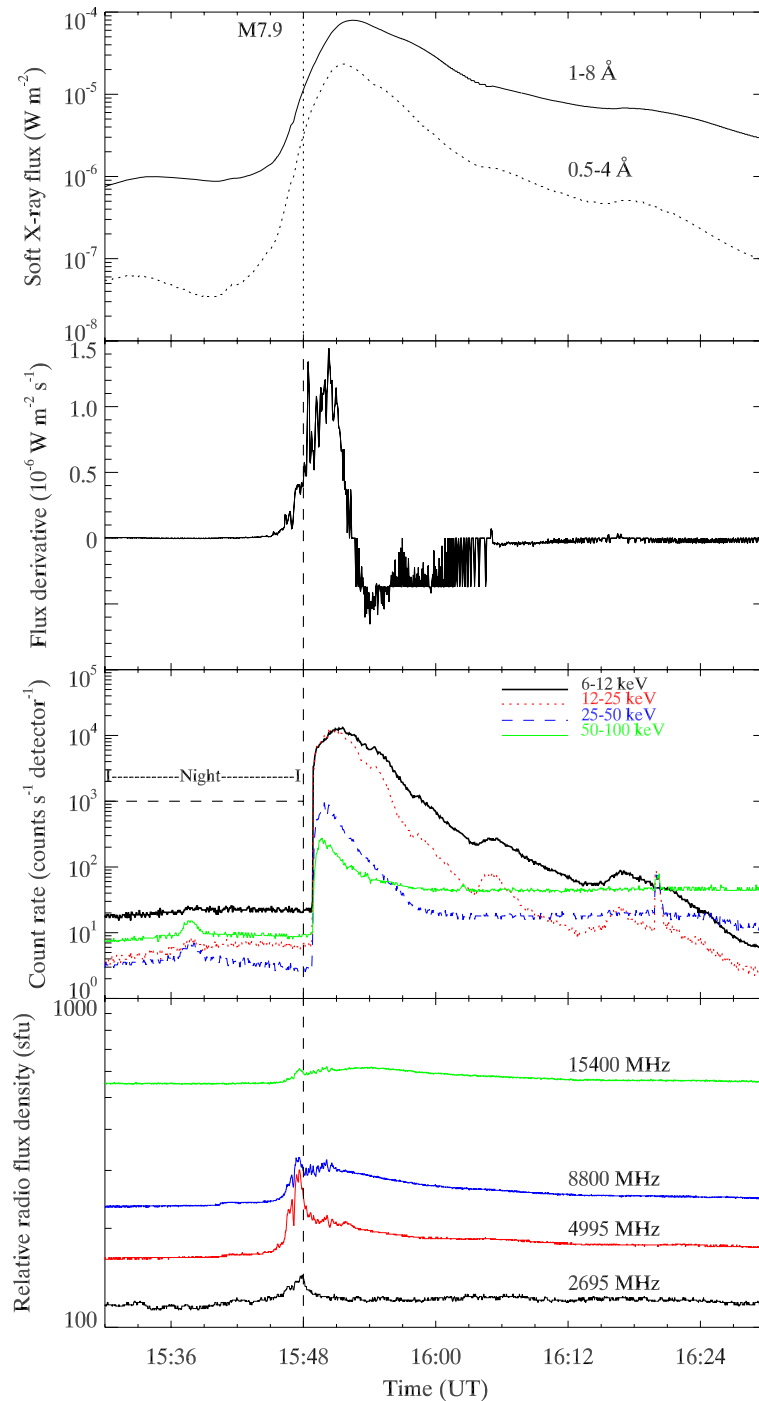


Figure 6.2: Soft X-ray flux, flux derivative, RHESSI and radio flux profiles for the M7.9 flare event on 27 April, 2006. The soft X-ray flux derivative matches well with the hard X-ray flux profile. This implies that the accelerated electrons that produce the hard-X-ray also heat the plasma that produces the soft X-ray (Neupert effect). The dotted line in the third panel indicates the RHESSI night time.

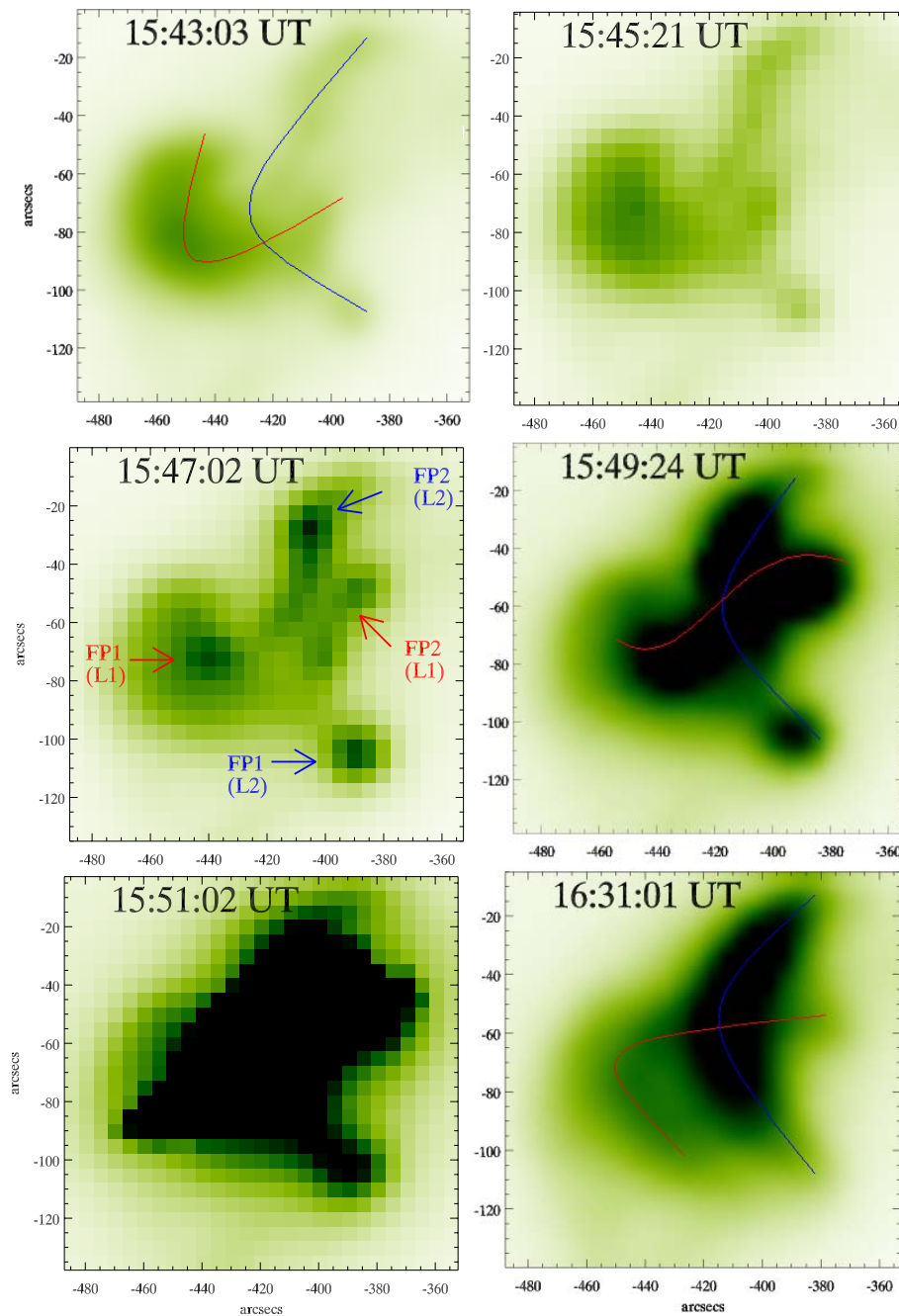


Figure 6.3: GOES Soft X-ray coronal negative images (6–60 Å) showing the flare evolution with the interaction of two coronal loops on 27 April, 2006. The upper left panel shows a lower loop system (blue) underlying a higher loop system (red). The lower loop first looks brighter during flare initiation. The middle left panel shows the corresponding footpoints of both interacting loops indicated by FP1 (L1) and FP2 (L1) for loop 1 and FP1 (L2) and FP2 (L2) for loop 2, respectively. The bottom left panels shows the flare maximum due to loop-loop interaction and the bottom right panel indicates the simplified 2 loops after the flare energy release.

Figure 6.3 displays the selected images of GOES SXI before and during the flare activity. Two loop systems have been observed before the flare initiation. One lower loop system (indicated by red line) is underlying a higher loop-system (blue). Initially, brightening starts in the lower loop during flare initiation at 15:43 UT. This loop becomes more brighter as the flare progresses. The four footpoints of both the loop-systems become evident at 15:47 UT mainly due to the precipitation of the accelerated electrons from the interaction or reconnection site. The corresponding footpoints of both interacting loops are indicated by FP1 (L1) and FP2 (L1) for loop 1 and FP1 (L2) and FP2 (L2) for loop 2, respectively. As the plasma is heated-up due to the dissipation of kinetic energy of the accelerated electrons from the reconnection site, chromospheric evaporation takes place and it fills the interacting loop-system in the corona and these loops look like as if they are crossing to each other. Now the X-type configuration becomes evident at 15:49 UT. The flare maximum takes place at 15:52 UT. After the interaction between the loops, the orientation of the lower loop has changed into a more relaxed state. The SXI image taken during the decay phase of the flare (at 16:31 UT) evidently shows the orientation change of the lower loop-system.

In this Figure, the red-pointed loop is marked in the upper-left panel as rooted somewhere close to roughly $X=-445''$, $Y=-50''$. However, in middle-left panel the left foot of this loop (marked FP1(L1)) has co-ordinates roughly $X=-440$, $Y=-70$. Therefore, the shift in the footpoint during the dynamical flare event is $\delta X = 5''$, $\delta Y = 20''$. Presumably, this apparent displacement of the footpoint FP1 (L1) may be due to two reasons:

(a) a displacement directed out from the photospheric neutral line, therefore, it is related to the motion of the flare ribbons in opposite directions. Such behavior is typical for the two-ribbon flares.

(b) a displacement directed parallel to the photospheric neutral line, which is related to the magnetic shear relaxation.

These two processes can cause jointly an increasing or decreasing distance between the footpoints. Investigations in the frame of a more detailed model should be done to interpret this feature. It is necessary to compare the kernel displacements observed during the flare with motions and evolution of magnetic fields in the photosphere before the flares (see Somov et al., 2002).

TRACE (Transition Region and Coronal Explorer) provides the opportunity to observe the Sun from chromosphere to corona (Handy et al., 1999). We have used TRACE 195 Å (Fe XII, $T \sim 1.5$ MK) and 1600 Å ($T \sim 4000$ -10000 K). The field of view for each image is 1024×1024 with $0.5''$ pixel⁻¹ resolution. The typical cadence for TRACE images is ~ 20 -60 sec. Figure 6.4

displays the selected TRACE 195 Å images during the flare activity. TRACE data have been calibrated and analyzed using standard routines in the solarsoft library². During the flare initiation, brightening was observed along both sides of the photospheric neutral line. Two bright sheared structures are observed at 15:46 UT. The image at 15:48 UT shows the loop-loop interaction and formation of an ‘X’ point in between the interacting loop-system. Many interacting small flux threads/tubes may be seen in this image. After the X-type interaction during the impulsive phase of the flare, it seems that loop threads are changing their footpoint connectivities. This is the signature of an ongoing reconnection process in the same global configuration of the active region. During 15:42–15:46 UT, the two interacting loops are visible in the soft X-ray GOES/SXI images, however, they are not visible in the TRACE images of the same duration. The GOES/SXI images represent the high temperature and high coronal part of the loop systems, while the TRACE images show the lower part of the loop systems joining the two brightened ribbons. In the pre-flare state, the GOES/SXI images show the loop segments visible due to the emission of the soft X-ray during loop-loop interaction, while at the same time the plasma at EUV temperature band is not uploaded in the lower segments of the two loops to brought them as visible as GOES/SXI images. However, near the flare maximum and even after the flare, the interacting loop systems are clearly evident in both X-ray as well as in EUV, and imply the presence of plasma at various temperatures. Since, we see the different segments of the interacting loop-systems in GOES/SXI and TRACE images. Therefore, they look like with a different orientations as the apex part may be more tilted compared to the lower segments. We can identify the four footpoints of the associated interacting two loop-systems.

During the interaction time, the thickness of the interaction region (indicated by arrows) reduces during the impulsive phase of the flare and it seems that the

²<http://hesperia.gsfc.nasa.gov/ssw/trace/>

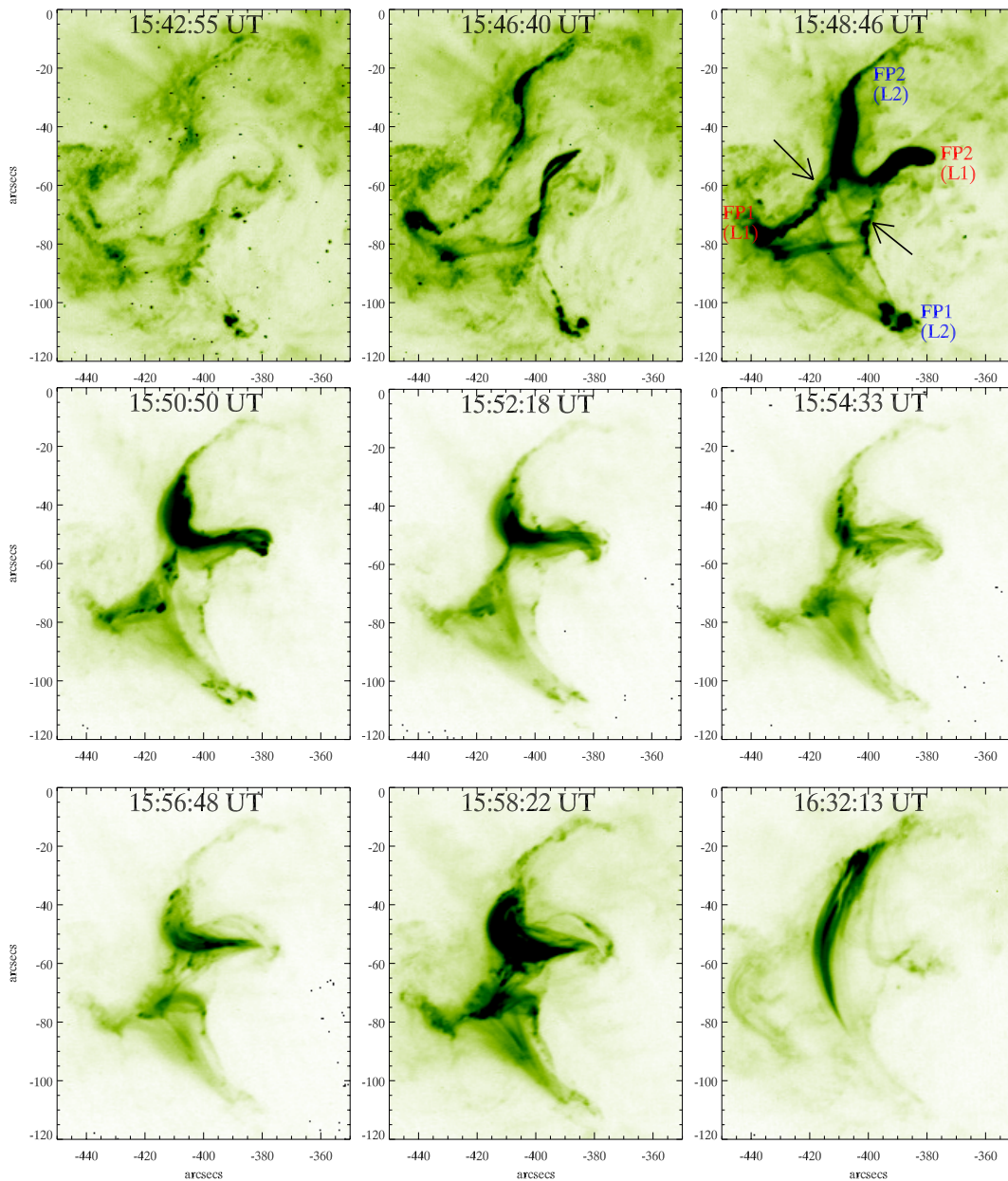


Figure 6.4: TRACE 195 Å negative images showing the flare evolution with the interaction of two coronal loops on 27 April, 2006. The upper and middle panels show approaching and interacting loops. The flare initiation takes place as the loops approach and maximizes at the time of interaction. The corresponding footpoints of the interacting loops are indicated by FP1 (L1) and FP2 (L1) for loop 1 and FP1 (L2) and FP2 (L2) for loop 2 respectively. The arrows indicate the interaction region/reconnection site. The bottom right panel shows the relaxation and orientation changes of the loops after interaction.

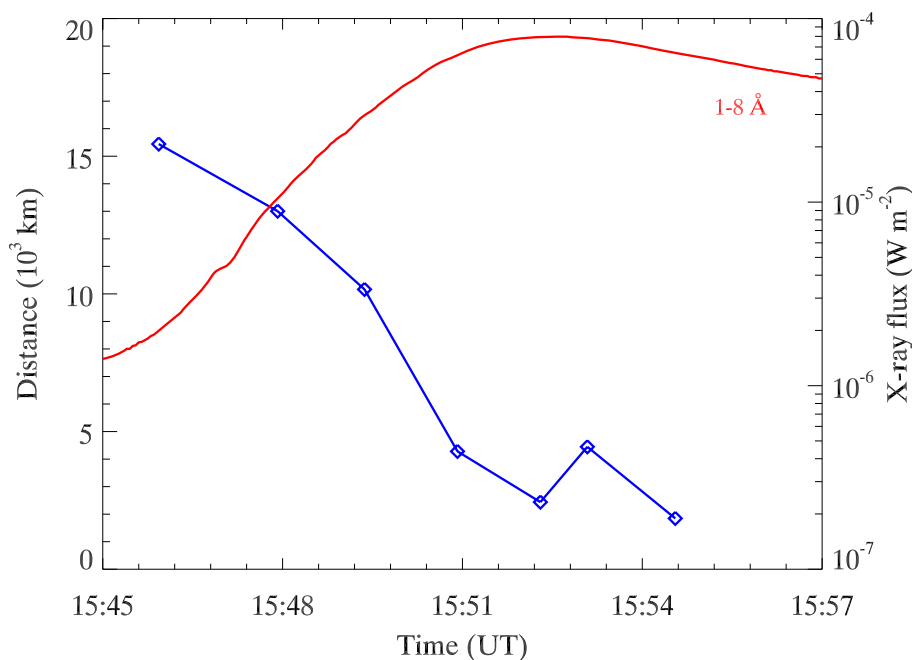


Figure 6.5: The thickness of interaction region shown by blue curve (estimated from TRACE 195 Å images) plotted against GOES soft X-ray flux profile (red curve). This plot reveals that as the thickness of interaction region decreases, the soft X-ray flux increases. This may be the most likely signature of ongoing reconnection at the site of loops-interaction. The typical converging speed of interacting region is $\sim 30 \text{ km s}^{-1}$.

orientation of the loops is changed during the flare maximum (refer to image at 15:50 UT and onwards images). During the sharp impulsive phase, the foot-points of the loop systems do not show significant changes (see TRACE movie). It means that the reconnection point is mostly fixed, i.e., the loops interaction site. The loop-system morphology becomes simple and relaxed during the decay phase of the flare as observed in SXI images (see SXI image at 16:31:01 UT). The thickness of the interaction region is plotted against the GOES soft X-ray flux profile (refer to Figure 6.5). This plot reveals that the X-ray flux rises up as the thickness of the interaction region decreases. This may be the most likely signature of ongoing reconnection at the loops interaction site. From the linear fit, the typical converging speed is estimated as $\sim 30 \text{ km s}^{-1}$. This speed may be related with the typical inflow speed as observed in other flares (Tsuneta et al.,

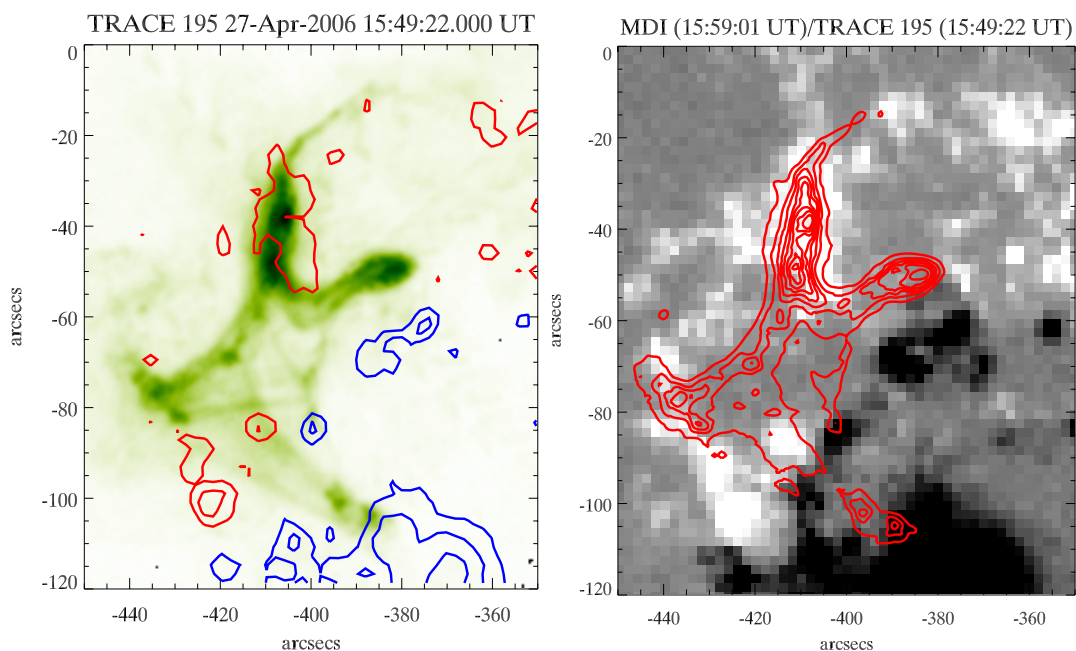


Figure 6.6: Left: MDI contours overlaid on TRACE 195 Å images during flare maximum (Blue contours indicate the negative whereas red contours show the positive polarity sunspots). The contour levels are ± 500 , ± 1000 , ± 2000 , ± 3000 G. Right: TRACE 195 Å contours overlaid on MDI magnetogram (Black=negative, White=positive).

1997; Yokoyama et al., 2001b).

We have overplotted MDI contours over TRACE 195 Å image and vice versa (refer to Figure 6.6). Left footpoints [FP1(L1) and FP2(L2)] of the associated loop-systems are anchored in positive polarity field regions whereas the right footpoints [FP1(L2) and FP2(L1)] are anchored in the negative polarity regions. For investigating the overlying magnetic field environment of this active region, we have used the potential field source surface (PFSS) extrapolation (Altschuler & Newkirk, 1969; Schatten et al., 1969) before the flare event at 00:05 UT (see Figure 6.7). The coronal magnetic field topology is on average in agreement with TRACE and SXI observations. Figure 6.8 displays the TRACE 1600 Å images during the flare event. Two ribbons, located on the both side of neutral line are observed at 15:44 UT. Left side ribbon shows the sheared ‘S’ shaped structure, whereas the ribbon at the right side shows simple structure.

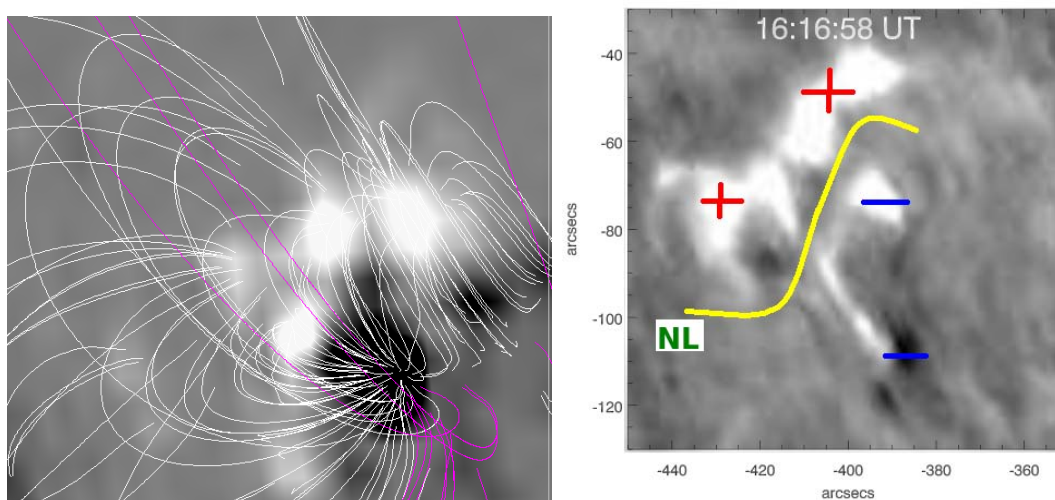


Figure 6.7: Left: PFSS (Potential Field Source Surface) extrapolations overlaid on MDI image at 00:05:00 UT on 27 April, 2006. Right: H α image during the decay phase of the flare showing flare ribbons on the both side of neutral line (NL), indicated by yellow line. The polarity at the location of flare ribbons is indicated by ‘+’ and ‘-’ symbols.

H α image observed at Meudon shows flare ribbons during the decay phase (at 16:16 UT) of the flare (refer to Figure 6.7). It shows mainly four bright kernels, which are the regions where most of the energy flux is concentrated i.e. the sites of particle precipitation. These are the footpoints of the corresponding reconnecting loop-system. These observations are in favour of loop-loop interaction mechanism.

6.2.2 Radio and RHESSI Observations

We have used Ondrejov dynamic radio spectrum data (2–4.5 GHz) during the flare (Jiricka et al., 1993; Jiříčka & Karlický, 2008). This radiospectrograph uses a 3-m dish and wide band horn antenna as primary feed. The time resolution is 10 ms and the frequency band is divided into 256 channels, which mean the frequency resolution is of about 10 MHz. Figure 6.9 (upper panel) displays the Ondrejov dynamic radio spectrum on 27 April, 2006 showing the intense DCIM radio burst during flare initiation. Moreover, there was no Type III burst during this time period (checked with Wind/WAVES spectrum). That means the open-

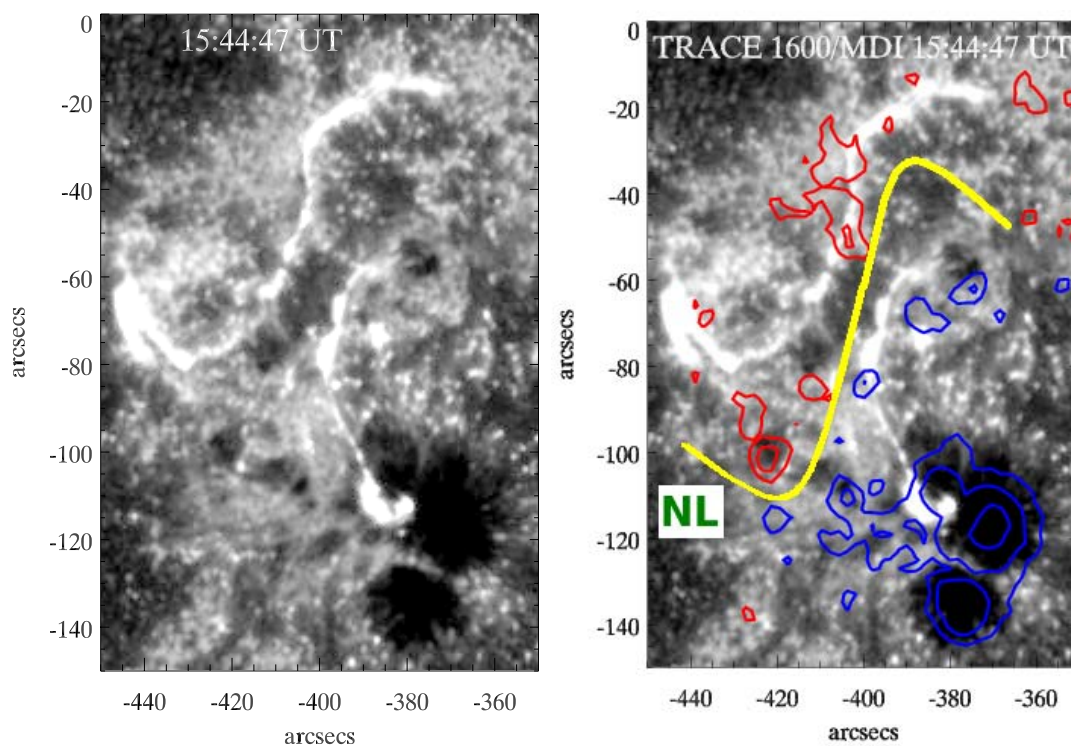


Figure 6.8: Left: TRACE 1600 Å images showing the morphology of flare ribbons during the flare. Right: SOHO/MDI magnetic field contours overlaid on TRACE 1600 Å image. Red one indicate the positive polarity whereas blue one show the negative polarity fields. The contour levels are $\pm 500, \pm 1000, \pm 2000, \pm 3000$ G. Ribbons are formed on the both sides of neutral line (NL), drawn by yellow color.

ing of field lines did not take place during the flare energy release (i.e. during reconnection). The DCIM burst starts in $\sim 2.5\text{--}3$ GHz frequency and continues upto 4.5 GHz. This frequency range covers the typical range of heights corresponding to reconnection site. The burst starts at 15:46 UT and continues upto 15:49 UT for the duration of ~ 3 minutes. The observed DCIM bursts reveal the signature of particle acceleration from the reconnection site during loop-loop interaction/coalescence.

The US Air Force operates four solar radio observatories at various locations around the world. These are collectively known as the Radio Solar Telescope Network or RSTN. Each observatory monitors solar radio emissions on 8 discrete

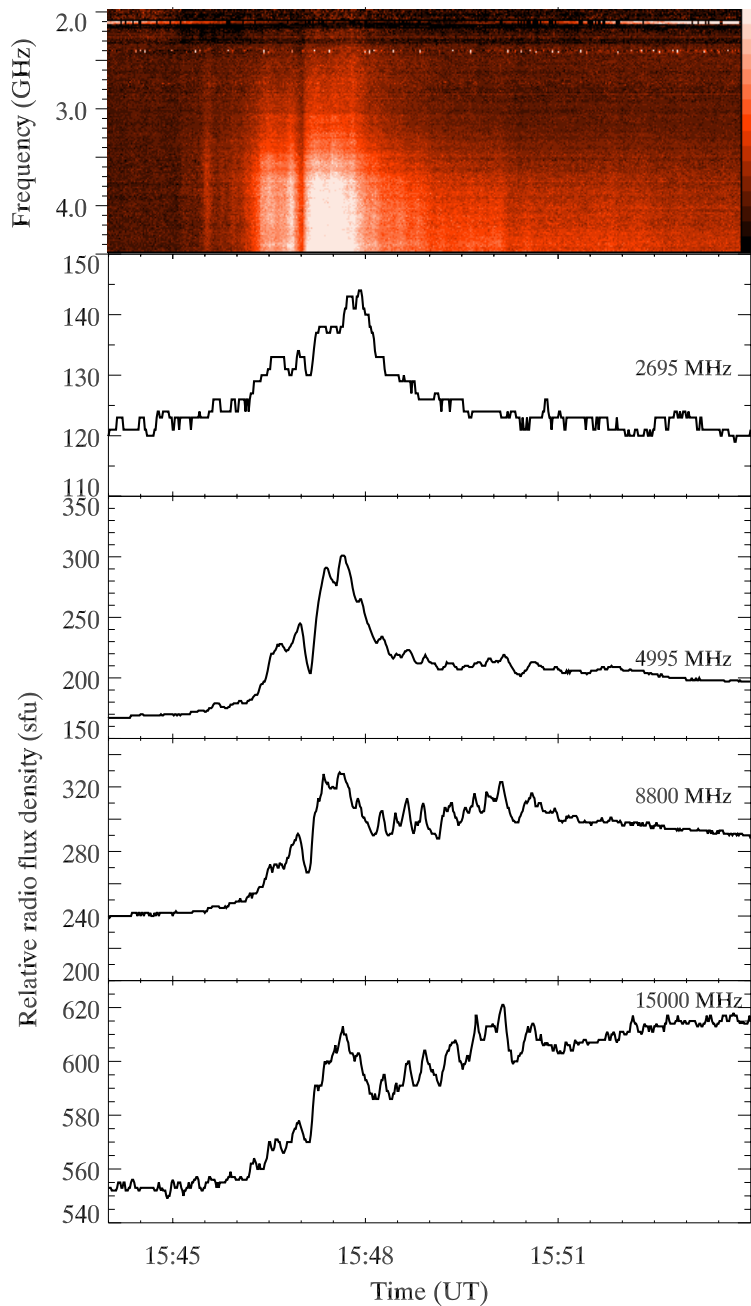


Figure 6.9: Top panel: Ondrejov dynamic radio spectrum on 27 April, 2006 showing the intense DCIM radio burst during flare initiation. Additionally, there was no Type III burst during this time period (checked with Wind/WAVES spectrum). That means the opening of field lines did not take place during the flare energy release (i.e. during reconnection). The observed DCIM burst is the signature of particle acceleration from the reconnection site during loop-loop interaction/coalescence. Bottom panel: RSTN 1 sec cadence radio flux profiles in 2.6, 4.9, 8.8 and 15 GHz frequencies observed at Sagamore-Hill station.

fixed frequencies (245, 410, 610, 1415, 2695, 4995, 8800 and 15400 MHz) as well as low frequency spectral emissions in the VHF band. We have used the radio flux data (1 sec cadence) from Sagamore Hill. We have selected four frequency bands, 2695, 4995, 8800 and 15000 MHz, which show significant variations. The radio burst is observed during $\sim 15:46\text{--}15:49$ UT (Figure 6.9, lower panels). The radio flux profiles in 4900 and 8800 MHz show double peak structures associated with the coalescence of loop-systems. It may be noted that second double peak structure is stronger in comparison to the first one, which shows the superthermal electrons generated the last double peak, accelerated from a higher amount of pre-accelerated electrons (Karlický & Jiříčka, 2003). After this burst, we observe the quasi-periodic oscillations specially in 4995, 8800 and 15400 MHz frequencies during $\sim 15:48\text{--}15:51$ UT for the duration of ~ 3 minutes, which may be attributed to modulations by MHD oscillations or nonlinear relaxational oscillations of wave particle interactions. Therefore, MHD waves can modulate the emission from trapped electrons (Aschwanden, 2004b).

The absence of Type III radio burst suggests the absence of opening of field lines during the reconnection process. Further, we do not see plasmoid ejection in soft X-ray images from the reconnection site. Therefore, the DCIM radio burst can not be interpreted as ejected plasmoid from the reconnection site. It should be noted that the burst starting frequency is $\sim 2.5\text{--}3$ GHz, which corresponds to the typical height of post flare loops and originates in magnetic reconnection regions (i.e. plasma density of $\sim 10^{10}\text{--}10^{11}$ cm $^{-3}$) (Aschwanden, 2004b). As this burst continuation can be seen upto 4.5 GHz in the radio spectrum and further in single frequencies radio flux profiles (i.e. in 2.6, 4.9, 8.8 and 15 GHz). Therefore, we interpret these emissions due to nonthermal electrons accelerated from the reconnection site along the soft X-ray loop systems. This may be confirmed by the soft X-ray image at 15:47:02 UT, which shows the four footpoints due to precipitated electrons during the time of radio burst.

The evolution of hard X-ray sources in two selected energy bands (12-25 and 25-50 keV) of RHESSI instrument is shown in Figure 6.10 and 6.11. These images have been reconstructed using PIXON method. In both the energy bands, the two separated loop-top sources are visible at 15:49 and 15:50 UT and then their

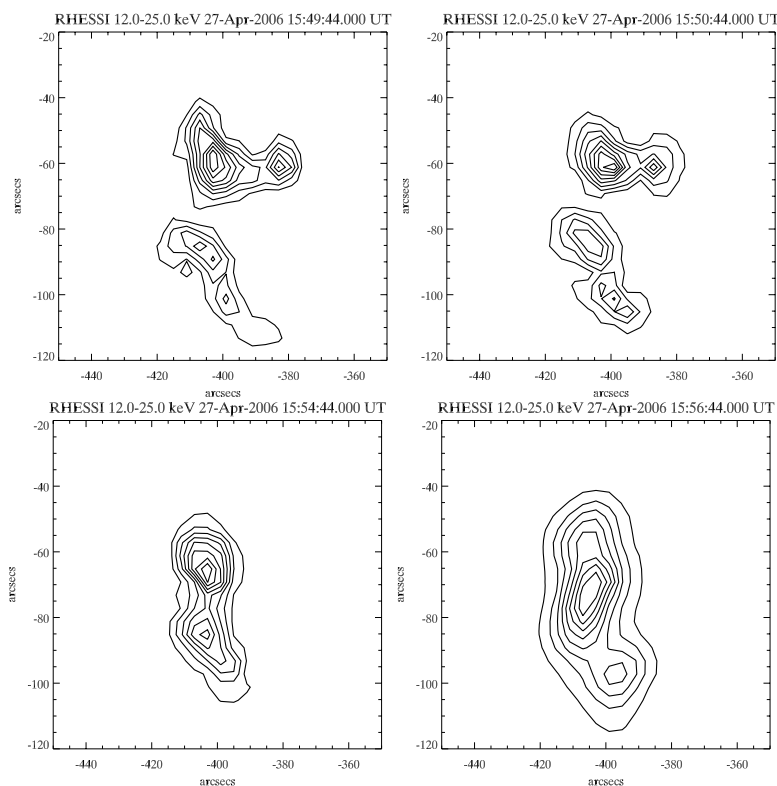


Figure 6.10: RHESSI images in 12-25 keV energy bands reconstructed with the PIXON algorithm (contour levels for each image are 40%, 60%, 80% and 95% of peak flux).

coalescence resulting into a single source (at 15:54 and 15:56 UT). These images also provide the evidence of two loops coalescence.

6.2.3 Evolution of Active Region

Figure 6.12 displays the selected images of TRACE white-light of active region on 27 April, 2006. The careful investigation of the TRACE movie reveals the linear/shear motion of small sunspot of negative polarity (indicated by blue contours) across the neutral line. We have made the time-distance plot to quantify the linear translational motion of the sunspot. From the linear fit to the data points, the speed of this motion is estimated as $\sim 0.2 \text{ km s}^{-1}$ (662 km h^{-1}) (see Figure 6.14). To identify the footpoint of the related loop-system anchored in this

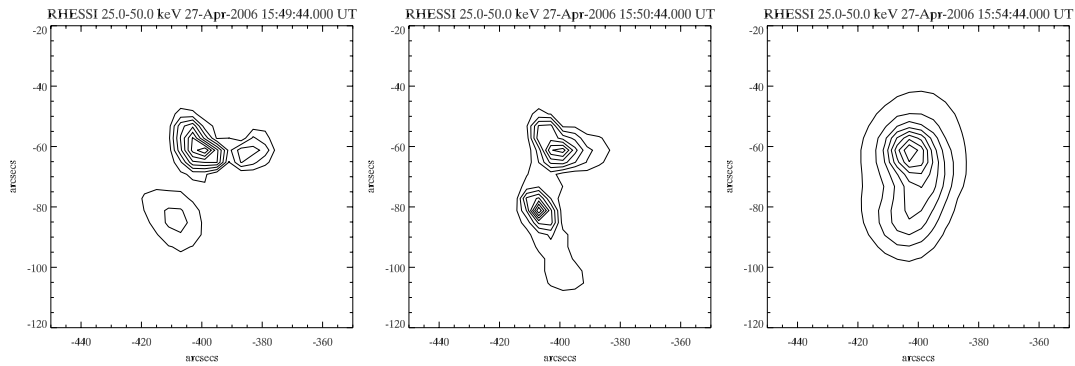


Figure 6.11: RHESSI images in 25-50 keV energy bands reconstructed with the PIXON algorithm (contour levels for each image are 40%, 60%, 80% and 95% of peak flux).

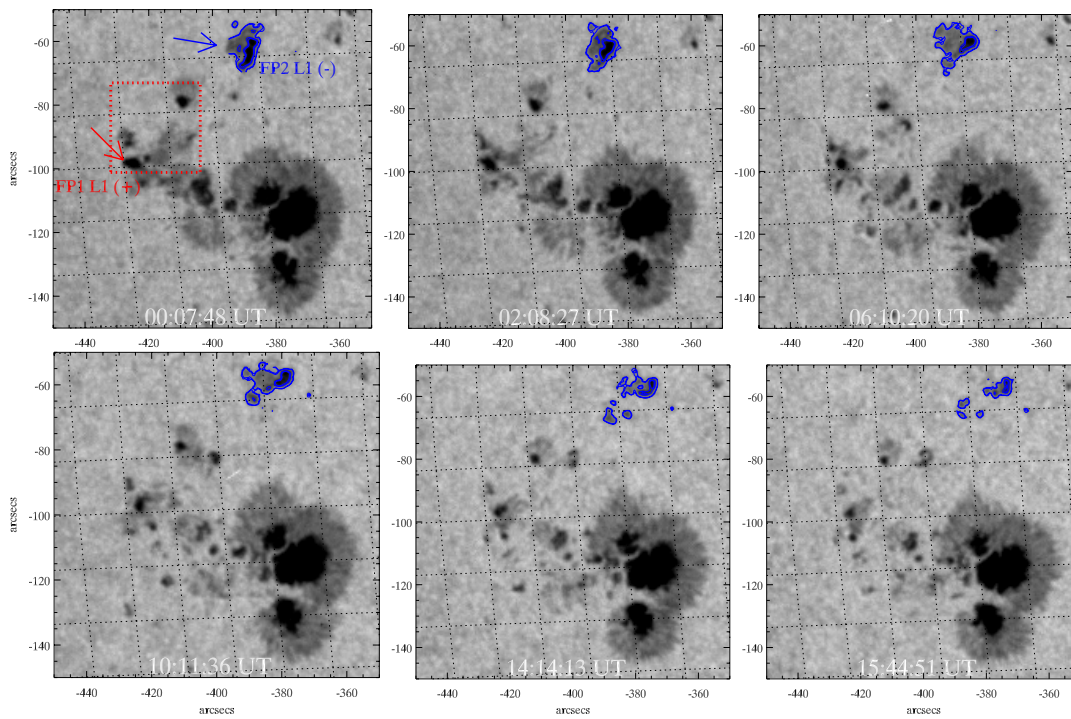


Figure 6.12: TRACE white-light images of the active region showing the linear/shear motion of negative polarity sunspot (indicated by blue contours). FP1 (red) and FP2 (blue) in the top first image indicate the ‘+ve’ and ‘-ve’ footpoints of the lower loop system respectively.

spot, we overlaid MDI and TRACE 195 Å contours over the white-light image (refer to Figure 6.13, left).

This image reveals that one footpoint of the loop-system is anchored in this spot. In order to view the photospheric horizontal flow pattern in and around the active region, we use the Fourier Local Correlation Tracking Technique (FLCT) on SOHO/MDI images. The FLCT method is described by Fisher & Welsch (2008). The main input parameters for this technique are, two images f_1 and f_2 , the pixel separation scale (Δs) and time separation (Δt), and a Gaussian window size scale (σ). This routine calculates the velocity (2D) by maximizing the cross-correlation of each image when weighted by the Gaussian window centered on each pixel location. In our study, we use the two SOHO/MDI frames at different times before the flare. After a careful investigation, a Gaussian window with a standard deviation of $15''$ was chosen. The right panel of Figure 6.13 displays the photospheric velocity map obtained from FLCT technique using SOHO/MDI magnetograms. The longest arrow corresponds to velocity of 0.291 km s^{-1} . It may be noted from the flow map that the small, negative polarity spot shows the clockwise shear flow motion whereas the positive polarity region (in which another footpoint was anchored of the lower loop-system) shows counter-clockwise flow motion. This linear translational motion as evident in TRACE white light images as well as velocity shear flows as evident in FLCT images near the spots most likely indicate the triggering of the shear in their locations. This physical mechanism most likely plays a role in the energy build-up for flare and generates the coalescence instability in the lower loop-system.

6.2.4 Magnetic Topology of the Interacting Loop-Systems

In this Section, we discuss the large-scale structure of a magnetic field responsible for the flare. The soft X-ray image of the flare clearly reveals the two large crossing loops, L1 and L2, providing X-type interaction; and the chromospheric images ($H\alpha$ and TRACE 1600 Å) show the two ribbon morphology with the four kernels, i.e. four footpoints of the reconnected loops. We illustrate these features of the interacting loop-systems in terms of the so-called *topological* models; see ch. 3 in Somov (2007). Figure 6.15 displays the field lines that connect the $H\alpha$ kernels:

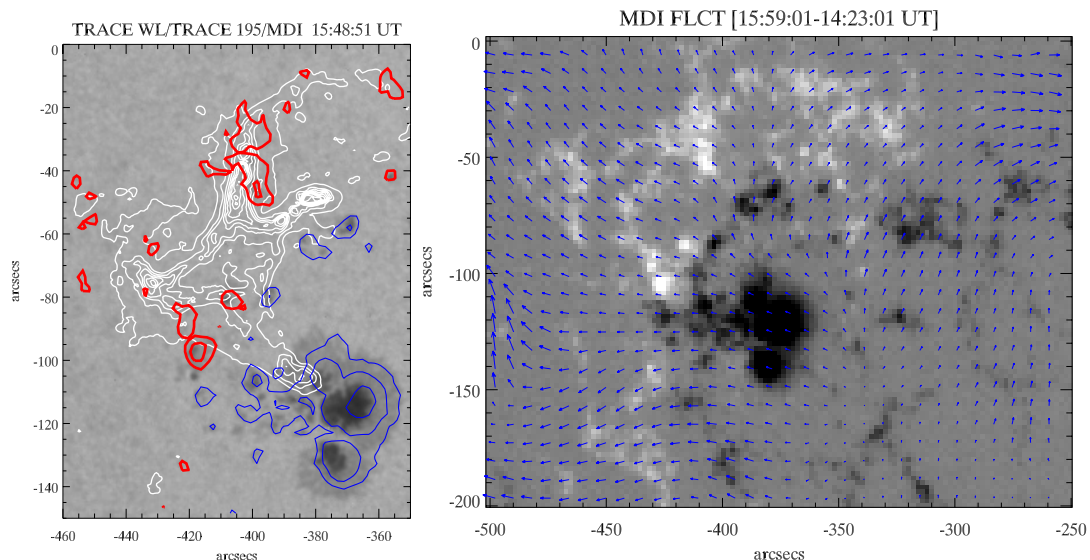


Figure 6.13: Left: TRACE 195 Å (white) and MDI magnetogram contours overlaid on TRACE white-light image. Red contours indicate the positive polarity sunspots whereas blue one show the negative polarity spots. The contour levels are ± 500 , ± 1000 , ± 2000 , ± 3000 G. Right: The photospheric velocity map obtained from FLCT (Fourier Local Correlation Tracking) technique using SOHO/MDI magnetograms. The longest arrow corresponds to velocity of 0.291 km s^{-1} .

FP1 (L1) with FP2 (L1), and FP1 (L2) with FP2 (L2). The shadowed regions FR1 and FR2 indicate the flare ribbons. They are located on both sides of the photospheric neutral line NL. Chromospheric evaporation along the reconnected field lines creates the SXR loops, that look like they are crossing or touching each other somewhere near the top of a magnetic-field separator X. The loops and ribbon morphology shown in the observations qualitatively matches with this cartoon.

We believe that, in addition to what is shown in Figure 6.15, the electric currents and twisted magnetic fields can be created inside the interacting loops by some under-photospheric or photospheric mechanism observed in the photosphere as shear motions or rotations. Such currents certainly must exist in complex active regions with sunspot rotation and large-scale photospheric shear flows. If the currents are mostly parallel they attract each other and can give energy to

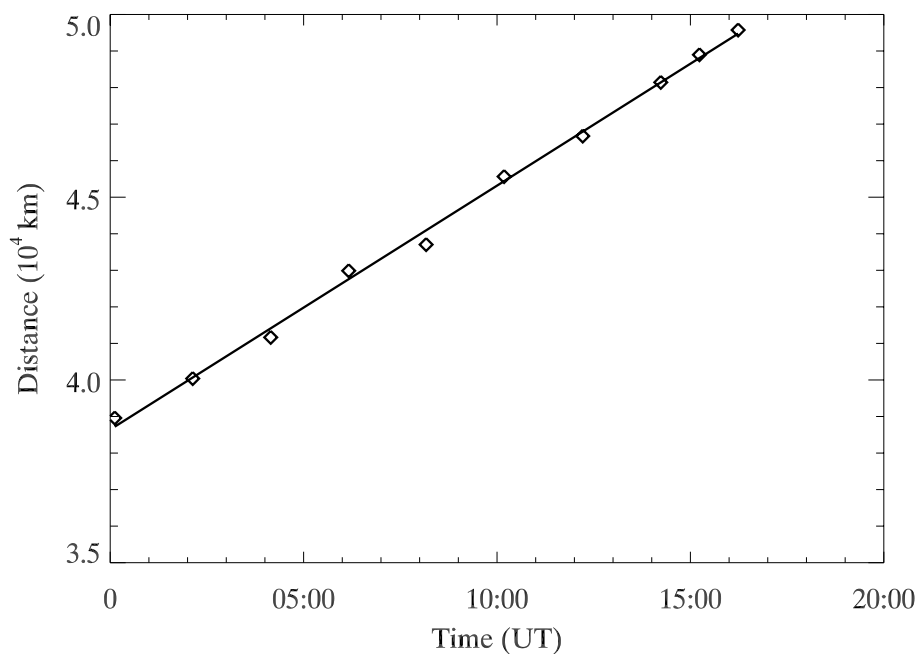


Figure 6.14: The linear motion of negative polarity sunspot on 27 April, 2006. One footpoint of the loop-system was anchored in this sunspot. The estimated speed of the sunspot from the linear fit is $\sim 0.2 \text{ km s}^{-1}$ (662 km h^{-1}). This motion probably caused the destabilization and interaction in the loop systems.

a flare (Gold & Hoyle, 1960). On the other hand, according to the simplified topological model presented in Figure 6.15,

the flare energy comes from an interaction of magnetic fluxes that can be mostly potential. If this would be the case, the flare energy should be stored before a flare mainly in slowly-reconnecting current layer at the separator of coronal magnetic field. This possibility seems to be in agreement with the quadrupole reconnection model of the solar flares. The morphology of the loops is also in agreement with the PFSS extrapolation of photospheric magnetic fields into the corona. That is why we consider both models at first from the view-point of global magnetic configuration of a quadrupole-type active region taking into account the interacting electric currents.

Figure 6.16 illustrates the possibility of two large-scale coronal currents J_1 and J_2 distributed inside two different magnetic cells, i.e. the two magnetic fluxes of different linkage, that interact and reconnect at the separator X . The

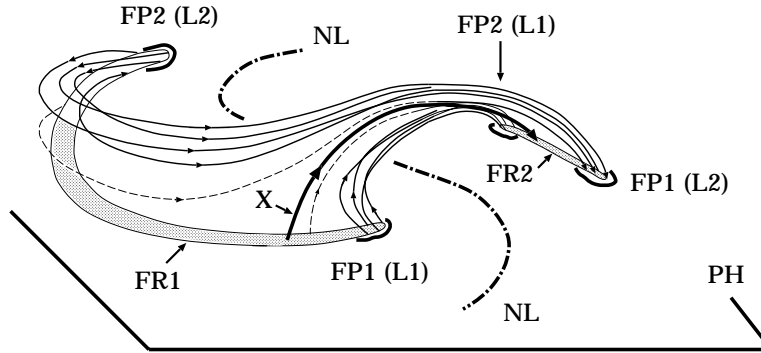


Figure 6.15: Magnetic field lines that connect the $H\alpha$ kernels FP1 (L1), FP2 (L1), FP1 (L2), and FP2 (L2) are passing through a region of primary energy release located somewhere near the top of the separator X. The flare ribbons FR1 and FR2 are formed where these field lines cross the photospheric plane PH. NL is the neutral line of photospheric magnetic field. Chromospheric evaporation creates a picture of the crossing soft X-ray loops.

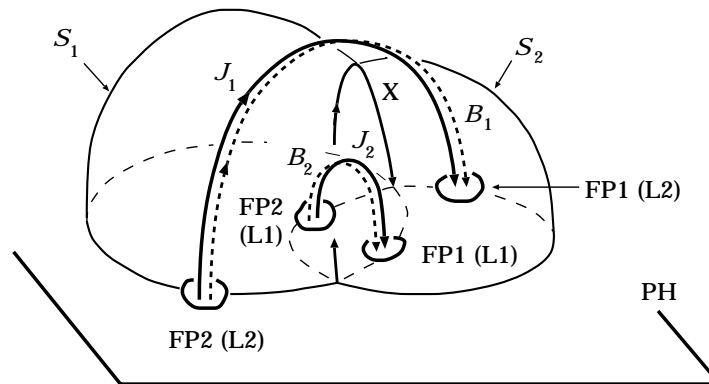


Figure 6.16: A 3D model of the coronal magnetic field with two interacting electric currents J_1 and J_2 . Four magnetic fluxes of different linkage are separated by the separatrices S_1 and S_2 that cross at the separator X above the photospheric plane PH. The two field lines B_1 and B_2 connect the kernel FP2 (L2) with FP1 (L2) and the kernel FP2 (L1) with FP1 (L1). The coronal currents are distributed somehow inside the two magnetic cells and are shown schematically as the total currents J_1 and J_2 along the field lines B_1 and B_2 .

two field lines B_1 and B_2 belong to the magnetic cells that connect the kernel FP2 (L2) with FP1 (L2) and the kernel FP2 (L1) with FP1 (L1) respectively. The coronal currents are distributed somehow inside the two different magnetic cells and shown schematically as the total currents J_1 and J_2 along the field lines B_1 and B_2 .

If the field lines B_1 and B_2 near the current layer along the separator have an opposite direction component, they can be reconnected. If the two current systems J_1 and J_2 flow more or less in the same direction, they attract each other according to Gold & Hoyle (1960). The components of the magnetic field transversal to the separator reconnect together with electric currents flowing along them (Henoux & Somov, 1987; Somov, 1992). In this way, with a perpendicular magnetic field inside the place of interruption, magnetic reconnection can create local interruptions of the electric currents in the solar atmosphere. If these currents are highly concentrated, their interruption can give rise to strong electric fields accelerating particles and can contribute significantly to the flare energetics.

What factors do determine the rate of magnetic reconnection in the current layer at the separator? – Let us consider the magnetic fields created by the currents J_1 and J_2 . These additional or secondary fields play the role of the longitudinal magnetic field near the reconnecting current layer. Being superimposed on the large-scale potential field, they create the two types of field line spirals: left-handed and right-handed. When looking along the positive direction of the field lines B_1 and B_2 , we see the two opposite orientations for the spirals: namely to the right for the *dextral* structure and to the left for the *sinistral* one. Depending on this handedness property known in our days as *chirality*, actually depending on the angle between the currents J_1 and J_2 , magnetic reconnection of electric currents will proceed faster or slowly (Henoux & Somov, 1987).

As evident in observations as well as in theoretical baseline, the X-type reconnection may produce the plasma jets. However we have no observational signature of such jets in our observations. In the flare under consideration, the reconnected fast outflows from a current layer relax quickly because they interact with: (i) closed field lines of a quadrupole-type of the active region (recall that there was no type III radioburst; thus, the opening of field lines did not take place during the flare energy release, i.e. reconnection); (ii) chromospheric evaporation

upflows (the energy released in closed magnetic configuration goes into impulsive heating of the upper chromosphere to high temperatures; that is why the soft X-ray images become so bright quickly).

6.3 Some Theoretical Estimations

The RHESSI temporal images (12-25 and 25-50 keV) reveal the coalescence of the loop-top sources of the interacting loop system. The two loop-top sources merge approximately vertical in the RHESSI field of view. Therefore, the lower bound change of the distance of the two approaching loops is

$$\Delta l_{coal} \approx 22000 \text{ km} \quad (6.1)$$

and the elapses time is

$$\Delta \tau_{coal} \approx 420 \text{ s} \quad (6.2)$$

The coalescence instability may activate in the observed interacting loops system, which is the effect that merges the two isolated magnetic islands into a single one (Aschwanden, 2004b; Haruki & Sakai, 2001a,b). This type of instability evolves in two phases, i.e. First phase in pairing of the current filament/loops as in ideal MHD process, while the second as the resistive phase of pairwise reconnection between the approaching current carrying flux tubes. The numerical MHD simulations reveal the different phases of coalescence instability in ideal/resistive solar plasma (Schumacher & Kliem, 1997).

The characteristic time scale of the ideal phase of coalescence instability is the multiple of Alfvénic transit time (Aschwanden, 2004b):

$$\tau_{coal} = \frac{1}{q_{coal}} \cdot \frac{l_{coal}}{v_A}, \quad (6.3)$$

where

$$q_{coal} = \frac{u_{coal}}{v_A}, \quad (6.4)$$

The l_{coal} , u_{coal} and v_A are respectively the distance between approaching loops, approaching velocity and local Alfvénic speed. Using equation (3) and (4), the differential coalescence speed

$$\Delta u_{coal} = \frac{\Delta l_{coal}}{\Delta \tau_{coal}}, \quad (6.5)$$

Therefore, using the observationally estimated values as mentioned in equation (1) and (2), we get the coalescence speed as $\sim 52 \text{ km s}^{-1}$. TRACE 195 Å images also show the interacting and paired loops. Using these images, the projected distance-time profile of the interaction region (i.e. converging motion at the interaction site) has been presented in Figure 4. The average converging speed of the interaction region is estimated as $\sim 30 \text{ km s}^{-1}$. The approximate approaching velocity of one magnetic island of a loop is evident as $\sim 26 \text{ km s}^{-1}$. The resemblance in these two speeds is in agreement with loop coalescence.

By assuming the typical Alfvénic speed at the interaction region as $\sim 1000 \text{ km s}^{-1}$ and the projected distance between the approaching loops ($\Delta l_{coal} \approx 22000 \text{ km}$), the estimated Alfvénic transit time of the region will be $\sim 22 \text{ s}$. Therefore the coalescence will occur $\sim 20 \tau_A$ for our observation, which is rather longer as predicted in various simulation results explained by Sakai & de Jager (1996) as well as Tajima et al. (1982) under various assumptions of the model atmosphere. However, for $L \sim 62800 \text{ km}$, $\tau_A = 16 \text{ s}$, the Reynolds number ($S=R$) = 500, $n_e = 10^{10} \text{ cm}^{-3}$ and $B_Z = 90 \text{ G}$, Milano et al. (1999) have found that two loops coalesce at $t = 11\tau_A$ and the magnetic energy and even its dissipation enhanced. The loop coalescence time depends upon various atmospheric parameters, and therefore further simulations will be interesting to study the dynamics and energetics of our observed coalesced loops.

We can estimate the amount of energy (\mathcal{E}_c) available due to coalescence instability (Smartt et al., 1993; Tajima et al., 1982) by:

$$\mathcal{E}_c \approx \frac{LB^2a^2}{2} \ln \frac{L}{a} \quad (6.6)$$

where L , B and a are length of the reconnecting region, loop magnetic field and radius of current loop respectively. We take $B = 100 \text{ G}$, $L = 22000 \text{ km}$ and $a = 11000 \text{ km}$, which gives

$$\mathcal{E}_c \approx 1.0 \times 10^{31} \text{ ergs} . \quad (6.7)$$

Therefore, this value is comparable with the energy released during M-class flare.

In general, the total magnetic field energy of the currents generated by photospheric vortex flows, sunspot rotation or shear flows in the photosphere can

exceed the energy of even the largest flares. However, in contrast to thin current layer at the separator, these currents are typically dispersed over a large volume of magnetic flux tubes in the corona. The dissipation rate of the currents so distributed in the coronal plasma of very high conductivity is vanishingly small. However, their interaction with each other and with the current layers at the separator is not small and must be treated within the framework of the global electro-dynamical coupling of a flare active region or complex.

As we saw in Section 6.2.4, a distinctive feature of this interaction is that the separator is orthogonal (in the sense of the magnetic field topology) to both systems of electric currents J_1 and J_2 . For this reason, not only the magnetic field components associated with the current layer, but also the longitudinal (guiding) components with respect to the separator are reconnected. Therefore, not only the energy associated with the current layer at the separator, but also a part of the energy of the currents generated by the photospheric vortex flows, sunspot rotation and shear flows is released in the flares (Henoux & Somov, 1987), see also Somov et al. (2002).

All the above have been concerned with the large-scale structure of magnetic fields and electric currents in large solar flares that can be qualitatively described in main features by the simplified topological models. As well known, however, in actual flares there are many different structures of different scales, including the smallest ones. In the flare under consideration, we see many interacting small flux threads/tubes, for example, in Figure 6.4. Moreover, the image at 15:48 UT in this Figure shows the loop-loop interaction and formation of 'X' point in between the interacting loop-system. So, it is likely that the observed flare was caused by interactions of not two but the multitude of the loops, forming more-or-less parallel systems and visible in low-resolution images as single, wide loops. From theoretical point of view this presumably means that the distributed currents J_1 and J_2 are deeply pinched in many thin current filaments. What we observe is some average picture of reconnection with some average reconnection rate.

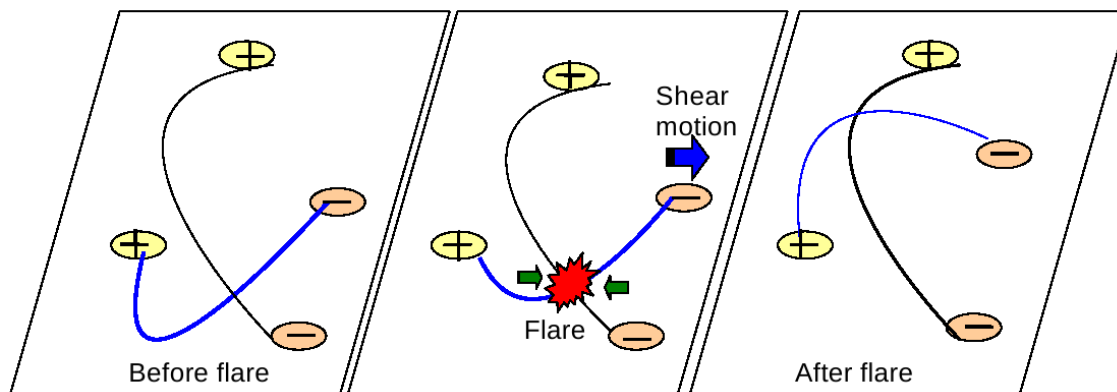


Figure 6.17: Schematic cartoons showing the flare triggering due to interaction of two X-ray loop-system. Black line shows the higher-loop system and dark blue line indicates the smaller underlying loop system. Due to shear motion of the right footpoint of smaller loop system, it becomes unstable and reconnects with the overlying higher loop system, triggering a flare event. After the flare event, the lower loop system becomes simplified as evident in GOES SXI image at 16:31:01 UT (Figure 6.3).

6.4 Discussions and Conclusions

We present the rare observational evidence of X-type loop-loop interaction associated with M7.9/1N flare. The coronal images observed by GOES SXI and TRACE 195 Å evidently show the interacting loop-system. TRACE white-light images reveal the sunspots shear motion (negative polarity) across the neutral line.

This shear motion probably might have produce the destabilization in the associated loop-system and cause the loop-interaction followed by the flare.

On the basis of multiwavelength observations, we draw a schematic cartoon to explain the whole event scenario (see Figure 6.17).

Before the flare there was two loop systems visible in SXI images. One higher loop in N-S direction and another smaller loop system in E-W direction lying below this higher loop system. Due to the shear motion of the right footpoint (anchored in negative polarity) of smaller loop system, the loop becomes unstable

and rises up due to instability and reconnects with the overlying higher loop system resulting X-type interaction in association with flare event. After the flare event, the connectivity of the smaller loop system changed into the relaxed state.

The regular variation of 4.9 and 8.8 GHz radio flux and accompanying flare effect observed during 27 April, 2006 are interpreted using X-type loop interaction model. We found the oscillatory behavior with double peak structure. Double peak in the radio flux gives the support for loop-interaction model (Sakai et al., 1986). According to the theoretical model, the double peak structure is more pronounced, when the currents in the two loops are sufficient for the explosive coalescence. Individual peak belongs to the electric field variation at the reconnection site. This electric field accelerates the electrons which generate the radio emission. The cause of quasiperiodic oscillation is as follows: after explosive reconnection of poloidal magnetic fields taking place at the ‘X’ point between approaching current loop and two plasma blobs pass through each other and overshoot (an approach that fails and gives way to another attempt), resulting the repetition of the process. Kliem et al. (2000) also proposed a model in which the pulsations of the radio flux are caused by quasi-periodic particle acceleration episodes that result from a dynamic phase of magnetic reconnection in a large-scale current sheet. The reconnection is dominated by repeated formation and sub-sequent coalescence of magnetic islands, while a continuously growing plasmoid is fed by newly coalescing islands. In our case, the coalescence speed of 52 km s^{-1} is much smaller than the Alfvén velocity of $\sim 1000 \text{ km s}^{-1}$.

The preflare stage in which multiple current filament structure might be generated due to the photospheric shear motion across the neutral line. The photospheric shear motion can give rise to plasma currents along the potential magnetic field produced by the sunspots nearby the active region. As the shear motion proceed, the current density may increase and current loop might move up, associated with relaxation of magnetic tension (Sakai et al., 1986). The absence of type III burst during flare energy release confirms the connectivity change and no opening of field lines. In addition, coalescence of hard X-ray sources also confirm the loop-loop interaction.

[Sakai et al. \(1986\)](#) presented the physical characteristics of the explosive coalescence of current loops through computer simulation and theory and mentioned canonical characteristics of the explosive coalescence as (i) impulsive increase of kinetic energy of electrons and ions (ii) simultaneous heating and acceleration of particles in high and low energy spectra (i.e. Neupert effect) (iii) quasi-periodic amplitude oscillations in field and particle quantities (iv) a double peak (or triple peak) structure in these profiles. Our observations clearly matches with all the above mentioned characteristics of the explosive coalescence and provide a unique evidence of X-type loop-loop interaction satisfying theories and simulations.

The interaction of large-scale current-carrying loops should be considered as a part of the global electrodynamic coupling in flare-productive active regions and active complexes as discussed in Section 6.2.4. On the one hand, the potential magnetic field in the corona determines a large-scale structure of active regions while the reconnecting current layers at separators in the corona together with other non-potential components (see Section 14.5 in [Somov, 2007](#)) of magnetic field determine energetic and dynamics of large flares. On the other hand, two large-scale current-carrying loops emerging from under the photosphere have the sufficient energy to provide a large flare too by their interaction and coalescent instability as considered in this paper. Moreover, these two currents could be incorporated in the large-scale structure with reconnecting current layer.

The principal question is in the relative role of two distinct sources of free magnetic energy: the interaction of magnetic fluxes, and the interaction of electric currents as demonstrated in this paper. Clearly the answer depends on the relation between: (a) the photospheric flows which create the preflare current layers at the separators, (b) the photospheric shear flows which induce the current layers extending along the separatrices ([Somov et al., 2002](#)), and (c) the other photospheric flows like sunspot rotations which twist the magnetic flux tubes. In any case, the separator is a special place where a fast conversion of free magnetic energy into bulk plasma motions, heat flows and energy of accelerated particles can take place.

In conclusions, we find the rare multiwavelength observational signature of the loop-loop interaction and triggering of the M-class flare, which is consistent with the earlier developed theories and simulations. However, further detailed

multiwavelength studies should be carried out statistically by analyzing such events to shed more lights on the dynamics and energetics related to the flare and eruptive phenomena related to loop-loop interactions.

Chapter 7

Summary and Future Scope

In this thesis, we have studied and presented the multiwavelength study of Solar Eruptive phenomena i.e. solar flares/CMEs and associated phenomena. This study encompasses different aspects of flare triggering mechanism on the Sun. Flares and CMES are the integral part of space weather. We have investigated the triggering mechanism of these events and their interplanetary consequences. This thesis also presents multiwavelength analyses of solar flares and coronal mass ejections to understand the structure of flaring regions during the eruption and subsequent reconnection at various heights in the solar atmosphere.

This thesis is divided into seven chapters. Chapter 1 gives a brief description about the space weather events. We also review our current observational and theoretical understanding on solar flares in this introductory chapter. In chapter 2, various data sources and instruments used to carry out the data acquisition and analysis are discussed. In the next four chapters (3-6), we have analyzed and investigated the triggering mechanism of solar flares/CMEs and their associated phenomena. A summary of these chapters is given below.

In chapter 3, we analyse $H\alpha$ images, soft X-ray profiles, magnetograms, extreme ultra-violet images and, radio observations of two homologous flare events (M1.4/1N and M9.6/2B) on 20 November 2003 in the active region NOAA 10501 and study properties of reconnection between twisted filament systems, energy release and associated launch of coronal mass ejections (CMEs). During both events twisted filaments observed in $H\alpha$ approached each other and initiated the flare processes. However, the second event showed the formation of cusp as the

filaments interacted. The rotation of sunspots of opposite polarities, inferred from the magnetograms likely powered the twisted filaments and injection of helicity. Along the current sheet between these two opposite polarity sunspots, the shear was maximum, which could have caused the twist in the filament. At the time of interaction between filaments, the reconnection took place and flare emission in thermal and non-thermal energy ranges attained the maximum. The radio signatures revealed the opening of field lines resulting from the reconnection. The $H\alpha$ images and radio data provide the inflow speed leading to reconnection and the scale size of particle acceleration region. The first event produced a narrow and slow CME, whereas the later one was associated with a fast full halo CME. The halo CME signatures observed between Sun and Earth using white-light and scintillation images and in-situ measurements indicated the magnetic energy utilized in the expansion and propagation. The magnetic cloud signature at the Earth confirmed the flux rope ejected at the time of filament interaction and reconnection.

In chapter 4, we study the solar sources of intense geomagnetic storm of solar cycle 23 occurred on 2003 November 20 using multiwavelength ground and space based observations. The coronal mass ejections responsible for the geomagnetic storm originated from the super-active region NOAA 10501. We investigate the $H\alpha$ observations of the flare events made with 15 cm Solar Tower Telescope at ARIES, Nainital, India. The propagation characteristics of the CMEs have been obtained from the three-dimensional images of the solar wind (density and velocity) obtained from the interplanetary scintillation technique, supplemented with the other ground and space-based missions. TRACE, SXI and $H\alpha$ observations revealed the two successive ejections originated from the same filament channel, which were associated with two high speed CMEs. The interaction of these CMEs along the Sun-Earth line has led to the severity of the storm. According to our investigation, the interplanetary medium consists of two merging magnetic clouds (MCs) that preserve their identity during their propagation. These magnetic clouds make the interplanetary magnetic field (IMF) southward for a long time, which reconnects with the geomagnetic field, resulting the super-storm ($Dst_{peak}=-472$ nT) on the Earth.

In chapter 5, we present a multiwavelength analysis of solar flares (B5.0, M8.9/3B) event that occurred on 04 June 2007 from AR NOAA 10960. These flares were observed by several spaceborne instruments, namely SOHO/MDI, HINODE/SOT, TRACE and STEREO/SECCHI. The flare was initiated near a small, positive-polarity, satellite sunspot at the centre of the active region, surrounded by opposite-polarity field regions. MDI images of the active region show considerable amount of changes in the small positive-polarity sunspot of δ configuration during the flare event. SOT/G-band (4305 Å) images of the sunspot also suggest the rapid evolution of this positive-polarity sunspot with highly twisted penumbral filaments before the flare event, which were oriented in a counterclockwise direction. It shows the change in orientation, and also remarkable disappearance of twisted penumbral filaments ($\approx 35-40\%$) and enhancement in umbral area ($\approx 45-50\%$) during the decay phase of the flare event. TRACE and SECCHI observations reveal the successive activation of two helical-twisted structures associated with this sunspot, and the corresponding brightening in the chromosphere as observed by the time-sequence images of SOT/Ca II H line (3968 Å). The activation of first helical twisted structure was associated with B5.0 class flare. The secondary, helical-twisted structure is found to be associated with the M8.9 flare event. The brightening starts six–seven minutes prior to the flare maximum with the appearance of secondary, helical-twisted structure. The flare intensity maximizes as the secondary, helical-twisted structure moves away from the active region. This twisted flux tube, associated with the flare triggering, is found to be failed in eruption. The location of the flare activity is found to coincide with the activation site of the helical twisted structures. We conclude that the activation of successive helical twists (especially the second one) in the magnetic flux tubes/ropes plays a crucial role in the energy build-up process and triggering of the M-class solar flare without a coronal mass ejection (CME).

In chapter 6, we analyze multiwavelength data of a M7.9/1N class solar flare which occurred on 27 April, 2006 from AR NOAA 10875. GOES soft X-ray images provide the most likely signature of two interacting loops and their reconnection, which triggers the solar flare. TRACE 195 Å images also reveal the loop-loop interaction and the formation of ‘X’ points with converging motion ($\sim 30 \text{ km s}^{-1}$) at the reconnection site in-between this interacting loop system. This provides the

evidence of progressive reconnection and flare maximization at the interaction site in the active region. The absence of type III radio burst during this time period indicates no opening of magnetic field lines during the flare energy release, which implies only the change of field lines connectivity/orientation during the loop-loop interaction and reconnection process. The Ondrejov dynamic radio spectrum shows an intense decimetric (DCIM) radio burst (2.5–4.5 GHz, duration~3 min) during flare initiation, which reveals the signature of particle acceleration from the reconnection site during loop-loop interaction. The double peak structures at 4.9 and 8.8 GHz provide the most likely confirmatory signature of the loop-loop interaction at the flare site in the active region. RHESSI hard X-ray images also show the loop-top and footpoint sources of the corresponding two loop system and their coalescence during the flare maximum, which act like the current carrying flux-tubes with resultant opposite magnetic fields and the net force of attraction.

Future scope

Solar flares and coronal mass ejections (CMEs) are prominent signatures of the explosive release of energy stored in the coronal magnetic field. Multiwavelength observations with increasing sensitivity and temporal resolution give a great deal of insights into the physics of solar flares/CMEs. Now it has widely been accepted that the magnetic reconnection is a key process of energy release in the solar atmosphere. Despite remarkable progress in observational and theoretical understanding about flares and CMEs since last couple of decades, there are a number of outstanding and fundamental questions yet to be answered:

- What is the most likely magnetic configuration in pre-flare phase and by what means are the magnetic fields stressed?
- Which physical processes trigger the energy release?
- Which physical processes convert magnetic energy to hot plasma, energetic particles, and mass motions ?
- Which configuration of corona leads to a CME ?
- What is the mechanism for CME acceleration?

-
- How does a CME interact with the heliosphere?

The recently launched STEREO (Solar TERrestrial RELation Observatory), HINODE (SOLAR -B) and SDO(Solar Dynamic Observatory) satellites aim to provide more complete picture of solar transients. Hinode, launched on September 22, 2006, is equipped with three advanced solar telescopes: Solar Optical Telescope (SOT), X-ray telescope (XRT) and EUV imaging spectrometer (EIS). The SOT has an unprecedented 0.2 arc sec resolution which is optimized for accurate measurement of the vector magnetic field in the photosphere and dynamics of both photosphere and chromosphere associated with the magnetic fields. The high resolution data in X-ray and EUV, together with vector magnetogram are expected to reveal the dynamics and evolution of magnetic configuration in active solar corona during the various stages of flares and CMEs. STEREO, launched on October 25, 2006, is designed to make the first 3D observations of the Sun and inner heliosphere. For this propose, STEREO employs two nearly identical spacecrafts - one ahead of Earth in its orbit, the other trailing behind - to provide the first ever stereoscopic measurements to study the solar processes. These measurements will help unveil the origin, evolution and interplanetary consequences of CMEs.

SDO is the first mission to be launched on February 10, 2010 for NASA's Living With a Star (LWS) Program, a program designed to understand the causes of solar variability and its impacts on Earth. SDO is designed to help us understand the Sun's influence on Earth and Near-Earth space by studying the solar atmosphere on small scales of space and time and in many wavelengths simultaneously. SDO's goal is to understand, driving towards a predictive capability, the solar variations that influence life on Earth and humanity's technological systems by determining

- How the Sun's magnetic field is generated and structured?
- How this stored magnetic energy is converted and released into the heliosphere and geospace in the form of solar wind, energetic particles, and variations in the solar irradiance?

SDO will study how solar activity is created and how Space Weather comes from that activity. Measurements of the interior of the Sun, the Sun's magnetic field, the hot plasma of the solar corona, and the irradiance that creates the ionospheres of the planets are our primary data products.

SDO has three scientific experiments:

- Atmospheric Imaging Assembly (AIA)
- EUV Variability Experiment (EVE)
- Helioseismic and Magnetic Imager (HMI)

Each of these experiments perform several measurements that characterize how and why the Sun varies. These three instruments will observe the Sun simultaneously, performing the entire range of measurements necessary to understand the variations on the Sun.

We hope that in the near future, new observations made by Hinode, STEREO and SDO in combination with other space and ground based instruments will be extremely useful to address the unresolved issues related to solar flares and CMEs. To understand the CME properties in the interplanetary medium, we plan to carry out more systematic and detailed analyses of Interplanetary Scintillation (IPS) measurements taken from Ooty Radio Telescope. The IPS images at various heliocentric distances and their comparison with STEREO measurements will be extremely useful to understand the propagation characteristics as well as radial evolution of CMEs. Further, the large data set of solar flares/CMEs, obtained from various ground and space based platforms, should be utilized to understand the initiation/triggering mechanism of flares/CMEs on the Sun.

References

- Alexander, D., Liu, R., & Gilbert, H. R. 2006, *ApJ*, 653, 719 [15](#)
- Altschuler, M. D., & Newkirk, G. 1969, *Sol. Phys.*, 9, 131 [140](#), [160](#)
- Amari, T., Luciani, J. F., Aly, J. J., Mikic, Z., & Linker, J. 2003, *ApJ*, 585, 1073 [43](#)
- Amari, T., Luciani, J. F., Mikic, Z., & Linker, J. 2000, *Astrophys. J.*, 529, L49 [118](#)
- Andrews, M. D. 2003, *Sol. Phys.*, 218, 261 [28](#), [29](#)
- Antiochos, S. K. 1998a, *Astrophys. J.*, 502, L181 [40](#)
- Antiochos, S. K. 1998b, *Astrophys. J.*, 502, L181 [147](#)
- Antiochos, S. K., DeVore, C. R., & Klimchuk, J. A. 1999, *ApJ*, 510, 485 [xvi](#), [40](#), [41](#), [43](#)
- Aschwanden, M. J. 2002, *Space Sci. Rev.*, 101, 1 [33](#)
- Aschwanden, M. J. 2004a, *Physics of the Solar Corona. An Introduction* (Praxis Publishing Ltd) [xvi](#), [38](#)
- Aschwanden, M. J. 2004b, *Physics of the Solar Corona. An Introduction* (Chichester, UK: Praxis Publishing Ltd) [164](#), [172](#)
- Aschwanden, M. J., & Alexander, D. 2001, *Sol. Phys.*, 204, 91 [33](#)
- Aulanier, G., DeLuca, E. E., Antiochos, S. K., McMullen, R. A., & Golub, L. 2000, *ApJ*, 540, 1126 [40](#)

REFERENCES

- Bastian, T. S., Benz, A. O., & Gary, D. E. 1998, *ARA&A*, 36, 131 [11](#), [63](#)
- Baty, H. 2001, *Astron. Astroph.*, 367, 321 [139](#)
- Bennett, K., Roberts, B., & Narain, U. 1999, *Sol. Phys.*, 185, 41 [139](#)
- Bothmer, V., & Schwenn, R. 1997, *Annales Geophysicae*, 16, 1 [112](#)
- Bougeret, J., et al. 1998, *Geophys. Res. Lett.*, 25, 2513 [22](#)
- Burkepile, J. T., & St. Cyr, O. C. 1993, NASA STI/Recon Technical Report N, 93, 26556 [36](#)
- Burlaga, L., et al. 1998, *J. Geophys. Res.*, 103, 277 [68](#)
- Burlaga, L., Sittler, E., Mariani, F., & Schwenn, R. 1981, *JGR*, 86, 6673 [23](#), [91](#)
- Burlaga, L. F., Klein, L., Sheeley, N. R., Jr., Michels, D. J., Howard, R. A., Koomen, M. J., Schwenn, R., & Rosenbauer, H. 1982, *Geophys. Res. Lett.*, 9, 1317 [23](#)
- Cane, H. V., Sheeley, N. R., Jr., & Howard, R. A. 1987, *J. Geophys. Res.*, 92, 9869 [20](#), [21](#)
- Cane, H. V., Stone, R. G., Fainberg, J., Steinberg, J. L., Hoang, S., & Stewart, R. T. 1981, *Geophys. Res. Lett.*, 8, 1285 [22](#)
- Canfield, R. C., Hudson, H. S., & McKenzie, D. E. 1999, *Geophys. Res. Lett.*, 26, 627 [42](#), [117](#)
- Carrington, R. C. 1859, *MNRAS*, 20, 13 [xiv](#), [4](#)
- Chandra, R., Pariat, E., Schmieder, B., Mandrini, C. H., & Uddin, W. 2010, *Sol. Phys.*, 261, 127 [68](#), [89](#), [92](#), [115](#)
- Chen, J., et al. 1997, *Astrophys. J.*, 490, L191 [36](#)
- Claßen, H. T., & Aurass, H. 2002, *Astron. Astroph.*, 384, 1098 [21](#), [22](#)
- Cliver, E., & Murdin, P. 2000, *Solar Flare Classification*, ed. Murdin, P. [5](#), [6](#)

- Cliver, E. W. 1989, *Sol. Phys.*, 122, 319 [16](#)
- Cliver, E. W., Webb, D. F., & Howard, R. A. 1999, *Sol. Phys.*, 187, 89 [21](#)
- Cremades, H., & Bothmer, V. 2004, *Astron. Astroph.*, 422, 307 [18](#)
- Culhane, J. L., et al. 2007, *Sol. Phys.*, 243, 19 [62](#)
- Czaykowska, A., de Pontieu, B., Alexander, D., & Rank, G. 1999, *Astrophys. J.*, 521, L75 [33](#)
- D’Azambuja, L. 1955, *Vistas in Astronomy*, 1, 695 [14](#)
- Delannée, C., Delaboudinière, J., & Lamy, P. 2000, *Astron. Astroph.*, 355, 725 [37](#)
- Démoulin, P., & Berger, M. A. 2003, *Sol. Phys.*, 215, 203 [68](#)
- Dere, K. P., Brueckner, G. E., Howard, R. A., Michels, D. J., & Delaboudinière, J. P. 1999, *ApJ*, 516, 465 [36](#)
- Domingo, V., Fleck, B., & Poland, A. I. 1995, *Sol. Phys.*, 162, 1 [56](#)
- Dryer, M. 1982, *Space Sci. Rev.*, 33, 233 [37](#)
- Dryer, M. 1994, *Space Sci. Rev.*, 67, 363 [29](#)
- Dryer, M. 1996, *Sol. Phys.*, 169, 421 [37](#)
- Dungey, J. W., & Loughhead, R. E. 1954, *Australian Journal of Physics*, 7, 5 [139](#)
- Eddy, J. A. 1974, *Astron. Astroph.*, 34, 235 [16](#)
- Falewicz, R., & Rudawy, P. 1999, *Astron. Astroph.*, 344, 981 [151](#)
- Fan, Y., Alexander, D., & Tian, L. 2009, *ApJ*, 707, 604 [138](#)
- Fan, Y., & Gibson, S. E. 2003, *Astrophys. J.*, 589, L105 [117](#)
- Filippov, B., & Koutchmy, S. 2002, *Sol. Phys.*, 208, 283 [142](#)
- Filippov, B. P., & Den, O. G. 2001, *J. Geophys. Res.*, 106, 25177 [145](#)

- Fisher, G. H., & Welsch, B. T. 2008, in *Astronomical Society of the Pacific Conference Series*, Vol. 383, *Subsurface and Atmospheric Influences on Solar Activity*, ed. R. Howe, R. W. Komm, K. S. Balasubramaniam, & G. J. D. Petrie, 373 [167](#)
- Fisher, R., Garcia, C. J., & Seagraves, P. 1981, *Astrophys. J.*, 246, L161 [16](#), [29](#)
- Forbes, T. G. 2000, *J. Geophys. Res.*, 105, 23153 [xv](#), [17](#), [18](#), [37](#), [40](#), [42](#)
- Forbes, T. G., & Acton, L. W. 1996, *ApJ*, 459, 330 [xvi](#), [11](#), [32](#)
- Forbes, T. G., & Isenberg, P. A. 1991, *ApJ*, 373, 294 [42](#)
- Forbes, T. G., & Priest, E. R. 1995, *ApJ*, 446, 377 [145](#)
- Foukal, P. 1971, *Sol. Phys.*, 19, 59 [14](#)
- Gaizauskas, V. 1989, *Sol. Phys.*, 121, 135 [10](#)
- Gaizauskas, V. 1998, in *Astronomical Society of the Pacific Conference Series*, Vol. 150, *IAU Colloq. 167: New Perspectives on Solar Prominences*, ed. D. F. Webb, B. Schmieder, & D. M. Rust, 257 [14](#)
- Gaizauskas, V., Zirker, J. B., Sweetland, C., & Kovacs, A. 1997, *ApJ*, 479, 448 [14](#)
- Gary, G. A., & Moore, R. L. 2004, *ApJ*, 611, 545 [118](#)
- Gary, G. A., Moore, R. L., Hagyard, M. J., & Haisch, B. M. 1987, *ApJ*, 314, 782 [42](#)
- Gerrard, C. L., Arber, T. D., & Hood, A. W. 2002, *Astron. Astroph.*, 387, 687 [119](#)
- Gesztelyi, L., Gerlei, O., Karlicky, M., Farnik, F., & Valnicek, B. 1986, in *The lower atmosphere of solar flares; Proceedings of the Solar Maximum Mission Symposium*, Sunspot, NM, Aug. 20-24, 1985 (A87-26201 10-92). Sunspot, NM, National Solar Observatory, 1986, p. 163-177., ed. D. F. Neidig, 163 [42](#)

- Gibson, S. E., et al. 2002, ApJ, 574, 1021 [15](#)
- Gibson, S. E., & Low, B. C. 1998, ApJ, 493, 460 [42](#)
- Gilbert, H. R., Alexander, D., & Liu, R. 2007, Sol. Phys., 245, 287 [14](#), [15](#)
- Gilbert, H. R., Holzer, T. E., & Burkepile, J. T. 2001, ApJ, 549, 1221 [12](#)
- Gilbert, H. R., Holzer, T. E., Burkepile, J. T., & Hundhausen, A. J. 2000, ApJ, 537, 503 [15](#), [30](#)
- Gissot, S. F., Hochedez, J., Chainais, P., & Antoine, J. 2008, Sol. Phys., 252, 397 [130](#)
- Gold, T., & Hoyle, F. 1960, MNRAS, 120, 89 [150](#), [169](#), [171](#)
- Golub, L., et al. 2007, Sol. Phys., 243, 63 [62](#)
- Golub, L., & Pasachoff, J. M. 1997, The Solar Corona, UK: Cambridge University Press [9](#)
- Gopalswamy, N. 2006, Journal of Astrophysics and Astronomy, 27, 243 [18](#), [19](#)
- Gopalswamy, N., Barbieri, L., Cliver, E. W., Lu, G., Plunkett, S. P., & Skoug, R. M. 2005a, Journal of Geophysical Research (Space Physics), 110, 9 [19](#), [68](#), [92](#)
- Gopalswamy, N., et al. 1998, J. Geophys. Res., 103, 307 [21](#)
- Gopalswamy, N., Shimojo, M., Lu, W., Yashiro, S., Shibasaki, K., & Howard, R. A. 2003, ApJ, 586, 562 [30](#)
- Gopalswamy, N., Yashiro, S., Liu, Y., Michalek, G., Vourlidas, A., Kaiser, M. L., & Howard, R. A. 2005b, Journal of Geophysical Research (Space Physics), 110, 9 [xv](#), [27](#)
- Gopalswamy, N., Yashiro, S., VonRosenvinge, T. T., & Leske, R. 2001, AGU Fall Meeting Abstracts, A735 [18](#), [108](#)
- Gorbachev, V. S., & Somov, B. V. 1989, Soviet Astronomy, 33, 57 [151](#)

- Gorbachev, V. S., & Somov, B. V. 1990, *Advances in Space Research*, 10, 105
[152](#)
- Gosling, J. T. 1993, *J. Geophys. Res.*, 98, 18937 [36](#)
- Gosling, J. T., Hildner, E., MacQueen, R. M., Munro, R. H., Poland, A. I., &
Ross, C. L. 1974, *J. Geophys. Res.*, 79, 4581 [16](#)
- Gosling, J. T., Hildner, E., MacQueen, R. M., Munro, R. H., Poland, A. I., &
Ross, C. L. 1976, *Sol. Phys.*, 48, 389 [28](#)
- Gosling, J. T., McComas, D. J., Phillips, J. L., & Bame, S. J. 1991, *J. Geo-
phys. Res.*, 96, 7831 [26](#)
- Hagyard, M. J., Teuber, D., West, E. A., & Smith, J. B. 1984, *Sol. Phys.*, 91, 115
[42](#)
- Hanaoka, Y. 1996, *Sol. Phys.*, 165, 275 [150](#)
- Handy, B. N., et al. 1999, *Sol. Phys.*, 187, 229 [xxix](#), [60](#), [61](#), [157](#)
- Harrison, R. 2006, Washington DC American Geophysical Union Geophysical
Monograph Series, 165, 73 [30](#)
- Harrison, R. A. 1986, *Astron. Astroph.*, 162, 283 [37](#)
- Harrison, R. A. 1991, *Advances in Space Research*, 11, 25 [29](#)
- Harrison, R. A. 1995, *Astron. Astroph.*, 304, 585 [29](#), [30](#)
- Harrison, R. A. 1996, *Sol. Phys.*, 166, 441 [30](#)
- Haruki, T., & Sakai, J. 2001a, *Astrophys. J.*, 552, L175 [172](#)
- Haruki, T., & Sakai, J. I. 2001b, *Physics of Plasmas*, 8, 1538 [172](#)
- Henoux, J. C., & Somov, B. V. 1987, *Astron. Astroph.*, 185, 306 [151](#), [171](#), [174](#)
- Heyvaerts, J., Priest, E. R., & Rust, D. M. 1977, *ApJ*, 216, 123 [42](#)
- Hill, S. M., et al. 2005, *Sol. Phys.*, 226, 255 [153](#)

- Hood, A. W., & Priest, E. R. 1979, *Sol. Phys.*, 64, 303 [138](#)
- Howard, R. A. 2006, Washington DC American Geophysical Union Geophysical Monograph Series, 165, 7 [16](#)
- Howard, R. A., Michels, D. J., Sheeley, N. R., Jr., & Koomen, M. J. 1982, *Astrophys. J.*, 263, L101 [19](#)
- Hundhausen, A. 1999, in *The many faces of the sun: a summary of the results from NASA's Solar Maximum Mission.*, ed. K. T. Strong, J. L. R. Saba, B. M. Haisch, & J. T. Schmelz, 143 [16](#), [29](#)
- Hurford, G. J., Krucker, S., Lin, R. P., Schwartz, R. A., Share, G. H., & Smith, D. M. 2006, *Astrophys. J.*, 644, L93 [5](#)
- Hurford, G. J., Schwartz, R. A., Krucker, S., Lin, R. P., Smith, D. M., & Vilmer, N. 2003, *Astrophys. J.*, 595, L77 [5](#)
- Ishii, T. T., Kurokawa, H., & Takeuchi, T. T. 1998, *ApJ*, 499, 898 [118](#), [144](#), [146](#)
- Ishii, T. T., Kurokawa, H., & Takeuchi, T. T. 2000, *PASJ*, 52, 337 [118](#)
- Ji, H., Wang, H., Schmahl, E. J., Moon, Y., & Jiang, Y. 2003, *Astrophys. J.*, 595, L135 [15](#), [142](#)
- Jing, J., Yurchyshyn, V. B., Yang, G., Xu, Y., & Wang, H. 2004, *ApJ*, 614, 1054 [30](#)
- Jiricka, K., Karlicky, M., Kepka, O., & Tlamicha, A. 1993, *Sol. Phys.*, 147, 203 [161](#)
- Jiříčka, K., & Karlický, M. 2008, *Sol. Phys.*, 253, 95 [161](#)
- Judge, D. L., et al. 1998, *Sol. Phys.*, 177, 161 [94](#)
- Kahler, S. W., & Reames, D. V. 2003, *ApJ*, 584, 1063 [21](#)
- Kane, S. R. 1974, in *IAU Symposium, Vol. 57, Coronal Disturbances*, ed. G. A. Newkirk, 105 [xiv](#), [8](#)

- Karlický, M., & Jiříčka, K. 2003, in ESA Special Publication, Vol. 535, Solar Variability as an Input to the Earth's Environment, ed. A. Wilson, 499 [164](#)
- Khan, J. I., & Hudson, H. S. 2000, Geophysical. Res. Lett., 27, 1083 [30](#)
- Kliem, B., Karlický, M., & Benz, A. O. 2000, Astron. Astroph., 360, 715 [176](#)
- Kliem, B., Titov, V. S., & Török, T. 2004, Astron. Astroph., 413, L23 [117](#)
- Klimchuk, J. A. 2001, Space Weather (Geophysical Monograph 125), ed. P. Song, H. Singer, G. Siscoe (Washington: Am. Geophys. Un.), 143 (2001), 125, 143 [xvi](#), [35](#), [36](#), [37](#), [38](#)
- Kosugi, T., & Acton, L. W. 2002, in Multi-Wavelength Observations of Coronal Structure and Dynamics, ed. P. C. H. Martens & D. Cauffman, D7 [5](#)
- Krall, J., Chen, J., Duffin, R. T., Howard, R. A., & Thompson, B. J. 2001, ApJ, 562, 1045 [118](#)
- Krall, J., Chen, J., & Santoro, R. 2000, ApJ, 539, 964 [37](#), [42](#)
- Kreplin, R. W., Chubb, T. A., & Friedmann, H. 1962, J. Geophys. Res., 67, 2231 [4](#)
- Kumar, P., Manoharan, P. K., & Uddin, W. 2010, ApJ, 710, 1195 [67](#), [117](#), [145](#), [151](#)
- Kumar, P., Srivastava, A. K., Filippov, B., & Uddin, W. 2010a, Sol. Phys., 266, 39 [117](#), [150](#)
- Kumar, P., Srivastava, A. K., Somov, B. V., Manoharan, P. K., Erdelyi, R., & Uddin, W. 2010b, ArXiv e-prints [149](#)
- Kurokawa, H. 1987, Sol. Phys., 113, 259 [68](#), [78](#)
- Kurokawa, H., Hanaoka, Y., Shibata, K., & Uchida, Y. 1987, Sol. Phys., 108, 251 [68](#), [78](#)
- Lang, K. R. 2001, The sun from space: Springer, Cambridge University Press [xvi](#), [34](#)

- Lara, A., Gopalswamy, N., Xie, H., Mendoza-Torres, E., Pérez-Erriquez, R., & Michalek, G. 2006, *Journal of Geophysical Research (Space Physics)*, 111, 6107 [19](#)
- Liewer, P. C., de Jong, E. M., Hall, J. R., Howard, R. A., Thompson, W. T., Culhane, J. L., Bone, L., & van Driel-Gesztelyi, L. 2009, *Sol. Phys.*, 256, 57 [130](#)
- Lin, J. 2004, *Sol. Phys.*, 219, 169 [31](#)
- Lin, J., & Forbes, T. G. 2000, *J. Geophys. Res.*, 105, 2375 [xvi](#), [32](#), [118](#)
- Lin, R. P., et al. 2002, *Sol. Phys.*, 210, 3 [5](#), [59](#)
- Liu, C., Deng, N., Liu, Y., Falconer, D., Goode, P. R., Denker, C., & Wang, H. 2005, *ApJ*, 622, 722 [136](#), [147](#)
- Liu, R., & Alexander, D. 2009, *ApJ*, 697, 999 [119](#)
- Liu, R., Gilbert, H. R., Alexander, D., & Su, Y. 2008, *ApJ*, 680, 1508 [150](#)
- Liu, Y., Akioka, M., Yan, Y., & Sato, J. 1998, *Sol. Phys.*, 180, 377 [151](#)
- Liu, Y., Jiang, Y., Ji, H., Zhang, H., & Wang, H. 2003, *Astrophys. J.*, 593, L137 [118](#)
- Liu, Y., & Zhang, H. 2001, *Astron. Astroph.*, 372, 1019 [78](#), [89](#)
- Low, B. C. 1996, *Sol. Phys.*, 167, 217 [39](#), [68](#)
- Low, B. C. 1999, in *American Institute of Physics Conference Series*, Vol. 471, American Institute of Physics Conference Series, ed. S. R. Habbal, R. Esser, J. V. Hollweg, & P. A. Isenberg, 109 [37](#), [39](#)
- Low, B. C. 2001, *J. Geophys. Res.*, 106, 25141 [37](#), [68](#)
- MacQueen, R. M. 1980, *Royal Society of London Philosophical Transactions Series A*, 297, 605 [16](#)

- MacQueen, R. M., Eddy, J. A., Gosling, J. T., Hildner, E., Munro, R. H., Newkirk, G. A., Jr., Poland, A. I., & Ross, C. L. 1974, *Astrophys. J.*, 187, L85 [16](#)
- MacQueen, R. M., & Fisher, R. R. 1983a, *Sol. Phys.*, 89, 89 [28](#)
- MacQueen, R. M., & Fisher, R. R. 1983b, *Sol. Phys.*, 89, 89 [28](#)
- Manchester, W. 2003, *Journal of Geophysical Research (Space Physics)*, 108, 1162 [43](#)
- Mann, G. 1995, in *Lecture Notes in Physics*, Berlin Springer Verlag, Vol. 444, Coronal Magnetic Energy Releases, ed. A. O. Benz & A. Krüger, 183 [20](#)
- Mann, G., Klassen, A., Aurass, H., & Classen, H. 2003, *Astron. Astroph.*, 400, 329 [21](#)
- Manoharan, P. K. 1993, *Sol. Phys.*, 148, 153 [53](#), [54](#)
- Manoharan, P. K. 2006a, *Sol. Phys.*, 235, 345 [23](#)
- Manoharan, P. K. 2006b, *Sol. Phys.*, 235, 345 [68](#), [85](#), [86](#), [90](#), [114](#)
- Manoharan, P. K. 2010, *Sol. Phys.*, 265, 137 [xvii](#), [55](#)
- Manoharan, P. K., & Ananthakrishnan, S. 1990, *MNRAS*, 244, 691 [53](#)
- Manoharan, P. K., Kojima, M., & Misawa, H. 1995, *Bulletin of the Astronomical Society of India*, 23, 430 [54](#)
- Manoharan, P. K., & Kundu, M. R. 2003, *ApJ*, 592, 597 [90](#)
- Manoharan, P. K., et al. 2001, *ApJ*, 559, 1180 [56](#), [85](#), [114](#)
- Manoharan, P. K., van Driel-Gesztelyi, L., Pick, M., & Demoulin, P. 1996, *Astrophys. J.*, 468, L73 [68](#)
- Martin, S. F. 1990, in *Lecture Notes in Physics*, Berlin Springer Verlag, Vol. 363, IAU Colloq. 117: Dynamics of Quiescent Prominences, ed. V. Ruzdjak & E. Tandberg-Hanssen, 1 [14](#)

- Martin, S. F. 1998, *Sol. Phys.*, 182, 107 [14](#)
- Martin, S. F., Bilimoria, R., & Tracadas, P. W. 1994, in *Solar Surface Magnetism*, ed. R. J. Rutten & C. J. Schrijver, 303 [14](#)
- Martin, S. F., Livi, S. H. B., & Wang, J. 1985, *Australian Journal of Physics*, 38, 929 [42](#)
- Martin, S. F., & Ramsey, H. E. 1972, in *Solar Activity Observations and Predictions*, 371 [10](#)
- Marubashi, K. 1986, *Advances in Space Research*, 6, 335 [68](#)
- Masuda, S., Kosugi, T., & Hudson, H. S. 2001, *Sol. Phys.*, 204, 55 [33](#)
- Maxwell, A., Dryer, M., & McIntosh, P. 1985, *Sol. Phys.*, 97, 401 [29](#)
- McKenzie, D. E. 2002, in *Multi-Wavelength Observations of Coronal Structure and Dynamics*, ed. P. C. H. Martens & D. Cauffman, 155 [33](#)
- Melrose, D. B. 1997, *ApJ*, 486, 521 [34](#)
- Michels, D. J., Howard, R. A., Koomen, M. J., Sheeley, N. R., Jr., & Rompolt, B. 1980, in *IAU Symposium, Vol. 91, Solar and Interplanetary Dynamics*, ed. M. Dryer & E. Tandberg-Hanssen, 387 [16](#)
- Mikic, Z., Barnes, D. C., & Schnack, D. D. 1988, *ApJ*, 328, 830 [43](#)
- Mikic, Z., & McClymont, A. N. 1994, in *Astronomical Society of the Pacific Conference Series, Vol. 68, Solar Active Region Evolution: Comparing Models with Observations*, ed. K. S. Balasubramaniam & G. W. Simon, 225 [43](#)
- Milano, L. J., Dmitruk, P., Mandrini, C. H., Gómez, D. O., & Démoulin, P. 1999, *ApJ*, 521, 889 [173](#)
- Min, S., & Chae, J. 2009, *Sol. Phys.*, 258, 203 [77](#), [117](#)
- Moon, Y., Choe, G. S., Wang, H., Park, Y. D., Gopalswamy, N., Yang, G., & Yashiro, S. 2002, *ApJ*, 581, 694 [28](#)

- Moore, R. L., & Roumeliotis, G. 1992, in *Lecture Notes in Physics*, Berlin Springer Verlag, Vol. 399, IAU Colloq. 133: Eruptive Solar Flares, ed. Z. Svestka, B. V. Jackson, & M. E. Machado, 69 [39](#)
- Moore, R. L., Sterling, A. C., Hudson, H. S., & Lemen, J. R. 2001, *ApJ*, 552, 833 [39](#), [43](#)
- Möstl, C., Miklenic, C., Farrugia, C. J., Temmer, M., Veronig, A., Galvin, A. B., Vršnak, B., & Biernat, H. K. 2008, *Annales Geophysicae*, 26, 3139 [92](#)
- Munro, R. H., Gosling, J. T., Hildner, E., MacQueen, R. M., Poland, A. I., & Ross, C. L. 1979, *Sol. Phys.*, 61, 201 [27](#)
- Nakajima, H., et al. 1994, *IEEE Proceedings*, 82, 705 [63](#)
- Nandy, D. 2008, in *CS-*, Vol. 383, *Subsurface and Atmospheric Influences on Solar Activity*, ed. Howe, R., Komm, R. W., Balasubramaniam, K. S., & Petrie, G. J. D. , 201 [117](#)
- Neupert, W. M. 1968, *Astrophys. J.*, 153, L59 [153](#)
- Petschek, H. E. 1964, *NASA Special Publication*, 50, 425 [89](#)
- Pevtsov, A. A. 2002, *Sol. Phys.*, 207, 111 [15](#)
- Pevtsov, A. A., Canfield, R. C., & Zirin, H. 1996, *ApJ*, 473, 533 [68](#)
- Pizzo, V. J., et al. 2005, *Sol. Phys.*, 226, 283 [153](#)
- Plunkett, S. P., et al. 2000, *Sol. Phys.*, 194, 371 [15](#)
- Pneuman, G. W. 1981, *Two-ribbon flares - /Post/-flare loops*, ed. Priest, E. R. 379 [11](#)
- Pohjolainen, S. 2003, *Sol. Phys.*, 213, 319 [151](#)
- Pohjolainen, S., van Driel-Gesztelyi, L., Culhane, J. L., Manoharan, P. K., & Elliott, H. A. 2007, *Sol. Phys.*, 244, 167 [108](#)
- Priest, E., & Forbes, T. 2000, *Magnetic Reconnection* [67](#)

- Priest, E. R. 1981, Solar flare magnetohydrodynamics, ed. Priest, E. R. 2, 6, 7
- Priest, E. R., & Forbes, T. G. 2002, A&A Rev., 10, 313 42, 44
- Priest, E. R., & Tandberg-Hanssen, E. A. 1989, Sol. Phys., 124, 193 12
- Reeves, K. K. 2006, ApJ, 644, 592 27
- Rickett, B. J., & Coles, W. A. 1991, J. Geophys. Res., 96, 1717 54
- Roussev, I. I., Forbes, T. G., Gombosi, T. I., Sokolov, I. V., DeZeeuw, D. L., & Birn, J. 2003, Astrophys. J., 588, L45 42
- Rust, D. M., & LaBonte, B. J. 2005, Astrophys. J., 622, L69 119
- Sakai, J., & de Jager, C. 1989, Sol. Phys., 123, 389 150
- Sakai, J., & de Jager, C. 1996, Space Science Reviews, 77, 1 150, 173
- Sakai, J., Nakajima, H., Zaidman, E., Tajima, T., Kosugi, T., & Brunel, F. 1986, in NASA Conference Publication, Vol. 2449, NASA Conference Publication, ed. B. R. Dennis, L. E. Orwig, & A. L. Kiplinger, 393 176
- Sakao, T. 1994, Ph.D. thesis (University of Tokyo), (1994) 11
- Sammis, I., Tang, F., & Zirin, H. 2000, ApJ, 540, 583 40
- Schatten, K. H., Wilcox, J. M., & Ness, N. F. 1969, Sol. Phys., 6, 442 140, 160
- Scherrer, P. H., et al. 1995, Sol. Phys., 162, 129 58, 131
- Schmidt, H. U. 1964, NASA Special Publication, 50, 107 145
- Schmieder, B., & van Driel-Gesztelyi, L. 2005, in IAU Symposium, Vol. 226, Coronal and Stellar Mass Ejections, ed. K. Dere, J. Wang, & Y. Yan, 149 26
- Schumacher, J., & Kliem, B. 1997, Advances in Space Research, 19, 1797 172
- Shanmugaraju, A., Moon, Y., Dryer, M., & Umapathy, S. 2003, Sol. Phys., 217, 301 21

- Sheeley, N. R., Walters, J. H., Wang, Y., & Howard, R. A. 1999, *J. Geophys. Res.*, 104, 24739 [28](#)
- Sheeley, N. R., Jr., Howard, R. A., Koomen, M. J., & Michels, D. J. 1983, *ApJ*, 272, 349 [28](#)
- Shimizu, T., et al. 2007, *PASJ*, 59, 845 [130](#)
- Smartt, R. N., Zhang, Z., & Smutko, M. F. 1993, *Sol. Phys.*, 148, 139 [173](#)
- Smith, H. J., & Smith, E. V. P. 1963, *Solar flares*, ed. Smith, H. J. & Smith, E. V. P. [5](#)
- Somov, B. V. 1992, *Physical Processes in Solar Flares.*, Dordrecht, Boston, London; Kluwer Academic Publ. [171](#)
- Somov, B. V. 2007, *Plasma Astrophysics, Part II: Reconnection and Flares* (New York: Springer) [167](#)
- Somov, B. V., Kosugi, T., Hudson, H. S., Sakao, T., & Masuda, S. 2002, *ApJ*, 579, 863 [174](#), [177](#)
- Srivastava, A. K., Zaqarashvili, T. V., Kumar, P., & Khodachenko, M. L. 2010, *ApJ*, 715, 292 [117](#), [120](#), [124](#), [126](#), [130](#), [134](#), [143](#), [150](#)
- Srivastava, N., Mathew, S. K., Louis, R. E., & Wiegmann, T. 2009, *Journal of Geophysical Research (Space Physics)*, 114, 3107 [92](#)
- St. Cyr, O. C., & Webb, D. F. 1991, *Sol. Phys.*, 136, 379 [28](#)
- Sterling, A. C., Moore, R. L., Qiu, J., & Wang, H. 2001, *ApJ*, 561, 1116 [40](#)
- Stewart, R. T. 1985, *Moving Type IV bursts*, ed. McLean, D. J. & Labrum, N. R. 361 [23](#)
- Stix, M. 1989, *The Sun. an Introduction* [47](#)
- Sturrock, P. A., ed. 1980, *Solar flares: A monograph from SKYLAB Solar Workshop II* [2](#)

- Su, J., Liu, Y., Kurokawa, H., Mao, X., Yang, S., Zhang, H., & Wang, H. 2007, *Sol. Phys.*, 242, 53 [68](#)
- Sui, L., Holman, G. D., & Dennis, B. R. 2004, *ApJ*, 612, 546 [90](#)
- Svestka, Z. 1976, *Solar Flares*, Springer-Verlag Berlin Heidelberg [2](#), [33](#)
- Svestka, Z. 1981, *Flare observations*, ed. Priest, E. R. 47 [2](#)
- Svestka, Z. 1986, in *The lower atmosphere of solar flares; Proceedings of the Solar Maximum Mission Symposium*, Sunspot, NM, Aug. 20-24, 1985 (A87-26201 10-92). Sunspot, NM, National Solar Observatory, 1986, p. 332-355., ed. D. F. Neidig, 332 [28](#), [31](#)
- Svestka, Z., Jackson, B. V., & Machado, M. E., ed. 1992, *Lecture Notes in Physics*, Berlin Springer Verlag, Vol. 399, *Eruptive Solar Flares* [2](#), [3](#), [4](#)
- Swarup, G., Kapahi, V. K., Sarma, N. V. G., Krishna, G., Joshi, M. N., & Rao, A. P. 1971, *APJL*, 9, 53 [xvi](#), [50](#), [51](#)
- Sweet, P. A. 1958, in *IAU Symposium*, Vol. 6, *Electromagnetic Phenomena in Cosmical Physics*, ed. B. Lehnert, 123 [40](#)
- Tajima, T., Brunel, F., & Sakai, J. 1982, *Astrophys. J.*, 258, L45 [173](#)
- Takano, T., et al. 1997, in *Lecture Notes in Physics*, Berlin Springer Verlag, Vol. 483, *Coronal Physics from Radio and Space Observations*, ed. G. Trottet, 183 [xvii](#), [63](#), [64](#)
- Tan, C., Chen, P. F., Abramenko, V., & Wang, H. 2009, *ApJ*, 690, 1820 [150](#)
- Tanaka, K., & Nakagawa, Y. 1973, *Sol. Phys.*, 33, 187 [42](#)
- Tandberg-Hanssen, E., & Emslie, A. G. 1988, *The physics of solar flares*, Cambridge University Press [2](#), [8](#), [10](#), [11](#)
- Tang, F. 1986, *Sol. Phys.*, 105, 399 [15](#)
- Tappin, S. J., 34, 93 [54](#)

- Tian, L., & Alexander, D. 2006, *Sol. Phys.*, 233, 29 [89](#)
- Tian, L., & Alexander, D. 2009, *ApJ*, 695, 1012 [138](#)
- Titov, V. S., & Démoulin, P. 1999, *Astron. Astroph.*, 351, 707 [36](#), [139](#)
- Török, T., & Kliem, B. 2005, *Astrophys. J.*, 630, L97 [145](#), [146](#), [147](#)
- Török, T., Kliem, B., & Titov, V. S. 2004, *Astron. Astroph.*, 413, L27 [117](#), [139](#), [143](#), [145](#)
- Tousey, R. 1973, in *Space Research*, ed. M. J. Rycroft & S. K. Runcorn, 713 [16](#)
- Tsuneta, S. 1996, *ApJ*, 456, 840 [33](#)
- Tsuneta, S., Hara, H., Shimizu, T., Acton, L. W., Strong, K. T., Hudson, H. S., & Ogawara, Y. 1992, *PASJ*, 44, L63 [11](#)
- Tsuneta, S., et al. 2008a, *Sol. Phys.*, 249, 167 [61](#)
- Tsuneta, S., et al. 2008b, *Sol. Phys.*, 249, 167 [124](#)
- Tsuneta, S., Masuda, S., Kosugi, T., & Sato, J. 1997, *ApJ*, 478, 787 [159](#)
- Tsurutani, B. T., Smith, E. J., Gonzalez, W. D., Tang, F., & Akasofu, S. I. 1988, *JGR*, 93, 8519 [92](#)
- Švestka, Z. 2001, *Space Sci. Rev.*, 95, 135 [28](#)
- van Driel-Gesztelyi, L., Schmieder, B., & Poedts, S. 2002, in *ESA Special Publication, Vol. 477, Solspa 2001, Proceedings of the Second Solar Cycle and Space Weather Euroconference*, ed. H. Sawaya-Lacoste, 47 [89](#)
- van Tend, W., & Kuperus, M. 1978, *Sol. Phys.*, 59, 115 [145](#)
- Vourlidis, A., Buzasi, D., Howard, R. A., & Esfandiari, E. 2002, in *ESA Special Publication, Vol. 506, Solar Variability: From Core to Outer Frontiers*, ed. A. Wilson, 91 [18](#)
- Vršnak, B., & Lulić, S. 2000a, *Sol. Phys.*, 196, 157 [20](#)

- Vršnak, B., & Lulić, S. 2000b, *Sol. Phys.*, 196, 181 [20](#)
- Vršnak, B., Sudar, D., & Ruždjak, D. 2005, *Astron. Astroph.*, 435, 1149 [28](#)
- Wang, H., Ji, H., Schmahl, E. J., Qiu, J., Liu, C., & Deng, N. 2002, *Astrophys. J.*, 580, L177 [118](#)
- Wang, H., Liu, C., Qiu, J., Deng, N., Goode, P. R., & Denker, C. 2004, *Astrophys. J.*, 601, L195 [136](#), [147](#)
- Wang, Y., Zhou, G., Ye, P., Wang, S., & Wang, J. 2006, *ApJ*, 651, 1245 [115](#)
- Webb, D. F., & Hundhausen, A. J. 1987, *Sol. Phys.*, 108, 383 [28](#)
- Williams, D. R., Török, T., Démoulin, P., van Driel-Gesztelyi, L., & Kliem, B. 2005, *Astrophys. J.*, 628, L163 [119](#)
- Wu, S. T. 1982, *Space Sci. Rev.*, 32, 115 [37](#)
- Wu, S. T., Guo, W. P., Michels, D. J., & Burlaga, L. F. 1999, *J. Geophys. Res.*, 104, 14789 [42](#)
- Wuelser, J., et al. 2004, in *Society of Photo-Optical Instrumentation Engineers*, ed. Fineschi, S. & Gummin, M. A., *SPIE CS-5170*, 111 [63](#), [126](#)
- Yan, X., Qu, Z., & Kong, D. 2008, *MNRAS*, 391, 1887 [68](#)
- Yashiro, S., Gopalswamy, N., & Akiyama, S. 2008, *AGU Spring Meeting Abstracts*, A3 [120](#)
- Yokoyama, T., Akita, K., Morimoto, T., Inoue, K., & Newmark, J. 2001a, *Astrophys. J.*, 546, L69 [74](#)
- Yokoyama, T., Akita, K., Morimoto, T., Inoue, K., & Newmark, J. 2001b, *Astrophys. J.*, 546, L69 [160](#)
- Yokoyama, T., & Shibata, K. 2001, *ApJ*, 549, 1160 [33](#)
- Yurchyshyn, V., Yashiro, S., Abramenko, V., Wang, H., & Gopalswamy, N. 2005, *ApJ*, 619, 599 [18](#)

REFERENCES

- Zarro, D. M., Sterling, A. C., Thompson, B. J., Hudson, H. S., & Nitta, N. 1999, *Astrophys. J.*, 520, L139 [85](#)
- Zhang, J., Dere, K. P., Howard, R. A., Kundu, M. R., & White, S. M. 2001, *ApJ*, 559, 452 [29](#), [37](#)
- Zhang, M., & Chye Low, B. 2005, *ARA&A*, 43, 103 [43](#), [68](#)
- Zhang, Y., Liu, J., & Zhang, H. 2008, *Sol. Phys.*, 247, 39 [68](#)
- Zirin, H. 1983, *ApJ*, 274, 900 [42](#)